Characterizing Ultra-hot Jupiters Through Theoretical Modelling and Precise Observations

Taylor James Bell

Doctor of Philosophy

McGill Space Insitute & Department of Physics

McGill University

Montréal, Québec

July 26, 2021

A thesis submitted to McGill University in partial fulfillment of the requirements of the degree of Doctor of Philosophy, Physics.

Abstract

Over the past few years, the exoplanet research community has been discovering that hot Jupiters with dayside temperatures above $\sim$2500 K exhibit distinct characteristics compared to their cooler peers. My thesis work provided new insights into the atmospheric composition and circulation of these "ultra-hot Jupiters" through physical modelling and space-based observations of their eclipses and phase variations.

With the second-ever spectrally resolved optical eclipse observation of an exoplanet, I showed that the dayside of the ultra-hot Jupiter WASP-12b was devoid of clouds and consisted primarily of atomic hydrogen and helium. This showed that the dayside atmospheres of ultra-hot Jupiters are similar to those of stars, with most molecules—including the dominant constituent H_2—becoming thermally dissociated. Realizing that the enormous day–night temperature contrast in ultra-hot Jupiter atmospheres would result in H from the dayside recombining into H_2 nearer the nightside, I developed a semi-analytical model of the thermodynamics of this process. This model qualitatively explained the unusually large phase offsets of WASP-12b and WASP-33b known at the time and successfully predicted the large phase offset and hot nightside temperature of KELT-9b.

I then co-wrote SPCA, an open-source pipeline for Spitzer phase curve observations, which I used to show that the highly unusual phase curve of WASP-12b was reproducible and was best explained by CO emission from a stream of gas being stripped from the planet. By leading the analyses of the new phase curves of ultra-hot Jupiters KELT-16b and MASCARA-1b, I explored the impact of differing Coriolis forces on hot Jupiter atmospheric circulation. Finally, I used SPCA to perform the first comprehensive reanalysis of 4.5 μm Spitzer phase curves, which showed that phase curve parameters are usually independent of the detector model used and that literature values were typically reproducible. I also confirmed population-level trends such as that of dayside and nightside temperatures with irradiation temperatures, clearly demonstrating the unusual behaviour of ultra-hot Jupiters.

This work provides a strong foundation for future observational studies of atmospheric phenomena, with an emphasis on improving reproducibility and progressing towards studies spanning a wider range of planetary properties.

Abrégé

Au cours des dernières années, la communauté de recherche sur les exoplanètes a découvert que les Jupiters chauds avec des températures diurnes supérieures à ∼2500 K présentent des caractéristiques distinctes par rapport à leurs amis plus froids. Mon travail de thèse a fourni de nouvelles perspectives sur la composition atmosphérique et la circulation de ces «Jupiters ultra-chauds» à travers la modélisation physique et les observations du télescope spatial de leurs éclipses et variations de phase.

Avec la deuxième observation d'éclipse optique résolue spectralement d'une exoplanète, j'ai montré que le côté jour du Jupiter WASP-12b ultra-chaud était dépourvu de nuages et se composait principalement d'hydrogène atomique et d'hélium. Cela a montré que les atmosphères diurnes des Jupiters ultra-chauds sont similaires à celles des étoiles, la plupart des molécules—y compris le constituant dominant H_2—devenant thermiquement dissociées. Réaliser que l'énorme contraste de température entre le côté jour et le côté nuit des atmosphères ultra-chaudes de Jupiter entraînerait la recombinaison de H du côté jour en H_2 plus près de la nuit, j'ai développé un modèle semi-analytique de la thermodynamique de ce processus. Ce modèle a expliqué qualitativement les décalages de phase inhabituellement grands de WASP-12b et WASP-33b connus à l'époque et a prédit avec succès le grand décalage de phase et la température chaude nocturne du KELT-9b.

J'ai ensuite co-écrit SPCA, un pipeline open-source pour les observations de la courbe de phase de Spitzer, que j'ai utilisé pour montrer que la courbe de phase très inhabituelle de WASP-12b était reproductible et était mieux expliquée par l'émission de CO d'un flux de gaz extrait de la planète. En menant les analyses des nouvelles courbes de phase des Jupiters ultra-chauds KELT-16b et MASCARA-1b, j'ai exploré l'impact des différentes forces de Coriolis sur la circulation atmosphérique de Jupiter chaud. Enfin, j'ai utilisé SPCA pour effectuer la première réanalyse complète des courbes de phase Spitzer 4,5 μm, qui ont montré que les paramètres de la courbe de phase sont généralement indépendants du modèle de détecteur utilisé et que les valeurs publiées étaient généralement reproductibles. De plus, j'ai confirmé les tendances au niveau de la population telles que celle des températures de jour et de nuit avec des températures d'irradiation, démontrant clairement le comportement inhabituel des Jupiters ultra-chauds.

Ces travaux fournissent une base solide pour les futures études d'observation des phénomènes atmosphériques, en mettant l'accent sur l'amélioration de la reproductibilité et la progression vers des études couvrant un plus large éventail de propriétés planétaires.

Table of Contents

I like stars more than anything else. I watch them as I fall asleep and wonder who lives on them and how to get there. The night sky looks so friendly with all those little twinkling eyes.

– Snufkin, from the book Comet in Moominland; Tove Jansson, 1951.

Acknowledgements

First, I want to thank my thesis supervisor, Nicolas Cowan, for providing years of research, professional, financial, and emotional support. Nick has been an ideal supervisor for me, and I will forever be grateful for his support and encouragement. I also want to thank Pierre Bastien who introduced me to the exciting field of high-precision polarimetry during long nights at the beautiful Mont Mégantic Observatory. I am also extremely grateful for the support and friendships I have found in my fellow graduate students in Nick's research group and especially to Lisa Dang and Dylan Keating with whom I've worked closely throughout my degree. Thanks also to the many members of the McGill Space Institute and the Institute for Research on Exoplanets for fostering such friendly and interactive communities; I have missed you all so much during this time of physical isolation.

Next, I would like to thank my undergraduate mentor, Stan Shadick, who first showed me the patterns in night sky and sparked my research interests in observational astronomy and exoplanets. Without Stan's encouragement, I would not have pursued undergraduate research opportunities, and I am confident I would not be where I am today without his kindness and support. I also want to thank my undergraduate research supervisors Doug Welch, Alison Sills, Allison Noble, and Howard Yee for teaching me how to approach research problems and to become comfortable with the uncertainty inherent in performing novel research. I also want to thank my many collaborators throughout the years who routinely make strong, positive contributions to my work.

I would also like to thank my immediate and extended family members for their never-ending and enthusiastic support and encouragement. I am especially indebted to my parents Dawn Bell and Trevor Bell and their financial and emotional support as well as their frequent reminders that "it doesn't need to be perfect" and to be willing to go where life leads me. I am also exceedingly grateful to my partner Ksenia Kolosova for her years of emotional and professional support and for grounding my thoughts when the years of built-up academic stress start to show.

Finally, I want to thank all those who made my work possible through more physical means. During my graduate studies, I was funded by the McGill Space Institute Graduate Fellowship (09/2016–08/2017) and by the NSERC Postgraduate Scholarships-Doctoral Program (09/2018–09/2021). I also received financial support from the Centre for Research in Astrophysics of Quebec, the Fonds de recherche du Québec – Nature et technologies, and the Technologies for Exo-Planetary Science NSERC CREATE program. I also want to thank the Department of Physics for their shared computing resources without which my last paper would have been near impossible. I also want to thank those responsible for planning, funding, launching, and operating the *Hubble* and *Spitzer* space telescopes whose data is the foundation of my research. Relatedly, I want to thank those who donate their time to the time allocation committees on which these great observatories depend. I also want to thank the many communities who have developed open-source and easy-to-use Python software, and especially those who contributed to the following packages: `numpy`, `matplotlib`, `scipy`, `astropy`, `emcee`, and `george`.

Contribution of Authors

This manuscript-based thesis is based on original work from four previously-published manuscripts for which I, T. J. Bell, was the first author. The contributions made by myself and all co-authors are described in detail below. All other sections are included to provide additional context for these manuscripts and to unite them into a single body of work; the contents of these additional sections represent original work by myself and have not been previously published. Nicolas B. Cowan was my thesis research supervisor and edited the thesis.

Paper 1: The Very Low Albedo of WASP-12b from Spectral Eclipse Observations with *Hubble*

Paper 1 was published as Bell et al. (2017) with co-authors N. Nikolov, N. B. Cowan, J. K. Barstow, T. S. Barman, I. J. M. Crossfield, N. P. Gibson, T. M. Evans, D. K. Sing, H. A. Knutson, T. Kataria, J. D. Lothringer, B. Benneke, and J. C. Schwartz. I led the writing of this publication. N. Nikolov performed the initial data reduction which consisted of extracting flux and other parameters from the raw *Hubble* images; N. Nikolov also wrote two paragraphs of the Observations and Data Reduction section detailing the data reduction. I then fitted different detector and astrophysical models to the reduced observations. J. K. Barstow provided the predictive `NEMISIS` models and T. S. Barman provided the predictive `PHOENIX` models, and T. S. Barman assisted in the interpretation of the *Hubble* observations in the context of the `NEMISIS` and `PHOENIX` model predictions. N. B. Cowan provided guidance throughout and contributed significant typographical edits. All authors aside from myself were investigators on the *Hubble* proposal (led by I. J. M. Crossfield) that procured these observations and contributed minor edits.

Paper 2: Increased Heat Transport in Ultra-hot Jupiter Atmospheres Through H_2 Dissociation/Recombination

Paper 2 was published as Bell & Cowan (2018) with co-author N. B. Cowan. I led the writing of this publication. The idea of modelling the thermodynamic effects of H_2 dissociation/recombination came from my initial attempts to model H^- opacity based on the findings of Bell et al. (2017) to propose for a *Spitzer* phase curve of the ultra-hot Jupiter KELT-9b. Together, myself and N. B. Cowan realized that the process of H_2 dissociation/recombination could have important thermodynamic effects on the atmospheres of ultra-hot Jupiters in a manner similar to latent heat from water vapour in the Earth's atmosphere. I led the development of the semi-analytical model used to describe this process in the atmospheres of ultra-hot Jupiters with guidance from N. B. Cowan. The numerical model used in this work was initially based on code previously written for Schwartz et al. (2017), but I later re-wrote the model in a separate, self-contained, object-oriented, and well-documented package (`Bell_EBM`) that can be accessed at `https://github.com/taylorbell57/Bell_EBM`. N. B. Cowan contributed significant typographical edits.

Paper 3: Mass Loss from the Exoplanet WASP-12b Inferred from *Spitzer* Phase Curves

Paper 3 was published as Bell et al. (2019) with co-authors M. Zhang, P. E. Cubillos,

L. Dang, L. Fossati, K. O. Todorov, N. B. Cowan, D. Deming, R. T. Zellem, K. B. Stevenson, I. J. M. Crossfield, I. Dobbs-Dixon, J. J. Fortney, H. A. Knutson, and M. R. Line. I led the writing of this publication. L. Dang and I co-wrote the `SPCA` pipeline that was used for the work described in Section 3.2.2 as "T. Bell's Reduction and Decorrelation Procedure". L. Dang developed the initial foundation used by this pipeline when writing Dang et al. (2018), and I improved upon and generalized this code to work for WASP-12b and significantly built upon the pipeline (see also the description of Paper 4). I also guided M. Zhang and P. E. Cubillos who provided independent analyses to further strengthen the work's claims. M. Zhang wrote the text in section 3.2.1 and P. E. Cubillos wrote the text in section 3.2.3, while I wrote nearly all of the remainder of the manuscript. L. Fossati assisted in evaluating the feasibility of the mass loss and radiation hypothesis that I developed. R. T. Zellem contributed one sentence in section 4.2.2 describing expected levels of stellar variability. K. B. Stevenson evaluated the dilution correction method used in this work leading to the discovery of an error in the dilution correction used by Stevenson et al. (2014). N. B. Cowan provided guidance throughout and contributed significant typographical and layout edits. K. O. Todorov led the *Spitzer* proposal which provided the repeated phase curve observation, and D. Deming, H. A. Knutson; J. J. Fortney were co-investigators on that proposal. All authors contributed minor edits.

Paper 4: A Comprehensive Reanalysis of *Spitzer*'s 4.5 μm Phase Curves, and the Phase Variations of the Ultra-hot Jupiters MASCARA-1b and KELT-16b

Paper 4 was published as Bell et al. (2021) with co-authors L. Dang, N. B. Cowan, J. Bean, J-M. Désert, J. J. Fortney, D. Keating, E. Kempton, L. Kreidberg, M. R. Line, M. Mansfield, V. Parmentier, K. B. Stevenson, M. Swain, R. T. Zellem. I led the writing of this publication with minor edits provided by all co-authors. L. Dang and I co-wrote the `SPCA` pipeline (as described above for Paper 3), and I made significant improvements to, and generalizations upon, the `SPCA` pipeline after publishing Paper 3 in preparation for Bell et al. (2021). These changes significantly increased the automatability, readability, and computational speed of the `SPCA` pipeline which were required to perform the hundreds of phase curve model fits performed for this work. I led the reduction and analyses of all 17 phase curves presented in this work and the discussions on model comparisons, comparisons to literature values, and population level trends. K. B. Stevenson assisted in resolving the discrepancies between previous analyses of WASP-43b's phase curve and provided additional insight into the optimization routine used by the `POET` pipeline on which `SPCA`'s BLISS algorithm is based. N. B. Cowan contributed significant typographical edits. J. Bean led the *Spitzer* proposal which provided the new phase curves of MASCARA-1b and KELT-16b, and all co-authors were co-investigators on that proposal.

Introduction

Thirty-three years ago, a team of Canadian astronomers discovered the first extrasolar planetary candidate orbiting the star Gamma Cephei A (Campbell et al., 1988). Although not confirmed until later (Hatzes et al., 2003), this first candidate was reminiscent of our own Solar System with a Jupiter-mass planet orbiting at several times the Earth-Sun distance on a nearly circular orbit about a star only $\sim$1000 K colder than the Sun. However, any sense of comfort that may have been afforded by the familiarity of this first exoplanetary candidate was rapidly shattered by the first two confirmed exoplanets which were found orbiting around a stellar corpse: the millisecond pulsar PSR1257+12 (Wolszczan & Frail, 1992). From then on, the study of exoplanets has been filled with surprises.

One of the earliest surprises was the detection of a gas giant exoplanet in close proximity to the star 51 Pegasi (Mayor & Queloz, 1995) which later earned the authors a Nobel Prize in Physics. The exoplanet, called 51 Pegasi b, was the archetype of a new class of exoplanets that were initially called "51 Pegasi type" planets but are now known as hot Jupiters. Hot Jupiters are some of the most easily detectable and characterizable planets due to their short orbital periods, large masses, large radii, and low density atmospheres. As such, hot Jupiters have been the focus of most atmospheric characterization efforts and have provided a sandbox for developing new characterization techniques and algorithms.

More recently, we have realized that hot Jupiters with dayside temperatures $\gtrsim$2500 K are qualitatively different beasts than their cooler cousins. In the atmospheres of these "ultra-hot Jupiters", many of the molecules—including the dominant constituent H_2—will thermally dissociate on the dayside (e.g., Arcangeli et al., 2018; Bell & Cowan, 2018; Kreidberg et al., 2018; Lothringer et al., 2018; Parmentier et al., 2018; Tan & Komacek, 2019) and recombine on the nightside (Bell & Cowan, 2018; Komacek & Tan, 2018; Parmentier et al., 2018; Tan & Komacek, 2019). This has first-order implications for both radiative transfer and thermodynamics such as introducing star-like opacity sources, transporting additional heat toward the nightside, and inflating the dayside atmosphere. In essence, the dayside of an ultra-hot Jupiter is star-like, while the nightside remains planet-like. My thesis research seeks to gain a better understanding of these alien worlds through high-precision, space-based observations and theoretical modelling.

In this thesis, I first provide an overview of the core and related concepts used throughout the following chapters in the Background. In Paper 1, I use *Hubble*/STIS low-resolution spectroscopy to study the light reflected by the ultra-hot Jupiter WASP-12b. In Paper 2, I develop a new theory for heat transport in the atmospheres of ultra-hot Jupiters. Paper 3 presents the highly unusual phase curve observations of WASP-12b. In Paper 4, I perform the first comprehensive reanalysis of *Spitzer*/IRAC phase curve observations. Each paper includes a preface which briefly introduces the paper and an epilogue which summarizes any related work I have completed since the publication of the paper. Finally, the Discussion and Conclusion chapter presents a comprehensive discussion, briefly summarizes later work influenced by the findings of Papers 1–4, and discusses the future outlook of the field of exoplanetary atmospheric characterization.

Background

1 Exoplanetary Atmospheric Dynamics and Thermal Structure

The collection of known exoplanets span an enormous range in irradiation levels, with the coldest known exoplanet having a radiative equilibrium temperature of $\sim$30 K (Bond et al., 2017; Shvartzvald et al., 2017) and the hottest known exoplanet having a radiative equilibrium temperature of $\sim$4600 K (Gaudi et al., 2017). Even on a single exoplanet, temperature gradients of hundreds to thousands of Kelvin are possible (e.g., Gaudi et al., 2017). By studying the thermal structure and atmospheric dynamics of diverse exoplanetary atmospheres, we can test theories constructed from Earth and Solar System observations in completely new temperature regimes. Overviews of exoplanetary irradiation, atmospheric dynamics, and temperature-pressure profiles are included below.

1.1 Radiative Forcing

For rapidly rotating planets like the Earth, incident stellar radiation can be approximated as being longitudinally uniform while irradiation becomes weaker towards the poles as the surface of the planet makes an increasingly oblique angle to the incident flux (in the absence of planetary obliquity). When combined with an adequately large heat capacity to slow cooling, this results in only minor diurnal temperature changes but a large equator-to-pole temperature difference. These latitudinal temperature differences drive atmospheric circulation which seeks to transport energy towards the poles.

Meanwhile, slowly rotating planets will show significant longitudinal temperature differences as the surface and/or atmosphere of the planet is able to cool significantly between periods of irradiation. On these planets, the primary force driving atmospheric flows are longitudinal temperature differences. In the limit, planets can have rotation periods that match their orbital periods (called synchronous rotation, a special form of tidal locking) which results in one side of the planet being permanently illuminated, the "dayside", while the other side of the planet is in permanent shadow, the "nightside" (see the left panel of Figure 1 for the illumination pattern of synchronously rotating planets). This is assumed to be the case for nearly all short-period exoplanets as tidal forces are expected to rapidly synchronize their orbital and rotational period and then later circularize their orbits (e.g., Rasio et al., 1996).

1.2 Modelling Heat Transport

Guided by the Second Law of Thermodynamics, winds in a planet's atmosphere tend to homogenize the atmosphere's temperature in response to longitudinal and/or latitudinal temperature gradients. Most simply, the effectiveness of atmospheric heat transport can be thought of as a competition between the timescale for advection to transport energy from the hot to the cold regions of the atmosphere ($\tau_{\rm adv}$) and the timescale for thermal radiation into the blackness of space to cool the hot gas ($\tau_{\rm rad}$). For planets where $\tau_{\rm adv} \gg \tau_{\rm rad}$, atmospheric heat transport is inefficient and large temperature gradients will persist. Meanwhile, for planets where $\tau_{\rm adv} \ll \tau_{\rm rad}$, atmospheric heat transport is efficient and only small temperature gradients will remain.

Many different tools have been developed to model the atmospheric response to non-uniform irradiation. The simplest of these are called "energy balance models" (EBMs)

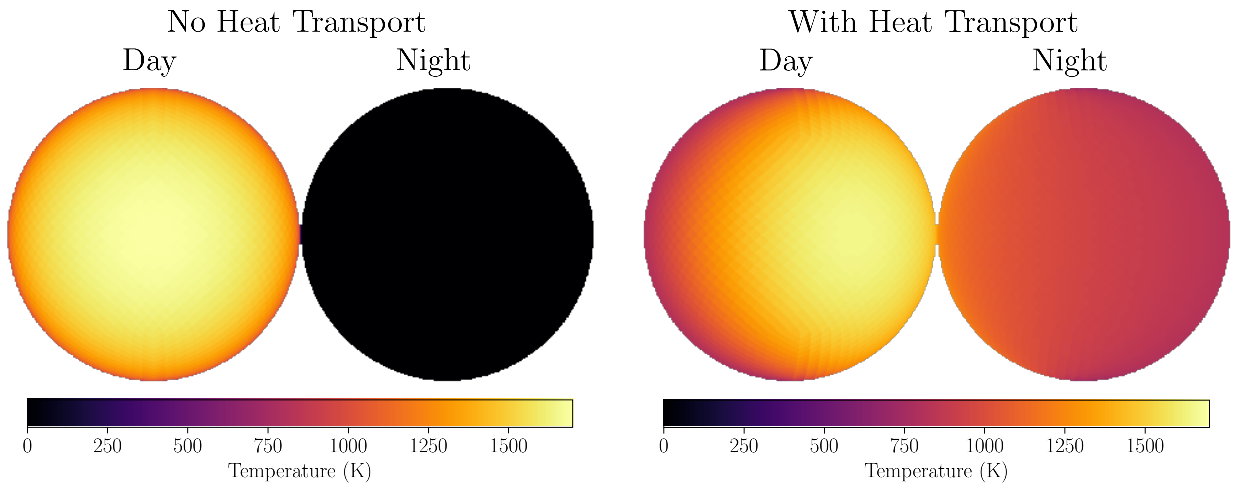

Figure 1: Energy balance models (EBMs) of the hot Jupiter HD 189733b showing atmospheric temperatures without atmospheric heat transport (*left*) and with atmospheric heat transport set to match the planet's observed 4.5 μm Spitzer/IRAC phase curve (*right*; Knutson et al., 2012). Note the eastward offset of the hottest point on the planet in the right panel, which matches earlier predictions from general circulation models (e.g., Showman & Guillot, 2002).

and use a simple prescription for heat transport rather than computing atmospheric flows (e.g. Pierrehumbert, 2010; Cowan & Agol, 2011b). EBMs also reduce the dimensionality of the atmosphere by assuming that an entire vertical column of the atmosphere can be described with a single temperature and sometimes by neglecting longitudinal variations (e.g. in models of the Earth's atmosphere). Due to their many simplifying assumptions, EBMs are computationally easy to run but do not provide a great deal of insight into the atmospheric dynamics. See the right panel of Figure 1 for an EBM model of the hot Jupiter HD 189733b with longitudinal atmospheric heat transport set to match the planet's observed 4.5 μm Spitzer/IRAC phase curve (Knutson et al., 2012).

Meanwhile, full 3D general circulation models (GCMs) seek to model the fluid dynamics underlying heat transport in exoplanetary atmospheres. A wide variety of GCMs exist with varying levels of simplifications. GCMs also include different prescriptions for radiative transfer to model the absorption and emission of photons in the atmosphere. A common approximation made in radiative transfer simulations is the two-stream approximation where latitudinal and longitudinal radiative transfer is neglected since the depth of the atmosphere which is affected by stellar heating is much smaller than the radius of the planet (Heng, 2017). In this approach, one first integrates over all incoming and outgoing radiation separately (the two streams) which results in two ordinary differential equations with three dependent variables; this under-constrained problem is remedied by assuming a set of Eddington coefficients which relate total fluxes and intensities (Heng, 2017). In addition, rather than treating the full wavelength dependence of the radiative transfer calculations, it is common to use a double-grey approximation where the incident starlight is approximated as "shortwave radiation" (SW) and the light emerging from the planet is approximated as "outgoing longwave radiation" (OLR); these approximations are based on the fact that hot stars emit the majority of their blackbody radiation at optical wavelengths while the much cooler planets radiate primarily at infrared wavelengths. The OLR and SW are then each treated as single wavelengths with different effective absorption and scattering coefficients. Clouds are typically post-processed, meaning the model is run with clear skies and then the effect of clouds on the incoming and outgoing radiation is added afterwards (e.g., Parmentier et al., 2016). With increasing computation power, however, it is becoming possible to remove many of these simplifications (e.g., Lines et al., 2018, which solves the full 3D Navier-Stokes equations using a detailed radiative transfer model and includes a radiatively active model of cloud formation). By comparing models with different levels of simplifying assumptions, it is possible to investigate the role of different effects on atmospheric heat transport.

One of the most ubiquitous predictions from GCMs for hot Jupiter atmospheres is the presence of an eastward equatorial jet that flows more rapidly than the interior of the planet (e.g., Showman & Guillot, 2002; Langton & Laughlin, 2008; Showman et al., 2009; Dobbs-Dixon et al., 2010; Heng et al., 2011; Rauscher & Menou, 2012). This equatorial jet is the result of interactions between atmospheric winds and standing Rossby waves formed by the strong longitudinal temperature gradients present on synchronously rotating planets (Showman & Polvani 2011, but see also Hammond & Pierrehumbert 2018). The rotated orientation of the Rossby waves act to pump eastward momentum from higher latitudes towards the equator which accelerates the winds at the equator, and a superrotating jet is formed (Showman & Polvani, 2011). This eastward equatorial jet shifts the hottest part of the atmosphere (sometimes called the hot spot) east of the sub-stellar point. The latitudinal extent of this jet is expected to change with the planetary rotation period, with more rapidly rotating planets having stronger Coriolis forces and hence a more confined jet and weaker day–to–night heat transport (e.g., Komacek et al., 2017). Models also predict that hotter planets should have smaller hot spot offsets and larger day–night temperature contrasts because the radiative timescale decreases with increasing temperature which leads to less efficient heat transport by atmospheric waves (Perez-Becker & Showman, 2013). The predicted eastward shift has been repeatedly observed using the phase curve technique (described below; starting with Knutson et al., 2007), but CoRoT-2b has been found to be inconsistent with this prediction with a hottest hemisphere that is significantly shifted to the west (Dang et al., 2018). While there appears to be a weak correlation between day–night temperature contrast in the observed sample of hot Jupiters, it appears to be far more complicated than has been predicted (e.g., Schwartz et al., 2017; Zhang et al., 2018).

Additionally, it has long been known that the atmospheric dynamics of hot Jupiters are partially governed by interactions with planetary magnetic fields (Perna et al., 2010a; Menou, 2012a,b; Rauscher & Menou, 2013; Batygin & Stanley, 2014; Rogers & Showman, 2014; Rogers & Komacek, 2014; Rogers, 2017). For hot Jupiters with temperatures of 1000–2000 K, atmospheric interactions with magnetic fields would primarily manifest as magnetic drag which reduces atmospheric heat transport (Perna et al., 2010a), possibly accompanied by Ohmic dissipation at depth. Ohmic dissipation is arguably responsible for the inflation of hot Jupiters (e.g., Batygin & Stevenson, 2010; Perna et al., 2010b); this would require strong planetary magnetic fields (Rogers & Komacek, 2014) which is consistent with recent observational studies (Cauley et al., 2019). Magnetic effects are expected to be even stronger for the population of ultra-hot Jupiters whose atmospheres are highly ionized (e.g., Tan & Komacek, 2019). However, observations of most hot Jupiters are significantly complicated by the presence of clouds (e.g., Dang et al., 2018; Keating et al., 2019; Beatty et al., 2019; Parmentier et al., 2020; Roman et al., 2021), making it impossible to clearly identify the impact of magnetic fields in typical hot Jupiter atmospheres. For example, Armstrong et al. (2016) reported a time-variable phase curve offset for the hot Jupiter HAT-P-7b which they attributed to variable clouds (see also, Lines et al., 2018, 2019) but which could also be caused by magnetohydrodynamic (MHD) effects (Rogers, 2017).

Very few MHD simulations of hot Jupiters have been performed due to their much higher computational cost and, more importantly, the numerical challenge of modelling non-ideal MHD across a large range of conditions and relevant timescales. Additionally, none of those simulations explicitly simulate the impact of MHD effects on observable properties as they were not run with realistic radiative transfer. Comprehensive hydrodynamic simulations without magnetic effects, on the other hand, routinely incorporate realistic radiative transfer (e.g., cloud-free, multi-wavelength radiative transfer, but no magnetic effects: Showman et al., 2009). Those hydrodynamic models that do model magnetic effects treat them as either a global or temperature-dependent magnetic drag timescale (e.g., double-gray radiative transfer but self-consistent magnetic drag and Ohmic dissipation: Rauscher & Menou, 2013). In order to more fully understand magneto-atmospheric interactions, further work is required to develop self-consistent, non-ideal MHD models as current models are unable to handle the orders of magnitude differences in conductivity that result from the hundreds to thousands of Kelvin day–night temperature contrasts present in hot Jupiter atmospheres.

1.3 Temperature-Pressure Profiles

Changes in temperature also occur with altitude in a planet's atmosphere. These changes are most commonly described as a function of pressure (called a temperature-pressure profile) rather than altitude as pressure plays an important role in controlling atmospheric opacity, and atmospheric pressure monotonically decreases with increasing altitude. Assuming hydrostatic equilibrium of an ideal gas under constant gravity and with constant temperature, atmospheric pressure as a function of height is typically described using the following equation:

$$P(z) = P_0 \exp\left(-\frac{z}{H}\right),$$

where z is altitude, P_0 is the pressure at $z = 0$. The atmospheric scale height, H, is calculated using

$$H = \frac{k_\mathrm{B} T}{\mu g}, \tag{1}$$

where k_B is the Boltzmann constant, T is the mean atmospheric temperature, μ is the mean molecular weight, and g is the gravitational acceleration.

On Earth, those experienced with mountain climbing will know that temperature decreases with altitude. Initially, this may seem surprising as it is also a well known fact that hot air rises (for example, the steam from a boiling pot rises), so one may wonder why it is stable to have temperature decreasing with altitude. However, it can be shown that adiabatically moving a parcel of hot gas from lower altitudes to higher altitudes will cause the parcel of gas to expand due to the decrease in atmospheric pressure and, in doing so, the parcel will cool. Indeed, the convective layers of planetary atmospheres tend to have adiabatic temperature-pressure profiles.

It is therefore surprising that observations of the Earth's atmosphere (and also, for example, the atmospheres of Jupiter, Titan, and many exoplanets) show that this trend of decreasing temperature with increasing altitude (or equivalently decreasing pressure) does not continue throughout the entire atmosphere (Assmann, 1902; Teisserenc de Bort, 1902, see also Figure 2). Instead, it is seen that atmospheric temperature begins to increase with decreasing pressure high up in some planetary atmospheres; on Earth this region is called the stratosphere, and more generally it is called a temperature inversion. Temperature inversions occur when something in the atmosphere absorbs a significant amount of the short wavelengths of incoming stellar irradiation, causing a localized heating; on Earth, this absorber is ozone, while it has been suggested that TiO, VO, SiO, atomic metals, metal hydrides, and H^- could be the cause of temperature inversions in hot Jupiter atmospheres (Hubeny et al., 2003; Fortney et al., 2008; Lothringer et al., 2018).

Temperature-pressure profiles play an important role in defining the spectral features seen in observations of the thermal emission from planetary atmospheres. In the absence of any wavelength-dependent scattering or absorbing mechanisms, all wavelengths of light would originate from the same parts of the atmosphere. However, atmospheres contain atoms, ions, and molecules which absorb only at specific wavelengths; at these wavelengths, the planet's emission originates from higher in the atmosphere due to the increased atmospheric opacity. In the absence of a temperature inversion, this would cause the planet to appear fainter at these wavelengths due to the colder temperature at lower pressures (higher altitudes); the decrease in planetary flux at these wavelengths would be called an absorption feature. For an example of absorption features in the Earth's emission spectrum, see Figure 3. Meanwhile, in the presence of a temperature inversion, the planet would appear brighter at wavelengths where there is increased atmospheric absorption; the increase in planetary flux at these wavelengths would be called an emission feature.

2 Exoplanetary Atmospheric Composition

While the Solar System contains a wide variety of planets and atmospheres, the diversity among exoplanets is far greater. The formation and evolution of these exoplanets posed a significant challenge to models of the Solar System's formation with the presence of gas giant

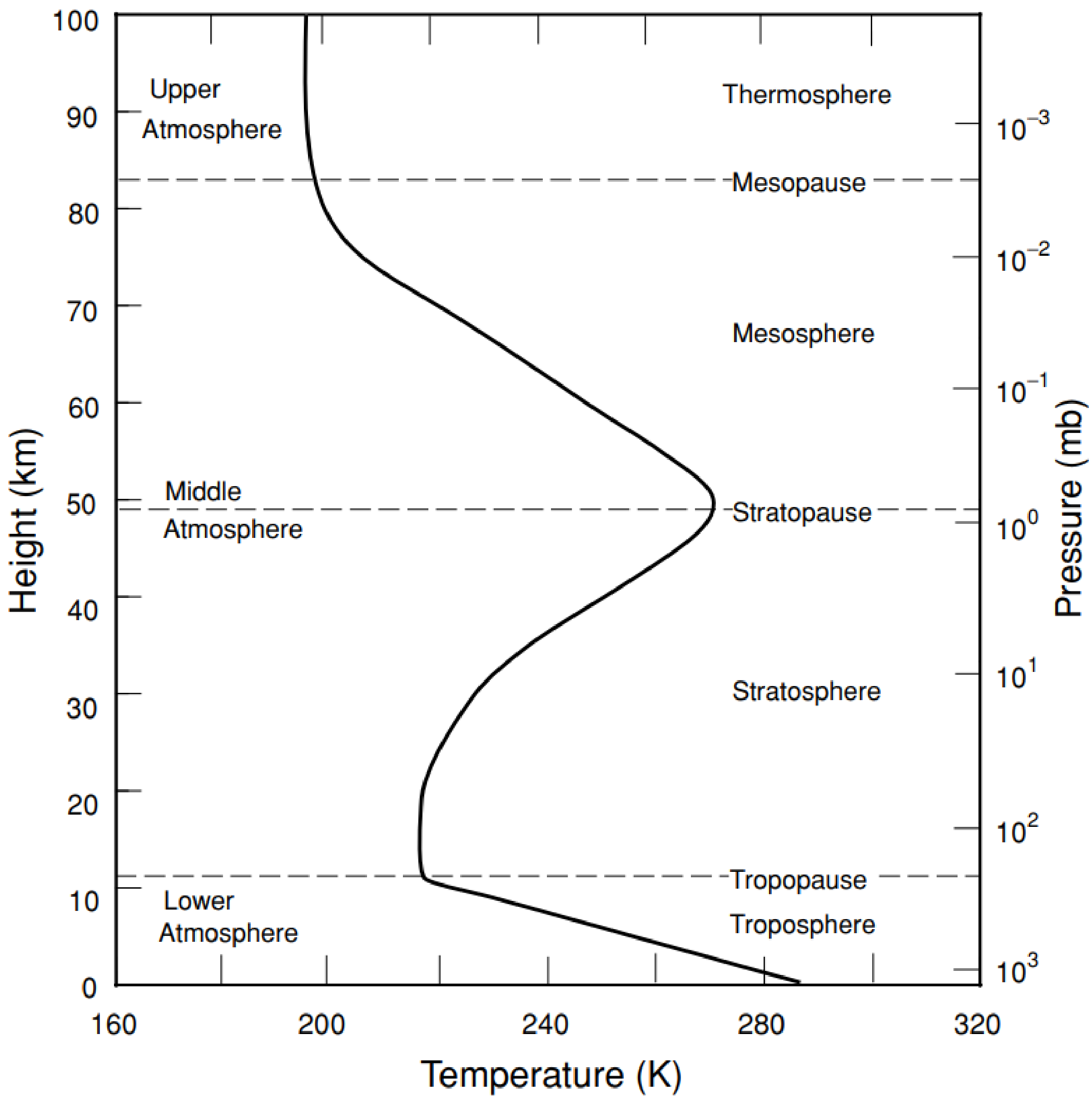

Figure 2: The relationships between temperature, pressure, and altitude in Earth's atmosphere. The pressure at sea level is approximately 1000 millibars. This image was originally published by Liou (2002) as their Figure 3.1. Reprinted from International Geophysics, 84, K.N. Liou, An Introduction to Atmospheric Radiation, Chapter 3 Absorption and Scattering of Solar Radiation in the Atmosphere, Page 66, © (2002), with permission from Elsevier.

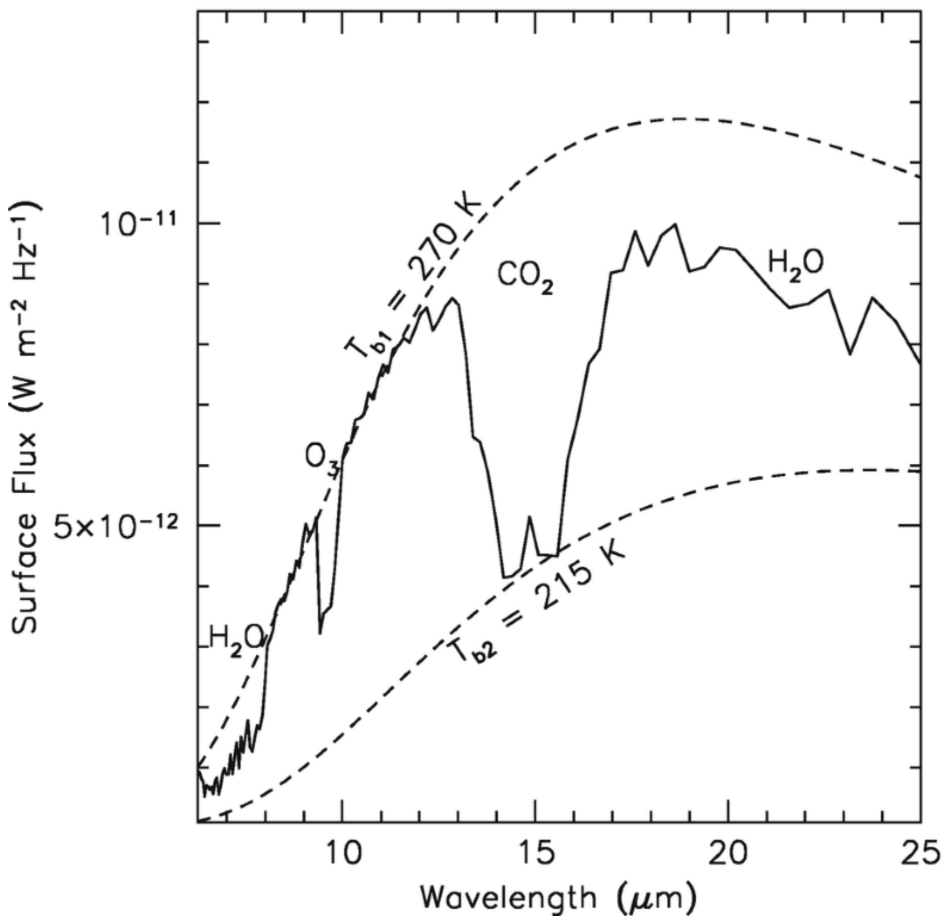

Figure 3: The emission spectrum of the Earth is shown with a solid black line which shows clear absorption features caused by H_2O, O_3, and CO_2. The emission spectrum is compared to two blackbody curves. The approximate average temperature of the Earth's surface is 270 K which is consistent with the Earth's emission spectrum where there is no significant molecular absorption. Meanwhile, the coldest region probed by the spectrum is 215 K, and the exact shapes of the absorption features tell us about the Earth's temperature-pressure profile (see also Figure 2). This image was originally published by Roberge & Seager (2018) as their Figure 6 with data from Christensen & Pearl (1997). Reprinted by permission from Springer Nature Customer Service Centre GmbH: Springer, Handbook of Exoplanets, Roberge & Seager © (2018).

exoplanets orbiting near to their host star (e.g., Mayor & Queloz, 1995), enormous numbers of planets intermediate to the sizes of Earth and Neptune (e.g., Youdin, 2011; Howard et al., 2012; Fressin et al., 2013; Fulton et al., 2017), and so called "super puffs" with bulk densities similar to that of cotton candy (e.g., Masuda, 2014; Lee & Chiang, 2016). By studying the composition of exoplanetary atmospheres, we can gain insight into the formation, evolution, and atmospheric dynamics of exoplanets and their atmospheres in regimes inaccessible within our own Solar System.

2.1 Atoms, Molecules, and Ions

When modelling or observing an exoplanet atmosphere, it is important to know its chemical composition. As a result of Big Bag nucleosynthesis, the most abundant element in the universe is hydrogen which comprises $\sim$76% of nuclear matter by mass, while helium makes up $\sim$24% (e.g., Carroll & Ostlie, 2006). The same approximate abundances hold true for stars and gas giant planets (e.g., for Jupiter: Niemann et al., 1996), but lower mass planets are richer in "metals" (elements heavier than helium) as they form primarily from the dust and ices in the protoplanetary disk (e.g., Carroll & Ostlie, 2006). The primary constituent of gas giant exoplanets is therefore H_2 as hydrogen is a diatomic element. However, H_2 and He interact little with light, and other trace molecules dominate the observable features in exoplanet atmospheres. Depending on the temperature of the exoplanet's atmosphere, commonly detected molecules are H_2O, CH_4, CO_2, and CO (e.g., Tinetti et al., 2007; Swain et al., 2008, 2009; Snellen et al., 2010). Other particularly relevant molecules include TiO and VO which some believe are the cause of temperature inversions in hot Jupiter atmospheres (e.g., Hubeny et al., 2003; Fortney et al., 2008). Atoms and ions produce only narrow features in exoplanetary spectra, but Na, He, Fe, Ti have been detected in exoplanetary atmospheres and exospheres (the extremely low density gas surrounding the atmosphere; e.g., Charbonneau et al., 2002; Hoeijmakers et al., 2018; Spake et al., 2018).

2.2 Bulk Metallicity & C/O Ratio

As an exoplanet forms, it grows from the material in the surrounding protoplanetary disk. In the core accretion model for exoplanet formation, planets initially form from dust and ice grains in the protoplanetary disk and later accrete an atmosphere from the gas in the disk (e.g., Carroll & Ostlie, 2006). The relative abundance of carbon and oxygen in the dust/ices in a protoplanetary disk varies throughout the disk as different molecules condense out of the gas at different temperatures, and therefore different distances from the host star (e.g., Öberg et al., 2011). It has therefore been suggested that a planet's final carbon-to-oxygen (C/O) ratio can be used to identify the formation and migration mechanisms of exoplanets (e.g., Öberg et al., 2011; Madhusudhan et al., 2014, 2016). While some idea of a planet's C/O ratio can be gleaned from observations of molecules in the planet's atmosphere, our limited knowledge of the chemical composition of the deeper regions of the planet and any exchange with the atmosphere significantly complicate the interpretation of such observations.

A planet's C/O ratio and its bulk metallicity also play an important role in determining the chemistry in an exoplanet's atmosphere and the atmosphere's observable features (e.g., Madhusudhan, 2012). For example, a high metallicity atmosphere around a low mass planet decreases the atmospheric scale height (see Equation 1) and hence the observability of atmospheric features in transit spectroscopy (e.g., Désert et al., 2011). Higher metallicity also increases the atmospheric opacity which results in the incident stellar radiation being absorbed higher in the atmosphere where radiative timescales are shorter. Meanwhile, different C/O ratios will result in varying ratios of oxygen- and carbon-bearing molecules like H_2O, CH_4, CO_2, and CO in exoplanetary atmospheres (e.g., Madhusudhan, 2012).

The pair of *Spitzer*/IRAC channel 1 and 2 filters (centred at 3.6 and 4.5 μm, respectively) offer constraints on the C/O ratio as, depending on the temperature, some combination of H_2O, CH_4, CO_2, and CO will be present which all have absorption features in one of these filters. The *HST*/WFC3 infrared grism provides low resolution spectra around the

1.4 μm H_2O feature. In the near future, *JWST*'s many different instruments will provide much broader and higher resolution spectra which will allow for much clearer inferences of C/O ratio and metallicity. Additionally, many ground-based telescopes possess extremely high resolution spectroscopy instruments which are already capable of clearly identifying atoms, ions, and molecules in exoplanetary atmospheres (e.g., Snellen et al., 2010; Birkby et al., 2013; Nugroho et al., 2017; Hoeijmakers et al., 2018).

2.3 Equilibrium vs Disequilibrium Chemistry

A common assumption made when forward modelling exoplanetary atmospheres is that the chemical composition of the gas is in local thermochemical equilibrium. The assumption of equilibrium chemistry greatly simplifies the modelling of exoplanet observations, only requiring one to set parameters like the C/O ratio, metallicity, and temperature-pressure profile. Another alternative is to use a 3D chemical kinetics model which can allow for chemical species out of local thermochemical equilibrium through the employment of chemical networks and timescales (e.g., Drummond et al., 2018a,b, 2020). Meanwhile, retrieval models with unconstrained chemistry may be used to search for non-equilibrium effects (e.g., Venot et al., 2012), but these models come at the cost of many more tunable parameters, and the outputs of such fits can be challenging to interpret. With each of these methods, it is important to use caution as biases can arise due to degeneracies between different molecular species when observing only limited spectral regions with low resolution spectroscopy or photometry. Additionally, one must also be on the lookout for non-equilibrium, photochemical hazes produced on the dayside (as described in the next section).

The assumption of chemical equilibrium has been drawn into question with previous *Spitzer*/IRAC observations of HD 189733b (Knutson et al., 2012) and GJ 436b (Stevenson et al., 2010). For example, CH_4 is energetically favoured on the nightside of the hot Jupiter HD 189733b while CO is favoured on the dayside, but *Spitzer*/IRAC phase curves suggest that the nightside may instead be rich in CO (Knutson et al., 2012). This could be explained, for example, if vertical and/or longitudinal mixing is transporting CO from hotter regions of the atmosphere more rapidly than atmospheric chemistry can restore chemical equilibrium (e.g., Cooper & Showman, 2006; Agúndez et al., 2014; Madhusudhan et al., 2016; Drummond et al., 2018a,b; Mendonça et al., 2018; Drummond et al., 2020). Meanwhile, there is debate in the literature as to the cause of GJ 436b's depleted levels of CH_4, with some suggesting vertical mixing (Stevenson et al., 2010) and others suggesting an atmospheric metallicity so high that H_2 is no longer the dominant constituent which increases the abundance of CO and CO_2 while suppressing CH_4 (Moses et al., 2013; Lanotte et al., 2014; Morley et al., 2017). Properly distinguishing between disequilibrium chemistry and general atmospheric properties as well as understanding the connection between atmospheric chemistry and bulk planetary composition is critical in order to study the different formation and evolution pathways of exoplanets and their atmospheres.

2.4 Clouds & Hazes

The term cloud is primarily used in exoplanet atmospheric science to mean material that has condensed out of an atmosphere due to its partial pressure having exceeded the saturation vapour pressure of the gas (Marley et al., 2013). Meanwhile, hazes are produced by non-equilibrium processes such as photochemical reactions on the planet's dayside (Marley et al., 2013). It is estimated that, on average, $\sim$67% of Earth's surface is covered in clouds (King et al., 2013), while Jupiter's atmosphere is entirely covered by clouds. Currently, haze is relatively rare on Earth but can, for example, be caused by forest fires; meanwhile, early Earth may have been covered in a layer of organic haze (e.g., Sagan & Chyba, 1997; Trainer et al., 2004). Within the solar system, Venus and Titan's atmospheres offer two additional examples of atmospheric hazes (e.g., Knollenberg & Hunten, 1980; Smith et al., 1982).

Clouds and hazes on exoplanets act to obscure the planets' deeper atmospheres and typically prohibit detailed atmospheric characterization (e.g., Kreidberg et al., 2014). Clouds and hazes can also affect the fraction of light reflected by exoplanets' atmospheres (called their albedo). While clouds and hazes prohibit most atmospheric characterization methods, it can be possible to study the properties of the clouds themselves by measuring the planets' albedos (e.g., Evans et al., 2013), measuring the spectral signatures of scattered thermal emission (e.g., Taylor et al., 2021), or using high-precision polarimetry (e.g., Hansen & Hovenier, 1974).

In the atmospheres of hotter exoplanets, it is believed that cloud coverage is not uniform but instead concentrated towards the nightsides of the planets (e.g., Parmentier et al., 2016). This is evidenced by the detection of cloud cover on the western portion of some hot Jupiters' atmospheres where the cold, cloudy gas from the planet's nightside is being advected towards the dayside (e.g. Demory et al., 2013; Parmentier et al., 2016). It is important to note that the clouds act to insulate the planet's nightside, and these radiative impacts can only be captured by fully-coupled cloud models such as those of Lee & Chiang (2016), Lines et al. (2018, 2019), and Roman et al. (2021). Hazes, meanwhile, are believed to be photochemically produced on the highly irradiated daysides of exoplanets but are expected to only be significant in the atmospheres of planets colder than $\sim$1000 K (e.g., Liang et al., 2004; Morley et al., 2015).

3 Atmospheric Characterization

The primary objective of exoplanetary atmospheric characterization is to test model predictions for the formation, evolution, atmospheric chemistry, and atmospheric dynamics of exoplanets. One of the other main objectives of the field of exoplanet characterization is to permit future studies of Earth-like exoplanets in their systems' habitable zones with the hopes of detecting life beyond the Earth and studying the processes that led to the formation of life on Earth. Due to the small size and cool temperatures of Earth-like exoplanets in comparison to their host stars, characterizing these planets is extraordinarily challenging and currently impossible in most cases. However, by developing and testing observation and modelling techniques on far more easily detectable planets like hot Jupiters, we can make

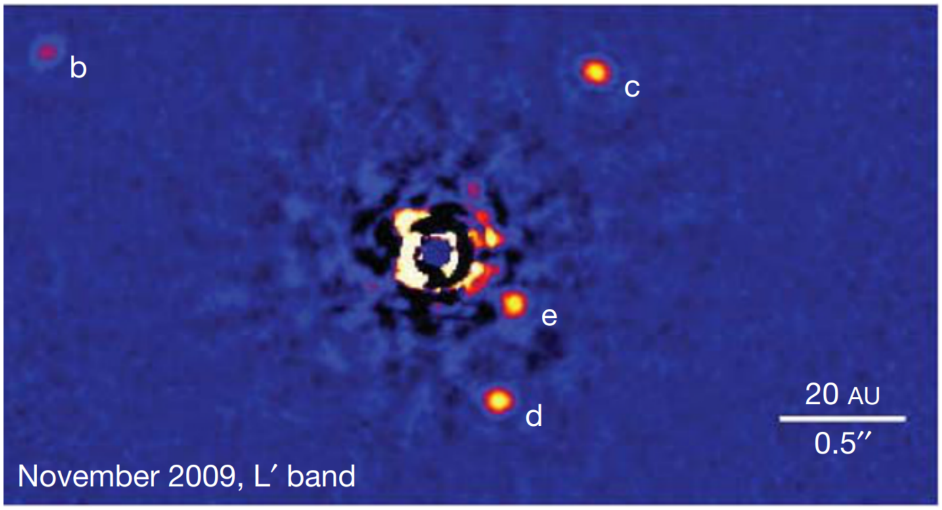

Figure 4: A high-contrast, near-infrared image of the HR 8799 system taken by the Keck II telescope showing the presence of four young, wide-orbit planets—labelled b, c, d, and e—seen from above the system's orbital plane. The star at the centre of the system has been masked out, leaving only noisy residuals from the star's diffraction pattern at the centre of the image. This image was originally published by Marois et al. (2010) as the bottom panel of their Figure 1. Reprinted by permission from Springer Nature Customer Service Centre GmbH: Nature, Images of a fourth planet orbiting HR 8799, Marois et al., © (2010).

gradual progress towards the future study of Earth-like exoplanets. Also, studying planets that are not Earth-like allows us to put exo-Earths into context and hence improve our understanding of habitability and the search for life; for example, with a better understanding of the potential chemical species that can be produced through abiotic processes, we can hopefully avoid false claims of biosignature detections in the future. Many methods have been developed to characterize the atmospheres of exoplanets, the most common of which are summarized below.

3.1 Direct Imaging

Directly observing an exoplanet separated from its host star (called direct imaging) is the most intuitive method of characterizing an exoplanetary atmosphere. Given the immense distances to exoplanet systems, it would require a telescope larger than the Earth to spatially resolve exoplanetary surfaces. However, in some special cases it is possible to spatially resolve the planets in an exoplanetary system from their host star (e.g., see Figure 4). This endeavour is extremely challenging as the immense contrast in brightness between planet and star combined with the close proximity of the two objects results in the planet being lost in the diffraction pattern of the host star's light. With the continued development of high contrast imaging techniques and coronographs, it is becoming increasingly possible to detect the faint signal from exoplanets. Currently, this technique can only detect the thermal emission from young planets orbiting far from their host star because such planets are still hot from their formation (e.g., Chauvin et al., 2005; Marois et al., 2008, 2010). Future missions like HabEx or LUVOIR would seek to study planets closer-in to their host star using reflected light, and ideally these missions would observe an Earth-like exoplanet orbiting within the habitable zone of a Sun-like star (Mennesson et al., 2016; Gaudi et al., 2018; Roberge & Moustakas, 2018; The LUVOIR Team, 2019). However, at present and for the foreseeable future, direct imaging will remain impossible for the vast majority of exoplanets, and other techniques must be used to characterize their atmospheres.

3.2 Transit

Numerous indirect methods have been developed to permit the characterization of exoplanetary atmospheres where direct imaging is impossible. One of the most common methods is the exoplanet transit method where an exoplanetary system is observed while the planet passes in front of its host star, causing a decrease in the total flux of the system (see Figure 5). Due to the special orbital alignment required for a transit to be observed from Earth, most planets will not transit their host star. However, transit surveys have been immensely successful due to the strong and repeated transit signal and due to the unexpected prevalence of short-period planets which are more likely to transit and can be rapidly confirmed. In 2000, HD 209458b became the first exoplanet detected using the transit method (Charbonneau

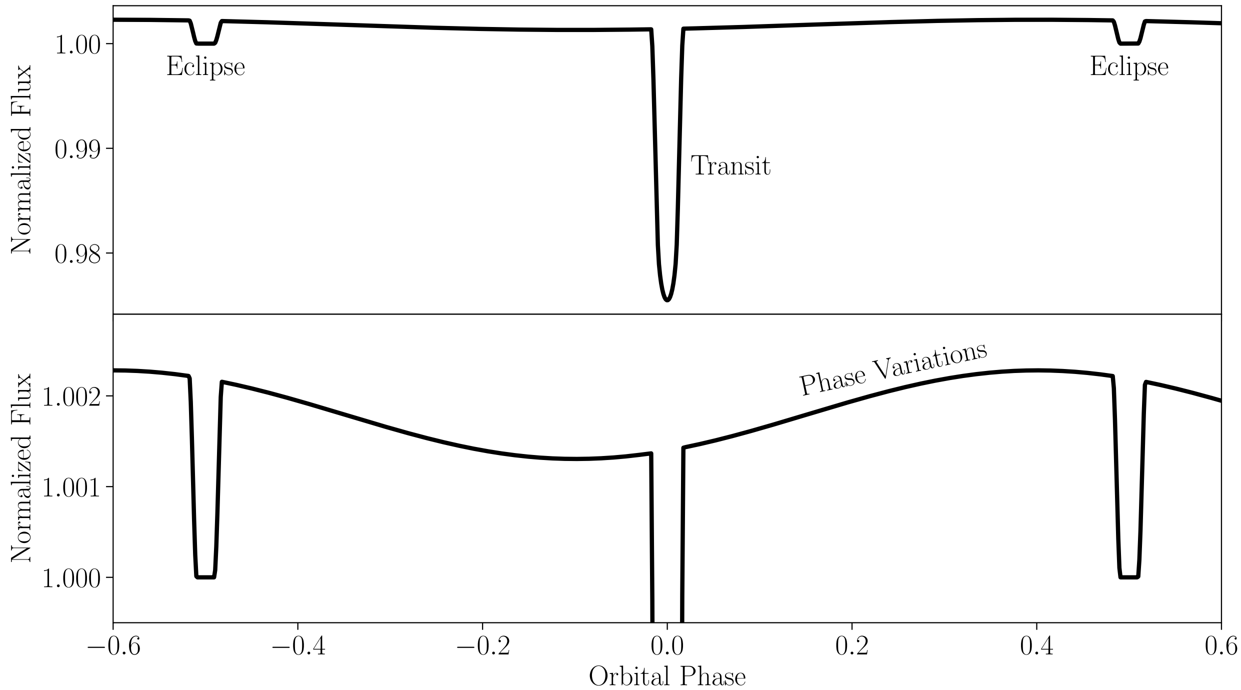

Figure 5: A plot showing a simulated lightcurve including the transit, eclipse, and phase variation signals for the hot Jupiter HD 189733b as observed by Spitzer/IRAC at 4.5 μm (Knutson et al., 2012). The y-axis has been normalized by the star's flux. The plot spans more than a full orbit and hence shows two eclipses. The bottom panel shows the same data as the top panel but zoomed in to show the planet's phase variations. The peak in the phase variations occurs before the eclipse which is indicative of an eastward shifted hottest hemisphere.

et al., 2000; Henry et al., 2000); since then, a total of 3353 confirmed exoplanets[1] have been discovered by the transit method, with 2398 of those confirmed exoplanets being discovered as part of the *Kepler* mission[1].

The depth of the transit is equal to the square of the planet-to-star radius ratio, $(R_{\rm p}/R_*)^2$, and is roughly 1% for hot Jupiters but only ∼0.008% for the Earth passing

[1] From `https://exoplanetarchive.ipac.caltech.edu` as of 2021-07-26 at 13h00 EDT.

in front of the Sun. When observing a transit, a small portion of the star's light that we receive passes through the limb of the planet's atmosphere (the ring of the atmosphere seen around the planet). At wavelengths corresponding to strong atomic or molecular absorption features like that of H_2O at 1.4 μm, the planet's atmosphere absorbs a larger fraction of the starlight and the planet appears slightly larger; measuring the variations in transit depth with wavelength is called transit spectroscopy. This technique provided the first detection of an exoplanetary atmosphere (Charbonneau et al., 2002) and more recently has been used to perform comparative planetology (e.g., Sing et al., 2016; Baxter et al., 2021).

Transit observations are complicated by the non-uniform brightness of the stellar surface that is being partially obscured. For example, over the past ∼33 years, the Sun's surface area was ∼0.003–0.3% covered by sunspots (colder regions of the photosphere; Shapiro et al., 2014) and ∼0.3–3% covered by faculae (hotter regions of the photosphere; Shapiro et al., 2014). Exoplanets orbit a wide diversity of stellar types, however, and starspot and plage coverage fractions can vary widely between stars. Starspot and plage coverage is also temporally variable as the star rotates about its axis and as the star's magnetic field strength fluctuates. When performing transit spectroscopy, it is assumed that the planet is blocking a portion of the star's surface which is representative of the average temperature and composition of the rest of the star's surface. However, if the planet's path across the star's atmosphere contains more or less star spots and/or plages than the average of the star's surface, transit spectroscopy can yield spurious detections (e.g., Rackham et al., 2018, 2019).

3.3 Eclipse

In the eclipse method (also known as the secondary eclipse method), an exoplanetary system is observed while the planet passes behind its host star, causing a decrease in the total flux received from the system (see Figure 5). While the eclipse depth depends on the square of the planet-to-star radius ratio, it also depends on the planet-to-star flux ratio, where the planet's flux is some combination of thermal emission and reflected light. As such, eclipse depths are typically smaller than transit depths by an order of magnitude or more. The eclipse depth also varies with wavelength due to atomic and molecular absorption in the atmospheres of both the planet and star. Eclipse observations are less affected than transits by the non-uniform surface of the host star as the star's surface is not occulted during the eclipse. At optical wavelengths, eclipse depths typically probe light emitted by the host star and reflected by the planet, while at infrared wavelengths eclipse depths typically probe the thermal emission from the planet. The first exoplanet eclipse detected was of HD 209458b (Charbonneau et al., 2005; Deming et al., 2005) and at least a hundred more exoplanets have been observed using the eclipse method since then (e.g., see Baxter et al., 2020; Garhart et al., 2020, for uniformly reanalyzed samples of *Spitzer*/IRAC eclipses).

Rauscher et al. (2007) first showed how the detailed shape of eclipse ingress/egress could constrain both longitudinal and latitudinal brightness markings on the dayside of a planet (see Figure 6). To date, this method has only been applied to the seven combined *Spitzer* 8 μm eclipses of HD 189733b (Majeau et al., 2012; de Wit et al., 2012). However, it has long been recognized that spectral eclipse mapping with *JWST* could allow for 3D maps as different wavelengths probe different atmospheric pressures due to differing opacities (Rauscher et al., 2007).

3.4 Phase Variations

By observing the variations in flux from an exoplanet system throughout the planet's orbit (called the planet's phase curve; see Figure 5), we are able to infer the brightness of the planet as a function of longitude. In the absence of planetary obliquity, it is impossible to measure latitudinal variations in brightness with the phase curve technique due to the disk-integrated nature of these observations. It is possible to observe the phase curve of non-transiting planets (e.g., Harrington et al., 2006; Cowan et al., 2007), although the lack of transits and eclipses make calibrating and interpreting these observations far more challenging. All told, 46 planets' phase curves have been observed with *Spitzer*, *Hubble*,

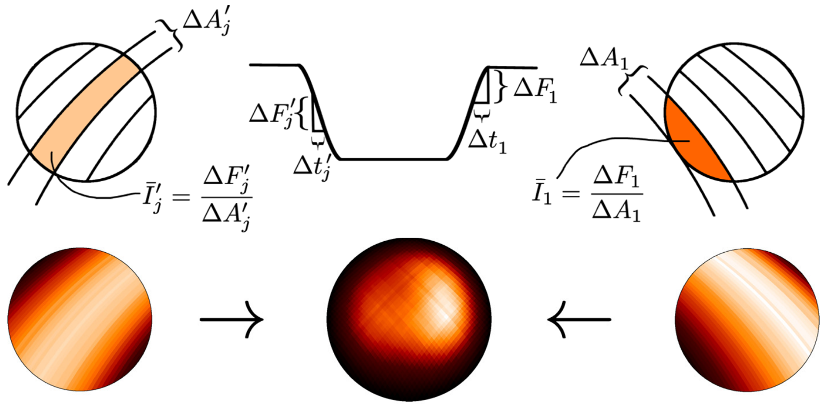

Figure 6: A demonstration of one eclipse mapping technique called the "slice mapping technique" where the planet's dayside is decomposed into thin slices that are gradually occulted by the star's limb during eclipse. For eclipsing planets with inclinations not exactly equal to 90 degrees, the star's limb is sloped compared to lines of constant longitude on the planet; this allows measurements during the start of eclipse to be compared with measurements at the end of the eclipse to provide north–south information inaccessible to most atmospheric characterization methods. This image was originally published by Majeau et al. (2012) as their Figure 1. © AAS. Reproduced with permission.

Kepler, and/or *TESS*, resulting in a total of 49 papers presenting new phase curves which cumulatively have garnered in excess of 3500 citations to date (see Table 1). The strength of phase curve observations is also demonstrated by the surprising number (7) of approved phase curve observations from the recent *JWST* Cycle 1 General Observer proposals.

In reflected light, phase curve observations allow us to probe longitudinal variations in the reflectivity of the planet's illuminated dayside while giving no information on the unilluminated nightside. For example, *Kepler* phase curve observations of the hot Jupiter Kepler-7b showed a westward offset which was inferred to be due to reflective clouds on the western parts of the planet's dayside hemisphere (Demory et al., 2013). Meanwhile, thermal infrared phase curve observations probe longitudinal variations in temperature and are uniquely sensitive to the nightsides of planets; as such, phase curves are the best tool

Table 1: Exoplanets with published *Spitzer*, *Hubble*, *Kepler*, and *TESS* phase curves. Bolded references were published in *Nature*, *Science*, or *Nature Astronomy*. Updated 2021-07-26.

Exoplanet	**Reference(s)**	**Citations**
51 Peg b	Cowan et al. (2007)	129
55 Cancri e	**Demory et al. (2016)**	129
CoRoT-2b	**Dang et al. (2018)**	39
GJ 436b	Stevenson et al. (2012b)	35
HAT-P-2b	Lewis et al. (2013); de Wit et al. (2017)	132; 15
HAT-P-7b	Esteves et al. (2015); Wong et al. (2016); **Armstrong et al. (2016)**	122; 80; 63
HATS-24b	Wong et al. (2020c)	12
HD 149026b	Knutson et al. (2009b); Zhang et al. (2018)	104; 58
HD 179949b	Cowan et al. (2007)†	129†
HD 189733b	**Knutson et al. (2007)**; Knutson et al. (2009a, 2012)	591; 203; 230
HD 209458b	Cowan et al. (2007)†; Crossfield et al. (2012); Zellem et al. (2014)	129†; 60; 108
HD 80606b	**Laughlin et al. (2009)**; de Wit et al. (2016)	91; 15
KELT-1b	Beatty et al. (2019); Beatty et al. (2020); von Essen et al. (2021)	38; 6; 2
KELT-9b	Mansfield et al. (2020); Wong et al. (2020b)	31; 33
KELT-16b	Bell et al. (2021)	7
Kepler-7b	Demory et al. (2013) Esteves et al. (2015)†	168; 122†
Kepler-8b	Esteves et al. (2015)†	122†
Kepler-10b	Hu et al. (2015)	48
Kepler-12b	Esteves et al. (2015)†	122†
Kepler-41b	Esteves et al. (2015)†	122†
Kepler-76b	Esteves et al. (2015)†	122†
LHS 3844b	**Kreidberg et al. (2019)**	56
LTT 9779b	Crossfield et al. (2020)	4
MASCARA-1b	Bell et al. (2021)†	7†
Qatar-1b	Keating et al. (2020)	11
TOI-519	Parviainen et al. (2021)	2
WASP-4b	Wong et al. (2020c)†	12†
WASP-5b	Wong et al. (2020c)†	12†
WASP-12b	Cowan et al. (2012); Bell et al. (2019); Arcangeli et al. (2021); Owens et al. (2021)	133; 23; 0; 1
WASP-14b	Wong et al. (2015); Krick et al. (2016)	60; 20
WASP-18b	Maxted et al. (2013); Arcangeli et al. (2019) Shporer et al. (2019)	81; 38; 48
WASP-19b	Wong et al. (2016)†; Wong et al. (2020a)	80†; 16
WASP-33b	Zhang et al. (2018)†; von Essen et al. (2020)	58†; 14
WASP-36b	Wong et al. (2020c)†	12†
WASP-43b	**Stevenson et al. (2014)**; Stevenson et al. (2017); Wong et al. (2020c)†	173; 91; 12†
WASP-46b	Wong et al. (2020c)†	12†
WASP-64b	Wong et al. (2020c)†	12†
WASP-76b	May et al. (2021)	0
WASP-77Ab	Wong et al. (2020c)†	12†
WASP-78b	Wong et al. (2020c)†	12†
WASP-82b	Wong et al. (2020c)†	12†
WASP-100b	Jansen & Kipping (2020)	10
WASP-103b	Kreidberg et al. (2018)	99
WASP-121b	Bourrier et al. (2020); Daylan et al. (2021)	30; 25;
WASP-142b	Wong et al. (2020c)†	12†
WASP-173Ab	Wong et al. (2020c)†	12†
υ Andromedae b	**Harrington et al. (2006)**; Crossfield et al. (2010)	186; 101
Total	47 planets, 50 papers (8 in magazines)	3771 citations

† Already listed above and not re-counted in total papers/citations.

available for characterizing exoplanetary atmospheric dynamics (Parmentier & Crossfield, 2018). One of *Spitzer*'s great scientific legacies was its mid-infrared, photometric phase curves which were used to constrain the planetary Bond albedo and the efficiency of day–night heat transport. *Hubble*, and in the future *JWST* and *ARIEL*, will build upon this legacy by collecting spectroscopic phase curves which will also permit the study of inhomogeneities in the composition and thermal structure of exoplanetary atmospheres.

3.5 High Resolution Spectroscopy

Most transit, eclipse, and phase curve observations have been collected using photometry or low resolution spectroscopy (sufficient to detect molecular bands, but not individual spectral lines). Another method of collecting these observations is high resolution spectroscopy where the spectrum of the star+planet light is measured with a large spectral resolving power ($R = \lambda/\Delta\lambda \approx 100\,000$). The main advantage of high resolution spectroscopy is that it permits the measurement of individual atomic emission/absorption lines and individual lines within molecular emission/absorption bands. While these lines are very strong compared to the continuum flux level, they are also very narrow, so photometry and coarse spectroscopy are only able to measure the much weaker wavelength average over some bandpass (Birkby, 2018, see also Figure 7). High resolution spectroscopy has been used to detect H_2O, CO, TiO, Fe, Ti^+, and other species in the absorption and emission spectra of hot Jupiters (e.g., Snellen et al., 2010; Birkby et al., 2013; Nugroho et al., 2017; Hoeijmakers et al., 2018).

High resolution spectroscopy offers many other benefits over photometric and low resolution spectroscopic observations; for example, it allows different molecules with overlapping molecular bands to be distinguished due to the unique fingerprint of the line spacings within those bands. The phase variations of non-transiting planets are also measurable with high resolution spectroscopy as the planet's radial velocity will change throughout its orbit, allowing the planet's spectral signatures to be separated from the star's (e.g., Rodler et al., 2010). High resolution spectroscopy can even be used to measure the atmospheric wind speeds on

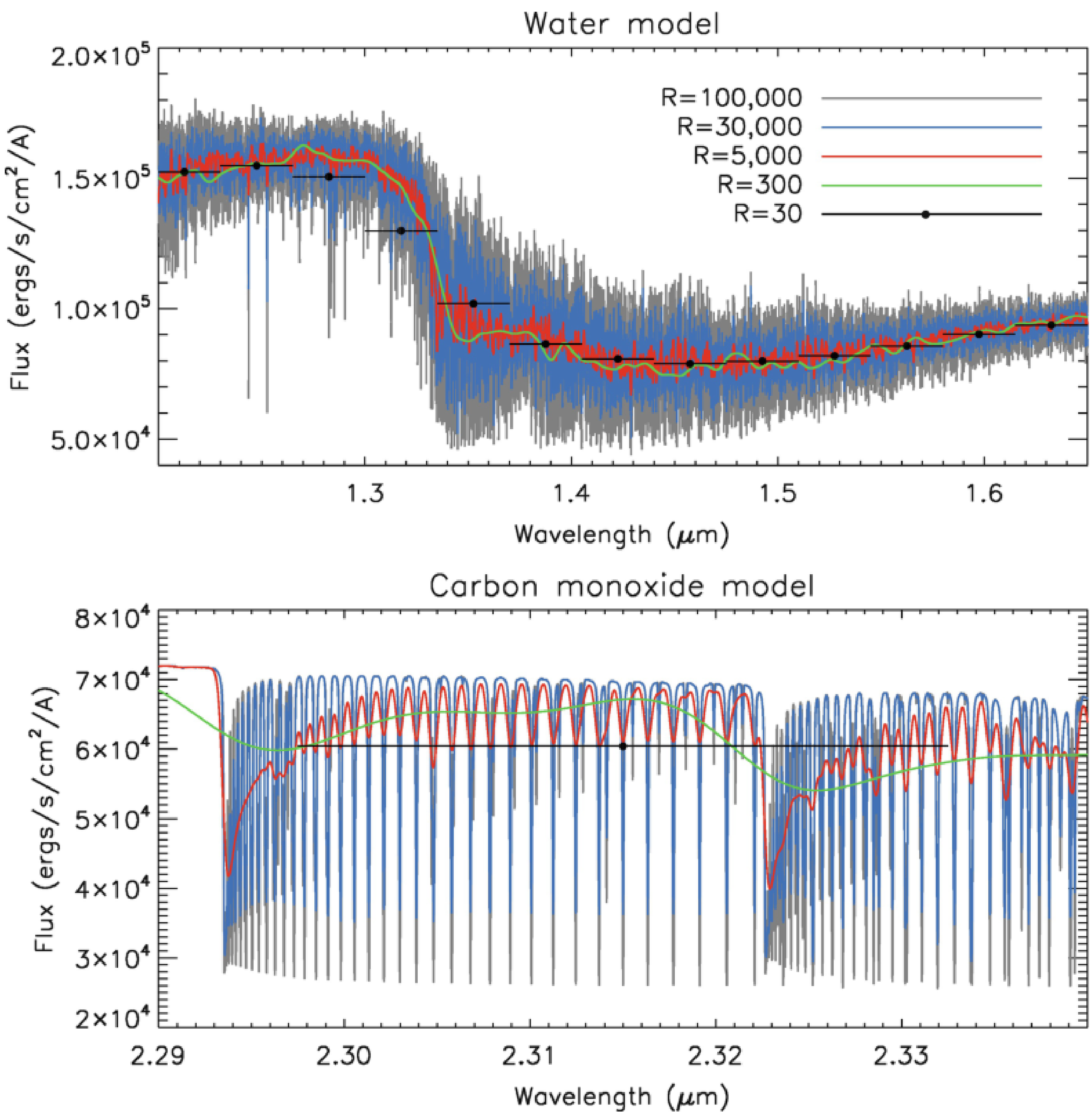

Figure 7: A demonstration of the power of high resolution spectroscopy for H_2O and CO. Because spectral lines are very narrow, low resolution spectroscopy (e.g. R = 30 or 3000) measures the average spectrum across some wavelength range which greatly reduces the signal strength. This image was originally published by Birkby (2018) as their Figure 2. Reprinted by permission from Springer Nature Customer Service Centre GmbH: Nature, Handbook of Exoplanets, Birkby © (2018).

exoplanets (e.g., Snellen et al., 2010; Miller-Ricci Kempton & Rauscher, 2012; Rauscher & Kempton, 2014; Louden & Wheatley, 2015; Zhang et al., 2017; Beltz et al., 2021). Due to the complexity and bulk of the equipment needed to perform high resolution spectroscopy, these instruments are exclusively ground-based; thanks to the precise measurement of the wavelength (and hence radial velocity) of the observed spectral lines, it is possible to reject the spectral features introduced by the Earth's atmosphere (telluric lines). However, due to the calibration steps required for high resolution spectroscopy, the technique is unable to measure the continuum flux outside of spectral lines.

3.6 High-Precision Polarimetry

Scattered light polarimetry was used as early as 1929 (Lyot, 1929) to study the atmosphere of Venus. Hansen & Hovenier (1974) used polarimetry to discover concentrated sulfuric acid clouds on Venus. When observing an exoplanetary system, unpolarized stellar light incident on an exoplanet scatters off particles in the exoplanet's atmosphere, causing a net polarization in the observed star+planet light. As the planet orbits its host star, the amplitude and orientation of the observed polarization will vary (see Figure 8). The change in the observed polarization is a function of orbital parameters such as inclination, as well as properties of the scattering particles in the atmosphere.

With modern advances in technology, high-precision exoplanet polarimetry is poised to make pioneering discoveries similar to those of earlier Solar System studies. Throughout my thesis, I was involved in the commissioning of the new high-precision polarimeter POMM for the Mont Mégantic Observatory in Québec (Polarimètre de l'Observatoire du Mont-Mégantic; Bastien et al., 2014) which is uniquely sensitive to red wavelengths. To date, only a few hot Jupiters have been observed with polarimetry (e.g., Berdyugina et al., 2008; Wiktorowicz, 2009; Wiktorowicz et al., 2015; Bott et al., 2016, 2018), while colder or smaller planets currently remain inaccessible as the polarimetric signal scales as $(R_\mathrm{p}/a)^2$, where R_p is the planetary radius, and a is the planet's orbital semi-major axis.

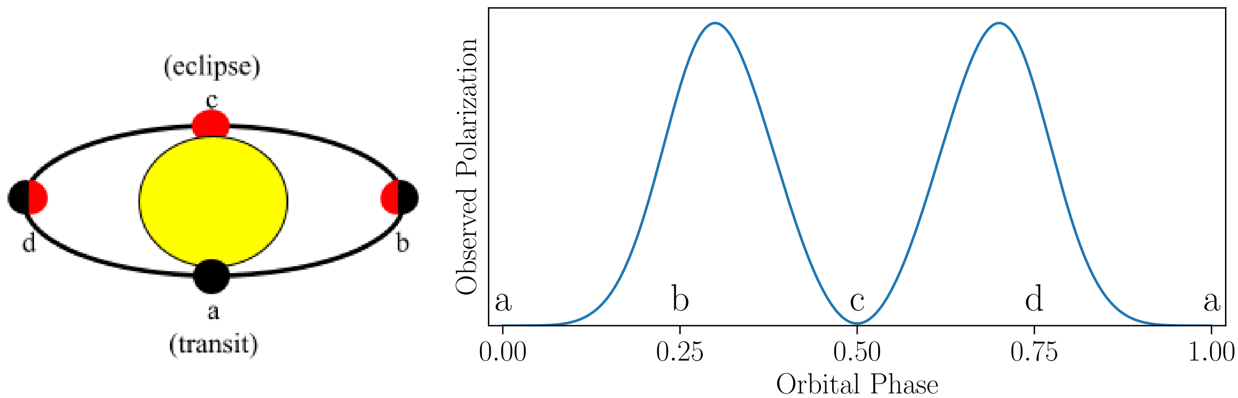

Figure 8: *Left*: A cartoon showing a hot Jupiter at various points in its orbit where the illuminated hemisphere is coloured red. *Right*: The predicted polarization amplitude variations of a transiting hot Jupiter throughout its orbit on an arbitrary y-scale. Peaks near quadrature (locations b and d) are caused by Rayleigh scattering which induces strong polarization at a scattering angle of 90°, but the peaks are shifted towards eclipse due to the lack of illumination on the planet's nightside.

4 Precise Space-Based Photometry and Spectroscopy

With recent improvements in instrumentation, observation, and calibration techniques, ground-based transit and eclipse spectroscopy is becoming increasingly feasible at wavelengths where the Earth's atmosphere is transparent (e.g., Hoeijmakers et al., 2018). However, the majority of exoplanet atmospheric characterization has been performed with space-based telescopes to reach the extreme precision required. In addition, space-based telescopes allow observations at wavelengths where Earth's atmosphere is opaque (e.g. within H_2O features). Space-based telescopes are also required for continuous phase curve observations due to the long orbital periods of exoplanets which last much longer than one full night of observing. While space-based telescopes are not affected by the variable levels of absorption and turbulence in the Earth's atmosphere, they do suffer from variable levels of solar irradiation and other detector systematics which limit their performance. The origins of the systematic noise for *Spitzer*/IRAC and *Hubble*/STIS—as well as methods to reduce their impact—are described below.

4.1 The Hubble Space Telescope and STIS

The Hubble Space Telescope (or *Hubble* for short) is a NASA-led satellite with contributions from ESA and was launched on April 24, 1990 and currently remains in operation. The telescope has a 2.4 m diameter primary mirror and has had instruments sensitive to wavelengths between 90 nm and 2.4 μm, but the telescope's currently active instruments are only sensitive to wavelengths between 90 nm and 1.7 μm. The spacecraft is in a low Earth orbit with an orbital altitude of ~545 km and an orbital period of ~96 minutes. As a result of *Hubble*'s geocentric orbit, it frequently passes in and out of the Earth's shadow which causes cyclical fluctuations in the solar heating of the telescope. These thermal fluctuations result in orbit-long modulations in instrumental sensitivity due to the thermal expansion and contraction of the instrumentation (e.g., Demory et al., 2015). *Hubble*'s orbit also requires that most observations be interrupted for up to 42 minutes per orbit (~44% of *Hubble*'s orbit) to avoid damage to *Hubble* caused by pointing the telescope at the Earth. This results in large gaps in the *Hubble*'s observations every ~96 minutes for all objects which do not lie withing *Hubble*'s continuous viewing zone (the regions of the sky where *Hubble* can stare continuously while maintaining a safe angle with respect to the Earth).

The Space Telescope Imaging Spectrograph (STIS; Kimble et al., 1998) is one of the primary *Hubble* instruments used to characterize exoplanetary atmospheres. STIS offers many different imaging options and STIS is able to perform spectroscopy between 114 nm and 1.027 μm (spread across many different spectroscopic modes). One of the most commonly used spectral elements for exoplanet atmospheric characterization is STIS's G430L grating which spans 290–570 nm with a resolving power of $R \sim 500$. In addition to the sensitivity variations throughout *Hubble*'s orbit caused by thermal expansion and contraction (e.g., Demory et al., 2015), STIS spectra also suffer from more minor effects including noise introduced by movement of the spectra on the detector caused by minor drifts in the telescope's orientation (e.g., Evans et al., 2013) as well as a visit-long drift in sensitivity that is potentially caused by charge trapping (especially visible in the long-duration observations of α Centuri A, which lies within *Hubble*'s continuous viewing zone; Demory et al., 2015). The data from *Hubble*'s first orbit while staring at an object are also significantly discrepant compared to the other orbits due to the change in the solar irradiation of the telescope, and the first exposure in an orbit is also normally significantly discrepant; as a result, these data are usually discarded (e.g., Sing et al., 2011). Intra-orbit sensitivity variations are often modelled using a fourth-order polynomial (e.g., Demory et al., 2015) and, when accounted for, the visit-long sensitivity drift is typically accounted for using a linear or second-order logarithmic ramp (e.g., Sing et al., 2011; Demory et al., 2015).

4.2 The Spitzer Space Telescope and IRAC

The Spitzer Space Telescope (or *Spitzer* for short; Werner et al., 2004) was a NASA spacecraft launched on August 25, 2003 and decommissioned on January 30, 2020. The telescope had an 85 cm diameter primary mirror and instruments that were sensitive to wavelengths from 3–180 μm. The spacecraft is in an Earth-trailing, heliocentric orbit and was roughly 260 million kilometers from Earth at the time of its decommissioning[2]. *Spitzer*'s primary mission had an expected duration of 5+ years at launch and ultimately ended when the liquid helium cryogen used to maintain the telescope's operating temperature was exhausted on May 15, 2009[3]. *Spitzer* then became the Spitzer Warm Mission where only the two shortest wavelength instruments, Infrared Array Camera (IRAC; Fazio et al., 2004)

[2] `https://www.jpl.nasa.gov/news/tarantula-nebula-spins-web-of-mystery-in-spitzer-image`

[3] `https://www.spitzer.caltech.edu/news/ssc2009-12-nasas-spitzer-begins-warm-mission`

channels 1 and 2, were operable due to the increased operating temperature. It was during the Warm Mission that the majority of *Spitzer*'s exoplanet atmosphere observations were collected.

Thanks to its heliocentric orbit, *Spitzer* did not face the same variable solar illumination and Earth exclusion angle issues *Hubble* experiences. However, *Spitzer*/IRAC's detectors suffered from strong intra-pixel sensitivity variations where the centres of individual pixels were more sensitive than their edges; when combined with sub-pixel scale motions in the telescope's orientation, this could cause $\sim$1% temporal variations in sensitivity for point sources like planet-hosting stars (e.g., Charbonneau et al., 2008). Early *Spitzer*/IRAC exoplanet observations also suffered from cyclic variations in telescope orientation with a period of $\sim$60 minutes that were later attributed[4] to cycling of a battery heater on the spacecraft and were much reduced after October 17, 2010 when the battery heater was set to cycle more rapidly which resulted in smaller thermal fluctuations. There was also typically a $\sim$30 minute ramp in the sensitivity of the detectors at the start of an observation which may have been due to trapped charges in the detectors or thermal settling of the telescope (e.g., Knutson et al., 2012); these data are sometimes discarded to ensure they do not affect the observations (e.g., Knutson et al., 2012). Numerous different models have been developed to remove the impact of intra-pixel sensitivity variations including 2D polynomials (e.g., Charbonneau et al., 2008), Gaussian kernel regression (e.g., Knutson et al., 2012), BiLinearly-Interpolated Subpixel Sensitivity (BLISS) mapping (e.g., Stevenson et al., 2012a), pixel level decorrelation (PLD; e.g., Deming et al., 2015), the independent component analysis of pixel time series (pixel-ICA; e.g., Morello et al., 2019), and Gaussian processes (GPs; e.g., Gibson et al., 2012; Evans et al., 2015). Each technique has its strengths and weaknesses and there is significant disagreement in the literature as to which technique is best and under what circumstances different techniques will give consistent results.

[4] `https://ssc.spitzer.caltech.edu/warmmission/news/21oct2010memo.pdf`

4.3 Fitting Techniques and Uncertainty Estimation

The foundation of most modern data analysis is built upon work done in the late 1700s and early 1800s by Reverend Thomas Bayes and Pierre-Simon Laplace that is typically attributed to Bayes. According to Bayes' theorem, the probability, P, of a hypothesis, H, given a set of observations, $\mathbf{X}$, and a collection of prior knowledge, I, is given by

$$P(H|\mathbf{X}, I) = \frac{P(\mathbf{X}|H, I)P(H|I)}{P(\mathbf{X}|I)},$$

where $|$ reads as "given" (that all terms to the right are assumed true), and the comma reads as "and". The power of Bayes' theorem is that it allows us to compute the *posterior probability*, $P(H|\mathbf{X}, I)$, using the much more easily calculable *likelihood function*, $P(\mathbf{X}|H, I)$, which is the probability that we would have observed the data $\mathbf{X}$ if the hypothesis and prior knowledge were correct. The $P(H|I)$ term is the *prior probability* and summarizes how our prior knowledge affects our hypothesis before having measured the data $\mathbf{X}$. Finally, the $P(\mathbf{X}|I)$ term is the *evidence* or *marginal likelihood* and is often omitted when fitting a model to data as it is only a normalization term and does not depend on the hypothesis.

When fitting a set of observations, a hypothesis typically consists of a function describing the model which depends on a collection of parameters, θ, and hyperparameters, α. Bayes' theorem can then be re-written as

$$P(\theta|\mathbf{X}, \alpha) \propto P(\mathbf{X}|\theta, \alpha)P(\theta|\alpha).$$

Fitting the observations usually starts by freezing the set of hyperparameters and then evaluating the posterior probability by comparing different model predictions to the observed data. Fitting the observations then requires determining the values of θ that maximize the posterior probability (called the Maximum A Posteriori estimate or MAP estimate), while determining the uncertainty on the model parameters involves determining the range of values of θ that provide an adequately good fit to the observations (called the confidence interval).

In principle, one could simultaneously estimate the optimal value of θ and its confidence interval from the posterior probability density function (PDF) by calculating the posterior probability for all values of θ; this is called a grid search. While this technique may be feasible for discrete parameters or low dimensional problems, performing a grid search when the vector θ contains tens or thousands of continuous variables becomes immensely challenging and computationally inefficient. Instead, various algorithms can be used to compute the MAP estimate and the confidence interval, some of which are described below.

Estimating the MAP value of θ is often done using a gradient descent algorithm. This technique starts by picking either a random or partially informed initial estimate for the value of θ and then computing or estimating the gradient in the posterior PDF depending on whether or not the model is differentiable. In practice, most optimization methods are formulated as minimization routines (hence the name gradient *descent*), so it is more common to seek the minimum of the *negative* posterior probability. The algorithm will then take a small step in the direction in which the posterior probability most rapidly increases and then re-evaluate the gradient in the posterior PDF. This procedure is then repeated (typically with a gradually decreasing step size) until the algorithm locates a local maximum in the posterior PDF. The distinction of a local maximum rather than a global maximum is important, as gradient descent routines do not explore the parameter space as thoroughly as a grid search, so it is possible for the algorithm to settle on a local maximum which compares poorly to the global maximum. This is typically overcome by running several gradient descent optimizations initialized at random locations in parameter space in the hopes that one of the optimizations will make its way to the global maximum (or at least alert you to the presence of many local maxima).

Estimating the confidence interval of θ could be done by extrapolating the posterior PDF from the MAP value using the first and second order gradient and then determining the extent to which each component of θ can be changed while still providing an adequately good fit to the observations. However, this technique can give inaccurate estimates especially in the presence of correlations between different parameters. Instead, a Markov Chain Monte-Carlo (MCMC) method is typically used to estimate parameter uncertainties. Monte-Carlo (MC) methods in general involve randomly sampling values of θ, while MCMCs are a specific variant where samples are randomly drawn based on the knowledge of the posterior probability from the previously drawn value; the draws of MCMC are typically called steps taken by a walker, and a collection of many walker steps are called a chain.

The starting point of an MCMC is typically either drawn at random or is set to the MAP estimate from a gradient descent algorithm. The walker will then explore the parameter space by proposing different steps and then accepting or rejecting the proposed step. The walker's location in parameter space at the end of each step (or lack thereof) is then recorded. After some number of steps (called the "burn-in" phase) where the walker's movement is strongly correlated from one step to the next (especially when starting from a randomly drawn starting location), the walker will begin to map out the posterior PDF where the time a walker spends at any one location in parameter space is proportional to the posterior probability at that location. In reality, it can be very challenging to determine when the burn-in phase has ended other than by running a very long chain. After the chain is run to completion, the confidence interval for each parameter can be estimated using the distribution of recorded walker steps excluding the burn-in phase. For example, assuming a Gaussian uncertainty in parameter estimates, one can compute the standard deviation in the walkers along each dimension. Plots showing the distribution of walker steps as a function of pairs of parameters are colloquially called "corner plots" or "triangle plots" and can be useful in diagnosing parameter correlations.

One common algorithm to propose steps in a MCMC is the Metropolis-Hastings algorithm (Metropolis et al., 1953; Hastings, 1970) where a step is drawn from a multi-dimensional Gaussian (whose standard deviations are tunable parameters) centred on the previous step and the probability that the step is accepted/rejected depends on the posterior probability at that new location compared to the posterior probability at the previous location; if the posterior probability has improved then the step is accepted, while if the posterior probability has worsened then the step is randomly accepted or rejected (the relative probability of which depends on the ratio of the posterior probabilities at the proposed and current step locations). However, the Metropolis-Hastings algorithm can be inefficient in the presence of strong correlations between parameters as the step proposal is not aware of the broader shape of the posterior PDF beyond the value at the previous and newly proposed steps. The Metropolis-Hastings algorithm can also be quite inconvenient to use as the efficiency and convergence of the algorithm strongly depend on the selected tunable parameters which can be difficult to estimate.

One popular MCMC step proposal algorithm to use in the presence of strong parameter correlations and to avoid the tunable parameter estimation of the Metropolis-Hastings algorithm is the Affine Invariant MCMC Ensemble sampler (Goodman & Weare, 2010) which is implemented in the Python programming language as the `emcee` package (Foreman-Mackey et al., 2013). In this method, a large number of chains are run concurrently (together called an ensemble), and each walker's next step depends on the position of the other walkers in the ensemble. In particular, a random walker is selected from the rest of the ensemble (excluding the walker currently being moved) and then a new step location is proposed along the ray originating from the other walker and passing through the walker currently being updated. The size and direction of this step is randomly drawn from a distribution with a single tunable parameter which is typically just left at a default value of 2. The probability that the step is accepted/rejected is then the same as that used in the Metropolis-Hastings algorithm. This step procedure is then serially applied for each walker, where the previously updated walker is added back into the ensemble of walkers. Adaptations on this algorithm also exist in order to allow for parallel computing which is especially useful when it takes a long time to evaluate the likelihood function (typically when slower than $\sim$1 ms).

Paper 1

The Very Low Albedo of WASP-12b from Spectral Eclipse Observations with *Hubble*

Preface

Eclipse observations at optical wavelengths are typically most sensitive to reflected light because exoplanets typically emit minimal light at such short wavelengths. In the following paper, published in the Astrophysical Journal Letters (Bell et al., 2017), we present the second-ever spectrally resolved optical eclipse observation of an exoplanet. The observations seek to measure the albedo of the ultra-hot Jupiter WASP-12b and were part of a larger proposal to observe the optical eclipse spectra of three other hot Jupiters. Based on `NEMISIS` modelling before the observations were collected, we expected a strong detection whether the planet was cloud-free or covered in an aluminum-oxide haze. When this paper was submitted, the term ultra-hot Jupiter was not commonly in use.

THE VERY LOW ALBEDO OF WASP-12b FROM SPECTRAL ECLIPSE OBSERVATIONS WITH *HUBBLE*

Taylor J. Bell,[1,*] Nikolay Nikolov,[2] Nicolas B. Cowan,[1,3,*] Joanna K. Barstow,[4] Travis S. Barman,[5] Ian J. M. Crossfield,[6] Neale P. Gibson,[7] Thomas M. Evans,[2] David K. Sing,[2] Heather A. Knutson,[8] Tiffany Kataria,[9] Joshua D. Lothringer,[5] Björn Benneke,[10] and Joel C. Schwartz[1,3,*]

[1] *Department of Physics, McGill University, 3600 rue University, Montréal, QC H3A 2T8, Canada*
[2] *Department of Physics and Astronomy, University of Exeter, Exeter EX4 4QL, UK*
[3] *Department of Earth & Planetary Sciences, McGill University, 3450 rue University, Montréal, QC H3A 0E8, Canada*
[4] *Department of Physics and Astronomy, University College London, Gower Street, London WC1E 6BT, UK*
[5] *Lunar and Planetary Laboratory, University of Arizona, 1629 E. University Boulevard, Tucson, AZ 85721, USA*
[6] *Department of Physics, Massachusetts Institute of Technology, Cambridge, MA, USA*
[7] *Astrophysics Research Centre, School of Mathematics and Physics, Queens University Belfast, Belfast, BT7 1NN, UK*
[8] *Division of Geological and Planetary Sciences, California Institute of Technology, Pasadena, CA 91125, USA*
[9] *Jet Propulsion Laboratory, California Institute of Technology, 4800 Oak Grove Drive, Pasadena, CA 91109, USA*
[10] *Department of Physics, Université de Montréal, 2900 boul. Édouard-Montpetit, Montréal, QC H3T 1J4, Canada*

(Received 2017 June 26; Revised 2017 August 17; Accepted 2017 August 19; Published 2017 September 14)

Submitted to ApJL

ABSTRACT

We present an optical eclipse observation of the hot Jupiter WASP-12b using the Space Telescope Imaging Spectrograph on board the Hubble Space Telescope. These spectra allow us to place an upper limit of $A_g < 0.064$ (97.5% confidence level) on the planet's white light geometric albedo across 290–570 nm. Using six wavelength bins across the same wavelength range also produces stringent limits on the geometric albedo for all bins. However, our uncertainties in eclipse depth are ∼40% greater

Corresponding author: Taylor J. Bell
taylor.bell@mail.mcgill.ca

than the Poisson limit and may be limited by the intrinsic variability of the Sun-like host star — the solar luminosity is known to vary at the 10^{-4} level on a timescale of minutes. We use our eclipse depth limits to test two previously suggested atmospheric models for this planet: Mie scattering from an aluminum-oxide haze or cloud-free Rayleigh scattering. Our stringent nondetection rules out both models and is consistent with thermal emission plus weak Rayleigh scattering from atomic hydrogen and helium. Our results are in stark contrast with those for the much cooler HD 189733b, the only other hot Jupiter with spectrally resolved reflected light observations; those data showed an increase in albedo with decreasing wavelength. The fact that the first two exoplanets with optical albedo spectra exhibit significant differences demonstrates the importance of spectrally resolved reflected light observations and highlights the great diversity among hot Jupiters.

Keywords: planets and satellites: atmospheres — stars: individual (WASP-12) — techniques: photometric

* McGill Space Institute; Institute for Research on Exoplanets

1. INTRODUCTION

Thermal measurements of hot Jupiters suggest that these gas giant exoplanets often have moderate Bond albedos ($A_B \approx 0.4$, the fraction of incident energy reflected to space; Schwartz et al. 2017). However, many previous searches for reflected light from hot Jupiters have found little-to-none at optical wavelengths where the host star emits most of its energy (geometric albedo $A_g < 0.1$; e.g., Rowe et al. 2008; Kipping & Spiegel 2011; Heng & Demory 2013; Dai et al. 2017). It is unclear what is causing this apparent contradiction between constraints from thermal emission and optical reflection. Previous Hubble Space Telescope (*HST*) eclipse observations of HD 189733b with the Space Telescope Imaging Spectrograph (STIS) showed an increase in reflectivity toward bluer wavelengths which may, at least in part, explain the discrepancies between these two techniques (Evans et al. 2013).

A direct way to probe the back scattering efficiency of a hot Jupiter's atmosphere is observing the planet at optical wavelengths (where thermal emission is negligible) during eclipse, when the planet is near full phase and passes behind its host star. This method requires at least an order of magnitude higher photometric precision than transit observations of the same planet because the planet will be fainter than its host star, while the occulted area remains the same.

Observing an atmosphere at different orbital phases can provide further information about the scattering particles (e.g., Demory et al. 2013; Esteves et al. 2013; Heng & Demory 2013; Garcia Munoz & Isaak 2015; Shporer & Hu 2015; Oreshenko et al. 2016). Parmentier et al. (2016) suggested a connection between reflected light phase curve measurements and a sequence of condensate cloud models, but this only covered temperatures up to $T_{\mathrm{eq}} \sim 2200$ K: well below the equilibrium temperature of WASP-12b ($T_{\mathrm{eq}} = 2580$ K; Collins et al. 2017).

WASP-12b orbits a G0V star with an orbital period of 1.09 days (Hebb et al. 2009). While the host star is fairly faint (V = 12), WASP-12b's close semi-major axis and large radius ($a = 0.0234$ au, $R_p = 1.90\ R_J$, $R_p = 0.19\ R_*$; Collins et al. 2017) make it an excellent target for detailed study. Transit observations of WASP-12b range from 0.3 to 4.5 μm, and eclipse observations range from 0.9 to 8.0 μm (e.g., Hebb et al. 2009; López-Morales et al. 2010; Campo et al. 2011; Madhusudhan et al. 2011; Cowan et al. 2012; Crossfield et al. 2012; Copperwheat et al. 2013; Föhring et al. 2013; Sing et al. 2013; Swain et al. 2013; Stevenson et al. 2014a,b; Croll et al. 2015; Sing et al. 2016). This work presents the first optical eclipse measurement of WASP-12b.

The atmospheric composition of WASP-12b has been extensively studied (e.g., Madhusudhan et al. 2011; Crossfield et al. 2012; Swain et al. 2013; Stevenson et al. 2014b), with initial claims of a C/O ratio greater than unity. This was first challenged by Crossfield et al. (2012) and Cowan et al. (2012), who instead reported an isothermal photosphere for WASP-12b. The recent detection of water in the planet's atmosphere has now firmly refuted the carbon-rich hypothesis (Kreidberg et al. 2015). Sing et al. (2013) found that the best-fit model for WASP-12b transmission spectroscopy was Mie scattering by an aluminum-oxide (Al_2O_3) haze. Barstow et al. (2017) found that an optically thick Rayleigh scattering aerosol with a 0.01 mbar top pressure best described the transmission observations, but the model poorly described the steep increase in transit depth at optical wavelengths. Schwartz et al. (2017) used thermal phase variations and eclipse depths to determine a Bond albedo of $A_B = 0.2^{+0.1}_{-0.12}$ and a dayside effective temperature of $T_{\rm day} = 2864 \pm 15$ K.

2. OBSERVATIONS AND DATA REDUCTION

On 2016 October 19, a single eclipse of WASP-12b was observed with five *HST* orbits, using the STIS G430L grating (290–570 nm). The first *HST* orbit has significantly worse systematics than the four later orbits as a result of the repointing of the telescope, so these data were removed from the subsequent analysis. This left two *HST* orbits out of eclipse (one before and one after) when the planet and host star were both visible with the planet near full phase, as well as two *HST* orbits during eclipse when the planet was behind its host star, leaving only the star's light visible. These observations were granted as a part of programme GO-14797 (PI: Crossfield).

We used the same data collection method as previously used for similar observations (Sing et al. 2011, 2013, 2016; Evans et al. 2013). The subarray readout mode with a wide $52'' \times 2''$ slit was used to minimize time-varying slit losses; this produced 1024×128 pixel images. In previous *HST*/STIS observations, the first frame from each *HST* orbit had systematically lower counts, so a 1 s dummy exposure was obtained at the beginning of each orbit, which successfully mitigated this systematic effect. This dummy exposure was then followed by 10 science exposures lasting 279 s each (the maximum recommended duration to avoid excessive cosmic-ray hits). Our final, analyzed dataset thus contains 40 exposures collected over 331 minutes.

The raw STIS data were reduced (bias-, dark-, and flat-corrected) using the latest version of the `CALSTIS1` pipeline and the relevant up-to-date calibration frames. Cosmic-ray events were identified and removed following Nikolov et al. (2014), as were all pixels identified as "bad" by `CALSTIS`. Overall, $\sim$9% of the pixels in each 2D spectrum were affected by cosmic-rays with another $\sim$5% identified as "bad", resulting in a total of $\sim$14% interpolated pixels.

Next, the IRAF procedure `apall` was used to extract spectra from the calibrated .flt science files. We tested apertures between 9.0 and 17.0 pixels in intervals of 2 pixels and found that an 11.0 pixel aperture resulted in the lowest lightcurve residual scatter after fitting the white light data. However, the difference between apertures was minute ($\sim$1 ppm). We then used cross-correlation to correct for subpixel shifts along the dispersion axis. The x1d files from `CALSTIS` were then used to calibrate the wavelength axis. Finally, both "white light" and six spectral channel lightcurves were produced by integrating the appropriate flux from each bandpass.

WASP-12b's host star WASP-12A is also orbited by two M-dwarf companions bound in a binary system 1.06″ away from WASP-12A (Bergfors et al. 2011; Sing et al. 2013; Bechter et al. 2014). For our observations, the spectrograph slit orientation was chosen to be perpendicular to the line connecting WASP-12A and WASP-12(B,C) to allow maximal separation in the spatial direction of the resulting FITS files. The spectrum of the stellar companions is visually distinguishable from WASP-12A in the raw spectra and does not fall within our small spatial-axis aperture.

3. LIGHTCURVE ANALYSIS

The top panel of Figure 1 shows the raw lightcurve binned across the entire STIS G430L bandpass ("white light"). There is a strong, repeated trend in flux, with exposures from each orbit appearing to follow a roughly polynomial trend. This systematic is well known and is believed to be the result of the thermal cycle of *HST* throughout its orbit as well as the movement of the spectral trace on the detector (e.g., Brown et al. 2001; Sing et al. 2011; Huitson et al. 2012; Evans et al. 2013).

These systematic trends are also observed during *HST*/STIS observations of planetary transits, and a standard approach to remove them is assuming polynomial variations as a function of auxiliary variables (e.g., Sing et al. 2011; Huitson et al. 2012). More recently, Gibson et al. (2011) used Gaussian processes (GPs) to model the *HST* systematics, as the choice of polynomial model can potentially bias the results. For this reason, we modelled the systematics with the GP library `george` (Foreman-Mackey 2015) and used the same method as Evans et al. (2013). A detailed discussion of modelling systematics with GPs can be found in Gibson et al. (2012a,b, 2013). We also attempted to fit the systematic variations with a polynomial model, which gave results consistent with our GP model.

3.1. *Gaussian Process Model*

The likelihood of a GP model is described as a multivariate normal distribution with

$$p(\boldsymbol{f}|\boldsymbol{X},\boldsymbol{\theta},\boldsymbol{\Omega},\boldsymbol{t}) = \mathcal{N}(\boldsymbol{E}(\boldsymbol{\Omega},\boldsymbol{t}),\boldsymbol{\Sigma}(\boldsymbol{X},\boldsymbol{\theta}))\,, \tag{1}$$

where $\boldsymbol{f}$ is the 40 measured fluxes, $\boldsymbol{E}$ is the eclipse function, and $\boldsymbol{\Sigma}$ is the *kernel* (covariance matrix). The time at the midpoint of each exposure is represented by $\boldsymbol{t}$. Further, $\boldsymbol{X} = [\boldsymbol{\phi},\boldsymbol{\psi}]^T$ is the matrix of covariates, where $\boldsymbol{\phi}$ is the orbital phase of *HST*, and $\boldsymbol{\psi}$ is the slope of the spectral trace on the detector (computed using IRAF's `apall` procedure). These two covariates were selected as they provided the lowest scatter in the residuals after calibration. We also tested the inclusion of two additional covariates: the y-intercept of the spectral trace on the detector and the measured shifts of the spectral trace along the dispersion axis. However, the inclusion of these additional covariates did not significantly impact our results or uncertainties, likely because the covariates themselves are significantly correlated with the other covariates.

Our eclipse parameters are given by $\boldsymbol{\Omega} = [\alpha,\delta,\beta]^T$, where α is the baseline flux consisting of light emitted from both the planet and star, δ is the fractional eclipse depth ($\delta = F_{\rm planet}/F_{\rm star}$), and β describes a constant rate of change in the baseline flux over time. Since we did not observe during eclipse ingress or egress, we used a boxcar function to describe the eclipse signal, with

$$E_i = \alpha(1 - \delta B_i)(1 + \beta(t_i - t_0))$$
$$B_i = \begin{cases} 0 & i \in \text{Orbit 2 or 5} \\ 1 & i \in \text{Orbit 3 or 4}\,, \end{cases} \tag{2}$$

where t_0 is the time of the first exposure.

Our GP parameters are given by $\boldsymbol{\theta} = [C, L_\phi, L_\psi, \sigma_w]^T$, where C^2 is the maximum covariance, L_ϕ and L_ψ are covariance lengthscales, and σ_w is the white noise level. We adopted the squared-exponential kernel:

$$\boldsymbol{\Sigma}_{nm} = C^2 \exp\left[-\sum_{i=0}^{1} \frac{(\boldsymbol{X}_{in} - \boldsymbol{X}_{im})^2}{L_i^2} \right] + \delta_{nm}\sigma_w^2\,, \tag{3}$$

where $L_i = [L_\phi, L_\psi]_i$ and δ_{nm} is the Kronecker delta function. This kernel can be simply understood as requiring that observations be strongly correlated if they have similar spectral trace slope and *HST* orbital phase, while observations further from each other in covariate space are more weakly correlated. This then describes a smoothly varying function of the covariates, with the addition of white noise.

The final model is then given by

$$f^* = \boldsymbol{\mu}(\boldsymbol{\phi}, \boldsymbol{\psi}) + \boldsymbol{E}(\boldsymbol{\Psi})\,, \tag{4}$$

where $\boldsymbol{\mu}(\boldsymbol{\phi}, \boldsymbol{\psi})$ is the GP model mean.

The Markov Chain Monte Carlo (MCMC) ensemble sampler software `emcee` (Foreman-Mackey et al. 2013) was used to explore the seven parameters, determining the most likely parameter values and their uncertainties. For computational reasons, the variables used in this MCMC were $\{\delta$, $\ln(\alpha)$, β, $\ln(L_\phi)$, $\ln(L_\psi)$, $\ln(\sigma_w^2)$, and $\ln(C^2)\}$. Using logarithms removes the need to use a prior to obtain strictly positive values. While the eclipse depth, δ, should be strictly positive, we allowed for negative values to ensure an unbiased estimate. A uniform prior was used so $\ln(L_\phi) < 0$ and $\ln(L_\psi) < 0$, which has the effect of ensuring that these lengthscales are within a few orders of magnitude of the variations in the covariates. For un-normalized white light data, the best-fit values from a 10^6 step MCMC chain were $\{\delta = (-5.3 \pm 7.4) \times 10^{-5},\ \alpha = (4.198^{+0.012}_{-0.008}) \times 10^{7},\ \beta = 0.0056 \pm 0.0015,\ L_{\phi} = 0.05^{+0.19}_{-0.03},$ $L_{\psi} = 0.03^{+0.27}_{-0.03}$, $\sigma_w^2 = (5.2^{+1.7}_{-1.3}) \times 10^{7}$, and $C^2 = (8^{+14}_{-5}) \times 10^{7}\}$.

The top panel of Figure 1 shows the median model and uncertainty from a 10^6 step MCMC chain overplotted on the raw white light flux measurements. The bottom panel of Figure 1 shows the lightcurve produced by subtracting the median model from the raw spectra (excluding the change in flux during eclipse), with the median eclipse model overplotted. The clear linear trend in the calibrated flux of *HST* orbit #5 (bottom panel of Figure 1) shows that there is still substantial correlated noise in the data that could not be described by any of the four considered covariates.

4. RESULTS

The STIS G430L spectra were binned into six spectral channels to allow moderate wavelength resolution while keeping uncertainties on each channel sufficiently small to be able to test atmospheric models. Each spectral channel was modelled independently using the GP method described above. Lightcurves after GP calibration are shown for each spectral channel in Figure 2, and the relevant results are tabulated in Table 1. Eclipse depths were found using the median value from a 10^6 step MCMC chain, while the 84 and 97.5 percentiles were used to determine upper limits. The larger uncertainties in eclipse depth at shorter wavelengths are due to lower stellar flux and detector sensitivity.

Because WASP-12b is so strongly irradiated, the peak of its thermal emission is expected to be at $\sim$1 μm for a $\sim$2800 K dayside temperature (Schwartz et al. 2017). For this reason, we calculated the predicted eclipse depths due to thermal radiation from WASP-12b, assuming a $T = 3000$ K blackbody for WASP-12b (hotter than inferred from infrared observations due to the greater depth of the optical photosphere; Cowan & Agol 2011) and a standard G0V spectrum from Pickles (1998) for WASP-12. These depths ($\delta_{\rm thermal}$) are summarized in Table 1 and are all within our 97.5% confidence interval upper limits.

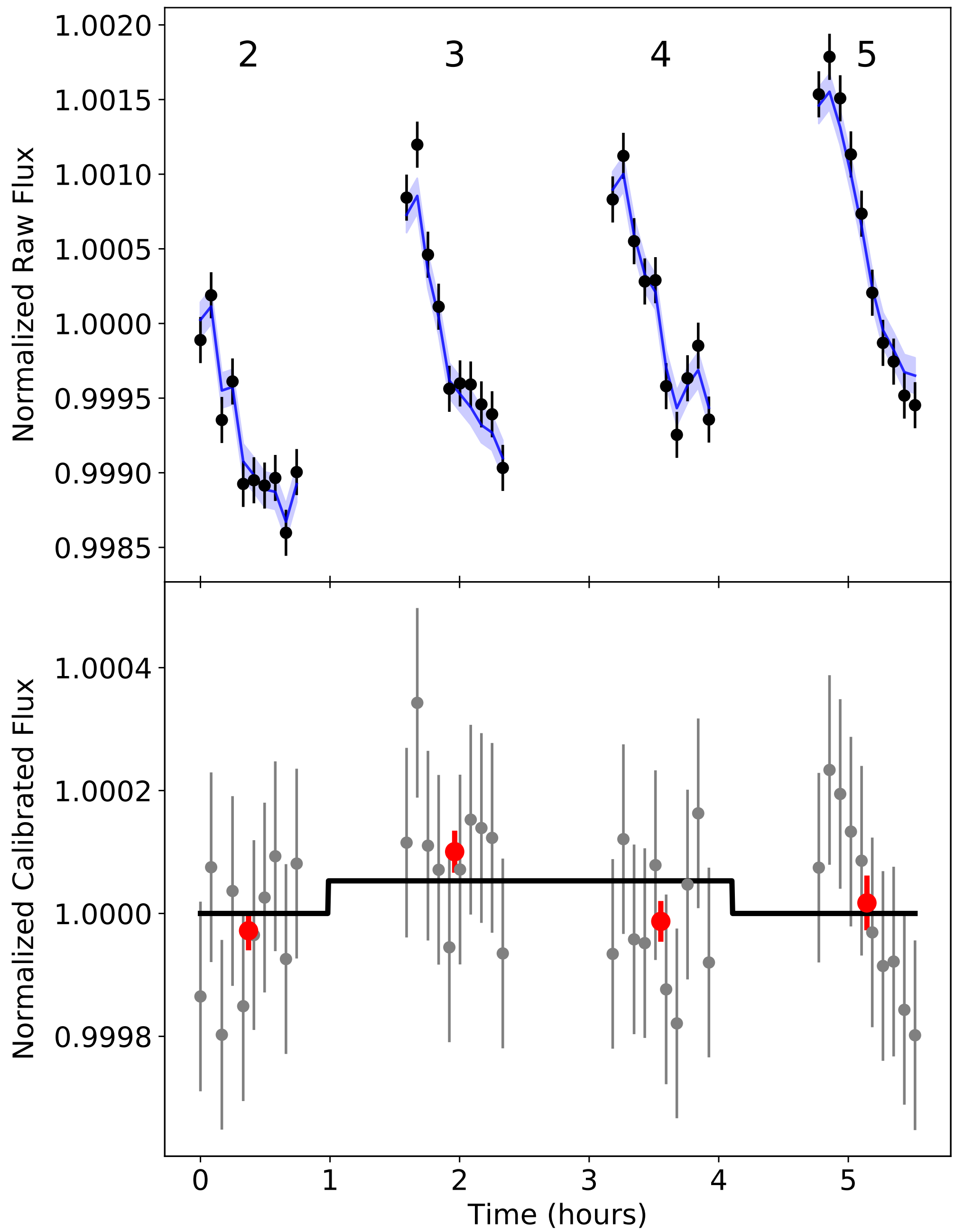

Figure 1. *Top:* raw flux with the entire spectral range of *HST*/STIS binned into a single white lightcurve. The median systematic model and 1σ model uncertainty are shown with a blue line and blue shaded region, respectively. Each individual *HST* orbit is labelled. *Bottom:* the white light data after calibration using a Gaussian Process are shown in grey. Also shown in red are the binned fluxes for each *HST* orbit, although these were not used during fitting. Overplotted is the best-fit eclipse signal that corresponds to a wavelength-averaged geometric albedo of $A_g = -0.035$ ($A_g < 0.064$ at 97.5% confidence). All plotted error bars in both panels only capture uncorrelated, white noise.

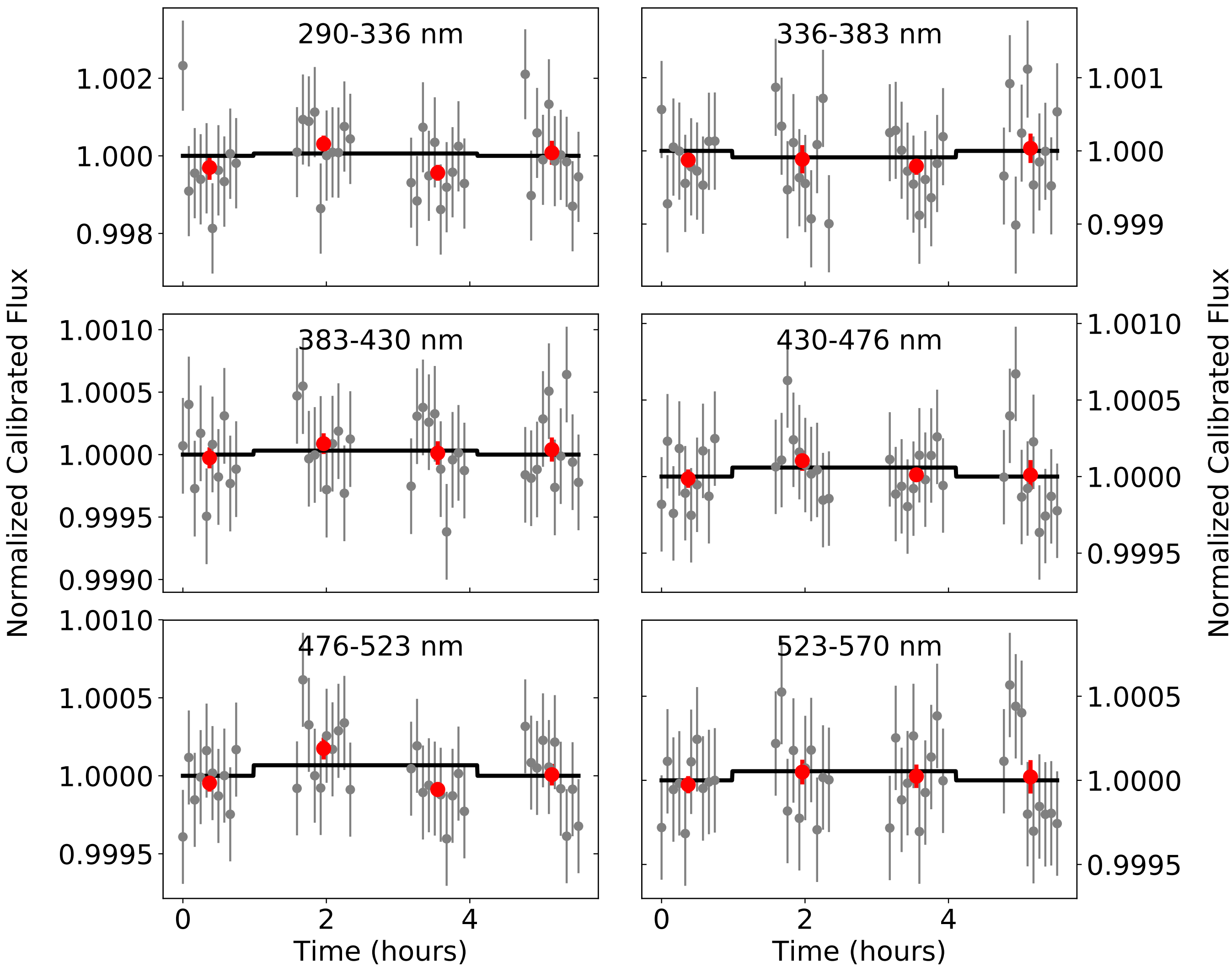

Figure 2. Lightcurves for each spectral channel after calibration using a Gaussian process are shown in grey, with the best-fit eclipse signal overplotted. Also shown in red are the binned fluxes for each *HST* orbit, although these were not used during fitting. All plotted error bars only capture uncorrelated, white noise; where no error bar is visible, it is smaller than the point size used.

If interpreted as solely due to reflected light, eclipse depths can be converted to geometric albedo using

$$A_g = \delta \left(\frac{R_p}{a} \right)^{-2}, \tag{5}$$

where $R_p = 1.90\ R_J$ is the radius of the planet, and $a = 0.0234$ AU is its orbital semi-major axis (Collins et al. 2017). Applying Equation (5) to the best-fit eclipse depths and their corresponding

Table 1. Eclipse Depths and Geometric Albedos

Wavelengths	Eclipse Depth, δ (ppm)		$\delta_{\mathrm{thermal}}$	Geometric Albedo, A_g	
(nm)	Best fit	97.5% Upper Limit	(ppm)	Best Fit	97.5% Upper Limit
290 – 570	-53 ± 74	96	56	-0.035 ± 0.050	0.064
290 – 336	-60 ± 540	1020	10	-0.04 ± 0.36	0.68
336 – 383	90 ± 290	670	20	0.06 ± 0.20	0.45
383 – 430	-30 ± 180	330	40	-0.02 ± 0.12	0.22
430 – 476	-60 ± 130	210	60	-0.039 ± 0.089	0.14
476 – 523	-70 ± 130	190	100	-0.045 ± 0.087	0.13
523 – 570	-50 ± 150	240	160	-0.036 ± 0.098	0.16

upper limits gives constraints on the geometric albedo across the STIS G430L wavelength range (summarized in Table 1)

Our reported uncertainties on eclipse depths are ∼40% higher than the photon limit. The increased scatter in our data may be the result of incomplete modelling of the systematic noise. Alternatively, our uncertainties may be limited by intrinsic stellar variability. Given the slow rotation period of WASP-12 compared to the observing window ($P_{rot} \gtrsim 23$ days given $v \sin i < 2.2$ km/s; Hebb et al. 2009), variability due to stellar rotation (e.g. starspots passing in and out of view) should not significantly affect our observations. However, our Sun's total irradiance (spatially and spectrally integrated) is known to vary at the 10^{-4} level on timescales of minutes to hours as a result of solar convection and oscillations (Kopp 2016). Given the G0V spectral class of WASP-12, similar variations may also be present and may explain the greater than Poisson limit uncertainties as well as the residual correlated noise in the calibrated time-series spectra.

5. DISCUSSION AND CONCLUSIONS

We use the `NEMESIS` spectral retrieval tool (Irwin et al. 2008; Barstow et al. 2014) to produce predicted model spectra given two previously proposed models for WASP-12b: an Al_2O_3 haze and a cloud-free atmosphere. `NEMESIS` is not a radiative equilibrium code; rather, it takes an atmospheric model and calculates incident and emergent flux and will not take into account heating from incoming stellar radiation. The limits from our *HST*/STIS eclipse observations firmly reject both models; we find χ^2 per datum (χ^2/N_{obs}, $N_{obs} = 6$) of 41 and 10 for the Al_2O_3 haze and cloud-free models.

Given its exceedingly high equilibrium temperature ($T_{\rm eq} = 2580$ K; Collins et al. 2017), WASP-12b would technically lie within Sudarsky et al.'s (2000) Class V ($T_{\rm eff} > 1500$ K) but is far hotter than any planet they considered. On the planet's dayside, WASP-12b is far too hot for condensates to form (Wakeford et al. 2017). However, temperatures near the planet's day–night terminator, and across the planet's nightside, may be cool enough to allow for the formation of condensates that could affect transmission spectroscopy without significantly affecting dayside eclipse spectroscopy.

Also, it is expected that Na I absorption (which is important at lower temperatures) will not contribute much to the low albedo of WASP-12b as most of the sodium will be ionized on the hot dayside. Instead, it is expected that the atmosphere will be dominated by Rayleigh scattering from atomic hydrogen and helium, with a small contribution from electron scattering. The red line in Figures 3 and 4 shows the predicted eclipse depth (binned to a resolution of 1 point per 5 nm) from Crossfield et al. (2012) made with the `PHOENIX` atmosphere code adapted for hot Jupiters as described in Barman et al. (2001, 2005). In this model, reflected light makes up $\lesssim 10\%$ of the eclipse depth ($A_g \lesssim 0.002$) at the shortest wavelengths and $\ll 1\%$ of the eclipse depth at infrared wavelengths; the remainder of the eclipse depth is due to thermal emission. This model gives a χ^2 per datum of 0.9 for our *HST*/STIS data ($N_{obs} = 6$), but a worse χ^2 per datum of 3 for all of the data plotted on Figure 4 ($N_{obs} = 21$).

There are significant differences between the `PHOENIX` model and the cloud-free model produced by `NEMISIS`, including but not limited to the inclusion of atomic hydrogen opacities (lines and bound-free opacities), as well as the typical opacities more commonly associated with cool stellar photospheres.

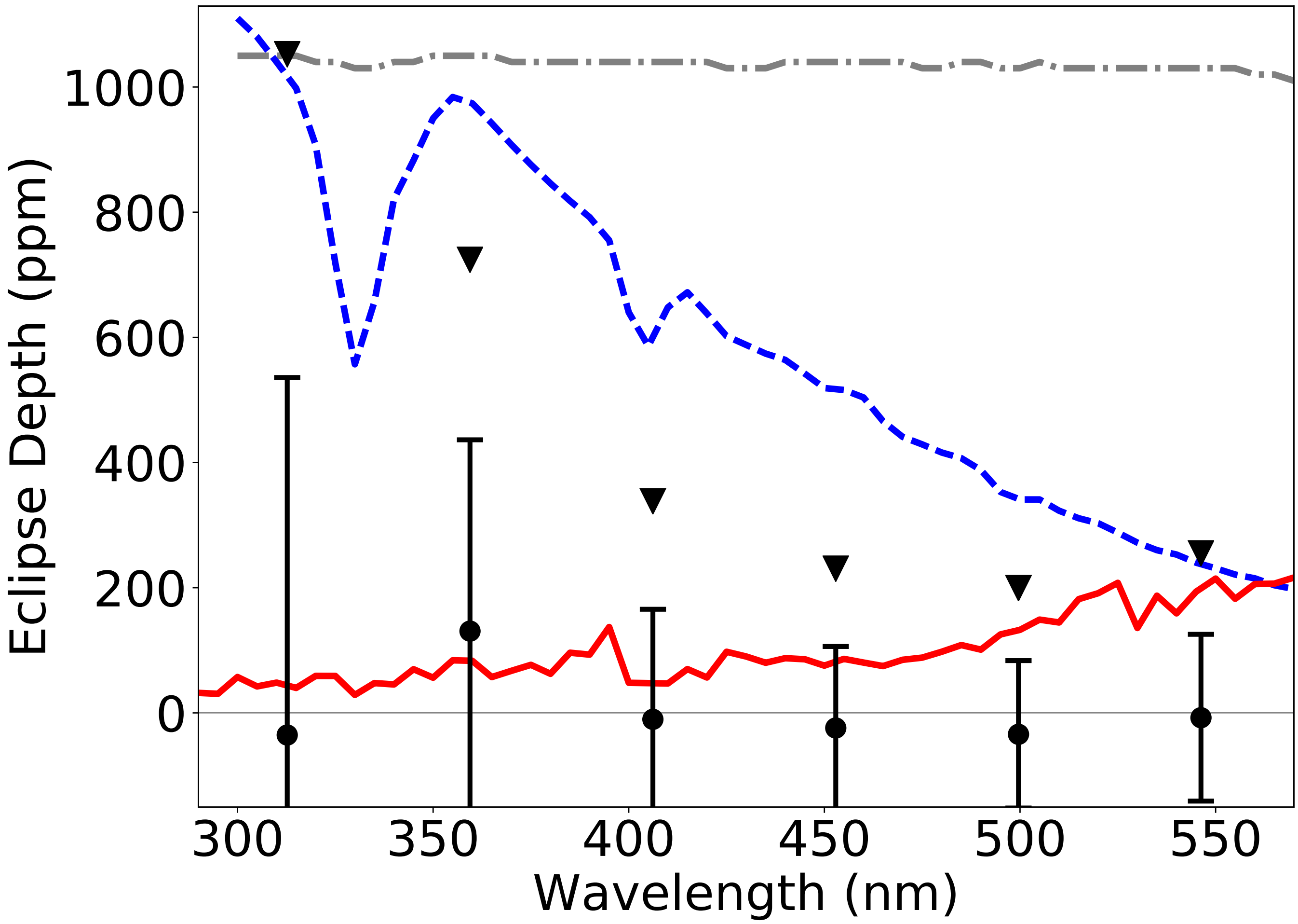

Figure 3. Best-fit eclipse depths and 1σ uncertainties are shown with black points and error bars, with black triangles denoting 97.5% confidence upper limits. Previously proposed models for WASP-12b made with `NEMESIS` are shown with a grey, dashed-dotted line (aluminum-oxide haze) and a blue, dashed line (cloud-free). The *HST*/STIS data firmly reject both models and are instead consistent with the thermally dominated `PHOENIX` model shown with a red solid line.

Also, the `PHOENIX` model results from a self-consistent calculation of the thermal structure, chemistry, line-by-line opacities (as well as scattering), and irradiation, thereby accounting for important changes that occur in the hot upper layers of WASP-12b (for example, the transition from H_2 to H at low pressures and the thermal ionization of Na and K).

Our observations cover the blackbody peak of WASP-12 (~450 nm) and show that little of the incident radiation at these wavelengths is reflected by the planet. Geometric albedo is related to spherical albedo through a phase integral q such that $A_s = qA_g$, and Bond albedo is equal to

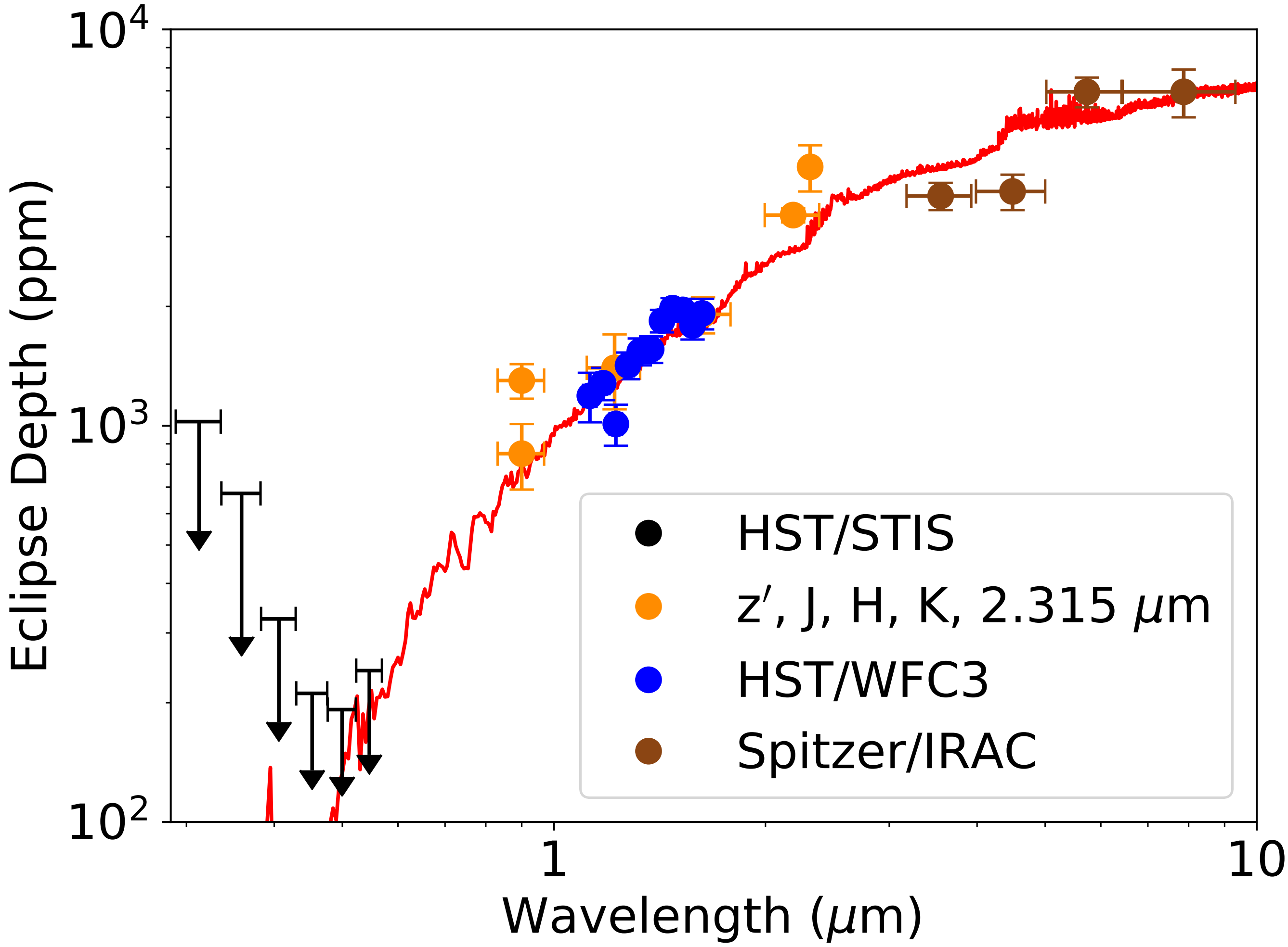

Figure 4. Our *HST*/STIS 97.5% confidence interval upper limits on the eclipse depth for each of the six considered spectral channels are shown with black arrows. All eclipse depths aside from *HST*/STIS are taken from Stevenson et al. (2014b, and references therein). The red line is the same as in Figure 3.

the flux-weighted, wavelength-averaged spherical albedo. If we assume diffuse scattering ($q = 1.5$), our "white light" 97.5% confidence upper limit on the geometric albedo across the STIS bandpass ($A_g < 0.064$) suggests < 10% of the energy received at these wavelengths is reflected. However, since the wavelengths observed cover only 36% of the incident stellar energy, the Bond albedo is not well constrained by these measurements and is consistent with Schwartz et al.'s (2017) measurement of $A_B = 0.2^{+0.1}_{-0.12}$.

Our results are in stark contrast with those for the much cooler HD 189733b, the only other hot Jupiter with spectrally resolved reflected light observations (Evans et al. 2013); those data showed an increase in albedo with decreasing wavelength. The fact that the first two exoplanets with optical albedo spectra exhibit significant differences demonstrates the importance of spectrally resolved reflected light observations and highlights the great diversity among hot Jupiters.

T.J.B. acknowledges support from the McGill Space Institute Graduate Fellowship and from the FRQNT through the Centre de recherche en astrophysique du Québec. J.K.B. acknowledges support from the Royal Astronomical Society Research Fellowship. I.J.M.C. was supported under contract with the Jet Propulsion Laboratory (JPL) funded by NASA through the Sagan Fellowship Program executed by the NASA Exoplanet Science Institute. The research leading to these results has received funding from the European Research Council under the European Union's Seventh Framework Programme (FP7/2007-2013) / ERC grant agreement No. 336792. This work is based on observations made with the NASA/ESA Hubble Space Telescope, obtained at the Space Telescope Science Institute, which is operated by the Association of Universities for Research in Astronomy, Inc., under NASA contract NAS 5-26555. The Al_2O_3 and cloud-free models tested in this work were made with the `NEMESIS` code developed by Patrick Irwin. We have also made use of free and open-source software provided by the Matplotlib, Python, and SciPy communities.

Facilities: HST(STIS)

REFERENCES

Barman, T. S., Hauschildt, P. H., & Allard, F. 2001, ApJ, 556, 885

Barman, T. S., Hauschildt, P. H., & Allard, F. 2005, ApJ, 632, 1132

Barstow, J. K., Aigrain, S., Irwin, P. G. J., et al. 2014, ApJ, 786, 154

Barstow, J. K., Aigrain, S., Irwin, P. G. J., & Sing, D. K. 2017, ApJ, 834, 50

Bechter, E. B., Crepp, J. R., Ngo, H., et al. 2014, ApJ, 788, 2

Bergfors, C., Brandner, W., Henning, T., & Daemgen, S. 2011, Proceedings of the International Astronomical Union, 6(S276), 397–398

Brown, T. M., Charbonneau, D., Gilliland, R. L., Noyes, R. W., & Burrows, A. 2001, ApJ, 552, 699

Campo, C. J., Harrington, J., Hardy, R. A., et al. 2011, ApJ, 727, 125

Collins, K. A., Kielkopf, J. F., & Stassun, K. G. 2017, AJ, 153, 78

Copperwheat, C. M., Wheatley, P. J., Southworth, J., et al. 2013, MNRAS, 434, 661

Cowan, N. B., & Agol, E. 2011, ApJ, 729, 54

Cowan, N. B., Machalek, P., Croll, B., et al. 2012, ApJ, 747, 82

Croll, B., Albert, L., Jayawardhana, R., et al. 2015, ApJ, 802, 28

Crossfield, I. J. M., Barman, T., Hansen, B. M. S., Tanaka, I., & Kodama, T. 2012, ApJ, 760, 140

Dai, F., Winn, J. N., Yu, L., & Albrecht, S. 2017, AJ, 153, 40

Demory, B.-O., de Wit, J., Lewis, N., et al. 2013, ApJL, 776, L25

Esteves, L. J., De Mooij, E. J. W., & Jayawardhana, R. 2013, ApJ, 772, 51

Evans, T. M., Pont, F., Sing, D. K., et al. 2013, ApJL, 772, L16

Föhring, D., Dhillon, V. S., Madhusudhan, N., et al. 2013, MNRAS, 435, 2268

Foreman-Mackey, D. 2015, George: Gaussian Process regression, Astrophysics Source Code Library, , , ascl:1511.015

Foreman-Mackey, D., Conley, A., Meierjurgen Farr, W., et al. 2013, emcee: The MCMC Hammer, Astrophysics Source Code Library, , , ascl:1303.002

Garcia Munoz, A., & Isaak, K. G. 2015, PNAS, 112, 13461

Gibson, N. P., Aigrain, S., Barstow, J. K., et al. 2013, MNRAS, 428, 3680

Gibson, N. P., Aigrain, S., Roberts, S., et al. 2012a, MNRAS, 419, 2683

Gibson, N. P., Pont, F., & Aigrain, S. 2011, MNRAS, 411, 2199

Gibson, N. P., Aigrain, S., Pont, F., et al. 2012b, MNRAS, 422, 753

Hebb, L., Collier-Cameron, A., Loeillet, B., et al. 2009, ApJ, 693, 1920

Heng, K., & Demory, B.-O. 2013, ApJ, 777, 100

Huitson, C. M., Sing, D. K., Vidal-Madjar, A., et al. 2012, MNRAS, 422, 2477

Irwin, P. G. J., Teanby, N. A., de Kok, R., et al. 2008, JQSRT, 109, 1136

Kipping, D. M., & Spiegel, D. S. 2011, MNRAS, 417, L88

Kopp, G. 2016, JSWSC, 6, A30

Kreidberg, L., Line, M. R., Bean, J. L., et al. 2015, ApJ, 814, 66

López-Morales, M., Coughlin, J. L., Sing, D. K., et al. 2010, ApJL, 716, L36

Madhusudhan, N., Harrington, J., Stevenson, K. B., et al. 2011, Nature, 469, 64

Nikolov, N., Sing, D. K., Pont, F., et al. 2014, MNRAS, 437, 46

Oreshenko, M., Heng, K., & Demory, B.-O. 2016, MNRAS, 457, 3420

Parmentier, V., Fortney, J. J., Showman, A. P., Morley, C., & Marley, M. S. 2016, ApJ, 828, 22

Pickles, A. J. 1998, PASP, 110, 863

Rowe, J. F., Matthews, J. M., Seager, S., et al. 2008, ApJ, 689, 1345

Schwartz, J. C., Kashner, Z., Jovmir, D., & Cowan, N. B. 2017, ApJ, 850, 154

Shporer, A., & Hu, R. 2015, AJ, 150, 112

Sing, D. K., Fortney, J. J., Nikolov, N., et al. 2016, Nature, 529, 59

Sing, D. K., Lecavelier des Etangs, A., Fortney, J. J., et al. 2013, MNRAS, 436, 2956

Sing, D. K., Pont, F., Aigrain, S., et al. 2011, MNRAS, 416, 1443

Stevenson, K. B., Bean, J. L., Madhusudhan, N., & Harrington, J. 2014a, ApJ, 791, 36

Stevenson, K. B., Bean, J. L., Seifahrt, A., et al. 2014b, AJ, 147, 161

Sudarsky, D., Burrows, A., & Pinto, P. 2000, ApJ, 538, 885

Swain, M., Deroo, P., Tinetti, G., et al. 2013, Icarus, 225, 432

Wakeford, H. R., Visscher, C., Lewis, N. K., et al. 2017, MNRAS, 464, 4247

Epilogue

I have continued the study of light reflected from exoplanet atmospheres throughout my graduate studies using the technique of high-precision polarimetry. I was introduced to high-precision polarimetry through the commissioning of the new high-precision polarimeter POMM for the Mont Mégantic Observatory in Québec (la Polarimètre de l'Observatoire du Mont-Mégantic; Bastien et al., 2014). While we have collected some science observations with POMM, we are still in the early stages of understanding the instrument's performance and have not yet published any of this work.

As a result of the technical and scientific knowledge I developed while commissioning POMM, I was invited to join a team of scientists and engineers writing a mission concept study proposal to the Canadian Space Agency. The successful proposal sought to understand the potential science objectives achievable with, and feasibility of, a space-based, high-precision polarimeter which we named ÉPPÉ (Extrasolar Planet Polarimetry Explorer / Explorateur polarimétrique des planètes extrasolaires). Throughout this concept study, I led the scientific simulations[1] of such a mission in order to determine the requirements of the instrumentation and mission. I also provided significant domain knowledge in the development of the mission operations concept and the identification of the scientific priorities. The final report from the concept study was presented to the Canadian Space Agency in October 2018, and the team is currently exploring potential avenues for scientific and technological maturation studies. I am also planning on leading a publication discussing the opportunities and challenges of performing high-precision polarimetry from space as a result of this concept study.

[1] Simulation code publicly available at `https://github.com/taylorbell57/EPPE`

Paper 2

Increased Heat Transport in Ultra-hot Jupiter Atmospheres Through H_2 Dissociation/Recombination

Preface

The following paper was published in the Astrophysical Journal Letters (Bell & Cowan, 2018). In it, we presented a new theory for atmospheric heat transport in ultra-hot Jupiter atmospheres. Paper 1 concluded that the dayside atmosphere of the ultra-hot Jupiter WASP-12b was primarily composed of atomic hydrogen and helium, but we knew that the nightside of WASP-12b was far colder and would potentially be dominated by molecular hydrogen instead. Knowing that the dissociation and recombination of molecular hydrogen is a highly energetic process, we adapted a previously developed energy balance model to understand the impact of these effects on ultra-hot Jupiter atmospheres. Since publishing this paper, we have found out that the thermodynamic impacts from H_2 dissociation/recombination were actually first briefly discussed by Showman & Guillot (2002) in their Section 2 and Figure 1, and the effects were incorporated into their GCM, although their models did not consider planets hot enough for this effect to have a strong impact.

INCREASED HEAT TRANSPORT IN ULTRA-HOT JUPITER ATMOSPHERES THROUGH H_2 DISSOCIATION/RECOMBINATION

Taylor J. Bell[1,*] and Nicolas B. Cowan[1,2,*]

[1]*Department of Physics, McGill University, 3600 rue University, Montréal, QC H3A 2T8, Canada*
[2]*Department of Earth & Planetary Sciences, McGill University, 3450 rue University, Montréal, QC H3A 0E8, Canada*

(Received 2018 January 30; Revised 2018 April 04; Accepted 2018 April 07; Published 2018 April 23)

Submitted to ApJL

ABSTRACT

A new class of exoplanets is beginning to emerge: planets with dayside atmospheres that resemble stellar atmospheres as most of their molecular constituents dissociate. The effects of the dissociation of these species will be varied and must be carefully accounted for. Here we take the first steps toward understanding the consequences of dissociation and recombination of molecular hydrogen (H_2) on atmospheric heat recirculation. Using a simple energy balance model with eastward winds, we demonstrate that H_2 dissociation/recombination can significantly increase the day–night heat transport on ultra-hot Jupiters (UHJs): gas giant exoplanets where significant H_2 dissociation occurs. The atomic hydrogen from the highly irradiated daysides of UHJs will transport some of the energy deposited on the dayside toward the nightside of the planet where the H atoms recombine into H_2; this mechanism bears similarities to latent heat. Given a fixed wind speed, this will act to increase the heat recirculation efficiency; alternatively, a measured heat recirculation efficiency will require slower wind speeds after accounting for H_2 dissociation/recombination.

Corresponding author: Taylor J. Bell
taylor.bell@mail.mcgill.ca

Keywords: planets and satellites: atmospheres — planets and satellites: gaseous planets — methods: analytical — methods: numerical

* McGill Space Institute; Institute for Research on Exoplanets; Centre for Research in Astrophysics of Quebec

1. INTRODUCTION

Most gas giant exoplanets have atmospheres dominated by molecular hydrogen (H_2). However, on planets where the temperature is sufficiently high, a significant fraction of the H_2 will thermally dissociate; one may call these planets ultra-hot Jupiters (UHJs). Only a handful of known planets have dayside temperatures this high, but the Transiting Exoplanet Survey Satellite (TESS) mission is expected to discover hundreds more as it includes many early-type stars (G. Zhou, private communication 2017). These UHJs are an interesting intermediate between stars and cooler planets, and they will allow for useful tests of atmospheric models.

At these star-like temperatures, the H^- bound–free and free–free opacities should play an important role in the continuum atmospheric opacity that has recently been detected in dayside secondary eclipse spectra (Bell et al. 2017; Arcangeli et al. 2018). These recently reported detections of H^- opacity provide evidence that H_2 is dissociating in the atmospheres of gas giants at this temperature range. However, the thermodynamical effects of H_2 dissociation/recombination have yet to be explored.

Both theoretically (e.g. Perez-Becker & Showman 2013; Komacek & Showman 2016) and empirically (e.g. Schwartz et al. 2017; Zhang et al. 2018), we expect the day–night temperature contrast on hot Jupiters to increase with increasing stellar irradiation; temperature gradients $\gtrsim 1000\,\mathrm{K}$ can be expected for UHJs. As temperatures vary drastically between day and night, the local thermal equilibrium (LTE) H_2 dissociation fraction will also vary. The recombination of H into H_2 is a remarkably exothermic process, releasing $q = 2.14{\times}10^8\,\mathrm{J\,kg^{-1}}$ (Dean 1999); this is $100\times$ more potent than the latent heat of condensation for water. For reference, latent heat is responsible for approximately half of the heat recirculation on Earth ($L/(c_p \Delta T) \sim 1$), while the effect of H_2 dissociation/recombination should be even stronger for UHJs ($q/(c_p \Delta T) \sim 10^2$).

Building on this intuition, we might expect that H will recombine into H_2 as gas carried by winds flows eastward from the sub-stellar point, significantly heating the eastern hemisphere of the planet. As the gas continues to flow around to the dayside, the H_2 will again dissociate and significantly cool the western hemisphere. A cartoon depicting this layout is shown in Figure 1. If unaccounted for

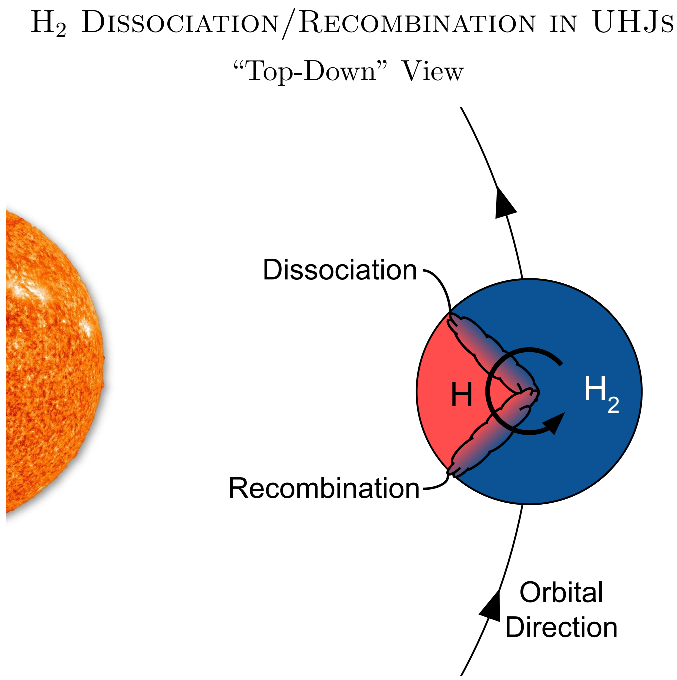

Figure 1. Cartoon showing a "top-down" view of the expected dissociation and recombination of H_2 on a UHJ. The orbital direction and the direction of winds on the planet are indicated with black arrows.

while modelling a phasecurve, this may manifest itself as an "unphysically" large eastward offset as was previously reported for WASP-12b (Cowan et al. 2012).

A large number of circulation models have been developed for studying exoplanet atmospheres, ranging from simple energy balance models (e.g. Cowan & Agol 2011) to more advanced general circulation models (e.g. Showman et al. 2009; Rauscher & Menou 2010; Amundsen et al. 2014; Dobbs-Dixon & Cowan 2017; Heng & Kitzmann 2017; Zhang & Showman 2017). To our knowledge, however, no published general circulation models account for the cooling/heating due to the energies of H_2 dissociation/recombination (although some planet formation models do account for this, e.g. Berardo et al. 2017). Here we aim to qualitatively explore the effects of H_2 dissociation/recombination using a simple energy balance model adapted from that described by Cowan & Agol (2011), using code based on that implemented by Schwartz et al. (2017). We leave it to those with more advanced circulation models to explore this problem in a more rigorous and quantitative manner.

2. ENERGY TRANSPORT MODEL

2.1. *Heating Terms*

First, let ϵ be the energy per unit area of a parcel of gas. Ignoring H_2 dissociation/recombination and any internal heat sources, and assuming the gas parcel cools radiatively, energy conservation gives

$$\frac{d\epsilon}{dt} = F_{\rm in} - F_{\rm out},$$

with $F_{\rm in}$ and $F_{\rm out}$ given by

$$F_{\rm in} = (1 - A_B) F_* \sin\theta \max\left(\cos\Phi(t), 0\right),$$

$$F_{\rm out} = \sigma T^4.$$

The planet's Bond albedo is given by A_B, θ is the co-latitude of the gas parcel, T is the temperature of the gas parcel, and σ is the Stefan–Boltzmann constant. The incoming stellar flux is given by $F_* = \sigma T_{*,\rm eff}^4 (R_*/a)^2$, where $T_{*,\rm eff}$ is the stellar effective temperature, R_* is the stellar radius, and a is the planet's semi-major axis. The stellar hour angle, $\Phi(t)$, incorporates both advection and planetary rotation.

In order to include H_2 dissociation/recombination, we add a new term accounting for the energy flux from these effects. This can be done with

$$\frac{d\epsilon}{dt} = F_{\rm in} - F_{\rm out} - \frac{d\mathbb{Q}}{dt}, \tag{1}$$

where the energy per unit area stored by H_2 dissociation is given by

$$\mathbb{Q} = q \chi_{\rm H} \Sigma,$$

where Σ is the mass per unit area of H and H_2 in the parcel of gas (in $\mathrm{kg\,m^{-2}}$), $q = 2.14{\times}10^8\,\mathrm{J\,kg^{-1}}$ is the H_2 bond dissociation energy per unit mass at $0\,\mathrm{K}$, and $\chi_{\rm H}$ is the dissociation fraction of the gas. $\chi_{\rm H} = 1$ means the gas is completely dissociated (all atomic). Assuming the gas parcel is in hydrostatic equilibrium, we can use

$$\Sigma = \int_{z_0}^{\infty} \rho(z) dz = (P_0/g)$$

where z_0 is some reference height, P_0 is the atmospheric pressure corresponding to z_0, and ρ is the density of the gas. This then allows us to rewrite $\mathbb{Q}$ as

$$\mathbb{Q} = (P_0/g)q\chi_{\mathrm{H}}.$$

The time derivative of $\mathbb{Q}$ is then

$$\frac{d\mathbb{Q}}{dt} = (P_0/g)q\frac{d\chi_{\mathrm{H}}}{dt} = (P_0/g)q\left.\frac{d\chi_{\mathrm{H}}}{dT}\right|_T \frac{dT}{dt}, \tag{2}$$

where we have assumed the gas parcel's P_0/g remains constant, and where we have made use of the chain rule to expand $d\chi_{\mathrm{H}}/dt$.

We model the LTE H_2 dissociation fraction by solving the Saha equation as stated in Appendix A of Berardo et al. (2017) for χ_{H}, assuming the atmosphere consists of only H and H_2:

$$\chi_{\mathrm{H}}(P,T) = \frac{n_{\mathrm{H}}}{n_{\mathrm{H}} + n_{\mathrm{H}_2}} = \frac{2}{1+\sqrt{1+4Y}}, \tag{3}$$

where n_{H} and n_{H_2} are the number densities of H and H_2,

$$Y = \frac{T^{-3/2}\exp(q/2m_{\mathrm{H}}k_{\mathrm{B}}T)P}{2(\pi m_{\mathrm{H}})^{3/2}k_{\mathrm{B}}^{5/2}h^{-3}\Theta_{\mathrm{rot}}},$$

where m_{H} is the mass of the hydrogen atom, k_{B} is the Boltzmann constant, h is the Planck constant, $\Theta_{\mathrm{rot}} = 85.4\,\mathrm{K}$ is rotational temperature of H_2 (Hill 1986), P is the gas pressure, and T is the temperature of the gas (in K). The LTE dissociation fraction is plotted in the top panel of Figure 2.

We can then find $d\chi_{\mathrm{H}}/dT$ using the chain rule:

$$\frac{d\chi_{\mathrm{H}}}{dT} = \frac{d\chi_{\mathrm{H}}}{dY}\frac{dY}{dT}.$$

After some simplification, we then determine

$$\frac{d\chi_{\mathrm{H}}}{dT} = \frac{\chi_{\mathrm{H}}^2 Y\left(\frac{3}{2}T^{-1} + (q/2m_{\mathrm{H}}k_{\mathrm{B}})T^{-2}\right)}{\sqrt{1+4Y}}. \tag{4}$$

To a good degree of accuracy, Equations (3) and (4) can be approximated at $P = 0.1\,\mathrm{bar}$ using

$$\chi_{\mathrm{H}}(0.1\,\mathrm{bar}, T) = \frac{1}{2}\left(1 + \mathrm{erf}\left(\frac{T-\mu}{\sigma\sqrt{2}}\right)\right) \tag{5}$$

and

$$\frac{d\chi_{\mathrm{H}}(0.1\,\mathrm{bar}, T)}{dT} = \frac{1}{\sigma\sqrt{2\pi}} e^{-(T-\mu)^2/2\sigma^2} \tag{6}$$

where $\sigma = 471\,\mathrm{K}$ and $\mu = 3318\,\mathrm{K}$, and erf is the error function; this approximation offers a 70% increase in computation speed. It should be noted that we assume that this H_2 dissociation/ recombination occurs instantaneously since the timescale in the temperature regime of UHJs at 0.1 bar is $\sim 10^{-3}$ s (Rink 1962; Shui 1973).

2.2. *Thermal Energy*

We assume that the planet's energy is stored entirely as thermal energy, as is done in other simple energy balance models (e.g. Pierrehumbert 2010; Cowan & Agol 2011). This assumption means

$$\begin{aligned} \frac{d\epsilon}{dt} &= \frac{d}{dt}(c_p T \Sigma) = \frac{d}{dt}((P_0/g) c_p T) \\ &= (P_0/g)\left(c_p \frac{dT}{dt} + T\frac{dc_p}{dt}\right) \\ &= (P_0/g)\frac{dT}{dt}\left(c_p + T\frac{dc_p}{dT}\bigg|_T\right). \end{aligned} \tag{7}$$

where c_p is the specific heat capacity of the gas, we have again assumed the gas parcel's P_0/g remains constant, and we have used the chain rule to expand dc_p/dt.

The specific heat capacity of the gas will change as a function of temperature due to the slightly different values for H and H_2, as well as the variations in the specific heat capacity of H_2 as a function of temperature (Chase 1998); any model properly accounting for H_2 dissociation should account for this effect. In our model, we assume the atmosphere is made entirely of hydrogen and model the specific heat capacity of the gas by assuming it is well mixed so that

$$c_p = c_{p,\mathrm{H}}\chi_{\mathrm{H}} + c_{p,\mathrm{H}_2}(1 - \chi_{\mathrm{H}}),$$

where both χ_{H} and c_{p,H_2} are functions of temperature. The temperature derivative of c_p is then given by

$$\frac{dc_p}{dT}\bigg|_T = (c_{p,\mathrm{H}} - c_{p,\mathrm{H}_2})\frac{d\chi_{\mathrm{H}}}{dT}\bigg|_T.$$

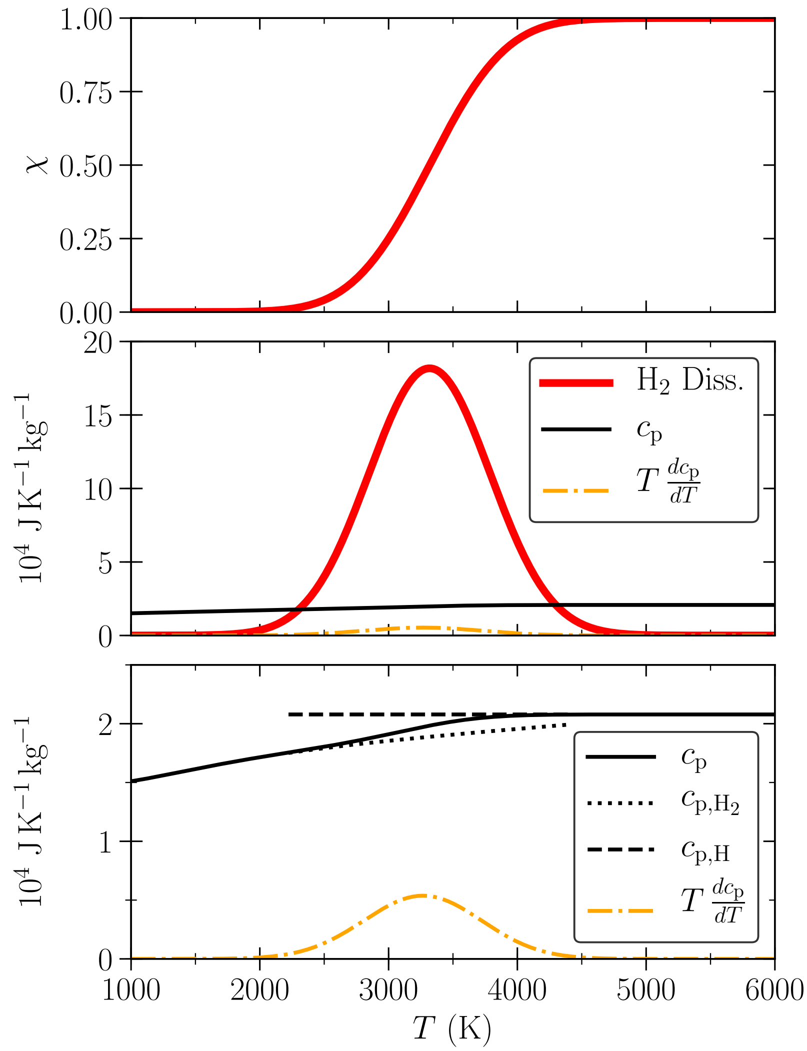

Figure 2. Top: the LTE dissociation fraction of H_2 in a parcel of gas. Middle: a demonstration of the relative importance of the H_2 dissociation/recombination term in Equation (8). For $2300 \lesssim T \lesssim 4300$, the energy absorbed by H_2 dissociation is greater than the energy stored as heat. Typical hot Jupiters are too cool to be affected by H_2 dissociation/recombination, but these processes should dominate on UHJs. Bottom: an inset showing the specific heat capacity of a gas composed of H and H_2 in LTE (the same black line from the middle panel), the specific heat capacities of H and H_2 where they are able to exist in equilibrium, and the additional $T(dc_p/dT)$ term. All panels assume a pressure of 0.1 bar.

2.3. *Putting Everything Together*

Putting together Equations (1), (2), and (7), we get

$$F_{\rm in} - F_{\rm out} - (P_0/g)\frac{dT}{dt}\left(q\frac{d\chi_{\rm H}}{dT}\bigg|_T\right) = (P_0/g)\frac{dT}{dt}\left(c_p + T\frac{dc_p}{dT}\bigg|_T\right).$$

After solving for dT/dt, we find

$$\frac{dT}{dt} = (F_{\rm in} - F_{\rm out})(P_0/g)^{-1}\left(c_p + T\frac{dc_p}{dT}\bigg|_T + q\frac{d\chi_{\rm H}}{dT}\bigg|_T\right)^{-1}.$$

Finally, a gas cell can then be updated using

$$\Delta T = \frac{\Delta t(F_{\rm in} - F_{\rm out})}{(P_0/g)\left(c_p + T\frac{dc_p}{dT}\bigg|_T + q\frac{d\chi_{\rm H}}{dT}\bigg|_T\right)}. \tag{8}$$

Note that the entire sum in the denominator can instead be thought of as the specific heat capacity of a gas comprised of a mixture of H and H_2 in thermal equilibrium. The relative importance of the terms in this sum are shown in the bottom two panels of Figure 2.

3. SIMULATED OBSERVATIONS AND QUALITATIVE TRENDS

We now explore the effects of this new term in the differential equation governing the temperature of a gas cell. For this purpose, we create a latitude+longitude HEALPix grid where each parcel's temperature is updated using Equation (8) with code based on that developed by Schwartz et al. (2017).

While Cowan & Agol (2011) were able to explore their model using dimensionless quantities, our updated model requires that we use dimensioned variables. We therefore adopt the values of the first discovered UHJ, WASP-12b (Hebb et al. 2009). In particular, we set $R_p = 1.90\,R_J$, $a = 0.0234\,\mathrm{au}$, $M_p = 1.470\,M_J$, $T_{*,\mathrm{eff}} = 6360\,\mathrm{K}$, $R_* = 1.657\,R_\odot$, $P = 1.0914203\,\mathrm{days}$ (Collins et al. 2017), and $A_B = 0.27$ (Schwartz et al. 2017). We have also assumed a photospheric pressure of 0.1 bar, the approximate pressure probed by near-IR (NIR) observations of WASP-12b (Stevenson et al. 2014), which gives a radiative timescale of a few hours (similar to the observed timescales for

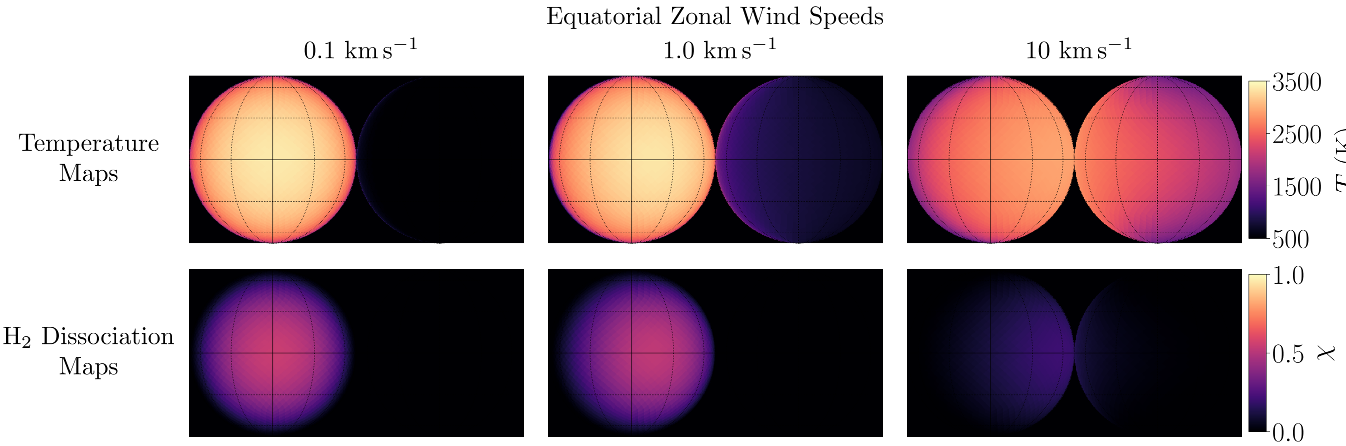

Figure 3. Planetary maps, showing temperature and H_2 dissociation fraction, assuming different eastward zonal wind speeds. The dayside hemisphere is shown on the left side of each map, with north at the top.

eccentric hot Jupiters, e.g. Lewis et al. 2013; de Wit et al. 2016). Wind speeds for WASP-12b have not been directly measured, but typical values for hot Jupiters are on the order of $1\,\mathrm{km\,s^{-1}}$ (e.g. Koll & Komacek 2018); for that reason, we focus on wind speeds around this order of magnitude.

First, let us explore the effects of H_2 dissociation/recombination at a spatially resolved scale. Figure 3 shows temperature and H_2 dissociation maps for three different wind speeds. In the limit of infinite wind speeds, there will be no temperature gradients and H_2 dissociation/recombination will not play a role. In the limit of an atmosphere in radiative equilibrium (wind speed = 0), there will be no variation in the temperature of a parcel and H_2 dissociation/recombination will play no role. Outside of these two unphysical limits, H_2 dissociation/recombination will always be occurring somewhere on UHJs.

We now consider phasecurve observations — this requires that we convolve the planet map with a visibility kernel at each orbital phase (Cowan et al. 2013), which acts as a low-pass filter. Figure 4 shows model phasecurves for three wind speeds; this figure shows that H_2 dissociation/recombination can have a significant effect. At a constant wind speed, the first obviously affected observable when accounting for dissociation/recombination is the increased offset of the peak in the phasecurve toward the east (the same direction as the prescribed wind). Another affected observable is the amplitude of the phase variations, which is reduced when H_2 dissociation/recombination is included. Also,

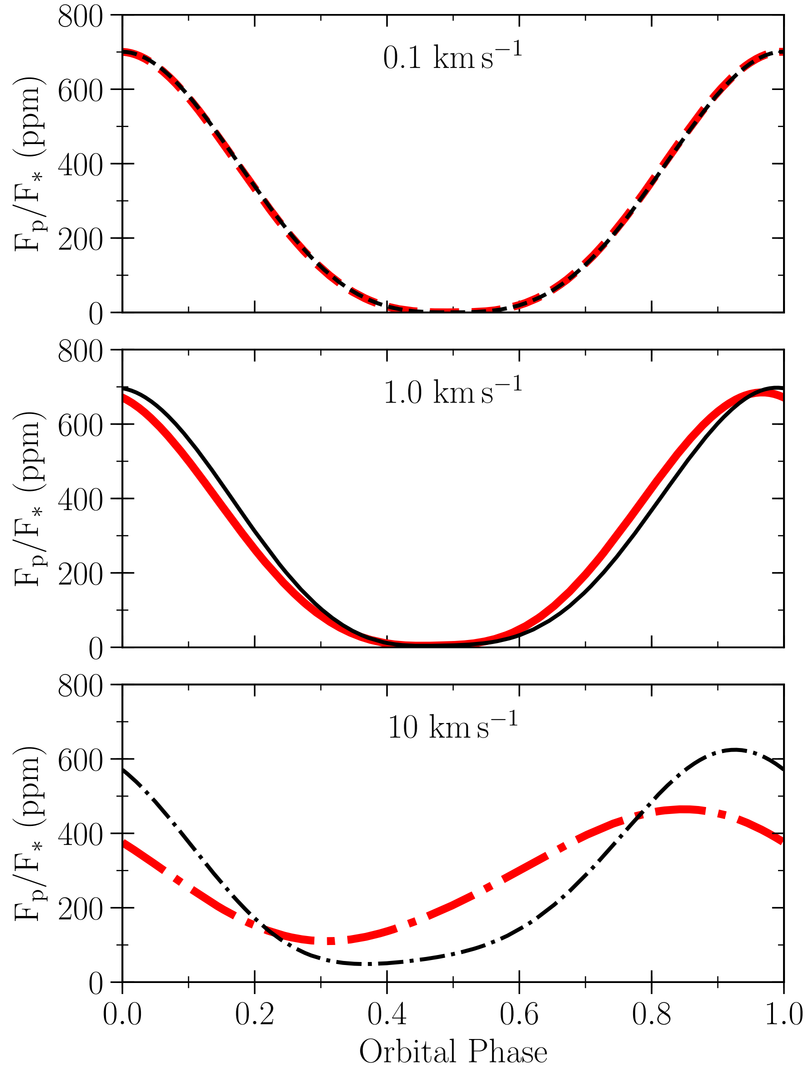

Figure 4. Model bolometric phasecurves assuming different eastward zonal wind velocities, ignoring eclipses and transits. The thick, red lines show the expected phasecurve accounting for H_2 dissociation/ recombination, while the thinner, black models neglect these processes. A secondary eclipse would occur at a phase of 0.0, while a transit would occur at 0.5.

a Fourier decomposition shows that nearly all of the power in the phasecurves accounting for H_2 dissociation/recombination is in the first and second-order Fourier series terms ($1f_{\rm orb}$ and $2f_{\rm orb}$). Finally, Figure 5 shows the trends in phase offset and nightside temperature for two wind speeds, both accounting for and neglecting H_2 dissociation/recombination.

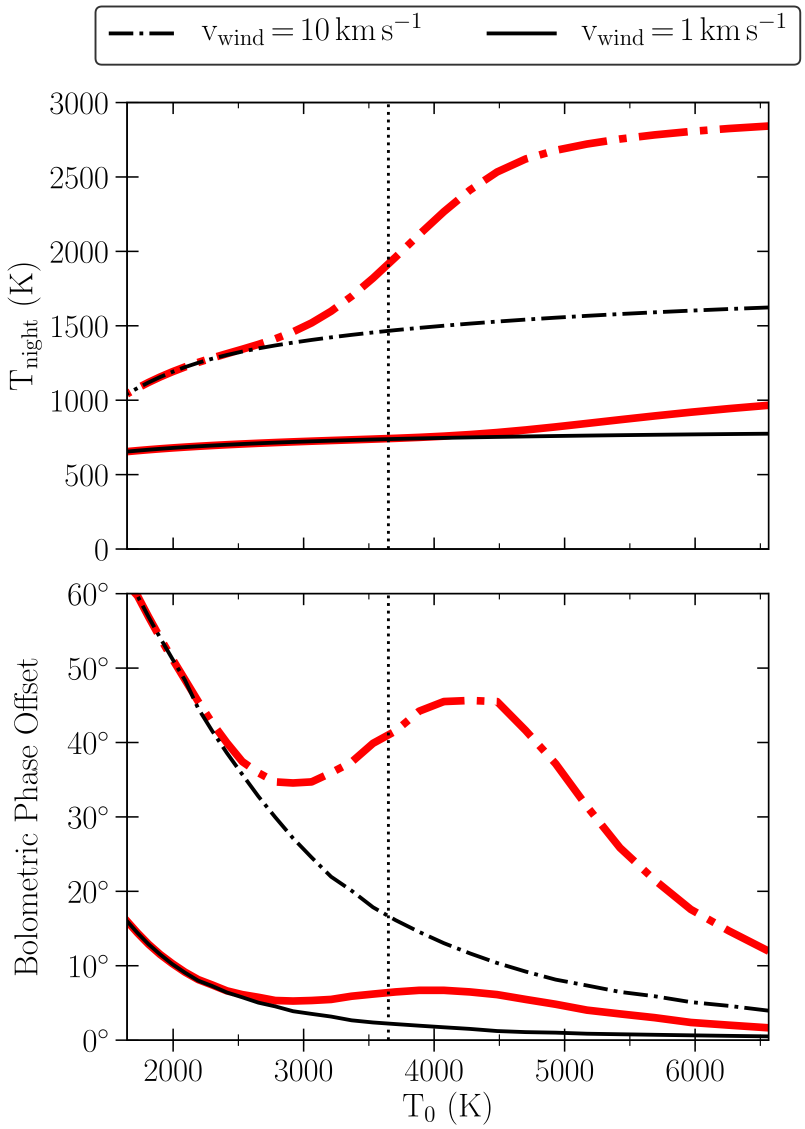

Figure 5. Trends in nightside apparent temperature and phase offset as a function of irradiation temperature ($T_0 \equiv T_{*,\mathrm{eff}}\sqrt{R_*/a}$), given theoretical bolometric phasecurve measurements. Thick, red lines show models including H_2 dissociation/recombination for WASP-12b, while thin, black lines show models neglecting these effects. Models sharing the same wind speed share linestyles, and all models assume a Bond albedo of 0.3 (which is typical for hot Jupiters; Schwartz et al. 2017; Zhang et al. 2018). A vertical dotted line shows the location of WASP-12b.

4. MODEL ASSUMPTIONS

With simplistic models, many important effects are necessarily swept under the rug. Here we aim to lift up the rug and shine a light on our assumptions to aid future work. While many of these assumptions will change the quantitative effects of H_2 dissociation/recombination, we expect that the overall qualitative impact of increased heat recirculation will be robust to these assumptions.

One important piece of physics that we have ignored (beyond a simple assumption of a 0.1 bar photosphere) is atmospheric opacity. As Dobbs-Dixon & Cowan (2017) demonstrated, variations in opacity sources as a function of longitude can change the depth of the photosphere by an order of magnitude or more. Changing the H_2 dissociation fraction will change the importance of H^- as an opacity source, and other standard opacity sources (e.g. H_2O and CO) will also likely be important, especially toward the cooler nightside. The insignificant detection of H_2O on the dayside of WASP-12b (Stevenson et al. 2014) but significant detection in the planet's transmission spectrum (Kreidberg et al. 2015) clearly demonstrates that opacity sources should be expected to change on UHJs. Several of the standard molecular opacity sources will also overlap with the far broader H^- absorption, which complicates a definitive detection of H^- using broadband photometry, such as with *Spitzer*/IRAC. The formation of clouds on the nightside of the planet would further complicate the interpretation of observed phasecurves, increasing the albedo of the west terminator while also insulating the nightside. While we have accounted for variations in the radiative timescale as a function of temperature, we have not accounted for changes due to varying opacity sources.

Additionally, as we have assumed all photons are emitted at a 0.1 bar photosphere, the effects of the atmosphere's T-P profile have been neglected. As the H_2 dissociation fraction has a fairly weak dependence on gas pressure, the bulk of vertical variations in the H_2 dissociation fraction will likely be controlled by the vertical temperature gradient. Due to the lower density of the dissociated gas, one may expect vertical advection on UHJs where temperature decreases with altitude. Interestingly, however, observations of most UHJs are best explained by atmospheres with thermal inversions (Evans et al. 2017; Arcangeli et al. 2018) or at least approximately isothermal profiles on the dayside (Cowan et al. 2012; Crossfield et al. 2012). Any non-isothermal T-P profile will alter the specifics of how efficiently heat is redistributed across the planet as different layers in a gas column will dissociate/recombine at different locations. Also, as we have neglected atmospheric opacity, we have assumed that each gas parcel emits as a blackbody with a single temperature.

Further, due to the changing scale height of the atmosphere at different latitudes and longitudes due to changes in temperature and H_2 dissociation fraction, there will likely be a tendency for gas to flow away from the sub-stellar point, both zonally and meridionally. This is not accounted for in our toy model, and would require a general circulation model. Instead, we have chosen eastward winds as they are predicted, and seen, for most hot Jupiters (e.g. Showman & Guillot 2002; Zhang et al. 2018), although there are some exceptions (e.g. Dang et al. 2018). Similarly, our assumption of solid-body atmospheric rotation is clearly an oversimplification which will need to be addressed in future work. Our model is also unable to predict the wind speeds of UHJs which would require the implementation of various drag sources such as magnetic drag, which Menou (2012) suggested will dominate at these high temperatures.

Also, we have assumed that all heating is due to H_2 dissociation and radiation from the host star, neglecting other heat sources such as residual heat from formation (which should be negligible for planets older than 1 Gyr; Burrows et al. 2006) as well as tidal, viscous, and ohmic heating. We have also neglected the presence of helium, which will partially dilute the strength of H_2 dissociation/recombination as only ∼80% of the atmosphere will be hydrogen. Finally, we have assumed that the planet has a uniform albedo, which will not be the case in general (e.g. Demory et al. 2013; Esteves et al. 2013; Angerhausen et al. 2015; Parmentier et al. 2016).

5. DISCUSSION AND CONCLUSIONS

A new class of exoplanets is beginning to emerge: planets with dayside atmospheres that resemble stellar atmospheres as their molecular constituents thermally dissociate. The impacts of this dissociation will be varied and must be carefully accounted for. Here we have shown that the dynamical dissociation and recombination of H_2 will play an important role in the heat recirculation of UHJs. In the atmospheres of UHJs, significant H_2 dissociation occurs on the highly irradiated dayside, absorbing some of the incident stellar energy and transporting it toward the nightside of the planet where the gas recombines. Given a fixed wind speed, this will act to increase the heat recirculation efficiency; alternatively, a measured heat recirculation efficiency will require slower wind speeds once H_2 dissociation/recombination has been accounted for.

Both theoretically and observationally, it has been shown that increasing irradiation tends to lead to poorer heat recirculation (e.g. Komacek & Showman 2016; Schwartz et al. 2017). However, there are a few notable exceptions to this rule at high temperatures. Recently, Zhang et al. (2018) reported a heat recirculation efficiency of $\varepsilon \sim 0.2$ for the UHJ WASP-33b, which is far higher than would be predicted by theoretical and observational trends. WASP-12b may also possess an unusually high heat recirculation efficiency and exhibit a greater phase offset than would be expected from simple heat advection[1] (Cowan et al. 2012). However, the power in the second-order Fourier series terms from H_2 dissociation/recombination seems to make the phasecurve more sharply peaked and does not seem to be able to explain the double-peaked phasecurve seen for WASP-12b by Cowan et al. (2012). Also, while Arcangeli et al. (2018) find evidence of H_2 dissociation/recombination in the atmosphere of WASP-18b, Maxted et al. (2013) found that the planet has minimal day–night heat recirculation. Given the expected increase in heat recirculation due to H_2 dissociation/recombination, this suggests that WASP-18b has only moderate winds and/or is too cool for these processes to play a strong role in the heat recirculation of this planet. Finally, NIR observations of KELT-9b, the hottest UHJ currently known (Gaudi et al. 2017), could provide a fantastic test of this theory in the very high temperature regime.

T.J.B. acknowledges support from the McGill Space Institute Graduate Fellowship and from the FRQNT through the Centre de recherche en astrophysique du Québec. The atmospheric model that we use in this work is based upon code originally developed by Diana Jovmir and Joel Schwartz. We also thank Gabriel Marleau and Ian Dobbs-Dixon for their helpful insights. We have also made use of free and open-source software provided by the Python, SciPy, and Matplotlib communities.

[1] Depending on the decorrelation method used to reduce the *Spitzer*/IRAC data for WASP-12b, the planet either has $\varepsilon \sim 0$ or $\varepsilon \sim 0.5$ (Cowan et al. 2012; Schwartz et al. 2017); although the former is the preferred model, further observations are critical to definitively choose between these values and test the predictions made in this article.

REFERENCES

Amundsen D. S., Baraffe I., Tremblin P., Manners J., Hayek W., Mayne N. J., Acreman D. M., 2014, A&A, 564, A59

Angerhausen D., DeLarme E., Morse J. A., 2015, PASP, 127, 1113

Arcangeli J., et al., 2018, ApJL, 855, L30

Bell T. J., et al., 2017, ApJL, 847, L2

Berardo D., Cumming A., Marleau G.-D., 2017, ApJ, 834, 149

Burrows A., Sudarsky D., Hubeny I., 2006, ApJ, 650, 1140

Chase M. W., 1998, J. Phys. Chem. Ref. Data, Monograph 9, 1

Collins K. A., Kielkopf J. F., Stassun K. G., 2017, AJ, 153, 78

Cowan N. B., Agol E., 2011, ApJ, 729, 54

Cowan N. B., Machalek P., Croll B., Shekhtman L. M., Burrows A., Deming D., Greene T., Hora J. L., 2012, ApJ, 747, 82

Cowan N. B., Fuentes P. A., Haggard H. M., 2013, MNRAS, 434, 2465

Crossfield I. J. M., Barman T., Hansen B. M. S., Tanaka I., Kodama T., 2012, ApJ, 760, 140

Dang L., et al., 2018, Nature Astronomy, 2, 220

Dean J., 1999, Lange's Handbook of Chemistry. McGraw-Hill, Inc. New York

Demory B.-O., et al., 2013, ApJL, 776, L25

Dobbs-Dixon I., Cowan N. B., 2017, ApJL, 851, L26

Esteves L. J., De Mooij E. J. W., Jayawardhana R., 2013, ApJ, 772, 51

Evans T. M., et al., 2017, Nature, 548, 58

Gaudi B. S., et al., 2017, Nature, 546, 514

Hebb L., et al., 2009, ApJ, 693, 1920

Heng K., Kitzmann D., 2017, ApJS, 232, 20

Hill T. L., 1986, An Introduction to Statistical Thermodynamics. Dover, New York

Koll D. D. B., Komacek T. D., 2018, ApJ, 853, 133

Komacek T. D., Showman A. P., 2016, ApJ, 821, 16

Kreidberg L., et al., 2015, ApJ, 814, 66

Lewis N. K., et al., 2013, ApJ, 766, 95

Maxted P. F. L., et al., 2013, MNRAS, 428, 2645

Menou K., 2012, ApJ, 745, 138

Parmentier V., Fortney J. J., Showman A. P., Morley C., Marley M. S., 2016, ApJ, 828, 22

Perez-Becker D., Showman A. P., 2013, ApJ, 776, 134

Pierrehumbert R. T., 2010, Principles of Planetary Climate. Cambridge University Press

Rauscher E., Menou K., 2010, ApJ, 714, 1334

Rink J. P., 1962, JChPh, 36, 262

Schwartz J. C., Kashner Z., Jovmir D., Cowan N. B., 2017, ApJ, 850, 154

Showman A. P., Guillot T., 2002, A&A, 385, 166

Showman A. P., Fortney J. J., Lian Y., Marley M. S., Freedman R. S., Knutson H. A., Charbonneau D., 2009, ApJ, 699, 564

Shui V. H., 1973, JChPh, 58, 4868

Stevenson K. B., Bean J. L., Madhusudhan N., Harrington J., 2014, ApJ, 791, 36

Zhang X., Showman A. P., 2017, ApJ, 836, 73

Zhang M., et al., 2018, AJ, 155, 83

de Wit J., Lewis N. K., Langton J., Laughlin G., Deming D., Batygin K., Fortney J. J., 2016, ApJL, 820, L33

Epilogue

The qualitative predictions made in this paper have since been validated using an analytic model (Komacek & Tan, 2018) and a general circulation model (Tan & Komacek, 2019). Additionally, I have made another EBM package to reproduce the model outputs from Bell & Cowan (2018). The EBM used by Bell & Cowan (2018) was adapted from the model made by Diana Jovmir and Joel Schwartz for the paper Schwartz et al. (2017); however, this model ran very slowly and the code was challenging to read and use. As a result, after publishing this work I wrote from scratch a new open-source[1], object-oriented, human-readable, and fast EBM named `Bell_EBM` which reproduces the model outputs from Bell & Cowan (2018) for both the model including H_2 dissociation/recombination and the model excluding it. This new EBM reduces the time it takes for model convergence for planets on circular orbits by at least an order of magnitude compared to the original model used by Bell & Cowan (2018).

I used the `Bell_EBM` model to provide predictive models for two successful proposals to observe the phase curve of KELT-9b with *Spitzer*/IRAC channel 1 and channel 2; I was co-investigator on both proposals. The significantly improved run-time for the `Bell_EBM` model allowed me to provide model fits to the channel 2 observations for Mansfield et al. (2020). These EBM fits were combined with the model outputs from a newly developed general circulation model that accounted for H_2 dissociation/recombination (Tan & Komacek, 2019) to clearly demonstrate that the added heat transport from H_2 dissociation/recombination was required to explain our observations. My EBM fits were able to provide a good fit to the observations with only 3 tunable parameters: the wind speed, the Bond albedo, and a deep redistribution term. This deep redistribution term was not present in the model of Bell & Cowan (2018) but can be thought of as some fraction of the incident stellar energy being absorbed deep enough in the atmosphere that it is only reradiated to space after being

[1] Code available at `https://github.com/taylorbell57/Bell_EBM`

completely homogenized at depth; a similar effect is seen in GCMs, which are approximately longitudinally isothermal below ∼10 bars (e.g., Showman et al., 2009; Rauscher & Menou, 2012). The channel 1 observations have not yet been published.

Finally, Lisa Dang is also using the `Bell_EBM` code to interpret the *Spitzer*/IRAC phase curve observations of the eccentric orbit hot Jupiter XO-3b; this work is currently in prep. with myself as a co-author. Because planets on eccentric orbits have varying orbital velocities but constant rotational velocities, the planets cannot be synchronously rotating. Interpreting the phase curves of eccentric planets is therefore much more challenging than for planets on circular orbits because the relationship between orbital phase and sub-observer longitude is unclear, and on top of that the typical assumption of a time-static temperature map is invalid for planets on eccentric orbits as they move closer to and further from their host star. By using an EBM, however, it is possible to quickly model the rotation rate and variable heating experienced by eccentric planets and generate synthetic phase curve observations which can be used to fit the *Spitzer*/IRAC observations.

Paper 3

Mass Loss from the Exoplanet WASP-12b Inferred from *Spitzer* Phase Curves

Preface

In the following paper, published in the Monthly Notices of the Royal Astronomical Society (Bell et al., 2019), we present analyses of two sets of *Spitzer*/IRAC phase curve observations of the ultra-hot Jupiter WASP-12b. The initial motivation for this work was to test the theory of increased heat transport in ultra-hot Jupiter atmospheres presented in Paper 2. We had anticipated that the highly unusual double-peaked 4.5 μm phase curve previously reported by Cowan et al. (2012) would not be reproduced by a repeated set of observations. However, seeing that the double-peaked signal at 4.5 μm was present in both sets of observations, we invited two other teams to contribute independent analyses to further test the reproducibility of this signal. We then explored and constrained different astrophysical explanations that could possibly explain our observations.

MASS LOSS FROM THE EXOPLANET WASP-12b INFERRED FROM *SPITZER* PHASE CURVES

Taylor J. Bell,[1,*] Michael Zhang,[2] Patricio E. Cubillos,[3] Lisa Dang,[1,*] Luca Fossati,[3] Kamen O. Todorov,[4] Nicolas B. Cowan,[1,5,*] Drake Deming,[6] Robert T. Zellem,[7] Kevin B. Stevenson,[8] Ian J. M. Crossfield,[9] Ian Dobbs-Dixon,[10] Jonathan J. Fortney,[11] Heather A. Knutson,[12] and Michael R. Line[13]

[1] *Department of Physics, McGill University, 3600 rue University, Montréal, QC H3A 2T8, Canada*
[2] *Department of Astronomy, California Institute of Technology, 1216 E California Blvd, Pasadena, CA 91125, USA*
[3] *Space Research Institute, Austrian Academy of Sciences, Schmiedlstrasse 6, A-8042 Graz, Austria*
[4] *Anton Pannekoek Institute for Astronomy, University of Amsterdam, Science Park 904, 1090 GE Amsterdam, The Netherlands*
[5] *Department of Earth & Planetary Sciences, McGill University, 3450 rue University, Montréal, QC H3A 0E8, Canada*
[6] *Department of Astronomy, University of Maryland, College Park, MD 20742, USA*
[7] *Jet Propulsion Laboratory, California Institute of Technology, 4800 Oak Grove Drive, Pasadena, CA 91109, USA*
[8] *Space Telescope Science Institute, Baltimore, MD 21218, USA*
[9] *Department of Physics, Massachusetts Institute of Technology, Cambridge, MA, USA*
[10] *Department of Physics, NYU Abu Dhabi, P.O. Box 129188, Abu Dhabi, UAE*
[11] *Other Worlds Laboratory, Department of Astronomy and Astrophysics, University of California, Santa Cruz, California 95064, USA*
[12] *Division of Geological and Planetary Sciences, California Institute of Technology, Pasadena, CA 91125, USA*
[13] *School of Earth & Space Exploration, Arizona State University, Tempe AZ 85287, USA*

(Received 2019 June 6; Revised 2019 July 16; Accepted 2019 July 17; Published 2019 July 25)

Submitted to MNRAS

ABSTRACT

The exoplanet WASP-12b is the prototype for the emerging class of ultra-hot, Jupiter-mass exoplanets. Past models have predicted—and near ultra-violet observations have shown—that this planet is losing mass. We present an analysis of two sets of 3.6 μm and 4.5 μm *Spitzer* phase curve observations of the system which show clear evidence of infrared radiation from gas stripped from the

Corresponding author: Taylor J. Bell
taylor.bell@mail.mcgill.ca

planet, and the gas appears to be flowing directly toward or away from the host star. This accretion signature is only seen at 4.5 μm, not at 3.6 μm, which is indicative either of CO emission at the longer wavelength or blackbody emission from cool, $\lesssim$ 600 K gas. It is unclear why WASP-12b is the only ultra-hot Jupiter to exhibit this mass loss signature, but perhaps WASP-12b's orbit is decaying as some have claimed, while the orbits of other exoplanets may be more stable; alternatively, the high energy irradiation from WASP-12A may be stronger than the other host stars. We also find evidence for phase offset variability at the level of 6.4σ (46.2°) at 3.6 μm.

Keywords: planets and satellites: individual (WASP-12b) – planet-star interactions – accretion, accretion discs – techniques: photometric

* McGill Space Institute; Institute for Research on Exoplanets;
Centre for Research in Astrophysics of Quebec

1. INTRODUCTION

The exoplanet WASP-12b (Hebb et al. 2009) is one of the hottest planets known to date and, as a result of its exceedingly tight orbit and inflated radius ($a/R_* = 3.039$, $R_p = 1.900\ R_J$; Collins et al. 2017), it is one of the best-studied exoplanets. WASP-12b is also the archetype of an emerging class of exoplanets called ultra-hot Jupiters (UHJs). Planets in this regime are so strongly irradiated by their host star that many of the molecules (e.g., H_2 & H_2O) in their dayside atmospheres thermally dissociate (Bell et al. 2017; Bell & Cowan 2018; Arcangeli et al. 2018; Kreidberg et al. 2018; Lothringer et al. 2018; Mansfield et al. 2018; Parmentier et al. 2018) and may recombine nearer the nightside (Bell & Cowan 2018; Komacek & Tan 2018; Parmentier et al. 2018). UHJs also bear some similarities to cataclysmic variable star (CV) systems and may undergo significant tidal distortion and mass loss, depending on the specifics of the star-planet system (e.g., Bisikalo et al. 2013a; Burton et al. 2014).

While tidal distortion is expected for WASP-12b, a 2010 *Spitzer* Infrared Array Camera (IRAC) thermal phase curve observation of WASP-12b at 4.5 μm demonstrated second order sinusoidal variations (with two maxima per planetary orbit) that were far greater than predicted (Cowan et al. 2012). The substellar axis would have to be 1.8 times as long as the dawn–dusk and polar axes if the observed variations were entirely due to the tidally distorted shape of the planet. Additionally, no evidence of these second order sinusoidal variations was found in a *Spitzer*/IRAC 3.6 μm phase curve also taken in 2010 (Cowan et al. 2012).

In this paper, we combine a new set of phase curves taken in 2013 with a reanalysis of the data from 2010 to determine the source of the unusually strong second order sinusoidal variations at 4.5 μm reported by Cowan et al. (2012). The observations are described in Section 2. Our three astrophysical models are described in Section 3.1, and our three independent reduction and decorrelation methods are described in Section 3.2. Results and their physical implications are presented in Section 4, and Section 5 contains the discussion and conclusion.

2. OBSERVATIONS

We combine two sets of two-channel (3.6 μm and 4.5 μm) *Spitzer*/IRAC observations taken in 2010 (PID 70060, PI Machalek) and 2013 (PID 90186, PI Todorov), all during the Post-Cryogenic *Spitzer* Mission. In all four phase curves, the system was observed nearly-continuously for ∼33 hours (breaking only once or twice to repoint the telescope), beginning shortly before one secondary eclipse and ending shortly after the subsequent secondary eclipse. The reduced and detrended observations are shown in Figure 1.

For both data sets, the sub-array mode was used with 2 s exposures which produced data cubes of 64 images with 32 × 32 pixel ($39'' \times 39''$) dimensions. The 2010 observations were divided into 2 Astronomical Observation Requests (AORs) with a total of 902 data cubes (57 728 exposures), while the 2013 observations were divided into 3 AORs with a total of 909 data cubes (58 176 exposures). The 2010 full-phase observations were published by Cowan et al. (2012), the eclipse timings from the 2013 observations were published by Patra et al. (2017), and some derived parameters from all four phase curves were published as part of a broad comparison between different planets (Zhang et al. 2018).

Past observations of WASP-12 show a nearby M-dwarf binary system WASP-12B,C $1\farcs06$ away from WASP-12A (Bergfors et al. 2011; Crossfield et al. 2012b; Bechter et al. 2014). As this binary system lies too close to WASP-12A to be resolved by *Spitzer*, we correct for blended light after analyzing the light curves, following past work (Stevenson et al. 2014a); see Appendix A for more details.

3. LIGHT CURVE ANALYSIS

3.1. *Astrophysical Models*

We model the observations as

$$F_{\rm model}(t) = A(t) \times \tilde{D}(t)$$

where $\tilde{D}(t)$ is the normalized detector model; see Section 3.2 for details on the specific models used which consist of both parametric (2D polynomials and pixel level decorrelation) and non-parametric models (bilinear interpolated subpixel sensitivity mapping). The astrophysical model is

$$A(t) = F_*(t) + F_p(t),$$

where F_* is the flux from the host star (assumed to be constant except during transits) and F_p is the planetary flux. Transits and eclipses are modelled using `batman` (Kreidberg 2015), assuming a quadratic limb-darkening model for the host star and a uniform disk for the planet. The planetary flux is modelled as

$$F_p(t) = F_{\rm day}\Phi\big(\psi(t)\big),$$

where $F_{\rm day}$ is the instantaneous eclipse depth at phase 0.5 (assumed to be constant over each ∼33 hour phase curve), Φ describes the phase variations, and the orbital phase with respect to eclipse is $\psi(t) = 2\pi(t - t_e)/P$, where t_e is the time of eclipse and P is the planet's orbital period.

We consider three different models for the astrophysical phase variations in the lightcurve. The simplest astrophysical model we consider is a first order sinusoid

$$\Phi_1(\psi) = 1 + C_1\Bigg(\cos(\psi) - 1\Bigg) + D_1\sin(\psi),$$

and we also consider a second order sinusoid

$$\Phi_2(\psi) = \Phi_1(\psi) + C_2\Bigg(\cos(2\psi) - 1\Bigg) + D_2\sin(2\psi),$$

where C_1, D_1, C_2, and D_2 are all constants. If the previously reported double peaked phase curve (Cowan et al. 2012) is astrophysical in nature, one potential interpretation is that some/all of the power in the second order sinusoidal variations is from tidal distortion of the planet. We model this scenario with

$$\Phi_{1,\rm ellipsoid}(\psi) = S(\psi)\Phi_1(\psi),$$

where $S(\psi)$ describes the projected area of an ellipsoid as it rotates. Rather than model a triaxial ellipsoid, we constrain the polar and dawn–dusk axes to share the same length since rotational deformation is expected to be negligible compared to tidal deformation (Leconte et al. 2011a). To find the deviations in the projected area of this biaxial ellipsoid, we adapt an equation from past work (Leconte et al. 2011b),

$$S(\psi) = \left[\sin^2(i)\left(\left(\frac{R_{p,2}}{R_p}\right)^2 \sin^2(\psi) + \cos^2(\psi)\right) + \left(\frac{R_{p,2}}{R_p}\right)^2 \cos^2(i)\right]^{1/2},$$

where i is the orbital inclination, R_p is the planetary radius along the polar and dawn-dusk axes (the two axes observed during transit and eclipse if $i = 90°$), and $R_{p,2}$ is the planetary radius along the line connecting the planet and star (the sub-stellar axis).

3.2. *Decorrelation Procedures*

To ensure our results are robust and independent of the methods used, we perform three independent reductions and analyses following previously employed methods (Zhang et al. 2018; Dang et al. 2018; Cubillos et al. 2014) which are summarized below. Each analysis considers all three phase variation models. The model priors for each analysis are described below and summarized in Table A1 for convenience. Within each analysis pipeline, models are selected based on the Bayesian Information Criterion (BIC). We cannot choose our fiducial models between our three analyses using the BIC as there are significant differences between the number of data used in each analysis because of different σ-clipping and binning. Instead, we choose to discriminate between the three analyses by selecting the model with the largest log-likelihood per datum, $\ln(L)/N_{\mathrm{data}}$; we therefore adopt the preferred models from M. Zhang's analyses as our fiducial models. The fiducial reductions of the four data sets are presented in Figure 1 and Table 1 (see also the Appendix and Supplementary Information).

3.2.1. *Fiducial Reduction and Decorrelation Procedure*

For reasons described below, M. Zhang's analyses were selected as our fiducial analyses and follow their previous work (Zhang et al. 2018). In this analysis, we perform aperture photometry with a radius of 2.7 pixels on the Spitzer BCD files to get the raw flux for all frames. The background is calculated by excluding all pixels within a radius of 12 pixels from the star, rejecting outliers using sigma clipping, and then calculating the biweight location of the remaining pixels. We then bin the background-subtracted raw fluxes with a bin size of 64, discard the first 0.05 days of data, and perform fitting with `emcee` (Foreman-Mackey et al. 2013). The fitting uses 250 walkers that walk for 20 000 burn-in steps and 20 000 post-burn-in steps. Our instrumental model uses first order PLD for all data except the 2010 3.6 μm data, in which case we find that second order PLD minimizes BIC. Aside from PLD, the instrumental model also includes a linear slope with respect to time. We fit for the following parameters, all with uniform priors: transit time, eclipse time, R_p/R_*, eclipse depth (assumed to be constant over each ~ 33 hour phase curve), sinusoidal phase variation amplitudes (C_1 and D_1 for the first order sinusoid, and C_2 and D_2 if running a second order sinusoidal model), photometric error, slope in flux with time, and PLD coefficients. We fixed P, a/R_*, and i to the highly precise values from the literature (Collins et al. 2017) as they are poorly constrained by our observations. As limb darkening is not that important in the *Spitzer* bands, we adopt the closest model from a grid of 1D stellar models (Sing 2010).

Our fiducial analyses find that the photon noise limits are 652 ppm and 637 ppm for the 2010 and 2013 3.6 μm observations, respectively, and the limits for the 2010 and 2013 4.5 μm observations are 866 ppm and 860 ppm, respectively. The differences between these two is likely due to the star falling on parts of the detector with slightly different sensitivities, as well as varying aperture sizes. The fitted photometric standard deviation from our fiducial analyses are 950 ppm and 976 ppm for the 2010 and 2013 3.6 μm observations (1.46 and 1.53 times greater than the photon noise limit). For the 2010 and 2013 4.5 μm observations, the fitted photometric standard deviations are 1134 ppm and 1158 ppm (1.31 and 1.35 times greater than the photon noise limit). Figures showing the normalized raw, decorrelated, and residual fluxes from all four phase curves analyzed with M. Zhang's pipeline can be found in the Appendix (Figures A5 and A6).

3.2.2. *T. Bell's Reduction and Decorrelation Procedure*

Reduction and decorrelation of these data follow Dang et al. (2018) and are summarized here. We convert the pixel intensity from MJy/str to electron counts and mask bad pixels, i.e., 4σ outliers with respect to the median of that pixel in the datacube as well as any NaN pixels. We discard all frames with a bad pixel within the aperture used for photometry. We also discard every first frame from each data cube from the 2010 observations and every first and second frame from each data cube for the 2013 observations because these frames consistently show the presence of significant outliers compared to other frames within the same data cube. The effect of this sigma clipping is minimal, given that model fitting is performed on the median binned values from each data cube. There is another star (other than WASP-12A,B,C) that falls on the detector but lies outside the considered photometric apertures ($\sim$10$''$ away); we place a 3×3 pixel mask around this star to ensure that it does not bias the background subtraction.

We then perform aperture photometry on each individual frame, with an aperture at the fixed pixel-location (15,15), and centroids were found using a flux-weighted mean algorithm and later used for decorrelation. Apertures ranging from 2 to 5 pixels in radius were considered as well as two different aperture edges: hard (the pixel's flux is included if the centre of the pixel lies within the aperture) and soft (each pixel is weighed by the exact fraction of its area included within the aperture). While some flux will be lost by smaller apertures, a smaller aperture better allows us to remove intra-pixel sensitivity variations, which are the dominant source of noise in our data. We select the aperture radius and edge which resulted in the lowest RMS after a copy of the raw data were smoothed by a boxcar filter of width 5 data cubes ($\sim$11 minutes which is approximately half the ingress/egress duration) to remove features such as transits, eclipses, and phase variations. Tests run with apertures centred on the flux-weighted mean derived centroids showed that the RMS was > 100 ppm higher than the fixed position apertures. For the 2010 data, we selected a hard-edged 2.5 pixel radius aperture for the 4.5 μm data and an soft-edged 4.3 pixel radius aperture for the 3.6 μm data; the previous analysis of these data (Cowan et al. 2012) used IDL's approximation on a soft-edged 2.5 pixel radius aperture for both wavelengths. For the 2013 data, we selected a hard-edged 3.2 pixel radius aperture for the 4.5 μm data and an soft-edged 2.9 pixel radius aperture for the 3.6 μm data. Before decorrelating and analyzing the data, we first bin the flux and centroid measurements from all 64 frames within a data cube using a median to reduce noise and decrease computation time. On average, each of our models take $\sim$0.5 hour to fit to the binned data, and computation time grows linearly with the number of data points, so running each of the different models on unbinned data is not feasible.

T. Bell's analyses used various systematic models as implemented in the open-source Spitzer Phase Curve Analysis (`SPCA`; Dang et al. 2018) pipeline[1]. In particular, we used two-dimensional polynomials of order 2 through 5 and BiLinear Interpolated Subpixel Sensitivity (BLISS) mapping. The two-dimensional polynomials (Charbonneau et al. 2008) assume the sensitivity of the detector can be described by an nth-order 2D polynomial in the measured centroid. BLISS mapping (Stevenson et al. 2012a; Ingalls et al. 2016; Schwartz & Cowan 2017) is a non-parametric method to account for the intra-pixel sensitivity variations which requires accurate centroid measurements; when fitting BLISS models we adopt an 8×8 grid of knots. For the 2013 observations at 3.6 μm, we also needed to add a slope in time to remove residual red noise.

Models were fit using the Markov Chain Ensemble Sampler `emcee` (Foreman-Mackey et al. 2013). The orbital parameters of WASP-12b in the literature (Collins et al. 2017) have smaller errors than we can achieve with our photometry. Additionally, numerous searches for eccentricity have found that WASP-12b's orbit is best described by a circular orbit (Campo et al. 2011; Croll et al. 2011; Bailey & Goodman 2019), so we set the orbital eccentricity to zero. Several orbital parameters are poorly constrained by a single phase curve observation compared to the literature values, so we adopted the following Gaussian priors to marginalize over the uncertainties in the literature values: $t_0 = 56176.16825800 \pm 0.00007765$ (BMJD), $a/R_* = 3.039 \pm 0.034$, $i = 83.37^\circ \pm 0.68^\circ$ (Collins et al. 2017). The orbital period is known to within 12 ms, so we simply fixed it at 1.09142030 days (Collins et al. 2017). The parameters that were always fitted were t_0, R_p/R_*, a/R_*, i, $F_{\rm day}/F_*$, two quadratic limb darkening parameters (Kipping 2013) q_1 and q_2, and the first order sinusoidal amplitudes C_1 and D_1. In some models, we also fitted $R_{p,2}/R_*$ or C_2 and D_2. A number of detector parameters were also fitted, with the exact number depending on the detector model used.

[1] `https://github.com/lisadang27/SPCA`

For T. Bell's apertures, the photon noise limits are 578 ppm and 566 ppm for the 2010 and 2013 3.6 μm observations, respectively, and the limits for the 2010 and 2013 4.5 μm observations are 795 ppm and 791 ppm, respectively. The fitted photometric standard deviation from T. Bell's analysis are 1493 ppm and 1246 ppm for the 2010 and 2013 3.6 μm observations (2.58 and 2.20 times greater than the photon noise limit). For the 2010 and 2013 4.5 μm observations, the fitted photometric standard deviations are both 1440 ppm (1.81 and 1.82 times greater than the photon noise limit). The fitted data and red noise tests from these analyses can be found in the Supplementary Information (Figures A7 and A8).

3.2.3. *P. Cubillos' Reduction and Decorrelation Procedure*

The models run by P. Cubillos use the Photometry for Orbits, Eclipses, and Transits (`POET`) pipeline (Stevenson et al. 2010; Stevenson et al. 2012a,b; Campo et al. 2011; Nymeyer et al. 2011; Cubillos et al. 2013, 2014). The `POET` pipeline starts by flagging bad pixels from the Spitzer BCD files using the permanent bad pixel masks and performing a sigma-rejection routine. Next, it estimates the target center position either fitting a two-dimensional Gaussian function or calculating the least asymmetry (Lust et al. 2014). Then it obtains raw light curves by applying a circular interpolated aperture photometry, testing several aperture radii between 2.0 and 4.0 pixels.

To determine the optimal centroiding method and photometry aperture, `POET` minimizes the standard deviation of the residuals, and minimizes time-correlated noise at timescales equal and larger than the transit duration (estimated through the time-averaging method). Least asymmetry centroiding outperformed Gaussian centring for all datasets, except the 2013 4.5 μm observation. The optimal apertures were 2.5 and 3.0 pixels (2010) and 4.0 and 2.0 pixels (2013) for the 3.6 and 4.5 μm observations, respectively. In any case, all relevant astrophysical parameters vary within their uncertainties as we vary the centroiding and photometry.

`POET` models the unbinned light curves, simultaneously fitting the astrophysical phase curve and the telescope systematics. The systematics model consists of the non-parametric BLISS intrapixel model, for which we set the map's bin size equal to the RMS of the frame-to-frame target position

(0.01 pixels), and require at least 8 points per bin. For the 2013 4.5 μm observation, we also apply a linear time-dependent ramp with the slope as a free parameter.

The astrophysical model consists of transit and eclipse models (Mandel & Agol 2002), combined with the sinusoidal and ellipsoid models described in the Methods section. The transit free fitting parameters are the epoch, ratio between the planetary and stellar radii, cosine of inclination, semi-major axis to stellar radius ratio, stellar flux, and quadratic limb-darkening coefficients. The eclipse free fitting parameters are the midpoint, duration, depth, and ingress duration (setting the egress duration equal to the ingress duration). We adopt uniform priors for all parameters, except for $\cos(i)$ and a/R_*, which have Gaussian priors, and kept the orbital period fixed (same values as in T. Bell's reduction and decorrelation procedure; Collins et al. 2017).

`POET` incorporates the MC3 statistical package (Cubillos et al. 2017) to find the best-fitting parameter values (using Levenberg-Marquardt optimization) and uncertainties (using a differential-evolution Markov Chain Monte Carlo algorithm; ter Braak & Vrugt 2008), requiring the Gelman-Rubin statistic (Gelman & Rubin 1992) to be within 1% of unity for each free parameter for convergence. `POET` uses Bayesian hypothesis testing to select the model best supported by the data, selecting the lowest BIC model. The `POET` results support the independent results of the other pipelines. Both 4.5 μm observations strongly favour the second order sinusoidal model, while both 3.6 μm observations strongly favour the first order sinusoidal model.

For P. Cubillos' apertures, the photon noise limits are 4886 ppm and 6664 ppm for the 2010 and 2013 3.6 μm observations, respectively, and the limits for the 2010 and 2013 4.5 μm observations are 8273 ppm and 7988 ppm, respectively. The fitted photometric standard deviation from P. Cubillos' analysis are 6915 ppm and 7360 ppm for the 2010 and 2013 3.6 μm observations (1.41 and 1.10 times greater than the photon noise limit). For the 2010 and 2013 4.5 μm observations, the fitted photometric standard deviations are 9130 ppm and 8658 ppm (1.10 and 1.08 times greater than the photon noise limit). The fitted data and red noise tests from these analyses can be found in the Supplementary Information (Figures A9 and A10).

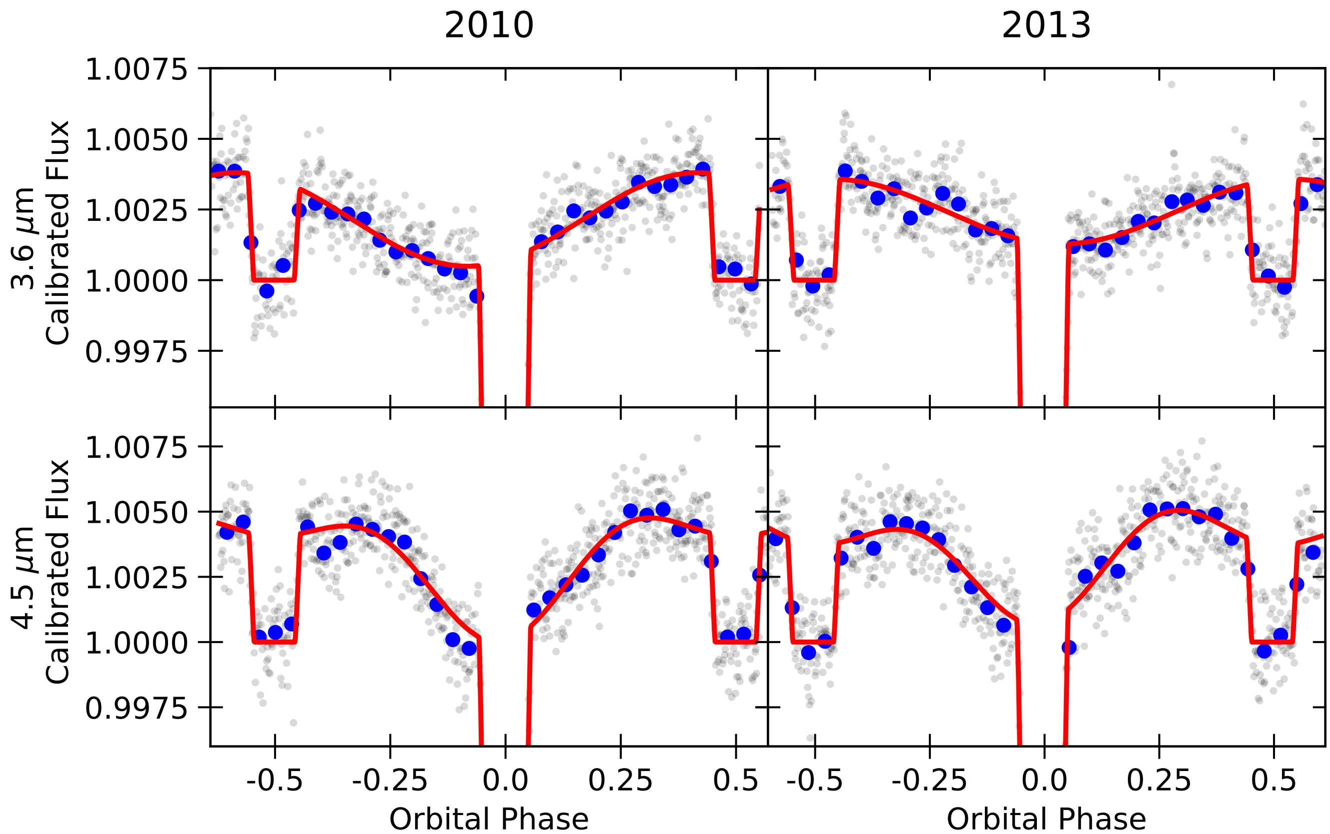

Figure 1. Fiducial analyses of 3.6 μm (top) and 4.5 μm (bottom) *Spitzer*/IRAC phase curve observations of WASP-12b taken in 2010 (left) and 2013 (right). Both 3.6 μm phase curves show one maximum per planetary orbit, while both 4.5 μm phase curves exhibit two maxima per planetary orbit. The detector systematics have been removed from the data, and our fiducial astrophysical models for each data set are overplotted in red. Grey data points show binned values from each *Spitzer* data cube (64 frames), and the blue points show more coarsely binned values (1664 frames).

4. RESULTS

4.1. *Comparison Between Pipelines and Epochs*

All three independent analyses confirm the presence of strong and persistent second order sinusoidal variations at 4.5 μm and the non-detection of these variations at 3.6 μm. The fitted phase curves parameters for the preferred models from all three independent pipelines are summarized in Figure 1 and Table A2. See the Supplementary Information for tabulated values for all considered models. The astrophysical parameters at 3.6 μm and 4.5 μm are mostly consistent between all three analyses,

Table 1. Key fiducial light curve parameters

Data Set	R_p/R_* ‡	1st Order Phase Offset† (degrees)	2nd Order Phase Offset† (degrees)	$F_{\rm day}/F_*$ ‡ (ppm)
2010, 3.6 μm	0.11642 ± 0.00063	-32.6 ± 6.2	—	3870 ± 130
2013, 3.6 μm	0.11327 ± 0.00068	13.6 ± 3.8	—	3840 ± 120
2010, 4.5 μm	0.10656 ± 0.00085	-9.5 ± 2.3	94.7 ± 1.6	4360 ± 140
2013, 4.5 μm	0.1049 ± 0.0010	-19.1 ± 3.9	93.2 ± 1.9	3920 ± 150

† These phase offsets are measured in degrees *after* eclipse and are derived quantities.

‡ These quantities have been corrected for dilution from WASP-12BC (see Appendix A).

with the preferred models from the three analyses generally differing by $< 2\sigma$. In the few cases where one model differs from the others by more than 2σ, the other two models are consistent with each other at a level of $< 1\sigma$. Also, there is low-frequency noise in the 2010 4.5 μm residuals between the first eclipse and the end of the transit that is seen by all three analysis pipelines; the source of these variations is not understood.

From 2010 to 2013, the three pipelines show that all 4.5 μm phase curve and planetary parameters remain constant within $< 2\sigma$. Most of the phase curve and planetary parameters at 3.6 μm also remain constant between the two observing epochs, with the main exception being the phase offset calculated using the first order sinusoidal terms. M. Zhang's, P. Cubillos', and T. Bell's pipelines find that it changes by 6.4σ (46.2°), 7.7σ (46.6°), and 3.1σ (28.1°), respectively. All three pipelines also agree that the sign of the hotspot offset changes between the two observing epochs, with the offset being "eastward" (before eclipse) in 2010 and "westward" (after eclipse) in 2013. It is interesting to note, however, that over this same time span both the first and second order sinusoidal phase offsets from the 4.5 μm observations do not change. No other parameter is found by all three analyses to vary by more than 3σ between the two observing epochs. Finally, if the first order sinusoidal phase variations are entirely attributable to WASP-12b's temperature map, our 2013 observations at

3.6 μm exhibit a $13\overset{\circ}{.}6 \pm 3\overset{\circ}{.}8$ westward hotspot offset. This may be a demonstration that eastward hotspot offsets are less ubiquitous than previously believed, with westward hotspot offsets reported for planets with irradiation temperatures spanning 2200–3700 K (Dang et al. 2018; Zhang et al. 2018; Wong et al. 2016).

4.2. *Physical Sources*

The previously favoured explanation for the double peaked phase curve reported for WASP-12b by Cowan et al. (2012) was detector systematics, but this hypothesis is now strongly disfavoured. To date, 23 papers have been published with new *Spitzer* phase curves of 18 different exoplanets (Harrington et al. 2006; Knutson et al. 2007; Cowan et al. 2007; Knutson et al. 2009b,a; Laughlin et al. 2009; Crossfield et al. 2010; Cowan et al. 2012; Knutson et al. 2012; Crossfield et al. 2012a; Lewis et al. 2013; Maxted et al. 2013; Zellem et al. 2014; Wong et al. 2015; de Wit et al. 2016; Wong et al. 2016; Krick et al. 2016; Demory et al. 2016; Wong et al. 2016; Stevenson et al. 2017; de Wit et al. 2017; Zhang et al. 2018; Dang et al. 2018; Kreidberg et al. 2018). Of these numerous observations, WASP-12 is the only system which has shown strong a double peaked phase curve not once, but twice. The observing strategy also differed between these two sets of WASP-12b phase curves, with the number and timing of AORs changing and the addition of PCRS Peak-Up before the 2013 observations. The consistency between the two sets of phase curves suggests that the observations probe an astrophysical source which does not vary significantly over a $\sim$3 year timescale. Cowan et al. (2012) suggested that tidal distortion and/or mass loss might be able to explain the *Spitzer* observations, if this signal was indeed astrophysical in nature. We explore these and other potential sources of emission below.

4.2.1. *Tidal Distortion*

One potential cause of second order sinusoidal variations is tidal deformation of the host star, as is seen at optical wavelengths for HAT-P-7 (Welsh et al. 2010) and WASP-18 (Shporer et al. 2019). However, stellar distortion is expected to be negligible for WASP-12 (Leconte et al. 2011a). We verified this by numerically solving for the equipotential stellar/planetary surfaces using the

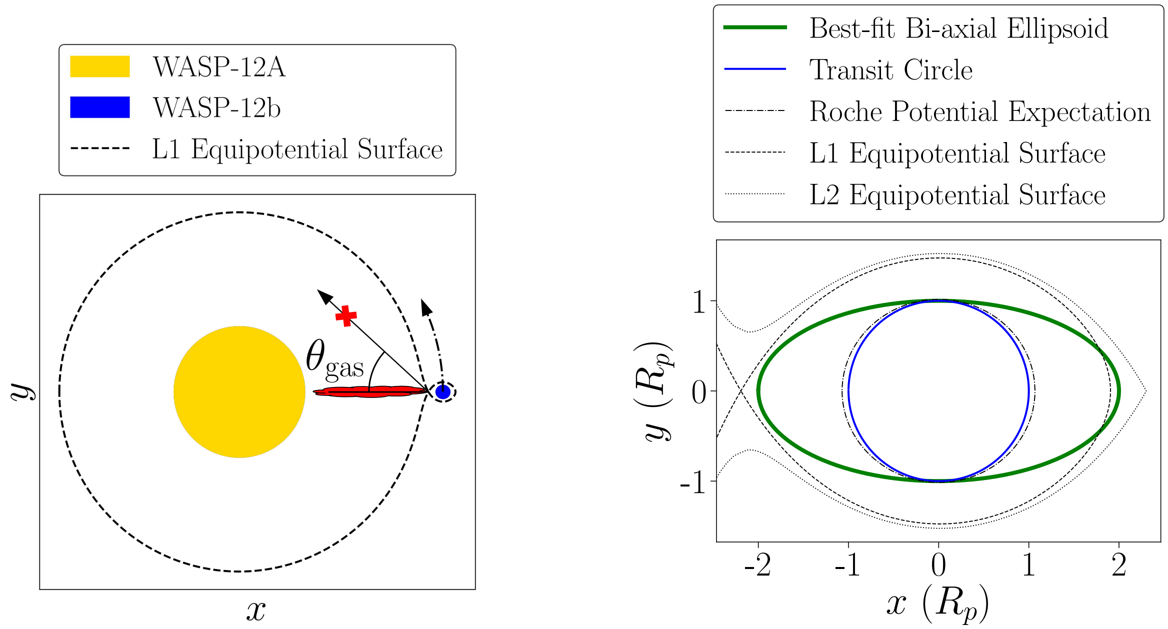

Figure 2. Bird's-eye views of the WASP-12 system to scale. *Left:* While the planet is appreciably filling its Roche lobe and is expected to be tidally distorted, the star should not. Over-plotted is a depiction of the direction that gas would flow after passing through the L1 Lagrange point ($\theta_{\rm gas}$) previously predicted to be 53.4° (Lai et al. 2010). If our observations probe the gas stream, we can firmly reject this ballistic trajectory hypotesis as the gas appears to be aligned along the star–planet axis (indicated by the red elongated patch of gas). The direction of the planet's orbit is shown with a dash-dotted arrow. *Right:* Best-fit bi-axial ellipsoid model fit to the 2013 phase curve observation at 4.5 μm, placed in the context of the planet's Roche lobe. This shape varies drastically from that of a Roche lobe and instead suggests that our observations are probing something other than the planet's tidally distorted shape. Also shown is a circle with the area seen at transit, the equipotential surface which would give that transit area, and the L1 and L2 equipotential surfaces. The x and y axes lie within the orbital plane; during transit the x-axis is parallel to our line of sight.

dimensionless Roche potential (see Appendix C). However, since the star contributes significantly more flux than the planet, we ran simple simulations of both the star and planet including the effects of gravity darkening to assess their expected amplitudes of ellipsoidal variations. We find that the stellar ellipsoidal variations are approximately the same amplitude at 3.6 μm and 4.5 μm and the amplitude of the stellar variations are far smaller than the observed amplitudes; we therefore conclude that tidal bulges on the host star cannot be the source of the strong second order variations observed at 4.5 μm. Our predicted ellipsoidal variations for WASP-12b are consistent with our limits on second order sinusoidal variations at 3.6 μm, but significantly under-predict the observed amplitude at 4.5 μm (also see the implied dimensions of the best-fit ellipsoidal variation model shown in the right panel of Figure 2). If we interpret the second order sinusoidal variations at 4.5 μm as planetary ellipsoidal variations, this would require the 4.5 μm photosphere to be significantly higher up than 3.6 μm as the layers nearer the Roche lobe are more distorted. However, this increased radius at 4.5 μm is inconsistent with the smaller transit depth at 4.5 μm compared to 3.6 μm. We therefore conclude that tidal distortion of the planet is also not the source of the strong second order variations observed at 4.5 μm.

4.2.2. *Stellar Variability and Inhomogeneities*

Stellar variability is also unlikely to be the cause of these observations given the comparable phase of the second order variations in the two data sets. For reference, the WASP-12BC dilution correction term is $\sim$400 ppm while the observed amplitude of the second order sinusoidal variations is $\sim$2000 ppm. Additionally, variability in WASP-12A is only predicted to modulate the planetary signal at a level of $\sim$1 ppm, and variability in WASP-12B,C should also only contribute at the level of $\sim$1 ppm (while these M-dwarfs should be $\sim 10\times$ more variable, they contribute $\sim 10\times$ less flux; Zellem et al. 2017). We therefore rule out standard stellar variability as the source of the strong second order sinusoidal variations seen at 4.5 μm. If the second order variations were produced by unusually strong inhomogeneities on the host star, both the sub-planet longitude and the anti-planet longitude would need to be darker than intermediate longitudes — this would imply star–planet interactions. However, these inhomogeneities would also need to be much more pronounced at 4.5 μm which would not be expected for the $\sim$6000 K star.

4.2.3. *Mass Loss*

There is significant observational evidence from near ultra-violet (NUV) transit observations that WASP-12b is undergoing mass loss and that there is a bow shock in the system (Fossati et al. 2010; Haswell et al. 2012; Nichols et al. 2015) (see the Supplementary Information). A potential explanation for the unusual 4.5 μm phase curve is that there is gas being stripped from the planet which emits more strongly within the 4.5 μm bandpass than the 3.6 μm bandpass. The observations favour a stream of dense gas stripped from the planet flowing directly toward/away from the host star or some other elongated patch of hot gas whose long axis is parallel to the star–planet axis, such as an accretion hot spot. Double-peaked phase curves have been seen for dwarf novae CVs, such as WZ Sge (Skidmore et al. 1997), however this feature was seen through the ultra-violet to infrared; for CVs these variations have been attributed to tidal distortion or an optically thick hot spot in an otherwise optically thin accretion disk (e.g., Skidmore et al. 1997)

The source of the 4.5 μm variations in the WASP-12 system must lie near the star–planet axis since there is no significant detection of an occultation of the source when the planet is not in transit or eclipse. Additionally, our *Spitzer* observations demonstrate that the planetary radius appears $\sim$8% (11σ) smaller at 4.5 μm than at 3.6 μm which is in disagreement with model predictions (Burrows et al. 2007, 2008; Cowan et al. 2012); this rules out the transit of a large exosphere that is opaque at 4.5 μm as this would make the planetary radii at the two wavelengths even more discrepant.

As shown in Table 1, the fitted second order offsets at 4.5 μm are consistent with being oriented along the star–planet axis (90°). However, previously published 3D magnetohydrodynamic (MHD) numerical simulations of hypothetical exoplanet systems mostly produced gas flows that significantly lead the star–planet axis (Matsakos et al. 2015). Indeed, gas streaming from the planet's L1 Lagrange point on a ballistic trajectory should flow $\theta_{\rm gas} = 53\overset{\circ}{.}4$ *ahead* of the star–planet axis (Lai et al. 2010) as angular momentum is conserved (see Figure 2 for a schematic depiction). Assuming our observations probe the gas stream, this prediction is 27σ discrepant with our offset of $4\overset{\circ}{.}0 \pm 2\overset{\circ}{.}1$ *behind* the star–planet axis found by averaging the offsets from the two fitted second order sinusoids at 4.5 μm. This discrepancy could potentially be explained if the 4.5 μm emitting area is much closer to the planet and is still aligned along the star–planet axis and then becomes more diffuse and flows ahead of the planet as it continues to fall toward the host star.

Alternatively, stellar effects could channel the infalling stream directly toward the star, but this may be inconsistent with past NUV transit observations (Fossati et al. 2010; Haswell et al. 2012;

Nichols et al. 2015). One previously published 3D MHD model (Matsakos et al. 2015) did exhibit a stream of gas directly along the star–planet axis (their name for this model was 'FvrB'). This model has high stellar ultra-violet (UV) flux, a low escape speed from the planet, the planet near to its host star, and a strong planetary magnetic field. In this model, the planet is experiencing Roche lobe overflow with a planetary wind that is weak compared to the stellar wind, producing an approximately linear stream of gas along the star–planet axis as well as a lower density tail trailing behind the planet (Matsakos et al. 2015). The non-detection of the gas trailing behind the planet could be explained if the gas has a lower density and/or has a lower temperature. As the dense gas stream in the 'FvrB' model is aligned along the star–planet axis, it may not contribute significantly to the transit depth and may remain consistent with the smaller apparent radius at 4.5 μm compared to 3.6 μm. Radiative transfer simulations based on the 'FvrB' mass-loss model (Matsakos et al. 2015) would allow for this hypothesis to be tested.

4.3. *Radiation Mechanisms*

4.3.1. *Blackbody Emission*

The discrepant second order sinusoidal amplitudes at 3.6 μm and 4.5 μm can be explained by one of two emission mechanisms. First, blackbody emission could allow for greater flux at 4.5 μm than at 3.6 μm if the gas is sufficiently cool that the 3.6 μm bandpass lies on the Wien side of the blackbody curve; this scenario would allow us to place an upper limit on the temperature and spatial extent of the emitting gas, which we pursue below.

Using the host star's effective temperature of 6300 ± 150 K (Hebb et al. 2009), we assume the host star emits as a blackbody and convert the second order sinusoidal curves from units of $F_{\rm day}/F_*$ to B_λ as shown in the middle panel of Figure 3. We adopt the fiducial 4.5 μm parameters from 2010, but set the phase offset to 90° since there is no evidence for an appreciable offset from the star–planet axis. We then take the best-fit and the 1σ and 2σ upper limits on the amplitude of the 3.6 μm second order sinusoidal variations from M. Zhang's analysis using the second order astrophysical model. We assume that none of the flux seen during planetary transit/eclipse is from emission by the gas. By

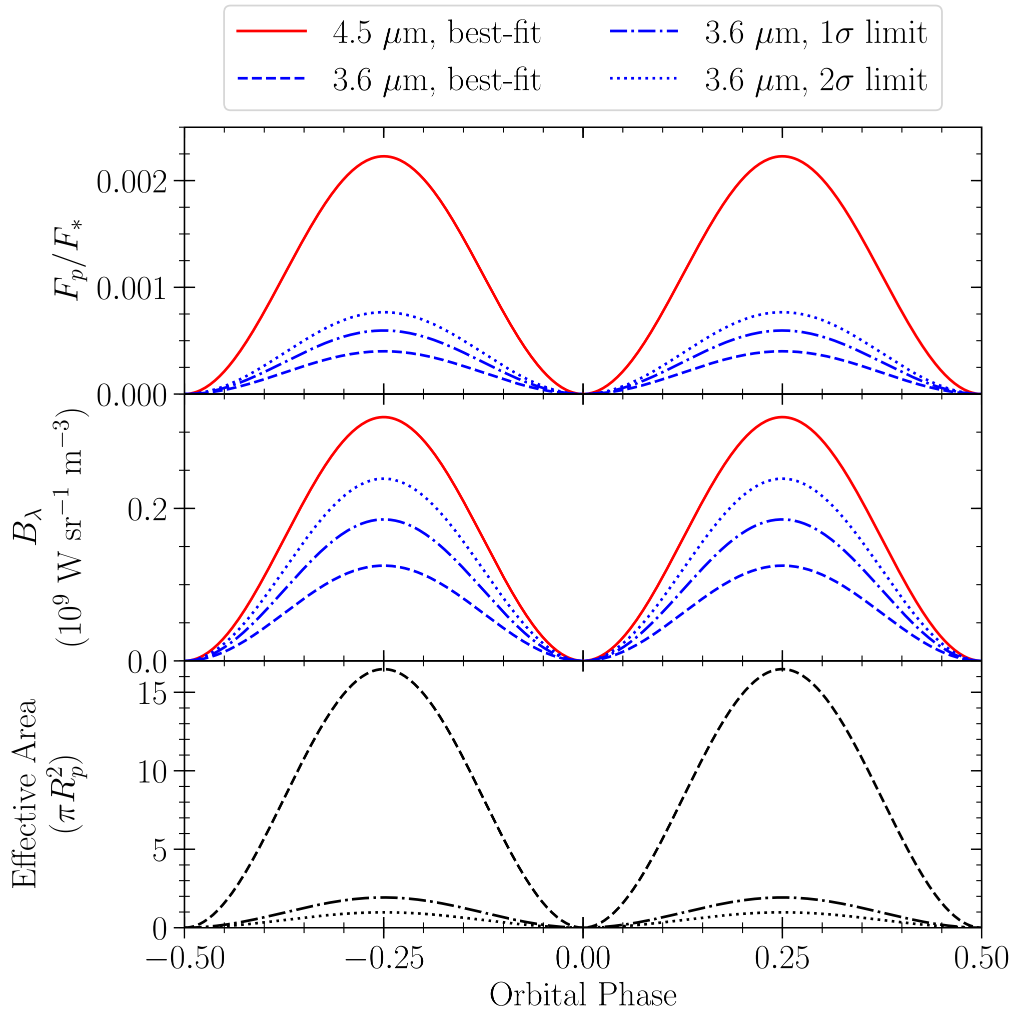

Figure 3. Limits on the emitting area required to explain the strong detection of second order sinusoidal variations at 4.5 μm but not at 3.6 μm. *Top*: the emitting-body to star flux ratio for the second-order sinusoidal component of the 4.5 μm and 3.6 μm data (temporarily assuming a constant radius of R_p). *Middle*: the emitting-body's blackbody flux assuming both wavelengths probe the same area. *Bottom*: the effective emitting area of the emitting blackbody required to explain the observations. The inferred gas temperatures for the 0σ, 1σ, and 2σ limits are 420 K, 549 K, and 619 K, respectively.

assuming the emitting area is the same at 3.6 μm and 4.5 μm, we can use the relative amounts of flux at these two wavelengths to determine the blackbody temperature of the gas.

Given the assumption that our observations are explained by blackbody emission, we can then place a 2σ upper limit of 619 K on the gas temperature. For reference, a temperature of 816 K would provide equal flux in both bandpasses. Attributing any of the "nightside" flux to emission from the gas only lowers this limit further. Also, as WASP-12b's skin temperature (Goody & Walker 1972) is $0.5^{0.25}\,T_{\rm b,day} \approx 2500$ K, this gas cannot be the upper layers of the planet's atmosphere.

By taking the ratio between the flux emitted by the gas and that emitted by the star, we can determine the effective emitting area required to produce the phase curve observations. As shown in the bottom panel of Figure 3, less emission at 3.6 μm requires lower temperature gas and therefore a larger emitting area. We can therefore place a 2σ lower-limit on the effective emitting area of the gas of 0.98 times the planet's transiting area when seen at planetary quadrature, given the assumption that our observations are explained by blackbody emission. Attributing any of the nightside flux to emission from the gas slightly increases this limit and allows for a non-zero emitting area during planetary transit and eclipse.

4.3.2. *CO Emission*

An alternative explanation for the increased flux at 4.5 μm is emission by CO which has its strong $\Delta V = 1$ band around 4.5 μm (see Figure A1 in the Appendix for the CO line intensities); CO emission has previously been predicted for gas lost from WASP-12b (Li et al. 2010; Deming et al. 2011). The CO molecule should be dissociated in the planetary upper atmosphere due to the strong UV and X-ray flux from the host star which also drives most of the observed atmospheric escape seen at NUV wavelengths (Fossati et al. 2010; Haswell et al. 2012; Nichols et al. 2015); the dissociation energy of CO corresponds to a wavelength of roughly 110 nm. However, the atomic carbon and oxygen from the upper layers of the planet's atmosphere could recombine in a gas stream where the density gets higher because of stellar wind confinement and the "shadow effect" from the material in the stream closer to the star. Given a gas temperature profile (Salz et al. 2016) and our calculations of the thermal dissociation fraction of CO using the Saha equation (Bell & Cowan 2018), we find that any CO emission must either be produced within $\sim$0.1 R_p of the planet's surface or beyond 2.5 R_p. In the case of a bow shock supported by mass loss from the planet, gas temperatures are predicted to reach 10^3–10^4 K (Turner et al. 2016) which should allow for stable CO, provided there is sufficient UV shielding from gas nearer to the star. Simulations of the behaviour of CO in these environments are required to determine the feasibility of this molecule recombining once in a stream and emitting sufficiently strongly to explain our observations.

4.4. *A Note on Eclipse Depths*

It is important to note that our reported "eclipse depths" ($F_{\rm day}/F_*$) are measured with respect to the phase curve value expected at the centre of eclipse and are not measured with respect to pre-ingress and post-egress flux measurements as would be the case for observations of only the eclipse. Given our fitted phase curve parameters for WASP-12b, the difference between our reported value and using the average of pre-ingress and post-egress baselines is ~9% of $F_{\rm day}/F_*$ at both *Spitzer* bandpasses (assuming these baseline durations are both the same duration as the eclipse duration). This bias in eclipse observations occurs because the phase variations before ingress and after egress are flattened out by most decorrelation routines when solely observing the eclipse. For most exoplanets whose phase variations will be concave down around eclipse (like WASP-12b when seen at 3.6 μm), eclipse observations will underestimate $F_{\rm day}/F_*$. For the unusual case of WASP-12b's 4.5 μm phase variations which are concave up near eclipse, eclipse observations will overestimate $F_{\rm day}/F_*$. This effect is particularly important for short period planets which undergo significant rotation throughout the duration of eclipse observations and whose strong day–night temperature contrast cause strong phase variations over this time span. Among other things, this may explain the discrepancies between reported 3.6 μm and 4.5 μm eclipse depths from full-orbit phase curves (Cowan et al. 2012) and eclipse-only observations (Madhusudhan et al. 2011; Stevenson et al. 2014b), and the associated inference of C/O ratio. See Figure 4 for a demonstration of this effect.

5. DISCUSSION AND CONCLUSIONS

By independently analyzing and then combining two sets of 3.6 μm and 4.5 μm *Spitzer* phase curves of the UHJ WASP-12b, we have conclusively detected strong and persistent second order sinusoidal variations at 4.5 μm and placed stringent upper limits on these variations at 3.6 μm. These observations of WASP-12b raise several questions which will require further study to resolve.

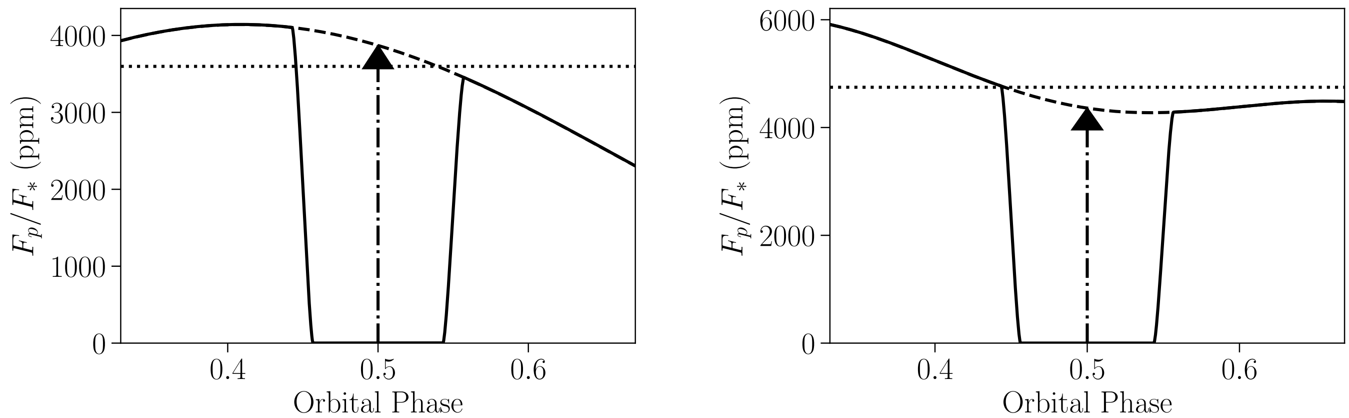

Figure 4. Bias present in eclipse-only observations of exoplanets. *Left*: Our fiducial model for the 2010 phase curve at 3.6 μm is shown with a solid line, while the model neglecting the secondary eclipse is shown with a dashed line. It is with respect to this line that we calculate our eclipse depth (shown with a dash-dotted arrow), while the eclipse depth that would be measured using eclipse-only observations is shown with a dotted line. This bias occurs because there is insufficient evidence of phase variations with eclipse-only observations, so a flat or a sloped line is used instead. *Right*: The same bias at 4.5 μm but in the opposite direction due to the abnormal concave-up phase variations near the 4.5 μm eclipse.

Our two emission hypotheses could be distinguished with phase curve observations of the $\sim$1.6 μm and/or 2.29 μm CO emission bands and/or with phase curve observations at wavelengths longer than 5 μm which should exhibit strong second order sinusoidal variations if the 3.6 μm vs. 4.5 μm amplitude discrepancy is the result of blackbody emission. The high precision and wavelength coverage achievable with the James Webb Space Telescope should allow these two emission hypotheses to be tested. The $\sim$1.6 μm CO emission band also lies within the Hubble/WFC3 bandpass and may be detectable with phase curve observations.

Critically, future models must also address the fact that the fitted planetary radius is significantly smaller at 4.5 μm than at 3.6 μm; this may be the result of unocculted emitting gas. Combined hydrodynamic and radiative transfer simulations are required to fully understand this system. These simulations will allow us to determine the location and spatial extent of the emitting gas, and they may resolve the apparent tension between the constraint from these observations that the gas is well aligned with the star–planet axis, while NUV observations which probe lower density gas show that the gas flows significantly ahead of the planet. Understanding the nature of the increased emission at 4.5 μm will also require modelling the mass loss and the UV dissociation and potential recombination of CO molecules as they flow from the planet's upper atmosphere through a gas stream and potentially experience a shock. These models may also assist in understanding the observed hot spot variability seen at 3.6 μm.

Finally, while WASP-12b is one of the exoplanets closest to overflowing it's Roche lobe (see Figure A2), there are several other UHJs with similar characteristics with published Spitzer phase curves that do not show strong second order sinusoidal variations at 4.5 μm: particularly WASP-19b (Wong et al. 2016), WASP-33b (Zhang et al. 2018), and WASP-103b (Kreidberg et al. 2018). One potential explanation is that WASP-12b's orbit may be decaying (Maciejewski et al. 2016; Patra et al. 2017) while the other exoplanets may be more stable; this could potentially be explained if WASP-12b was locked in a high obliquity state due to a resonance with a perturbing planet which could drive orbital decay and inflate the planet beyond it's Roche lobe (Millholland & Laughlin 2018). Alternatively, the high energy irradiation from WASP-12A may be stronger than the other UHJ host stars. Further research is required to understand why WASP-12b is the only exoplanet known to be exhibiting these exceptionally strong second order sinusoidal variations at 4.5 μm.

ACKNOWLEDGEMENTS

T.J.B. acknowledges support from the McGill Space Institute Graduate Fellowship, the Natural Sciences and Engineering Research Council of Canada's Postgraduate Scholarships-Doctoral Fellowship, and from the Fonds de recherche du Québec – Nature et technologies through the Centre de recherche en astrophysique du Québec. The research leading to these results has received funding from the European Research Council (ERC) under the European Union's Horizon 2020 research and innovation programme (grant agreement no. 679633; Exo-Atmos). We have also made use of open-source software provided by the Python, Astropy, SciPy, and Matplotlib communities.

REFERENCES

Arcangeli J., et al., 2018, ApJL, 855, L30

Armstrong D. J., de Mooij E., Barstow J., Osborn H. P., Blake J., Saniee N. F., 2016, Nature Astronomy, 1, 0004

Artigau É., Bouchard S., Doyon R., Lafrenière D., 2009, ApJ, 701, 1534

Bailey A., Goodman J., 2019, MNRAS, 482, 1872

Bechter E. B., et al., 2014, ApJ, 788, 2

Bell T. J., Cowan N. B., 2018, ApJL, 857, L20

Bell T. J., et al., 2017, ApJL, 847, L2

Bergfors C., Brandner W., Henning T., Daemgen S., 2011, in Sozzetti A., Lattanzi M. G., Boss A. P., eds, IAU Symposium Vol. 276, The Astrophysics of Planetary Systems: Formation, Structure, and Dynamical Evolution. pp 397–398, doi:10.1017/S1743921311020503

Bisikalo D. V., Kaigorodov P. V., Ionov D. E., Shematovich V. I., 2013a, Astronomy Reports, 57, 715

Bisikalo D., Kaygorodov P., Ionov D., Shematovich V., Lammer H., Fossati L., 2013b, ApJ, 764, 19

Budaj J., 2011, AJ, 141, 59

Burrows A., Hubeny I., Budaj J., Knutson H. A., Charbonneau D., 2007, ApJL, 668, L171

Burrows A., Budaj J., Hubeny I., 2008, ApJ, 678, 1436

Burton J. R., Watson C. A., Fitzsimmons A., Pollacco D., Moulds V., Littlefair S. P., Wheatley P. J., 2014, ApJ, 789, 113

Campo C. J., et al., 2011, ApJ, 727, 125

Charbonneau D., Knutson H. A., Barman T., Allen L. E., Mayor M., Megeath S. T., Queloz D., Udry S., 2008, ApJ, 686, 1341

Cherenkov A. A., Bisikalo D. V., Kaigorodov P. V., 2014, Astronomy Reports, 58, 679

Collins K. A., Kielkopf J. F., Stassun K. G., 2017, AJ, 153, 78

Cowan N. B., Agol E., 2011, ApJ, 729, 54

Cowan N. B., Agol E., Charbonneau D., 2007, MNRAS, 379, 641

Cowan N. B., Machalek P., Croll B., Shekhtman L. M., Burrows A., Deming D., Greene T., Hora J. L., 2012, ApJ, 747, 82

Cowan N. B., Fuentes P. A., Haggard H. M., 2013, MNRAS, 434, 2465

Croll B., Lafreniere D., Albert L., Jayawardhana R., Fortney J. J., Murray N., 2011, AJ, 141, 30

Crossfield I. J. M., Hansen B. M. S., Harrington J., Cho J. Y.-K., Deming D., Menou K., Seager S., 2010, ApJ, 723, 1436

Crossfield I. J. M., Knutson H., Fortney J., Showman A. P., Cowan N. B., Deming D., 2012a, ApJ, 752, 81

Crossfield I. J. M., Barman T., Hansen B. M. S., Tanaka I., Kodama T., 2012b, ApJ, 760, 140

Cubillos P., et al., 2013, ApJ, 768, 42

Cubillos P., Harrington J., Madhusudhan N., Foster A. S. D., Lust N. B., Hardy R. A., Bowman M. O., 2014, ApJ, 797, 42

Cubillos P., Harrington J., Loredo T. J., Lust N. B., Blecic J., Stemm M., 2017, AJ, 153, 3

Dang L., et al., 2018, Nature Astronomy, 2, 220

Debrecht A., Carroll-Nellenback J., Frank A., Fossati L., Blackman E. G., Dobbs-Dixon I., 2018, MNRAS, 478, 2592

Deming D., et al., 2011, ApJ, 726, 95

Demory B.-O., Gillon M., Madhusudhan N., Queloz D., 2016, MNRAS, 455, 2018

Espinosa Lara F., Rieutord M., 2011, A&A, 533, A43

Foreman-Mackey D., Hogg D. W., Lang D., Goodman J., 2013, PASP, 125, 306

Fossati L., et al., 2010, ApJL, 714, L222

Fossati L., Ayres T. R., Haswell C. A., Bohlender D., Kochukhov O., Flöer L., 2013, ApJL, 766, L20

Gelman A., Rubin D. B., 1992, Statistical Science, 7, 457

Goody R. M., Walker J. C. G., 1972, Atmospheres, Foundations of Earth Science Series. Prentice-Hall

Harrington J., Hansen B. M., Luszcz S. H., Seager S., Deming D., Menou K., Cho J. Y.-K., Richardson L. J., 2006, Science, 314, 623

Haswell C. A., et al., 2012, ApJ, 760, 79

Hebb L., et al., 2009, ApJ, 693, 1920

Husser T.-O., Wende-von Berg S., Dreizler S., Homeier D., Reiners A., Barman T., Hauschildt P. H., 2013, A&A, 553, A6

Ingalls J. G., et al., 2016, AJ, 152, 44

Kipping D. M., 2013, MNRAS, 435, 2152

Knutson H. A., et al., 2007, Nature, 447, 183

Knutson H. A., et al., 2009a, ApJ, 690, 822

Knutson H. A., Charbonneau D., Cowan N. B., Fortney J. J., Showman A. P., Agol E., Henry G. W., 2009b, ApJ, 703, 769

Knutson H. A., Howard A. W., Isaacson H., 2010, ApJ, 720, 1569

Knutson H. A., et al., 2012, ApJ, 754, 22

Komacek T. D., Tan X., 2018, Research Notes of the American Astronomical Society, 2, 36

Kreidberg L., 2015, PASP, 127, 1161

Kreidberg L., et al., 2018, AJ, 156, 17

Krick J. E., et al., 2016, ApJ, 824, 27

Lai D., Helling C., van den Heuvel E. P. J., 2010, ApJ, 721, 923

Laughlin G., Deming D., Langton J., Kasen D., Vogt S., Butler P., Rivera E., Meschiari S., 2009, Nature, 457, 562

Leconte J., Lai D., Chabrier G., 2011a, A&A, 528, A41

Leconte J., Lai D., Chabrier G., 2011b, A&A, 536, C1

Lewis N. K., et al., 2013, ApJ, 766, 95

Li S.-L., Miller N., Lin D. N. C., Fortney J. J., 2010, Nature, 463, 1054

Llama J., Wood K., Jardine M., Vidotto A. A., Helling C., Fossati L., Haswell C. A., 2011, MNRAS, 416, L41

Llama J., Vidotto A. A., Jardine M., Wood K., Fares R., Gombosi T. I., 2013, MNRAS, 436, 2179

Lothringer J. D., Barman T., Koskinen T., 2018, ApJ, 866, 27

Lust N. B., Britt D., Harrington J., Nymeyer S., Stevenson K. B., Ross E. L., Bowman W., Fraine J., 2014, PASP, 126, 1092

Maciejewski G., et al., 2016, A&A, 588, L6

Madhusudhan N., et al., 2011, Nature, 469, 64

Mandel K., Agol E., 2002, ApJL, 580, L171

Mansfield M., et al., 2018, AJ, 156, 10

Matsakos T., Uribe A., Königl A., 2015, A&A, 578, A6

Maxted P. F. L., et al., 2013, MNRAS, 428, 2645

Millholland S., Laughlin G., 2018, ApJL, 869, L15

Nichols J. D., et al., 2015, ApJ, 803, 9

Nymeyer S., et al., 2011, ApJ, 742, 35

Parmentier V., et al., 2018, A&A, 617, A110

Patra K. C., Winn J. N., Holman M. J., Yu L., Deming D., Dai F., 2017, AJ, 154, 4

Radigan J., Jayawardhana R., Lafrenière D., Artigau É., Marley M., Saumon D., 2012, ApJ, 750, 105

Roche E., 1847, Mém. Sect. Sci, 1, 243

Rogers T. M., 2017, Nature Astronomy, 1, 0131

Rothman L. S., et al., 2010, JQSRT, 111, 2139

Salz M., Czesla S., Schneider P. C., Schmitt J. H. M. M., 2016, A&A, 586, A75

Schwartz J. C., Cowan N. B., 2017, PASP, 129, 014001

Shporer A., et al., 2019, AJ, 157, 178

Sing D. K., 2010, A&A, 510, A21

Skidmore W., Welsh W. F., Wood J. H., Stiening R. F., 1997, MNRAS, 288, 189

Stevenson K., et al., 2010, Nature, 464, 1161

Stevenson K. B., et al., 2012a, ApJ, 754, 136

Stevenson K. B., et al., 2012b, ApJ, 755, 9

Stevenson K. B., Bean J. L., Seifahrt A., Désert J.-M., Madhusudhan N., Bergmann M., Kreidberg L., Homeier D., 2014a, AJ, 147, 161

Stevenson K. B., Bean J. L., Madhusudhan N., Harrington J., 2014b, ApJ, 791, 36

Stevenson K. B., et al., 2017, AJ, 153, 68

Turner J. D., Christie D., Arras P., Johnson R. E., Schmidt C., 2016, MNRAS, 458, 3880

Vidotto A. A., Jardine M., Helling C., 2010, ApJL, 722, L168

Vidotto A. A., Jardine M., Helling C., 2011, MNRAS, 414, 1573

Welsh W. F., Orosz J. A., Seager S., Fortney J. J., Jenkins J., Rowe J. F., Koch D., Borucki W. J., 2010, ApJL, 713, L145

Winn J. N., et al., 2007, AJ, 134, 1707

Wong I., et al., 2015, ApJ, 811, 122

Wong I., et al., 2016, ApJ, 823, 122

Zellem R. T., et al., 2014, ApJ, 790, 53

Zellem R. T., et al., 2017, ApJ, 844, 27

Zhang M., et al., 2018, AJ, 155, 83

de Wit J., Lewis N. K., Langton J., Laughlin G., Deming D., Batygin K., Fortney J. J., 2016, ApJL, 820, L33

de Wit J., et al., 2017, ApJL, 836, L17

ter Braak C. J. F., Vrugt J. A., 2008, Statistics and Computing, 18, 435

APPENDIX

APPENDIX A: CORRECTION FOR DILUTION BY STELLAR COMPANIONS

To correct for the dilution of our lightcurves by the nearby stellar companions WASP-12BC, we apply the dilution factors from Stevenson et al. (2014a): $\alpha_{\rm comp} = 0.1149 \pm 0.0039$ and 0.1196 ± 0.0042 for 3.6 μm and 4.5 μm respectively. Since our phase curve amplitudes are normalized by the eclipse depth, no corrections need to be made to C_1, D_1, C_2, or D_2. Additionally, while the planetary radii need to be corrected for dilution from WASP-12BC, the ratio $R_{p,2}/R_p$ remains the same for models with ellipsoidal variations. Following Stevenson et al. (2014b,a), the multiplicative correction factor is

$$C_{\rm corr}(\lambda) = 1 + g(\beta, \lambda)\alpha_{\rm comp}(\lambda),$$

where $g(\beta, \lambda)$ is the fraction of WASP-12BC's flux which falls within our aperture of size β. We estimated $g(\beta, \lambda)$ using `STINYTIM`[2], the point response function modelling software for Spitzer. We made 10$\times$ oversampled point response functions calculated at the pixel position (25,25) assuming a $T = 3660$ blackbody source (the effective temperature of WASP-12BC; Stevenson et al. 2014b). We found $g(2.5, 4.5\ \mu{\rm m}) = 0.8147$, $g(3.2, 4.5\ \mu{\rm m}) = 0.8608$, $g(4.3, 3.6\ \mu{\rm m}) = 0.9089$, and $g(2.9, 3.6\ \mu{\rm m})$ $= 0.8580$. For the 3×3 pixel stamp used in M. Zhang's PLD analyses, we find $g(3{\times}3, 3.6\ \mu{\rm m}) =$ 0.6518 and $g(3{\times}3, 4.5\ \mu{\rm m}) = 0.6291$. For P. Cubillos' analyses, we find $g(3.0, 4.5\ \mu{\rm m}) = 0.8533$, $g(2.5, 4.5\ \mu{\rm m}) = 0.6957$, $g(2.5, 3.6\ \mu{\rm m}) = 0.8254$, and $g(4.0, 3.6\ \mu{\rm m}) = 0.9015$. We also checked $g(2.25, 3.6\ \mu{\rm m})$ and $g(2.25, 4.5\ \mu{\rm m})$ to compare our calculation to that of Stevenson et al. (2014b); we find values of 0.8007 and 0.7586, where Stevenson et al. (2014b) found 0.7116 and 0.6931. This discrepancy is likely caused by an incorrect angular separation used in the previous work's calculation.

The planet's radius was then corrected using

$$R_{p,\rm corr}(\lambda) = \sqrt{C_{\rm corr}(\lambda)}\, R_{p,\rm meas}(\lambda),$$

[2] `http://irsa.ipac.caltech.edu/data/SPITZER/docs/dataanalysistools/tools/contributed/general/stinytim/`

with the elongated axis, $R_{p,2}$, in bi-axial ellipsoid models corrected similarly. The dayside flux was corrected using

$$F_{\mathrm{day,corr}}(\lambda) = C_{\mathrm{corr}}(\lambda)\, F_{\mathrm{day,meas}}(\lambda),$$

with the white noise amplitude, σ_F, corrected similarly.

APPENDIX B: COMPUTING ASTROPHYSICAL PARAMETERS

Tables A2–A9 present many of the fitted astrophysical values from all models run in all three independent analyses. $T_{b,\mathrm{day}}$ and $T_{b,\mathrm{night}}$ are the apparent brightness temperatures of the planet's day and night hemispheres which we calculate using *only the contribution from the first order sinusoid.* In doing so, we are assuming that the second order sinusoidal variations are attributable to something other than the planet, although the second-order sinusoidal variations end up having negligible contributions during transit and eclipse anyway. These brightness temperatures are calculated by inverting the Planck function (Cowan & Agol 2011), using

$$T_b(\lambda) = \frac{hc}{\lambda k_B}\left[\ln\left(1 + \frac{\exp(hc/\lambda k_B T_{*,\mathrm{b}}) - 1}{\psi(\lambda)}\right)\right]^{-1},$$

where h is Planck's constant, c is the speed of light, k_B is the Boltzmann constant, λ is the wavelength. For $T_{b,\mathrm{day}}$, $\psi = (F_{\mathrm{day}}/F_*)(R_p/R_*)^{-2}$, and for $T_{b,\mathrm{night}}$, $\psi = (F_{\mathrm{day}}/F_*)(1 - 2\,C_1)(R_p/R_*)^{-2}$. The stellar brightness temperature, $T_{*,\mathrm{b}}$ was calculated by fitting blackbodies to the relevant wavelengths from a `PHOENIX` stellar model (Husser et al. 2013) with previously measured (Hebb et al. 2009) values of $T_{*,\mathrm{eff}} = 6300$ K and $\log(g) = 4.5$. We find $T_{*,\mathrm{b}} = 6000$ K for 4.5 μm and 5800 K for 3.6 μm. The tabulated first and second order offsets are measured in degrees after the secondary eclipse and are calculated using:

$$\psi_1 = -(180/\pi)\arctan(D_1/C_1)$$

$$\psi_2 = 180 - 0.5(180/\pi)\arctan(D_2/C_2).$$

APPENDIX C: TIDAL DISTORTION CALCULATIONS

To assess the impact of stellar and planetary tidal distortion, we model the stellar/planetary surfaces using the dimensionless Roche potential, defined by

$$\Omega(r,\theta,\phi) = \frac{1}{r} + q\left(\frac{1}{\sqrt{1-2r\sin\theta\cos\phi+r^2}} - r\sin\theta\cos\phi\right) + \frac{q+1}{2}r^2\sin^2\theta,$$

where r is the distance from the host star, θ is the polar angle, ϕ is the azimuthal angle, and q is the mass ratio, M_*/M_p. We find that the star's radius should be 0.0085% longer along the star–planet axis compared to the perpendicular equatorial axis, while the planet's radius should be 5.5% longer along the star–planet axis compared to the dawn–dusk axis seen at transit.

We first assume that the planet and star have a constant temperature of 3000 K and 6300 K, respectively, and then perturb these temperatures to account for gravity darkening using the $T_{\rm eff} \propto g_{\rm eff}^{\beta}$ model (Espinosa Lara & Rieutord 2011) where β is 0.24 for the appreciably distorted planet and 0.25 for the more spherical host star. Next, we convert these temperature maps into flux maps using the Planck blackbody function. We then compute disk-integrated phase curves (Cowan et al. 2013) while also accounting for the variations in apparent areas of the two objects. Our calculations show that the planet's expected variations are only ~3.5 times stronger than that of the host star at *Spitzer*/IRAC wavelengths (see Figure A3 for a depiction).

Our predicted ellipsoidal and gravity darkening variations are consistent with past predictions (Budaj 2011) and with the amplitude of the Zhang PLD model with second order sinusoidal variations fitted to the 3.6 μm data collected in 2010 (we set the offset to zero as there is no significant detection of an offset in this phase curve). However, the expected ellipsoidal and gravity darkening variations are highly discrepant with the observed amplitude at 4.5 μm (see Figure A4). Running simulations where the planet fills its Roche lobe ($R_{p,2}/R_p \approx 1.4$), our ellipsoidal variations and gravity darkening model would be able to explain the full amplitude of the 4.5 μm phase curve, but the variations remain mostly monochromatic and the model drastically over predicts the variations in the 3.6 μm phase curve.

APPENDIX D: RED NOISE TESTS

The bottom rows of Figures A5–A10 show the observed standard deviation in the residuals versus the number of data cubes binned together for each lightcurve made using the `binrms` routine from the `Multi-Core Markov-Chain Monte Carlo (MC3)`[3] package (Cubillos et al. 2017); this allows us to test for any red noise remaining in our residuals (Winn et al. 2007; Cowan et al. 2012). These figures show that minimal red noise remains after our fiducial models have been subtracted from the data (the photometric uncertainty decays roughly as $\sqrt{N_{\rm binned}}$). There is, however, some lower-frequency noise in the 2010 4.5 μm observations between the first eclipse and the transit that cannot be modelled by any of the three decorrelation pipelines.

APPENDIX E: NUV EVIDENCE FOR MASS LOSS

Across the NUV, WASP-12b appears to be larger than the planet's Roche radius, implying significant mass loss (Fossati et al. 2010; Haswell et al. 2012; Nichols et al. 2015). The first Hubble Space Telescope, Cosmic Origins Spectrograph transit observation of WASP-12b (Fossati et al. 2010) also detected an early ingress in the NUV; this suggests the presence of a stream of gas stripped from the planet flowing in toward the star (Lai et al. 2010; Bisikalo et al. 2013b; Matsakos et al. 2015) which forms a bow shock ahead of the planet (Vidotto et al. 2010; Llama et al. 2011; Bisikalo et al. 2013b; Cherenkov et al. 2014; Matsakos et al. 2015; Turner et al. 2016), although the position of this shock can vary (Vidotto et al. 2011; Llama et al. 2013). There is also evidence for variable NUV ingress times (Haswell et al. 2012; Nichols et al. 2015) which suggests variable mass-loss rates and/or a variations in the planet–shock distance (Vidotto et al. 2011). The non-detection of stellar activity indicators from WASP-12A (Knutson et al. 2010; Fossati et al. 2013) may also suggest that WASP-12b is undergoing mass loss. The final resting place of the gas stripped from WASP-12b is debated, with some suggesting an accretion disk interior to the planet's orbit (Lai et al. 2010; Li et al. 2010) and others suggesting an extended circumstellar torus of gas with the planet embedded inside (Debrecht et al. 2018).

[3] `http://pcubillos.github.io/MCcubed/`

Table A1. A summary of all the priors used in the three independent analyses. Uniform priors were used where there are inequalities below, Gaussian priors were used where uncertainties are indicated, variables were fixed where only a value is indicated, and parameters were unconstrained where Free is written.

	Zhang PLD	Bell SPCA	Cubillos POET
t_0 (BMJD)	$54508.20396 < t_0 < 54508.74968$	$56176.16825800 \pm 0.00007765$	Free
R_p/R_*	> 0	$0 < R_p/R_* < 1$	> 0
a/R_*	3.039	3.039 ± 0.034	3.039 ± 0.034
i (degrees)	83.37	83.37 ± 0.68	83.37 ± 0.68 (fitted $\cos i$)
P (days)	1.09142245	1.0914203	1.0914203
F_p/F_*	Free	$0 < F_p/F_* < 1$	> 0
C_1	Free	Positive Phasecurve	Positive Phasecurve
D_1	Free	Positive Phasecurve	Positive Phasecurve
C_2	Free	Positive Phasecurve	Positive Phasecurve
D_2	Free	Positive Phasecurve	Positive Phasecurve
$R_{p,2}/R_*$	> 0	$0 < R_{p,2} < 1$	> 0
σ_F/F_* (white noise)	$0 < \sigma_F/F_* < 1$	> 0	Free
Limb Darkening	Sing 2010 Model	$0 < q_1 < 1$; $0 < q_2 < 1$	$0 < q_1 < 1$; $0 < q_2 < 1$
e	0	0	t_{eclipse}: Free; $t_{14,\mathrm{eclipse}} > 0$; $t_{12,\mathrm{eclipse}} > 0$; $t_{34} = t_{12}$
Instrumental Variables	Free (PLD coefficients, Slope in time)	Free (Polynomial coefficients, Slope in time for 2013 3.6 μm)	Free (Slope in time for 2013 4.5 μm)

APPENDIX F: DISCUSSION OF VARIABILITY

To date, no *Spitzer* phase curve observation has shown variability in the phase curve offset of an exoplanet, although significant near-infrared variability has been seen for brown dwarfs and isolated planetary mass objects (Artigau et al. 2009; Radigan et al. 2012), and *Kepler* phase curves of the hot Jupiter HAT-P-7b have been reported to vary (Armstrong et al. 2016). Variability is expected for WASP-12b due to coupling between the planet's partially ionized atmosphere and the planet's magnetic field (Rogers 2017). The timescale of this variability is set by the Alfvén timescale (∼115 days for WASP-12b assuming magnetic effects occur on the dayside where the atmosphere is dominated by atomic hydrogen; Rogers 2017; Dang et al. 2018). Variability may also arise in the presence of time-variable cloud coverage, although optically reflective clouds on the planet's dayside were stringently rejected using *Hubble*/STIS optical eclipse spectroscopy of WASP-12b (Bell et al. 2017). Any time-variability in the gas streaming from the planet could also obscure different portions of the planet over time and lead to an apparent variation in the 3.6 μm phase curve.

APPENDIX G: MODEL SELECTION

The preferred model for each phase curve was chosen to be the model with the lowest Bayesian Information Criterion (BIC), defined as

$$\mathrm{BIC} = -2\ln(L) + N_{\mathrm{par}}\ln(N_{\mathrm{dat}}),$$

where N_{par} is the number of model parameters and N_{dat} is the number of data. The log-likelihood is

$$\ln(L) = -\frac{\chi^2}{2} - N_{\mathrm{dat}}\ln(\sigma_F) - \frac{N_{\mathrm{dat}}}{2}\ln(2\pi)$$

where σ_F is the fitted photometric uncertainty (assumed to be constant throughout the observation) and

$$\chi^2 = \frac{\sum_i \left(F_{\mathrm{obs},i} - F_{\mathrm{model},i}\right)^2}{\sigma_F^2}$$

is a measure of the badness-of-fit, where $F_{\mathrm{obs},i}$ are the observed flux measurements. We adopt the threshold that models with a $\Delta\mathrm{BIC} \leq 5$ with respect to the favoured model cannot be strongly ruled out.

Table A2. 3.6 and 4.5 μm phase curve parameters from the preferred models for 2010 and 2013. Fiducial models are indicated with bolding.

3.6 μm

Data Set	Model	C_1	D_1	C_2	D_2	$F_{\rm day}/F_*$ ‡ (ppm)	$\frac{\ln(L)}{N_{\rm data}}$ †
2010	Bell Poly4, 2nd Order	0.436 ± 0.033	-0.067 ± 0.061	0.027 ± 0.028	0.076 ± 0.022	3840 ± 210	5.2
2010	**Zhang PLD, 1st Order**	0.371 ± 0.051	-0.239 ± 0.046			3870 ± 130	**5.62**
2010	Cubillos BLISS, 1st Order	0.395 ± 0.036	-0.237 ± 0.036			3780 ± 120	3.65
2013	Bell Poly3*f(t), 1st Order	0.299 ± 0.029	0.105 ± 0.030			3970 ± 150	5.37
2013	**Zhang PLD, 1st Order**	0.320 ± 0.024	0.079 ± 0.025			3840 ± 120	**5.6**
2013	Cubillos BLISS, 1st Order	0.324 ± 0.024	0.091 ± 0.023			3810 ± 120	3.59

3.6 μm, cont.

Data Set	Model	R_p/R_* ‡	Phase Offset (degrees) 1st Order†	2nd Order†	$T_{b,\rm day}$ † (K)	$T_{b,\rm night}$ † (K)	$\frac{\ln(L)}{N_{\rm data}}$ †
2010	Bell Poly4, 2nd Order	0.1197 ± 0.0012	-8.8 ± 7.9	144.7 ± 9.6	2655 ± 76	1190 ± 180	5.2
2010	**Zhang PLD, 1st Order**	0.11642 ± 0.00063	-32.6 ± 6.2		2744 ± 48	1510 ± 210	**5.62**
2010	Cubillos BLISS, 1st Order	0.11782 ± 0.00096	-30.9 ± 4.5		2603 ± 49	1360 ± 160	3.65
2013	Bell Poly3*f(t), 1st Order	0.1159 ± 0.0011	19.3 ± 4.3		2795 ± 64	1830 ± 110	5.37
2013	**Zhang PLD, 1st Order**	0.11327 ± 0.00068	13.6 ± 3.8		2813 ± 48	1760 ± 97	**5.60**
2013	Cubillos BLISS, 1st Order	0.1169 ± 0.0011	15.7 ± 4.0		2637 ± 47	1658 ± 83	3.59

4.5 μm

Data Set	Model	C_1	D_1	C_2	D_2	$F_{\rm day}/F_*$ ‡ (ppm)	$\frac{\ln(L)}{N_{\rm data}}$ †
2010	Bell BLISS, 2nd Order	0.414 ± 0.044	-0.218 ± 0.054	-0.265 ± 0.037	0.031 ± 0.025	4200 ± 200	5.22
2010	**Zhang PLD, 2nd Order**	0.489 ± 0.016	-0.080 ± 0.020	-0.252 ± 0.019	0.042 ± 0.014	4360 ± 140	**5.45**
2010	Cubillos BLISS, 2nd Order	0.476 ± 0.030	-0.137 ± 0.030	-0.263 ± 0.027	0.043 ± 0.017	4380 ± 170	3.37
2013	Bell BLISS, 2nd Order	0.271 ± 0.053	-0.096 ± 0.046	-0.303 ± 0.043	0.122 ± 0.034	3920 ± 210	5.22
2013	**Zhang PLD, 2nd Order**	0.395 ± 0.036	-0.136 ± 0.025	-0.307 ± 0.023	0.034 ± 0.021	3920 ± 150	**5.43**
2013	Cubillos BLISS, 2nd Order	0.376 ± 0.030	-0.091 ± 0.027	-0.292 ± 0.029	0.041 ± 0.020	4120 ± 160	3.41

4.5 μm, cont.

Data Set	Model	R_p/R_* ‡	Phase Offset (degrees) 1st Order†	2nd Order†	$T_{b,\rm day}$ † (K)	$T_{b,\rm night}$ † (K)	$\frac{\ln(L)}{N_{\rm data}}$ †
2010	Bell BLISS, 2nd Order	0.1078 ± 0.0013	-27.9 ± 6.1	93.4 ± 2.7	2879 ± 91	1250 ± 240	5.22
2010	**Zhang PLD, 2nd Order**	0.10656 ± 0.00085	-9.5 ± 2.3	94.7 ± 1.6	2989 ± 66	790 ± 150	**5.45**
2010	Cubillos BLISS, 2nd Order	0.1075 ± 0.0014	-16.0 ± 3.5	94.6 ± 1.9	2965 ± 78	940 ± 210	3.37
2013	Bell BLISS, 2nd Order	0.1092 ± 0.0016	-19 ± 11	100.9 ± 3.1	2722 ± 92	1800 ± 200	5.22
2013	**Zhang PLD, 2nd Order**	0.1049 ± 0.0010	-19.1 ± 3.9	93.2 ± 1.9	2854 ± 74	1340 ± 180	**5.43**
2013	Cubillos BLISS, 2nd Order	0.1104 ± 0.0014	-13.6 ± 4.0	94.0 ± 1.9	2768 ± 73	1400 ± 140	3.41

† These are derived quantities and are not fitted directly.

‡ These quantities have been corrected for dilution from WASP-12BC (see supplementary text).

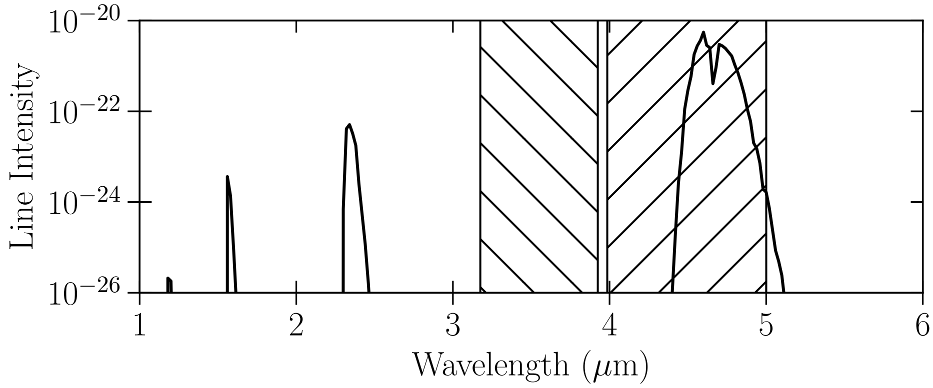

Figure A1. CO line intensities at 296 K from HITEMP (Rothman et al. 2010) in units of $\mathrm{cm}^{-1}/(\mathrm{molecule} \times \mathrm{cm}^{-2})$ which has been binned to a spectral resolution of 10 cm. The bandwidths of *Spitzer*/IRAC channels 1 and 2 are respectively shown with downward sloping and upward sloping hatched regions.

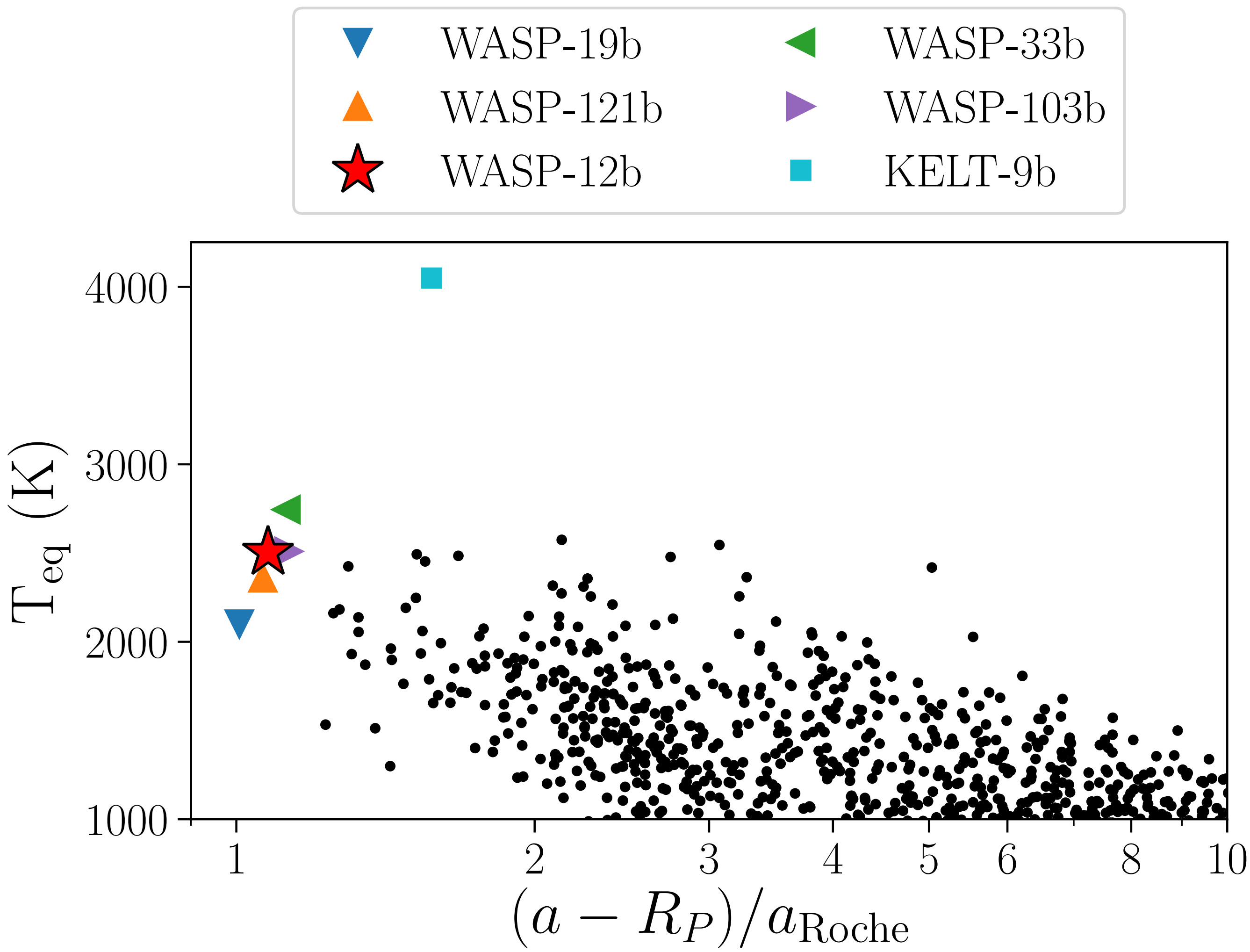

Figure A2. A comparison of WASP-12b to other exoplanets. The y-axis is the planets' equilibrium temperature ($\mathrm{T_{eq}} = 0.25^{0.25}\mathrm{T}_*\sqrt{\mathrm{R}_*/\mathrm{a}}$), and this x-axis is the distance of the substellar point on the planets from their L1 Lagrange point (Roche 1847), where $a_{\mathrm{Roche}} = 2.44(R_p)(M_*/M_p)^{1/3}$. While WASP-12b is one of the exoplanets closest to overflowing it's Roche lobe, there are several others with similar characteristics for which Spitzer phase curves do not show strong second order sinusoidal variations at 4.5 μm (Wong et al. 2016; Zhang et al. 2018; Kreidberg et al. 2018). One potential explanation is that WASP-12b's orbit may be decaying (Maciejewski et al. 2016; Patra et al. 2017) while the other exoplanets may be more stable.

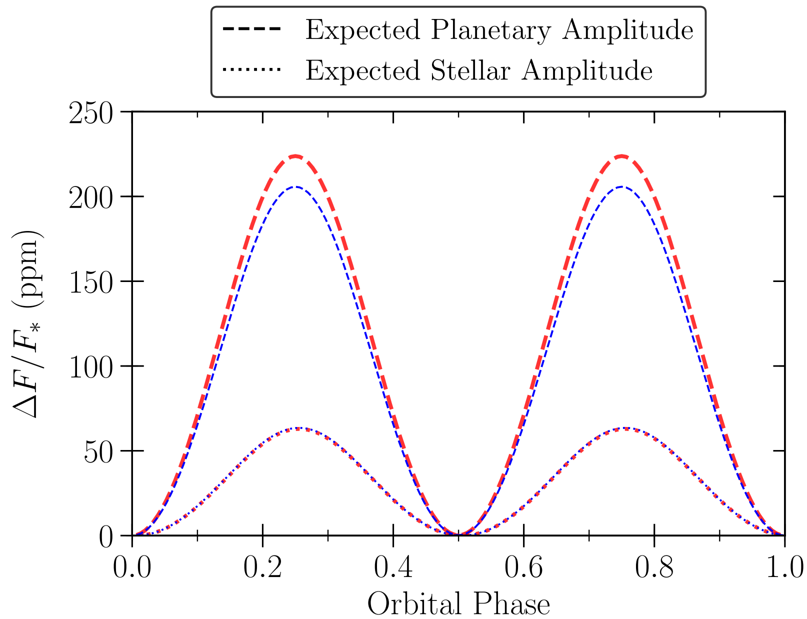

Figure A3. Expected amplitude of tidal distortion from the host star compared to that from the planet. Thin blue lines show the amplitudes at 3.6 μm, while thick red lines show the amplitudes at 4.5 μm.

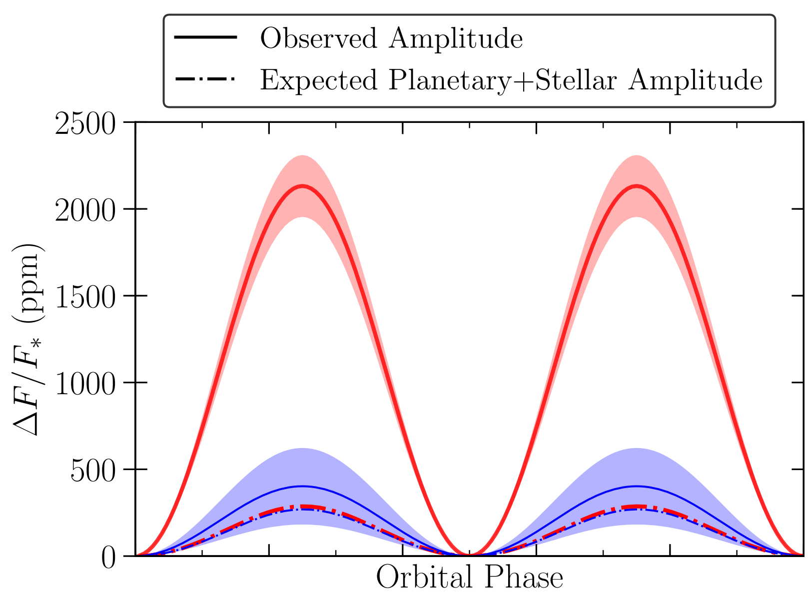

Figure A4. Observed second order sinusoidal variations at 3.6 μm and 4.5 μm and their 1σ uncertainties compared to the expected amplitude of tidal distortion from the host star and the planet. The 3.6 μm phase curve is consistent with the expected amplitudes while the 4.5 μm phase curve is highly discrepant. Thin blue lines show the amplitudes at 3.6 μm, while thick red lines show the amplitudes at 4.5 μm.

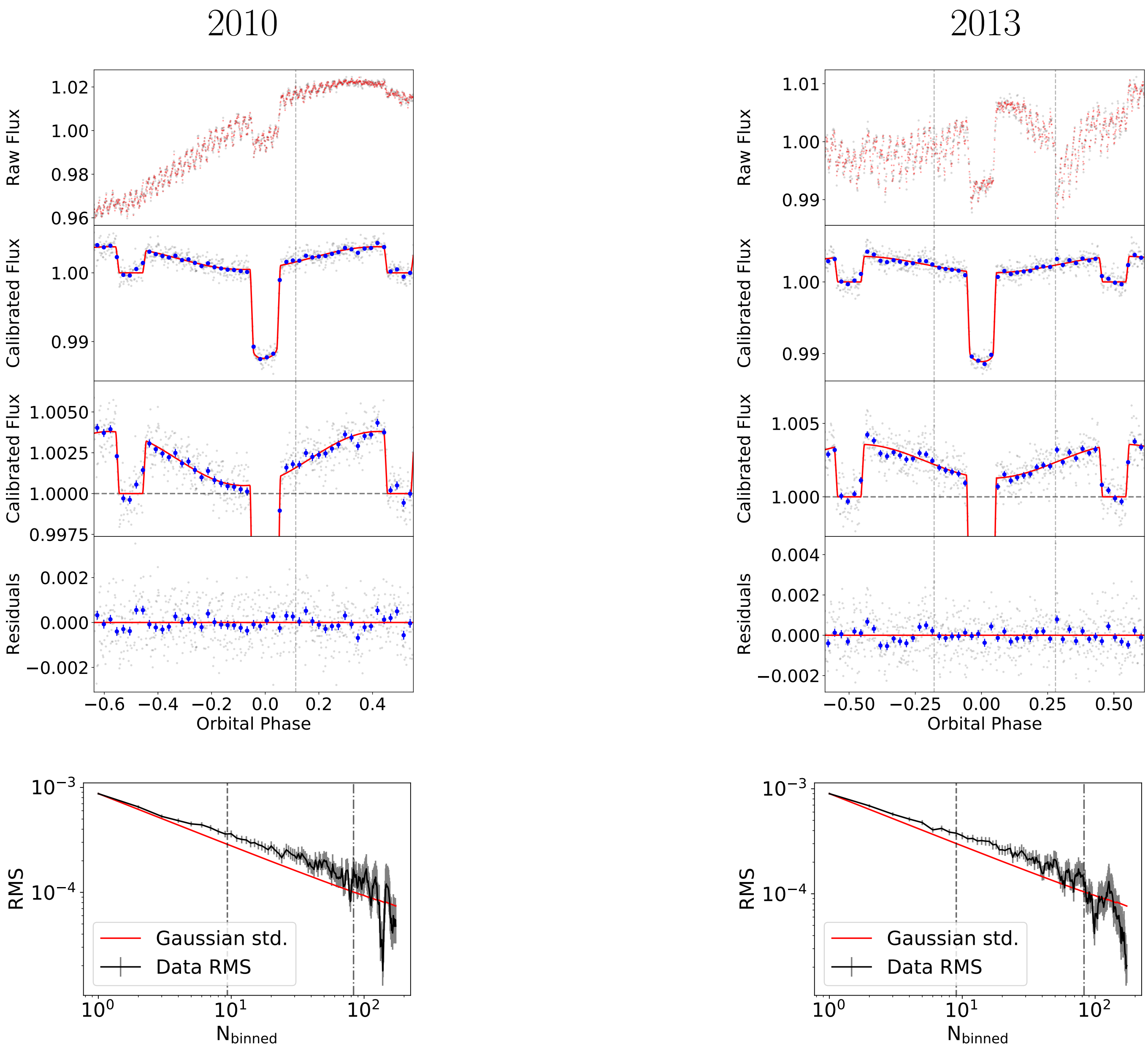

Figure A5. *Top row:* WASP-12b 2010 (left) and 2013 (right) 3.6 μm observations, fit using the Zhang PLD detector model and second- (2010) and first order (2013) phase variations model. Vertical dashed lines mark the transitions between AORs. *Bottom row:* Red noise test for the 2010 (left) and 2013 (right) 3.6 μm observations of WASP-12b for the above fits. The black line shows the decrease in the observed standard deviation in the residuals as N_{binbed} (the number of datapoints binned together) increases. The red line shows the expected decrease in standard deviation, assuming the noise is entirely white. The close match between the two curves suggests that little-to-no red-noise remains in the residuals. A vertical, dashed line shows the timescale for transit/eclipse ingress and egress, while the dash-dotted line shows the t_1–t_4 transit duration.

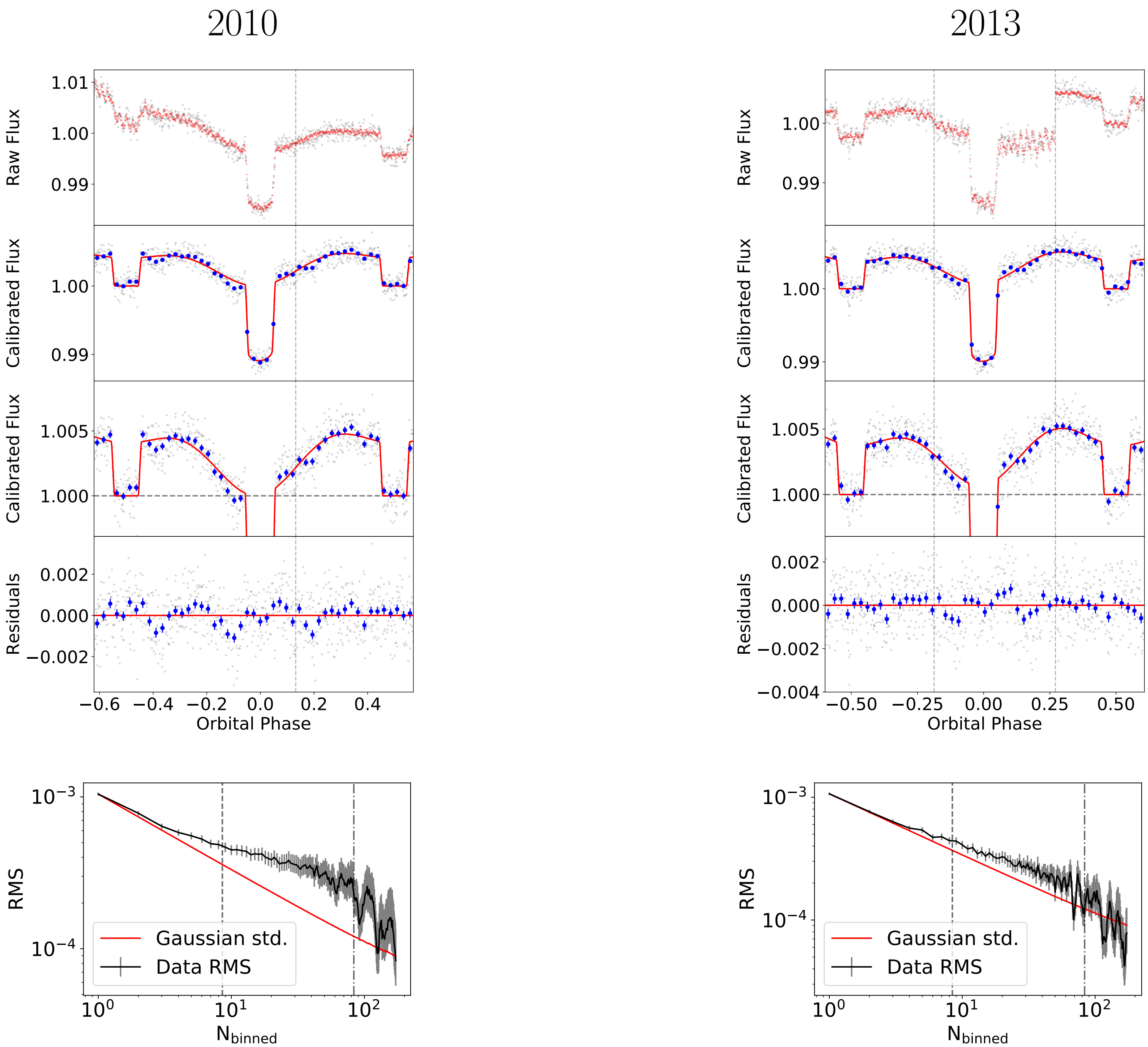

Figure A6. Same figure as the left panel of Figure A5 but for the 2010 (left column) and 2013 (right column) 4.5 μm observations of WASP-12b, both fit using the Zhang PLD detector model and the second order phase variations model.

Supplementary Information

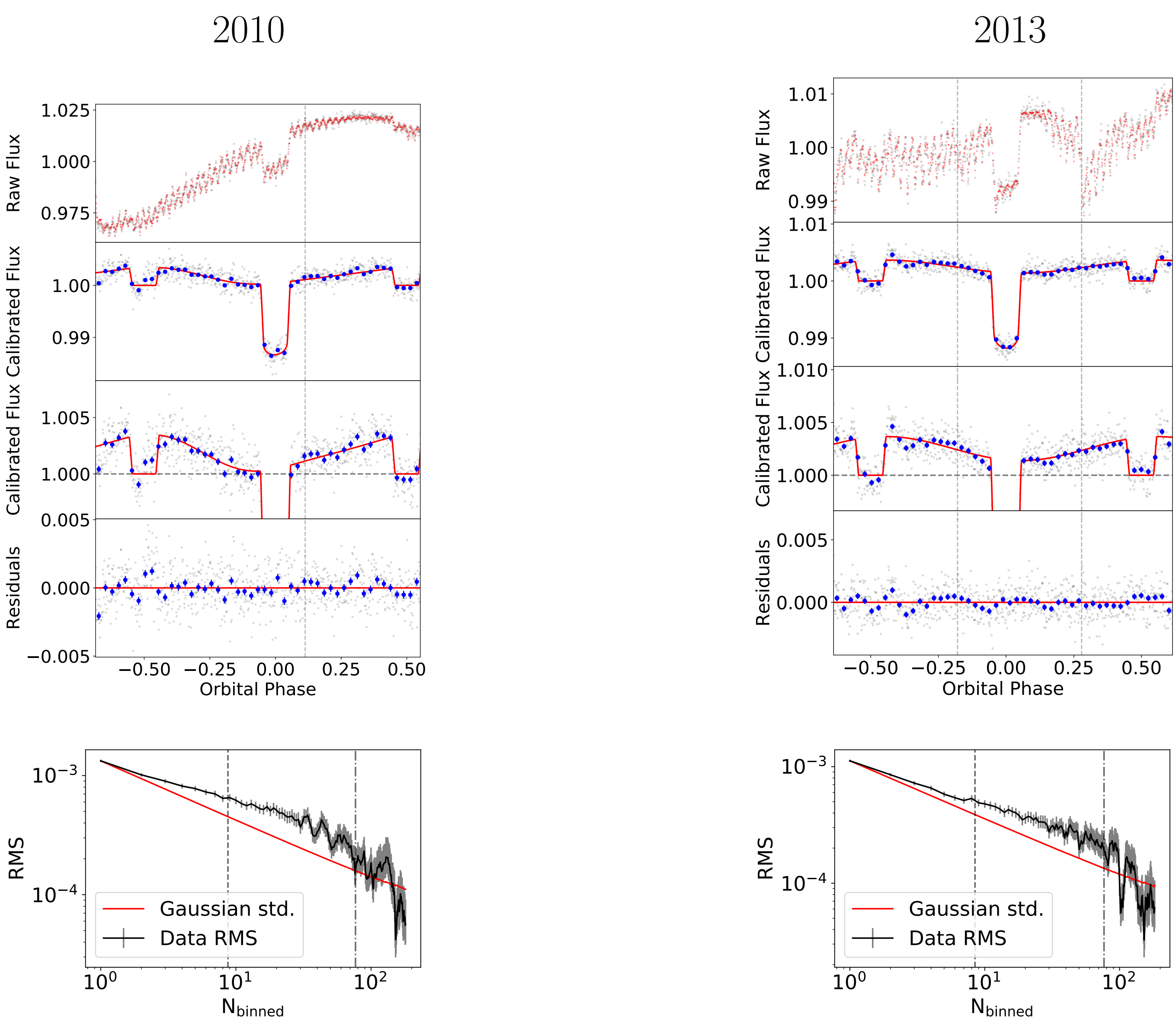

Figure A7. Same as Figure A5 but for the 2010 (left) and 2013 (right) 3.6 μm observations of WASP-12b, fit using the SPCA Poly4 (2010) and SPCA Poly3*$f(t)$ (2013) detector models and the second- (2010) and first order (2013) phase variations model.

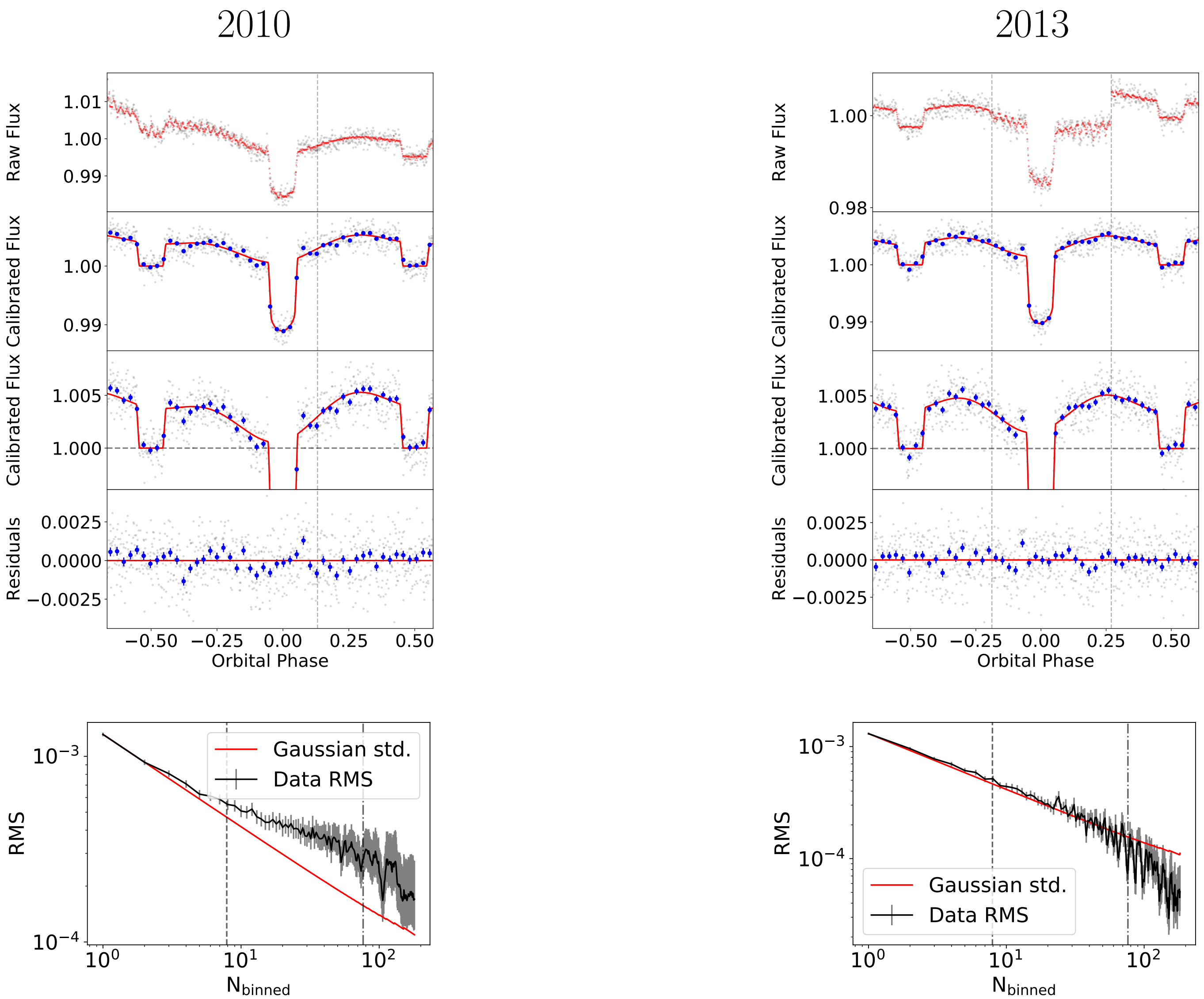

Figure A8. Same figure as Figure A5 but for the 2010 (left) and 2013 (right) 4.5 μm observations of WASP-12b, both fit using the SPCA BLISS detector model and the second order phase variations model.

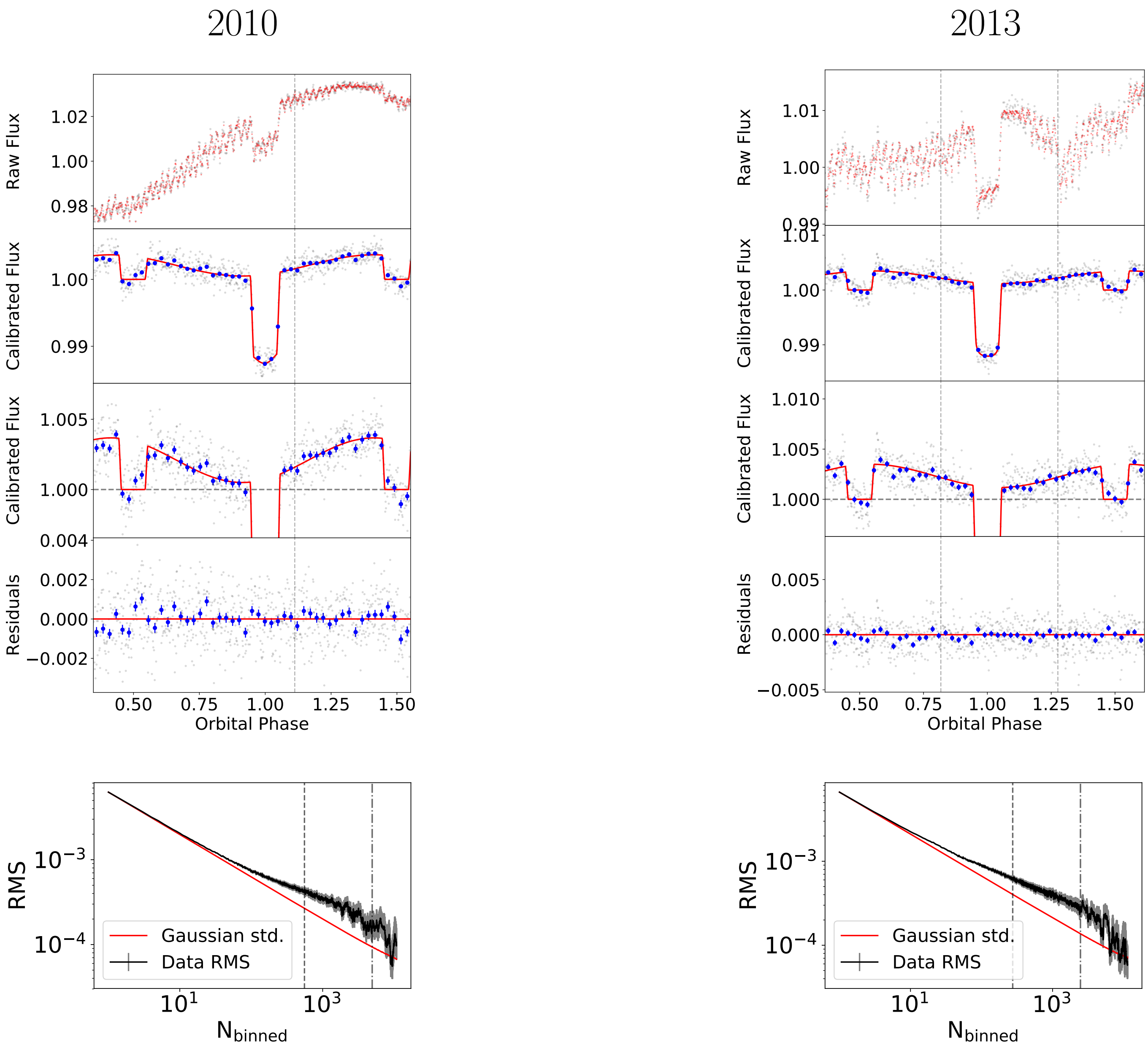

Figure A9. Same figure as Figure A5 but for the 2010 (left) and 2013 (right) 3.6 μm observations of WASP-12b, both fit using the `POET` pipeline.

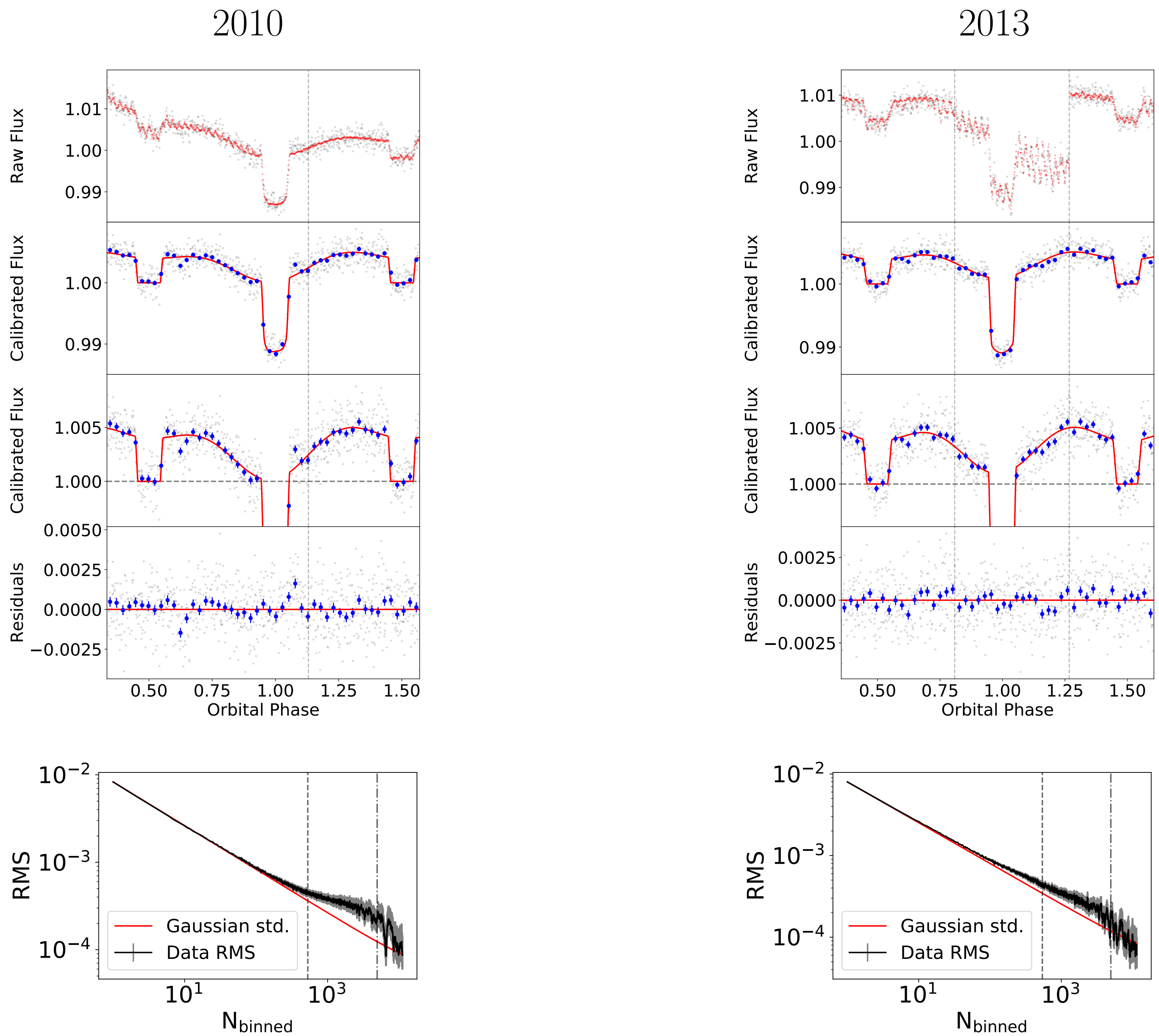

Figure A10. Same figure as Figure A5 but for the 2010 (left) and 2013 (right) 4.5 μm observations of WASP-12b, both fit using the `POET` pipeline.

Table A3: Best-fit 3.6 μm Phase Curve Parameters from 2010

Detector Model	Astrophysical Model	C_1	D_1	C_2	D_2	$F_{\rm day}/F_*$ ‡ (ppm)	σ_F ‡ (ppm)	χ^2	ΔBIC[†a]
Bell Poly2	1st Order	-0.553 ± 0.064	-0.850 ± 0.074			4460 ± 270	2274 ± 53	907.9	716
Bell Poly2	2nd Order	-0.573 ± 0.073	-0.874 ± 0.088	-0.016 ± 0.039	-0.004 ± 0.029	4340 ± 330	2276 ± 55	906.58	730
Bell Poly2	1st Order + Ellipse	-0.551 ± 0.067	-0.852 ± 0.079			4460 ± 290	2275 ± 53	907.42	723
Bell Poly3	1st Order	0.308 ± 0.027	-0.603 ± 0.042			3810 ± 160	1648 ± 39	900.38	155
Bell Poly3	2nd Order	0.265 ± 0.028	-0.528 ± 0.046	0.035 ± 0.024	0.091 ± 0.022	4140 ± 220	1634 ± 39	896.46	149
Bell Poly3	1st Order + Ellipse	0.298 ± 0.027	-0.621 ± 0.042			4180 ± 210	1645 ± 39	896.58	154
Bell Poly4	1st Order	0.453 ± 0.038	-0.064 ± 0.067			3620 ± 170	1493 ± 35	889.85	**0**
Bell Poly4	2nd Order	0.436 ± 0.033	-0.067 ± 0.061	0.027 ± 0.028	0.076 ± 0.022	3840 ± 210	1484 ± 35	887.37	**0**
Bell Poly4	1st Order + Ellipse	0.461 ± 0.028	-0.126 ± 0.074			3890 ± 210	1493 ± 36	885.35	**3**
Bell Poly5	1st Order	0.415 ± 0.064	-0.055 ± 0.074			3490 ± 200	1481 ± 34	885.42	26
Bell Poly5	2nd Order	0.418 ± 0.048	-0.070 ± 0.064	0.037 ± 0.030	0.064 ± 0.024	3720 ± 210	1473 ± 33	888.5	34
Bell Poly5	1st Order + Ellipse	0.429 ± 0.047	-0.175 ± 0.089			3740 ± 230	1477 ± 35	882.2	26
Bell BLISS	1st Order	0.374 ± 0.059	-0.235 ± 0.070			4280 ± 240	1792 ± 43	901.76	244
Bell BLISS	2nd Order	0.366 ± 0.054	-0.248 ± 0.065	0.032 ± 0.037	0.021 ± 0.032	4420 ± 270	1793 ± 42	899.5	256
Bell BLISS	1st Order + Ellipse	0.381 ± 0.048	-0.326 ± 0.079			4550 ± 270	1786 ± 42	902.16	245
Zhang PLD	1st Order	0.371 ± 0.051	-0.239 ± 0.046			3870 ± 130	950 ± 23	865.0	**0**
Zhang PLD	2nd Order	0.374 ± 0.047	-0.222 ± 0.045	0.025 ± 0.018	0.038 ± 0.014	3990 ± 150	946 ± 23	865.07	**4**
Zhang PLD	1st Order + Ellipse	0.367 ± 0.052	-0.234 ± 0.047			3840 ± 130	952 ± 23	865.01	8
Cubillos BLISS	1st Order	0.395 ± 0.036	-0.237 ± 0.036			3780 ± 120	6915 ± 87	54053	**0**
Cubillos BLISS	2nd Order	0.399 ± 0.037	-0.253 ± 0.037	-0.015 ± 0.022	0.048 ± 0.020	3790 ± 140	6915 ± 87	54047	18
Cubillos BLISS	1st Order + Ellipse	0.397 ± 0.036	-0.275 ± 0.041			4040 ± 290	6915 ± 87	54049	15

† These are derived quantities and are not fitted directly.

‡ These quantities have been corrected for dilution from WASP-12BC (see supplementary text).

[a] ΔBIC is defined from the preferred model from each analysis pipeline.

Table A4: Best-fit 3.6 μm Phase Curve Parameters from 2013

Detector Model	Astrophysical Model	C_1	D_1	C_2	D_2	$F_{\rm day}/F_*$ [‡] (ppm)	σ_F [‡] (ppm)	χ^2	ΔBIC[†a]
Bell Poly2	1st Order	0.419 ± 0.023	0.159 ± 0.028			4430 ± 180	1527 ± 36	900.39	342
Bell Poly2*f(t)	1st Order	0.208 ± 0.026	0.010 ± 0.029			3900 ± 160	1327 ± 31	899.48	93
Bell Poly2*f(t)	2nd Order	0.209 ± 0.030	-0.046 ± 0.032	-0.058 ± 0.036	0.168 ± 0.024	3740 ± 170	1290 ± 30	896.13	52
Bell Poly2*f(t)	1st Order + Ellipse	0.209 ± 0.028	0.012 ± 0.031			3900 ± 180	1328 ± 32	897.58	100
Bell Poly3*f(t)	1st Order	0.299 ± 0.029	0.105 ± 0.030			3970 ± 150	1246 ± 29	893.46	**0**
Bell Poly3*f(t)	2nd Order	0.317 ± 0.042	0.092 ± 0.037	-0.036 ± 0.039	0.018 ± 0.030	3870 ± 170	1247 ± 30	891.96	13
Bell Poly3*f(t)	1st Order + Ellipse	0.299 ± 0.032	0.108 ± 0.031			3970 ± 180	1246 ± 29	893.65	7
Bell Poly4*f(t)	1st Order	0.302 ± 0.031	0.108 ± 0.033			3970 ± 150	1246 ± 30	888.32	29
Bell Poly4*f(t)	2nd Order	0.313 ± 0.043	0.074 ± 0.046	-0.053 ± 0.043	0.029 ± 0.033	3840 ± 180	1246 ± 29	887.08	41
Bell Poly4*f(t)	1st Order + Ellipse	0.301 ± 0.034	0.106 ± 0.036			3970 ± 170	1247 ± 29	888.07	36
Bell Poly5*f(t)	1st Order	0.276 ± 0.036	0.086 ± 0.036			3950 ± 150	1244 ± 29	883.38	65
Bell Poly5*f(t)	2nd Order	0.281 ± 0.049	0.051 ± 0.046	-0.045 ± 0.044	0.033 ± 0.036	3830 ± 180	1244 ± 30	884.77	80
Bell Poly5*f(t)	1st Order + Ellipse	0.270 ± 0.038	0.089 ± 0.036			3970 ± 180	1243 ± 29	884.16	71
Bell BLISS*f(t)	1st Order	0.4683 ± 0.0082	0.219 ± 0.024			4440 ± 180	1504 ± 35	904.44	288
Bell BLISS*f(t)	2nd Order	0.484 ± 0.012	0.108 ± 0.045	-0.165 ± 0.038	0.142 ± 0.034	3930 ± 190	1478 ± 35	903.4	269
Bell BLISS*f(t)	1st Order + Ellipse	0.4751 ± 0.0078	0.188 ± 0.025			4090 ± 230	1500 ± 35	901.6	287
Zhang PLD	1st Order	0.320 ± 0.024	0.079 ± 0.025			3840 ± 120	976 ± 24	866.03	**0**
Zhang PLD	2nd Order	0.349 ± 0.028	0.073 ± 0.027	-0.038 ± 0.027	-0.021 ± 0.021	3770 ± 130	975 ± 23	866.06	12
Zhang PLD	1st Order + Ellipse	0.326 ± 0.024	0.070 ± 0.025			3760 ± 130	976 ± 24	866.0	8
Cubillos BLISS	1st Order	0.324 ± 0.024	0.091 ± 0.023			3810 ± 120	7360 ± 90	56764	**0**
Cubillos BLISS	2nd Order	0.331 ± 0.032	0.052 ± 0.029	-0.052 ± 0.027	0.050 ± 0.023	3680 ± 130	7361 ± 90	56756	28
Cubillos BLISS	1st Order + Ellipse	0.296 ± 0.029	0.046 ± 0.038			4010 ± 240	7361 ± 90	56762	31

[†] These are derived quantities and are not fitted directly.

[‡] These quantities have been corrected for dilution from WASP-12BC (see supplementary text).

[a] ΔBIC is defined from the preferred model from each analysis pipeline.

Table A5: Best-fit 3.6 μm Planetary Parameters from 2010

Detector Model	Astrophysical Model	R_p/R_* ‡	$R_{p,2}/R_*$ †‡	$R_{p,2}/R_p$	Phase Offset (degrees) 1st Order†	2nd Order†	$T_{b,\mathrm{day}}$ †	$T_{b,\mathrm{night}}$ †	ΔBIC†[a]
Bell Poly2	1st Order	0.1221 ± 0.0016			-123.1 ± 3.2		2810 ± 100	4380 ± 140	716
Bell Poly2	2nd Order	0.1219 ± 0.0017			-123.1 ± 3.1	263 ± 51	2780 ± 110	4360 ± 150	730
Bell Poly2	1st Order + Ellipse	0.1222 ± 0.0018	0.1217 ± 0.0049	0.996 ± 0.044	-122.7 ± 3.4		2810 ± 100	4370 ± 140	723
Bell Poly3	1st Order	0.1207 ± 0.0012			-62.9 ± 3.6		2625 ± 69	1710 ± 83	155
Bell Poly3	2nd Order	0.1213 ± 0.0013			-63.2 ± 3.8	145.6 ± 7.0	2723 ± 78	1910 ± 95	149
Bell Poly3	1st Order + Ellipse	0.1216 ± 0.0013	0.1029 ± 0.0064	0.846 ± 0.056	-64.3 ± 3.6		2729 ± 77	1797 ± 92	154
Bell Poly4	1st Order	0.1194 ± 0.0012			-8.1 ± 8.5		2586 ± 70	1080 ± 230	**0**
Bell Poly4	2nd Order	0.1197 ± 0.0012			-8.8 ± 7.9	144.7 ± 9.6	2655 ± 76	1190 ± 180	**0**
Bell Poly4	1st Order + Ellipse	0.1198 ± 0.0012	0.10 ± 0.010	0.830 ± 0.093	-15.3 ± 8.6		2671 ± 79	1050 ± 180	**3**
Bell Poly5	1st Order	0.1189 ± 0.0012			-8 ± 10		2547 ± 76	1270 ± 300	26
Bell Poly5	2nd Order	0.1194 ± 0.0012			-9.5 ± 8.6	150 ± 11	2622 ± 78	1280 ± 230	34
Bell Poly5	1st Order + Ellipse	0.1196 ± 0.0012	0.090 ± 0.011	0.749 ± 0.098	-23 ± 11		2625 ± 85	1220 ± 230	26
Bell BLISS	1st Order	0.1196 ± 0.0015			-32.6 ± 8.5		2814 ± 91	1530 ± 260	244
Bell BLISS	2nd Order	0.1197 ± 0.0016			-34.4 ± 8.3	163 ± 25	2860 ± 100	1590 ± 230	256
Bell BLISS	1st Order + Ellipse	0.1199 ± 0.0016	0.094 ± 0.011	0.781 ± 0.092	-40.9 ± 8.1		2902 ± 100	1540 ± 220	245
Zhang PLD	1st Order	0.11642 ± 0.00063			-32.6 ± 6.2		2741 ± 54	1530 ± 220	**0**
Zhang PLD	2nd Order	0.11693 ± 0.00072			-30.6 ± 6.2	152 ± 11	2782 ± 57	1530 ± 190	**4**
Zhang PLD	1st Order + Ellipse	0.11635 ± 0.00063	0.1180 ± 0.0019	1.014 ± 0.023	-32.4 ± 6.3		2736 ± 50	1550 ± 210	8
Cubillos BLISS	1st Order	0.11782 ± 0.00096			-30.9 ± 4.5		2603 ± 46	1390 ± 150	**0**
Cubillos BLISS	2nd Order	0.11776 ± 0.00098			-32.4 ± 4.5	126 ± 13	2604 ± 53	1360 ± 160	18
Cubillos BLISS	1st Order + Ellipse	0.11790 ± 0.00096	0.92 ± 0.17	7.8 ± 2.5	-34.7 ± 4.7		2700 ± 110	1390 ± 170	15

† These are derived quantities and are not fitted directly.

‡ These quantities have been corrected for dilution from WASP-12BC (see supplementary text).

[a] ΔBIC is defined from the preferred model from each analysis pipeline.

Table A6: Best-fit 3.6 μm Planetary Parameters from 2013

Detector Model	Astrophysical Model	R_p/R_* ‡	$R_{p,2}/R_*$ †‡	$R_{p,2}/R_p$	Phase Offset (degrees) 1st Order†	2nd Order†	$T_{b,\mathrm{day}}$†	$T_{b,\mathrm{night}}$†	ΔBIC†[a]
Bell Poly2	1st Order	0.1151 ± 0.0013			20.7 ± 3.1		3086 ± 96	1400 ± 130	342
Bell Poly2*f(t)	1st Order	0.1166 ± 0.0012			2.7 ± 7.7		2753 ± 67	2117 ± 79	93
Bell Poly2*f(t)	2nd Order	0.1164 ± 0.0012			-12.4 ± 9.0	125.5 ± 5.7	2696 ± 68	2080 ± 100	52
Bell Poly2*f(t)	1st Order + Ellipse	0.1166 ± 0.0012	0.1161 ± 0.0090	0.996 ± 0.080	3.4 ± 8.3		2752 ± 71	2116 ± 91	100
Bell Poly3*f(t)	1st Order	0.1159 ± 0.0011			19.3 ± 4.3		2795 ± 64	1830 ± 110	**0**
Bell Poly3*f(t)	2nd Order	0.1154 ± 0.0012			16.0 ± 5.8	103 ± 23	2769 ± 68	1750 ± 160	13
Bell Poly3*f(t)	1st Order + Ellipse	0.1161 ± 0.0011	0.1147 ± 0.0094	0.988 ± 0.084	19.6 ± 4.9		2789 ± 69	1820 ± 120	7
Bell Poly4*f(t)	1st Order	0.1163 ± 0.0012			19.6 ± 4.9		2787 ± 62	1810 ± 110	29
Bell Poly4*f(t)	2nd Order	0.1159 ± 0.0012			13.2 ± 7.4	105 ± 17	2745 ± 69	1750 ± 160	41
Bell Poly4*f(t)	1st Order + Ellipse	0.1163 ± 0.0012	0.1156 ± 0.0095	0.994 ± 0.086	19.3 ± 5.4		2786 ± 69	1810 ± 130	36
Bell Poly5*f(t)	1st Order	0.1161 ± 0.0012			17.5 ± 5.6		2785 ± 63	1910 ± 130	65
Bell Poly5*f(t)	2nd Order	0.1158 ± 0.0013			10.3 ± 8.6	108 ± 20	2749 ± 71	1870 ± 180	80
Bell Poly5*f(t)	1st Order + Ellipse	0.1161 ± 0.0012	0.1130 ± 0.0099	0.973 ± 0.091	18.2 ± 6.3		2791 ± 70	1930 ± 140	71
Bell BLISS*f(t)	1st Order	0.1169 ± 0.0014			25.0 ± 2.5		2945 ± 82	1041 ± 67	288
Bell BLISS*f(t)	2nd Order	0.1155 ± 0.0014			12.4 ± 4.9	110.4 ± 4.7	2794 ± 85	870 ± 130	269
Bell BLISS*f(t)	1st Order + Ellipse	0.1164 ± 0.0014	0.147 ± 0.013	1.26 ± 0.12	21.8 ± 2.7		2826 ± 93	963 ± 73	287
Zhang PLD	1st Order	0.11327 ± 0.00068			13.6 ± 3.8		2814 ± 50	1757 ± 95	**0**
Zhang PLD	2nd Order	0.11274 ± 0.00075			11.6 ± 4.0	256 ± 15	2800 ± 56	1640 ± 120	12
Zhang PLD	1st Order + Ellipse	0.11313 ± 0.00067	0.1195 ± 0.0055	1.056 ± 0.058	11.9 ± 3.9		2792 ± 53	1723 ± 95	8
Cubillos BLISS	1st Order	0.1169 ± 0.0011			15.7 ± 4.0		2633 ± 48	1666 ± 90	**0**
Cubillos BLISS	2nd Order	0.1167 ± 0.0012			9.0 ± 5.0	112.0 ± 9.9	2595 ± 52	1620 ± 110	28
Cubillos BLISS	1st Order + Ellipse	0.1173 ± 0.0012	0.95 ± 0.12	8.1 ± 1.8	8.9 ± 7.2		2696 ± 87	1790 ± 100	31

† These are derived quantities and are not fitted directly.

‡ These quantities have been corrected for dilution from WASP-12BC (see supplementary text).

[a] ΔBIC is defined from the preferred model from each analysis pipeline.

Table A7: Best-fit 4.5 μm Phase Curve Parameters from 2010

Detector Model	Astrophysical Model	C_1	D_1	C_2	D_2	$F_{\rm day}/F_*$ ‡ (ppm)	σ_F ‡ (ppm)	χ^2	ΔBIC[†a]
Bell Poly2	1st Order	0.444 ± 0.023	-0.165 ± 0.020			5410 ± 170	1581 ± 38	891.63	180
Bell Poly2	2nd Order	0.481 ± 0.012	-0.150 ± 0.022	-0.258 ± 0.031	0.031 ± 0.017	4380 ± 180	1485 ± 35	891.74	81
Bell Poly2	1st Order + Ellipse	0.409 ± 0.022	-0.099 ± 0.017			3940 ± 270	1518 ± 36	894.4	117
Bell Poly3	1st Order	0.443 ± 0.027	-0.166 ± 0.028			5420 ± 180	1577 ± 37	888.79	200
Bell Poly3	2nd Order	0.470 ± 0.018	-0.207 ± 0.035	-0.281 ± 0.033	0.020 ± 0.019	4280 ± 190	1480 ± 36	885.72	96
Bell Poly3	1st Order + Ellipse	0.378 ± 0.028	-0.120 ± 0.022			3930 ± 270	1512 ± 36	892.02	134
Bell Poly4	1st Order	0.445 ± 0.029	-0.166 ± 0.035			5400 ± 170	1574 ± 37	884.83	227
Bell Poly4	2nd Order	0.387 ± 0.047	-0.061 ± 0.046	-0.328 ± 0.037	0.036 ± 0.019	4240 ± 190	1462 ± 35	881.29	104
Bell Poly4	1st Order + Ellipse	0.253 ± 0.035	-0.010 ± 0.027			3740 ± 260	1482 ± 36	885.06	125
Bell Poly5	1st Order	0.415 ± 0.040	-0.228 ± 0.046			5210 ± 190	1564 ± 39	876.41	252
Bell Poly5	2nd Order	0.394 ± 0.052	-0.061 ± 0.055	-0.325 ± 0.037	0.038 ± 0.019	4220 ± 210	1459 ± 36	876.54	141
Bell Poly5	1st Order + Ellipse	0.254 ± 0.040	-0.011 ± 0.032			3730 ± 260	1482 ± 34	878.21	164
Bell BLISS	1st Order	0.384 ± 0.037	-0.336 ± 0.046			4800 ± 190	1500 ± 35	898.23	56
Bell BLISS	2nd Order	0.414 ± 0.044	-0.218 ± 0.054	-0.265 ± 0.037	0.031 ± 0.025	4200 ± 200	1444 ± 34	897.25	**0**
Bell BLISS	1st Order + Ellipse	0.301 ± 0.038	-0.106 ± 0.040			3940 ± 250	1467 ± 34	897.38	21
Zhang PLD	1st Order	0.479 ± 0.015	-0.135 ± 0.017			5170 ± 130	1240 ± 30	860.05	149
Zhang PLD	2nd Order	0.489 ± 0.016	-0.080 ± 0.020	-0.252 ± 0.019	0.042 ± 0.014	4360 ± 140	1134 ± 27	860.09	**0**
Zhang PLD	1st Order + Ellipse	0.437 ± 0.031	-0.062 ± 0.016			3740 ± 210	1167 ± 28	860.01	46
Cubillos BLISS	1st Order	0.406 ± 0.024	-0.190 ± 0.026			5160 ± 150	9120 ± 100	55965	95
Cubillos BLISS	2nd Order	0.476 ± 0.030	-0.137 ± 0.030	-0.263 ± 0.027	0.043 ± 0.017	4380 ± 170	9130 ± 100	55807	**0**
Cubillos BLISS	1st Order + Ellipse	0.365 ± 0.022	-0.069 ± 0.020			3940 ± 210	9130 ± 100	55844	50

† These are derived quantities and are not fitted directly.

‡ These quantities have been corrected for dilution from WASP-12BC (see supplementary text).

[a] ΔBIC is defined from the preferred model from each analysis pipeline.

Table A8: Best-fit 4.5 μm Phase Curve Parameters from 2013

Detector Model	Astrophysical Model	C_1	D_1	C_2	D_2	F_{day}/F_* ‡ (ppm)	σ_F ‡ (ppm)	χ^2	ΔBIC†[a]
Bell Poly2	1st Order	0.250 ± 0.031	0.035 ± 0.028			4950 ± 180	1613 ± 39	899.32	223
Bell Poly2	2nd Order	0.317 ± 0.041	-0.136 ± 0.041	-0.370 ± 0.045	0.133 ± 0.029	3730 ± 200	1492 ± 36	897.58	93
Bell Poly2	1st Order + Ellipse	0.314 ± 0.029	-0.025 ± 0.022			3080 ± 290	1512 ± 36	911.73	125
Bell Poly3	1st Order	0.267 ± 0.036	0.067 ± 0.030			4940 ± 180	1583 ± 38	895.72	213
Bell Poly3	2nd Order	0.312 ± 0.049	-0.104 ± 0.041	-0.336 ± 0.043	0.144 ± 0.029	3830 ± 200	1472 ± 35	895.32	93
Bell Poly3	1st Order + Ellipse	0.337 ± 0.032	0.007 ± 0.023			3180 ± 290	1495 ± 35	906.96	126
Bell Poly4	1st Order	0.228 ± 0.038	0.088 ± 0.032			4920 ± 190	1567 ± 38	891.32	224
Bell Poly4	2nd Order	0.304 ± 0.050	-0.097 ± 0.047	-0.330 ± 0.045	0.139 ± 0.032	3880 ± 210	1475 ± 33	888.38	124
Bell Poly4	1st Order + Ellipse	0.317 ± 0.036	0.015 ± 0.026			3300 ± 300	1489 ± 34	892.09	138
Bell Poly5	1st Order	0.190 ± 0.040	0.080 ± 0.031			4840 ± 190	1537 ± 35	887.39	231
Bell Poly5	2nd Order	0.254 ± 0.054	-0.097 ± 0.046	-0.299 ± 0.043	0.138 ± 0.032	3910 ± 200	1461 ± 34	885.64	150
Bell Poly5	1st Order + Ellipse	0.291 ± 0.036	0.016 ± 0.025			3430 ± 290	1476 ± 36	890.63	167
Bell BLISS	1st Order	0.182 ± 0.040	0.076 ± 0.031			4890 ± 180	1509 ± 35	908.0	75
Bell BLISS	2nd Order	0.271 ± 0.053	-0.096 ± 0.046	-0.303 ± 0.043	0.122 ± 0.034	3920 ± 210	1440 ± 34	905.23	**0**
Bell BLISS	1st Order + Ellipse	0.293 ± 0.038	0.018 ± 0.025			3490 ± 280	1449 ± 34	908.11	8
Zhang PLD	1st Order	0.276 ± 0.028	-0.063 ± 0.019			4940 ± 150	1275 ± 31	867.11	163
Zhang PLD	2nd Order	0.395 ± 0.036	-0.136 ± 0.025	-0.307 ± 0.023	0.034 ± 0.021	3920 ± 150	1158 ± 28	867.01	**0**
Zhang PLD	1st Order + Ellipse	0.348 ± 0.028	-0.058 ± 0.015			3370 ± 220	1164 ± 28	867.04	**4**
Cubillos BLISS	1st Order	0.269 ± 0.021	0.004 ± 0.017			5290 ± 140	8657 ± 97	57185	148
Cubillos BLISS	2nd Order	0.376 ± 0.030	-0.091 ± 0.027	-0.292 ± 0.029	0.041 ± 0.020	4120 ± 160	8658 ± 97	56998	**0**
Cubillos BLISS	1st Order + Ellipse	0.317 ± 0.023	-0.038 ± 0.018			3610 ± 210	8657 ± 97	57010	6

† These are derived quantities and are not fitted directly.

‡ These quantities have been corrected for dilution from WASP-12BC (see supplementary text).

[a] ΔBIC is defined from the preferred model from each analysis pipeline.

Table A9: Best-fit 4.5 μm Planetary Parameters from 2010

Detector Model	Astrophysical Model	R_p/R_* ‡	$R_{p,2}/R_*$ †‡	$R_{p,2}/R_p$	Phase Offset (degrees) 1st Order†	Phase Offset (degrees) 2nd Order†	$T_{b,\mathrm{day}}$ †	$T_{b,\mathrm{night}}$ †	ΔBIC†[a]
Bell Poly2	1st Order	0.1140 ± 0.0012			-20.4 ± 2.2		3143 ± 79	1130 ± 160	180
Bell Poly2	2nd Order	0.1090 ± 0.0012			-17.5 ± 2.5	93.4 ± 1.9	2918 ± 81	810 ± 120	81
Bell Poly2	1st Order + Ellipse	0.1122 ± 0.0011	0.20 ± 0.015	1.79 ± 0.15	-13.5 ± 2.2		2650 ± 110	1210 ± 110	117
Bell Poly3	1st Order	0.1141 ± 0.0012			-20.7 ± 3.4		3142 ± 81	1140 ± 190	200
Bell Poly3	2nd Order	0.1084 ± 0.0013			-24.0 ± 3.8	92.0 ± 1.9	2894 ± 86	900 ± 150	96
Bell Poly3	1st Order + Ellipse	0.1118 ± 0.0012	0.201 ± 0.015	1.80 ± 0.15	-17.5 ± 3.4		2650 ± 100	1360 ± 130	134
Bell Poly4	1st Order	0.1142 ± 0.0012			-20.7 ± 4.1		3132 ± 76	1120 ± 200	227
Bell Poly4	2nd Order	0.1081 ± 0.0013			-8.8 ± 6.5	93.1 ± 1.7	2888 ± 84	1390 ± 230	104
Bell Poly4	1st Order + Ellipse	0.1082 ± 0.0014	0.215 ± 0.014	1.99 ± 0.14	-2.3 ± 6.1		2678 ± 95	1840 ± 140	125
Bell Poly5	1st Order	0.1137 ± 0.0013			-29.0 ± 5.6		3078 ± 85	1300 ± 230	252
Bell Poly5	2nd Order	0.1079 ± 0.0013			-8.8 ± 7.7	93.3 ± 1.7	2888 ± 89	1360 ± 260	141
Bell Poly5	1st Order + Ellipse	0.1081 ± 0.0014	0.214 ± 0.015	1.98 ± 0.15	-2.7 ± 7.2		2675 ± 97	1840 ± 160	164
Bell BLISS	1st Order	0.1121 ± 0.0012			-41.3 ± 4.9		2979 ± 84	1430 ± 180	56
Bell BLISS	2nd Order	0.1078 ± 0.0013			-27.9 ± 6.1	93.4 ± 2.7	2879 ± 91	1250 ± 240	**0**
Bell BLISS	1st Order + Ellipse	0.1090 ± 0.0014	0.187 ± 0.014	1.71 ± 0.14	-19.6 ± 6.8		2737 ± 96	1700 ± 160	21
Zhang PLD	1st Order	0.11042 ± 0.00084			-15.9 ± 2.0		3174 ± 59	880 ± 150	149
Zhang PLD	2nd Order	0.10656 ± 0.00085			-9.5 ± 2.3	94.7 ± 1.6	2992 ± 63	780 ± 150	**0**
Zhang PLD	1st Order + Ellipse	0.10913 ± 0.00081	0.203 ± 0.014	1.86 ± 0.14	-8.3 ± 1.9		2656 ± 91	1070 ± 170	46
Cubillos BLISS	1st Order	0.1124 ± 0.0013			-25.1 ± 3.2		3111 ± 75	1360 ± 140	95
Cubillos BLISS	2nd Order	0.1075 ± 0.0014			-16.0 ± 3.5	94.6 ± 1.9	2960 ± 84	930 ± 200	**0**
Cubillos BLISS	1st Order + Ellipse	0.1102 ± 0.0013	1.92 ± 0.12	17.4 ± 1.2	-10.6 ± 3.1		2703 ± 95	1434 ± 99	50

† These are derived quantities and are not fitted directly.

‡ These quantities have been corrected for dilution from WASP-12BC (see supplementary text).

[a] ΔBIC is defined from the preferred model from each analysis pipeline.

Table A10: Best-fit 4.5 μm Planetary Parameters from 2013

Detector Model	Astrophysical Model	R_p/R_* ‡	$R_{p,2}/R_*$ †‡	$R_{p,2}/R_p$	Phase Offset (degrees) 1st Order†	2nd Order†	$T_{b,\mathrm{day}}$ †	$T_{b,\mathrm{night}}$ †	ΔBIC†a
Bell Poly2	1st Order	0.1145 ± 0.0015			8.1 ± 5.9		2958 ± 85	2010 ± 110	223
Bell Poly2	2nd Order	0.1102 ± 0.0015			-23.2 ± 7.6	99.9 ± 2.2	2619 ± 86	1580 ± 150	93
Bell Poly2	1st Order + Ellipse	0.1108 ± 0.0013	0.252 ± 0.027	2.27 ± 0.27	-4.5 ± 4.3		2340 ± 120	1460 ± 120	125
Bell Poly3	1st Order	0.1141 ± 0.0015			13.9 ± 5.2		2967 ± 85	1950 ± 140	213
Bell Poly3	2nd Order	0.1107 ± 0.0014			-18.6 ± 8.5	101.6 ± 2.5	2644 ± 86	1610 ± 180	93
Bell Poly3	1st Order + Ellipse	0.1112 ± 0.0013	0.244 ± 0.026	2.20 ± 0.26	1.3 ± 4.0		2370 ± 120	1400 ± 130	126
Bell Poly4	1st Order	0.1136 ± 0.0014			21.1 ± 6.1		2975 ± 84	2120 ± 140	224
Bell Poly4	2nd Order	0.1106 ± 0.0015			-17.8 ± 9.5	101.4 ± 2.7	2668 ± 89	1650 ± 190	124
Bell Poly4	1st Order + Ellipse	0.1082 ± 0.0016	0.225 ± 0.022	2.08 ± 0.23	2.7 ± 4.5		2490 ± 110	1530 ± 150	138
Bell Poly5	1st Order	0.1119 ± 0.0016			23.2 ± 7.2		3002 ± 90	2280 ± 150	231
Bell Poly5	2nd Order	0.110 ± 0.0015			-21 ± 12	102.4 ± 3.0	2692 ± 88	1850 ± 190	150
Bell Poly5	1st Order + Ellipse	0.1075 ± 0.0015	0.208 ± 0.020	1.94 ± 0.21	3.1 ± 4.9		2570 ± 110	1650 ± 150	167
Bell BLISS	1st Order	0.1109 ± 0.0016			22.5 ± 7.6		3056 ± 92	2350 ± 150	75
Bell BLISS	2nd Order	0.1092 ± 0.0016			-19 ± 11	100.9 ± 3.1	2722 ± 92	1800 ± 200	**0**
Bell BLISS	1st Order + Ellipse	0.1086 ± 0.0015	0.207 ± 0.020	1.91 ± 0.21	3.4 ± 4.9		2560 ± 120	1640 ± 160	8
Zhang PLD	1st Order	0.11094 ± 0.00091			-13.1 ± 4.1		3075 ± 66	1960 ± 120	163
Zhang PLD	2nd Order	0.1049 ± 0.0010			-19.1 ± 3.9	93.2 ± 1.9	2859 ± 77	1350 ± 180	**0**
Zhang PLD	1st Order + Ellipse	0.10653 ± 0.00085	0.217 ± 0.017	2.04 ± 0.17	-9.6 ± 2.5		2561 ± 91	1450 ± 120	**4**
Cubillos BLISS	1st Order	0.1141 ± 0.0013			0.8 ± 3.7		3096 ± 64	2004 ± 97	148
Cubillos BLISS	2nd Order	0.1104 ± 0.0014			-13.6 ± 4.0	94.0 ± 1.9	2768 ± 73	1410 ± 130	**0**
Cubillos BLISS	1st Order + Ellipse	0.1115 ± 0.0013	2.01 ± 0.13	18.0 ± 1.2	-6.9 ± 3.3		2527 ± 87	1540 ± 88	6

† These are derived quantities and are not fitted directly.

‡ These quantities have been corrected for dilution from WASP-12BC (see supplementary text).

[a] ΔBIC is defined from the preferred model from each analysis pipeline.

Epilogue

In order to test the hypotheses put forward by Bell et al. (2019), I have led two successful observing proposals. First, I was the Principal Investigator for a Canada France Hawaii Telescope proposal to observe parts of the phase curve of WASP-12b with the SPIRou (SPectropolarimètre InfraROUge) instrument. Our observations will allow us to test the hypothesis of CO emission from a stream of gas by observing the 2.292 μm CO band—the second strongest CO emission feature (see Figure 3–1)—which is spectroscopically inaccessible with *Hubble*, NIRPS, HARPS, or ESPaDOnS. Should we reject the CO hypothesis, this would imply that the gas stream is far colder than the planet's equilibrium temperature which in turn implies that the gas must be flowing directly away from the host star in the shadow of the planet. Meanwhile, should we detect CO emission, we will be able to infer the CO number density and gas temperature since the gas would be at very low pressures where the line shapes are purely determined by Doppler-broadening and the line strengths depend only on the temperature and the CO number density. Additionally, by measuring the strength of the emission lines and their radial velocity at different points in the planet's orbit, we will be able to determine the direction that the gas stream is flowing and test whether the associated angular momentum loss is sufficient to affect the planet's orbital evolution. This will provide a test of our team's hypothesis that WASP-12b's observed orbital decay (Maciejewski et al., 2016; Patra et al., 2017; Yee et al., 2020) could be explained by mass loss which preferentially flows away from the host star through the planet's L2 Lagrange point as this would steal angular momentum from the planet's orbit and lead to orbital decay on a timescale of $P/\dot{P} \sim fM/\dot{M}$ where $f < 1$.

Additionally, I was the Principal Investigator for a *Hubble*/WFC3 G141 spectroscopic phase curve which is currently scheduled for early March 2022. As demonstrated in Figure 3–2, this phase curve observation of WASP-12b is expected to show clear variations in the depth of the 1.4 μm water feature; this is caused by longitudinal variations in temperature

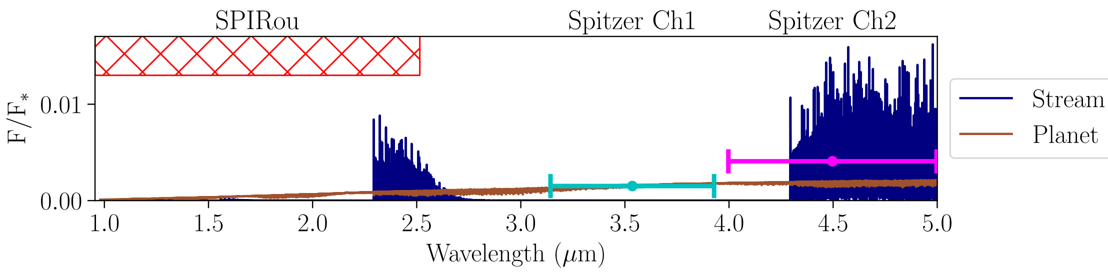

Figure 3–1: Model spectra binned to SPIRou's resolution and normalized by stellar flux, showing the expected strength of the planetary absorption features in brown and gas stream's CO emission features in navy. The *Spitzer*/IRAC Channel 1 and 2 bandpasses and fluxes at quadrature (y errorbars are too small to be seen) from Bell et al. (2019) are shown in cyan and magenta and were used to constrain the model spectra. The SPIRou bandpass is indicated with a hatched region.

which alter the dissociation and ionization state of the gas. These observed variations in the abundance of H_2O and H^- opacity will provide the first spectroscopic test of the $H_2 \leftrightarrow 2H$ dissociation/recombination cycle predicted to play an important role in the thermodynamics of ultra-hot Jupiters by Bell & Cowan (2018). This work will also provide an additional measure of the ellipsoidal variations of the host star and planet (Cowan et al., 2012; Bell et al., 2019) and further constrain the rate of orbital decay for the system (e.g., Yee et al., 2020).

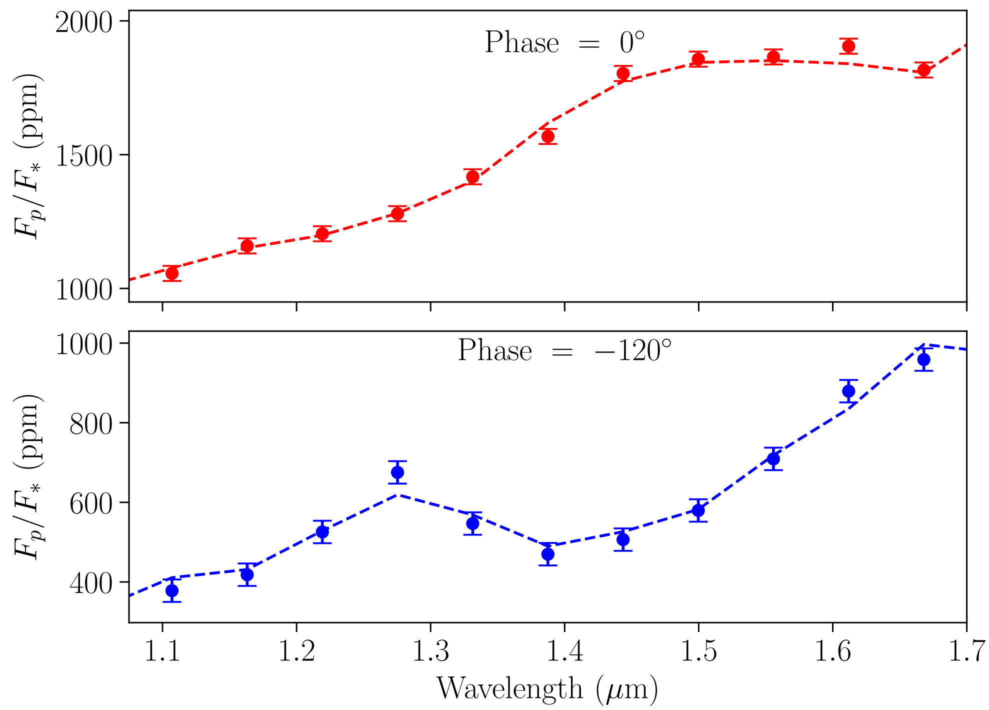

Figure 3–2: Model predictions for my upcoming *Hubble*/WFC3 observations of WASP-12b. Predictions were based on the SPARC/MITgcm models (Parmentier et al., 2018) of the ultra-hot Jupiter WASP-121b (with similar properties to WASP-12b); these models were then scaled to the temperature map of WASP-12b derived from 3.6 μm Spitzer phase curves (Bell et al., 2019) and the known dayside *Hubble*/WFC3 spectrum of WASP-12b (Stevenson et al., 2014). The spectra at two orbital phases are shown: the dayside eclipse spectrum (top) and 60° before mid-transit (bottom). Variations in the water feature are expected to be easily detectable above photon and systematic noise levels.

Paper 4

A Comprehensive Reanalysis of *Spitzer*'s 4.5 μm Phase Curves, and the Phase Variations of the Ultra-hot Jupiters MASCARA-1b and KELT-16b

Preface

In the following paper which is published in the Monthly Notices of the Royal Astronomical Society (Bell et al., 2021), we presented the uniform reanalysis of nearly all previously published *Spitzer*/IRAC phase curve observations. This work built on the reproducibility tests of the WASP-12b phase curves and sought to understand whether the entire body of exoplanetary atmospheric characterization through phase curve observations is built upon a reliable foundation. Additionally, there has historically been significant disagreement as to which detector model is best able to cleanly remove the systematic noise present in phase curve observations, with each research group having their own preferred technique and software; with this paper, we made strides towards resolving this conflict. Finally, we sought to determine whether previously reported population-level trends are reproducible with a uniformly analyzed set of phase curve observations.

A COMPREHENSIVE REANALYSIS OF *SPITZER*'S 4.5 μm PHASE CURVES, AND THE PHASE VARIATIONS OF THE ULTRA-HOT JUPITERS MASCARA-1b AND KELT-16b

Taylor J. Bell,[1,*] Lisa Dang,[1,*] Nicolas B. Cowan,[1,2,*] Jacob Bean,[3] Jean-Michel Désert,[4] Jonathan J. Fortney,[5] Dylan Keating,[1,*] Eliza Kempton,[6] Laura Kreidberg,[7] Michael R. Line,[8] Megan Mansfield,[9] Vivien Parmentier,[10] Kevin B. Stevenson,[11] Mark Swain,[12] and Robert T. Zellem[12]

[1]*Department of Physics, McGill University, 3600 rue University, Montréal, QC H3A 2T8, Canada*
[2]*Department of Earth & Planetary Sciences, McGill University, 3450 rue University, Montréal, QC H3A 0E8, Canada*
[3]*Department of Astronomy & Astrophysics, University of Chicago, Chicago, IL 60637, USA*
[4]*Anton Pannekoek Institute for Astronomy, University of Amsterdam, 1090 GE Amsterdam, The Netherlands*
[5]*Other Worlds Laboratory, Department of Astronomy and Astrophysics, University of California, Santa Cruz, California 95064, USA*
[6]*Department of Astronomy, University of Maryland, College Park, MD 20742, USA*
[7]*Max-Planck-Institut für Astronomie, Königstuhl 17, 69117 Heidelberg, Germany*
[8]*School of Earth & Space Exploration, Arizona State University, Tempe AZ 85287, USA*
[9]*Department of Geophysical Sciences, University of Chicago, Chicago, IL 60637, USA*
[10]*Atmospheric, Ocean, and Planetary Physics, Clarendon Laboratory, Department of Physics, University of Oxford, Oxford OX1 3PU, UK*
[11]*Johns Hopkins University Applied Physics Laboratory, 11100 Johns Hopkins Rd, Laurel, MD 20723, USA*
[12]*Jet Propulsion Laboratory, California Institute of Technology, 4800 Oak Grove Drive, Pasadena, CA 91109, USA*

(Received 2020 October 1; Revised 2021 February 25; Accepted 2021 March 23; Published 2021 April 15)

Submitted to MNRAS

ABSTRACT

We have developed an open-source pipeline for the analysis of *Spitzer*/IRAC channel 1 and 2 time-series photometry, incorporating some of the most popular decorrelation methods. We applied this pipeline to new phase curve observations of ultra-hot Jupiters MASCARA-1b and KELT-16b, and we performed the first comprehensive reanalysis of 15 phase curves. We find that MASCARA-1b

Corresponding author: Taylor J. Bell
taylor.bell@mail.mcgill.ca

and KELT-16b have phase offsets of 6^{+11}_{-11} °W and 38^{+16}_{-15} °W, dayside temperatures of 2952^{+100}_{-97} K and 3070^{+160}_{-150} K, and nightside temperatures of 1300^{+340}_{-340} K and 1900^{+430}_{-440} K, respectively. We confirm a strong correlation between dayside and irradiation temperatures with a shallower dependency for nightside temperature. We also find evidence that the normalized phase curve amplitude (peak-to-trough divided by eclipse depth) is correlated with stellar effective temperature. In addition, while our different models often retrieve similar parameters, significant differences occasionally arise between them, as well as between our preferred model and the literature values. Nevertheless, our preferred models are consistent with published phase offsets to within -8 ± 21 degrees (-1.6 ± 3.2 sigma), and normalized phase curve amplitudes are on average reproduced to within -0.01 ± 0.24 (-0.1 ± 1.6 sigma). Finally, we find that BLISS performs best in most cases, but not all; we therefore recommend future analyses consider numerous detector models to ensure an optimal fit and to assess model dependencies.

Keywords: planets and satellites: individual (MASCARA-1b) – planets and satellites: individual (KELT-16b) – techniques: photometric

* McGill Space Institute; Institute for Research on Exoplanets;
Centre for Research in Astrophysics of Quebec

1. INTRODUCTION

The thermal phase curve observations collected by *Spitzer* have been one of its greatest scientific legacies. *Spitzer* demonstrated that we can detect the variations in disk-integrated flux from an exoplanet as a function of orbital phase (e.g., Harrington et al. 2006; Deming & Knutson 2020), allowing us to probe atmospheric dynamics and heat transport (e.g., Parmentier & Crossfield 2018). The success of phase curve observations from *Spitzer* and *Hubble* has ushered in the era of comparative atmospheric dynamics (e.g., Zhang et al. 2018; Keating et al. 2019; Beatty et al. 2019), which *JWST* and *ARIEL* will carry on in the 2020s and beyond.

However, reaching the level of precision required to make phase curve observations with *Spitzer* has been challenging, as strong intra-pixel sensitivity variations in *Spitzer*'s Infrared Array Camera (IRAC) channels 1 and 2 can be an order of magnitude larger than the astrophysical signals (e.g., Charbonneau et al. 2005). Many methods have been developed to model out these detector systematics, each with strengths and weaknesses, and most research groups have their own preferred method and code. Some of these codes are open source, but those who want to compare different decorrelation techniques are stuck learning (or building) new packages.

Here we present `SPCA`[1]: the *Spitzer* Phase Curve Analysis pipeline, developed by Lisa Dang and Taylor Bell. `SPCA` seeks to reduce the cost of entry for all while providing flexibility and effectiveness. `SPCA`'s routines have been developed for *Spitzer*/IRAC channel 1 and channel 2 (3.6 μm and 4.5 μm, respectively) time-resolved photometry; these channels were used for the vast majority of *Spitzer* phase curves and share similar detector noise characteristics. `SPCA` has implementations of 2D polynomial (Charbonneau et al. 2008), Pixel Level Decorrelation (PLD; Deming et al. 2015), BiLinearly-Interpolated Sub-pixel Sensitivity mapping (BLISS mapping; Stevenson et al. 2012), and Gaussian Process (GP; Gibson et al. 2012; Evans et al. 2015) decorrelation methods, allowing the user to change between techniques by setting a single variable. The modular structure of the code also allows the user to integrate custom astrophysical models and decorrelation methods. Built with

[1] Details about how to use and install `SPCA` can be found at `https://spca.readthedocs.io`

automation in mind, `SPCA` can reduce and decorrelate multiple data sets with a single command. Earlier versions of `SPCA` were described in Dang et al. (2018) and Bell et al. (2019), but the pipeline has undergone significant development in the intervening years.

Our goal is to implement a collection of some of the most common decorrelation methods within a single framework so that it becomes feasible for anyone to perform uniform and repeatable reanalyses of phase curves with each of these decorrelation techniques. This allows for comparisons between detector model performances and results on phase curve observations with different observing techniques, exposure times, stellar fluxes, etc., while previous comparisons were restricted either to just the secondary eclipses of XO-3b (Ingalls et al. 2016) or individual phase curves (e.g., Wong et al. 2015; Dang et al. 2018; Bell et al. 2019; Keating et al. 2020). The automation within `SPCA` also makes it possible for us to test the reproducibility of literature phase curve values for most exoplanets, something that has only been done on an individual basis so far (e.g., Knutson et al. 2009, 2012; Mendonça et al. 2018; Morello et al. 2019; Bell et al. 2019; May & Stevenson 2020).

In Section 2, we introduce the data sets that we will analyze, and in Section 3 we present `SPCA`'s photometry techniques. In Section 4 we detail `SPCA`'s decorrelation methods and analysis techniques. In Section 5, we validate our models against the collection of 10 XO-3b eclipses first published by Wong et al. (2014) and later used in the IRAC Data Challenge 2015 and described in Ingalls et al. (2016). In Section 6 we present the results for our new phase curves of KELT-16b and MASCARA-1b (Talens et al. 2017; Oberst et al. 2017), as well as our reanalyses of most previously published phase curves, and in subsection 6.3 we compare our results to the literature values. Finally, Section 7 presents our discussion and conclusions.

2. OBSERVATIONS

As part of the final *Spitzer* phase curve study that was conducted in Cycle 14 (PID 14059; PI Bean), we collected new *Spitzer*/IRAC 4.5 μm phase curve for a total of 10 planets with a range of temperatures and orbital periods. Mansfield et al. (2020) previously published the phase curve of KELT-9b from this program, and we present here the phase curves of ultra-hot Jupiters KELT-16b and MASCARA-1b. This pair of planets were selected to permit comparative studies of their atmospheric dynamics since they share similar radii, masses, and irradiation temperatures ($T_0 = T_{*,\rm eff}\sqrt{R_*/a}$, where $T_{*,\rm eff}$ is the stellar effective temperature, R_* is the stellar radius, and a is the planet's orbital semi-major axis). Meanwhile, the two planets have orbital periods that differ by a factor of two and stellar effective temperatures differing by 1300 K. This pairing can, therefore, provide insight into the impacts of Coriolis forces and stellar spectra on the energy budgets of hot Jupiters.

We also present our reanalyses of nearly all previously published 4.5 μm phase curves: specifically those of CoRoT-2b (Dang et al. 2018, PID 11073); HAT-P-7b (Wong et al. 2016, PID 60021); HD 189733b (Knutson et al. 2012, PID 60021); HD 209458b (Zellem et al. 2014, PID 60021); KELT-1b (Beatty et al. 2019, PID 11095); KELT-9b (Mansfield et al. 2020, PID 14059); Qatar-1b (Keating et al. 2020, PID 13038); WASP-12b (Cowan et al. 2012, PID 70060; Bell et al. 2019, PID 90186); WASP-14b (Wong et al. 2015, PID 80073); WASP-18b (Maxted et al. 2013, PID 60185); WASP-19b (Wong et al. 2016, PID 80073); WASP-33b (Zhang et al. 2018, PID 80073); WASP-43b (Stevenson et al. 2017, PID 11001); and WASP-103b (Kreidberg et al. 2018, PID 11099). We exclude the phase curve of HD 149026b (Zhang et al. 2018, PID 60021) as our initial attempts to fit these observations showed that they were especially challenging to fit and would hinder our attempts at a uniform treatment of each phase curve. We also exclude the observations of 55 Cnc e (Demory et al. 2016, PID 90208) due to the very different nature of that system and the enormous size of that dataset. Finally, we do not consider any phase curves that were not already published when we started this work.

All data sets we consider, except that of WASP-103b, used the subarray mode which produces datacubes of 64 frames, each 32 $\times$ 32 pixels (39 arcsec $\times$ 39 arcsec) in size. Meanwhile, the data set for WASP-103b was taken in full-frame mode, which gives individual frames that are 256 $\times$ 256 pixels (312 arcsec $\times$ 312 arcsec) in size. All data sets we consider were continuous, full-orbit phase curves, and all data sets start and end with a secondary eclipse (with the exception of WASP-18b which started mid-transit and ended shortly after a second transit). Information about the exposure times and other observing parameters of each previously published data set can be found in their respective papers referenced above. For both KELT-16b and MASCARA-1b we used a 2 s exposure time which resulted in 835 datacubes (53 440 frames) and 1664 datacubes (106 496 frames), respectively.

3. PHOTOMETRY AND DATA REDUCTION

`SPCA` starts by unzipping the zip files for each phase curve downloaded from the *Spitzer* Heritage Archive[2], and then loads all of the files for one phase curve into RAM. For the subarray data sets, we perform an initial 4σ clipping and masking of each pixel along the time axis for each datacube to remove any artifacts like cosmic ray hits. Any frames where a masked pixel lies within the 5×5 pixel grid centered on the target star are masked entirely. For the full-frame photometry data set (WASP-103b), we extract just the 32×32 pixel stamp used in subarray mode: indices (9:40, 217:248). While `SPCA` allows oversampling frames using bi-linear interpolation as is sometimes used in the literature (e.g., Stevenson et al. 2017), we do not use the functionality in this work.

For the subarray data, we identify any subframes in which the aperture flux deviates by more than 4σ from the median of the datacube after having performed a median average along the entire time axis. We then tried our photometry routines with and without these consistently bad frames and ultimately choose the photometry with the lowest scatter after being smoothed with a high-pass filter to remove any astrophysical signals. Our high-pass filter had a width of 5×64 data points (5 data cubes) for sub-array data or 64 data points for full-frame data. These timescales were selected to be shorter than the ingress/egress timescale which was greater than 5×64 frames for all sub-array data and greater than 64 frames for WASP-103b.

In order to compute photon noise limits, we convert all our data sets to electron counts using $\mathrm{Image} \times \mathrm{gain} \times \tau_{\mathrm{exp}}/\mathrm{FLUXCONV}$. This is an approximation of the photon limit, the full calculation of which is laid out in Section 3.3 of Ingalls et al. (2016). We then 5σ clip and mask each pixel along the entire time axis to remove any remaining artifacts. Any frames where a masked pixel lies within the 5×5 pixel grid centered on the target star are masked entirely. Finally, we subtract the background computed for each frame using the median of the frame's pixels, excluding a box

[2] `https://sha.ipac.caltech.edu/applications/Spitzer/SHA/`

(indices (11:19, 11:19)) around the target star. `SPCA` then performs its various photometry techniques, described in detail below. We then bin all of the sub-array mode data sets by datacube (64 frames) to reduce the computational cost of fitting the data with our many different decorrelation models, but we also save the unbinned data which we later use to test our decorrelation models. For the WASP-103b observations taken in full-frame mode, we chose not to temporally bin the data since the integration time was already much longer than the sub-array mode (12 s compared to 0.1–2 s).

3.1. *Aperture Photometry*

`SPCA`'s aperture photometry routine uses a flux-weighted mean (FWM) centroiding algorithm on the central 5×5 pixels:

$$\mathrm{x_{cent}} = \frac{\sum_{i=0}^{5}\sum_{j=0}^{5} i\ \mathbf{I}_{i,j}}{\sum_{i=0}^{5}\sum_{j=0}^{5}\mathbf{I}_{i,j}},$$

where x_{cent} is the x-centroid in the 2D image, $\mathbf{I}$, and i and j are the x and y indices of each pixel. The similar equation for the y-centroid simply multiplies $\mathbf{I}$ by j instead of i. The point spread function (PSF) width along each axis is also approximated using

$$\sigma_{\mathrm{x}} = \frac{\sum_{i=0}^{5}\sum_{j=0}^{5} i^2\ \mathbf{I}_{i,j}}{\sum_{i=0}^{5}\sum_{j=0}^{5}\mathbf{I}_{i,j}},$$

where the equation for the PSF-width along the y-axis replaces i^2 with j^2.

Centroid and PSF widths are then put through a cleaning algorithm where the data are first 10σ clipped. Any clipped data are then replaced by the median of the two preceding and two following data points. Subsequently, a copy of the data is smoothed using a high-pass filter with a width of 5×64 data points for sub-array data or 64 data points for full-frame data, any 5σ outliers are identified, and the original data point is replaced by the median of the two preceding and two following data points. This data cleaning algorithm was inspired by that of Zellem et al. (2014).

`SPCA` makes accessible any `astropy` aperture, but little support is provided for non-circular apertures. For each of our data sets, we considered circular apertures with radii from 2.0 to 6.0 pixels in steps of 0.2 pixels, each of which was attempted with two types of aperture edges (hard, where a pixel is only included if its centre lies with the aperture, or exact, where a pixel is weighted by the fraction of the pixel which lies within the aperture). `SPCA` allows the aperture to either remain at a fixed location on the detector or to follow the centroid position, but initial tests suggested that having the aperture track the centroid gave cleaner photometry. The fluxes from all of these apertures were then subjected to the same cleaning algorithm as the centroid positions. Finally, `SPCA` chooses an aperture photometry technique by smoothing a copy of the fluxes with a high-pass filter with a width of 5×64 data points for sub-array data or 64 data points for full-frame data to remove transit, eclipse, and phase variation signals, and then selects the photometry with the lowest scatter under the premise that the data with the lowest high frequency noise will be the easiest to model cleanly (see Figure 1). While this method is not guaranteed to give the cleanest possible photometry, it is more computationally efficient than trying all of our numerous detector models on each of the different photometry outputs. Moreover, previous comparisons (Bell et al. 2019; Keating et al. 2020) have found that `SPCA`'s photometry routine gives qualitatively similar photometry to that from the Photometry for Orbits, Eclipses, and Transits (`POET`) pipeline (Stevenson et al. 2012; Cubillos et al. 2013). `SPCA`'s algorithm also offers a potential improvement over the `POET` pipeline as we do not choose the photometry that best fits an assumed astrophysical model which could potentially bias the resulting phase curve parameters.

3.2. *PSF Photometry*

Our PSF photometry is initialized using the centroid and PSF-width algorithms described above, and then a 2D Gaussian is fitted to a 5×5 stamp centered at the pixel position (15,15) of each frame. The flux, centroid, and PSF width values are then cleaned using the same algorithm described above. As our PSF fitting fluxes are far noisier than the aperture fluxes, we only try using the centroids from this method to decorrelate the aperture photometry fluxes.

3.3. *PLD Photometry*

Our PLD photometry routine takes either a 3×3 or 5×5 stamp centered at the pixel position (15,15). Each pixel's lightcurve then undergoes the same cleaning routine described above. Additionally, we compute a total flux by summing the stamps and renormalize the sum of bad stamps using the same cleaning routine. When fitting observations with PLD, we ultimately use our aperture

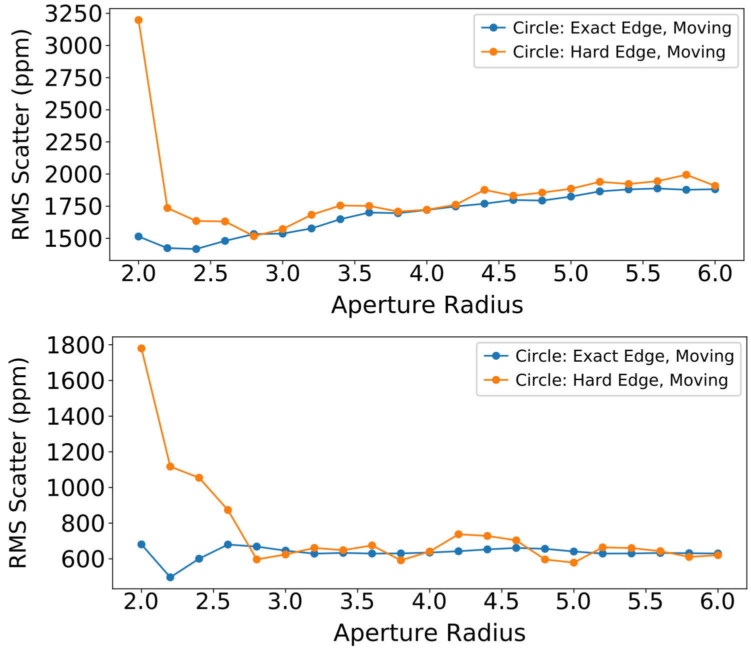

Figure 1. Comparison of the photometric root mean squared (RMS) after smoothing with a high-pass filter for the many apertures considered for KELT-16b (top) and MASCARA-1b (bottom). The aperture radius and edge combination that gives the lowest RMS after smoothing is considered to be our optimal aperture.

photometry as our flux measurement since it is much cleaner than the sum of the pixel stamps and then just use the individual pixel lightcurves as our covariates.

4. ANALYSES

`SPCA` models the photometry as a multiplicative combination of an astrophysical model and one or more detector models, each of which are described below. Except for the eclipse depth and phase curve coefficients, all astrophysical parameters are initialized to their best constrained values found on the NASA Exoplanet Archive[3]. We set the initial eclipse depth to 3000 ppm which is typical of most of our phase curves. Finally, we set the initial phase curve semi-amplitude to 35% of the eclipse depth and the phase offset to 0°.

We chose to place a Gaussian prior on the linear ephemeris, t_0, the orbital period, P, the ratio of the semi-major axis to the stellar radius, a/R_*, and the orbital inclination, i, constraining them

[3] `https://exoplanetarchive.ipac.caltech.edu/`

to the most precise values in the literature as these parameters are generally better constrained by the repeated transit observations used to discover these planets. We also constrain the orbital inclination, i, to be below 90°. We place simple uniform priors constraining the planet-to-star radius ratio, R_p/R_*, the planet-to-star flux ratio, F_p/F_*, and the white noise amplitude normalized by the stellar flux, σ_F, to between 0 and 1 to ensure physicality.

After initializing our models, we begin with an initial stage of model optimization based on the method described by Evans et al. (2015). For all detector models except BLISS, we start by freezing the astrophysical parameters and perform an initial round of maximum likelihood estimation (MLE) on the detector models using `scipy.optimize.minimize`'s Nelder-Mead routine (Nelder & Mead 1965) to ensure that our detector parameters begin in a reasonable location. We then run 10 rounds of optimization on all parameters, randomly drawing the starting position of all parameters within their uncertainty range or 10% of the value where no uncertainty is known. We randomly draw starting phase curve semi-amplitudes between 0.2 and 0.5 and phase curve offsets between 10°W and 30°E. We then run 10 short Markov Chain Monte-Carlo (MCMC) chains containing 25 500 samples using the `emcee.Ensemble_Sampler` (Foreman-Mackey et al. 2013) initialized about the end points of the optimization runs to ensure that we are able to break free from any local minima; this proved to be very important and time-saving for our few model fits with the GP model. We then run 10 final rounds of optimization on all parameters, starting at the highest log-likelihood sample from each of the MCMC chains. The highest log-likelihood location found during this entire optimization routine is then used as the starting position for our MCMC marginalizations.

We start our MCMC with a dense, Gaussian ball about our maximum log-likelihood estimate, with a standard deviation of 0.01% the parameter's value except for those parameters on which we have placed a Gaussian prior where we use the published uncertainty. We then run a 5000 step burn-in chain using `emcee.Ensemble_Sampler` (Foreman-Mackey et al. 2013) with 150 walkers. Visual inspection of the tracks and distribution of MCMC walkers throughout this burn-in phase suggest that we had achieved convergence by the end of these chains. We then continue with a 1000 step production run with 150 walkers, providing us with a total of 150 000 samples of the posterior. We use the maximum log-likelihood position from this chain as our fitted value, and use the 16th and 84th percentiles to compute our parameter uncertainties.

We name each of our model runs using a "mode string" to indicate the model choices that were made for that run. The mode string starts with a string describing the detector model used, followed by a description of the phase curve model, and potentially followed by "_PSFX" when the PSF centroiding method used (when absent, FWM centroiding was used).

4.1. *Astrophysical Models*

`SPCA`'s astrophysical model consists of a constant flux from the host star (except during transits), transit and eclipse signals modelled using `batman` (Kreidberg 2015), and either a first order (single-peaked) or second order (double-peaked) sinusoidal phase variation. This can be written as

$$A(t) = F_*(t) + F_{\rm day}\Phi\big(\psi(t)\big),$$

where F_* is the stellar flux, $F_{\rm day}$ is the planetary flux at a phase of 0.5, and Φ is our phase variation model which is a function of the orbital phase with respect to eclipse, $\psi(t) = 2\pi(t - t_e)/P$, where t_e is the time of eclipse and P is the planet's orbital period. Our transit model assumes a reparameterized quadratic limb-darkening model (with parameters q_1 and q_2) to ensure efficient sampling and easy imposition of a physicality prior of $0 < \{ {}^{q_1,}_{q_2} \} < 1$, following Kipping (2013). We also fit for eccentricity using the parameters $e\cos\omega$ and $e\sin\omega$ to allow for efficient sampling and a simple prior of $-1 < \{ {}^{e\cos\omega,}_{e\sin\omega} \} < 1$ (e.g., Butler et al. 2006).

Our first order sinusoidal phase variation model is implemented as

$$\Phi_1(\psi) = 1 + C_1\Bigg(\cos(\psi) - 1\Bigg) + D_1\sin(\psi),$$

and our second order phase variation model (permitting steeper day-night temperature transitions or ellipsoidal variations) is implemented as

$$\Phi_2(\psi) = \Phi_1(\psi) + C_2\Bigg(\cos(2\psi) - 1\Bigg) + D_2\sin(2\psi),$$

where C_1, C_2, D_1, D_2 are fitted parameters. We add an appendix of "_v1" to our mode string for first order phase variation models and "_v2" for second order models. For our first order models, we compute the phase curve semi-amplitude using $\sqrt{C_1^2 + D_1^2}$ and compute the phase offset in degrees east using $-\arctan2(D_1, C_1)$. For our second order models, we numerically compute the phase curve semi-amplitude and phase offset. When fitting, we require that the first order phase offset lie between -90° and 90°. To ensure that our light curves remain physical, we also require that $\Phi\big(\psi(t)\big)$ be greater than zero for all phases; we do not require the physicality of an inferred temperature map.

DILUTION CORRECTION

Three of the systems that we consider in this work (CoRoT-2b, WASP-12b, and WASP-103b) are host to a nearby star which acts to dilute the amplitude of the transit depth, eclipse depth, phase curve amplitude, and σ_F. CoRoT-2B, the stellar companion to the planet hosting star CoRoT-2A, is a K9 star with an effective temperature of 4000 K (Schröter et al. 2011) which is separated by 4.087$''$ at a position angle of 208.5° (Gaia Collaboration 2018). WASP-103B is a K5V star with $T_{\rm eff} = 4400$ K located 0.240$''$ away at a position angle of 208.5° (Cartier et al. 2017). Finally, WASP-12A has two nearby M-dwarfs, WASP-12B,C, that are 1.06$''$ away at a position angle of 249.05° (Bergfors et al. 2011; Crossfield et al. 2012; Bechter et al. 2014) which have an effective temperature of 3660 K (Stevenson et al. 2014a).

We correct for the dilution from these nearby companions following a procedure similar to that described by Stevenson et al. (2014a) and Bell et al. (2019). We start by making 10× oversampled simulated observations of the companion stars using the `STINYTIM`[4] point response function modelling software for *Spitzer*. We place the companion stars at the center of the subarray (24,232), and use the companion stars' blackbody temperatures described above. We use apertures that match the radius, β, of the selected aperture photometry for the three phase curves, and we place the apertures at the location where the host star would be to compute the fraction of the star's flux that falls within our aperture, $g(\beta)$. To compute the companion-to-host stellar flux ratio, $\alpha_{\rm comp}(\lambda)$, we integrate matching PHOENIX stellar models over the IRAC channel 2 bandpass using a uniform weighting. For CoRoT-

[4] `http://irsa.ipac.caltech.edu/data/SPITZER/docs/dataanalysistools/tools/contributed/general/stinytim/`

2B, we assume $R_* = 0.65 R_\odot$, $\log g = 4.28$, and $[Fe/H] = -0.17$ which are the parameters of of the star HD 113538 of the same spectral type (Moutou et al. 2011). For the M-dwarf companions WASP-12B,C, we assume both stars have radii of $R_* = 0.65 R_\odot$ (Stevenson et al. 2014c) and median M-dwarf values of $\log g = 5.0$ and $[Fe/H] = 0$ (Rajpurohit et al. 2018). For WASP-103B, we assume the star has the same parameters as 61 Cygni A which has the same spectral type: $R_* = 0.665 R_\odot$, $\log g = 4.40$, and $[Fe/H] = -0.20$ (Kervella et al. 2008). The dilution correction parameters are summarized in Table 1. Our computed dilution parameters are generally consistent with those used by Stevenson et al. (2014a), Bell et al. (2019), and Garhart et al. (2020) for WASP-12b and Garhart et al. (2020) for WASP-103b, with only minor differences likely caused by different photometric aperture sizes.

We then correct the planet's radius using

$$\left(\frac{R_\mathrm{p}}{R_*}(\lambda)\right)_\mathrm{corr} = \sqrt{C_\mathrm{corr}(\beta, \lambda)} \left(\frac{R_\mathrm{p}}{R_*}(\lambda)\right)_\mathrm{meas},$$

and the dayside flux was corrected using

$$\left(\frac{F_\mathrm{p}}{F_*}(\lambda)\right)_\mathrm{corr} = C_\mathrm{corr}(\beta, \lambda) \left(\frac{F_\mathrm{p}}{F_*}(\lambda)\right)_\mathrm{meas},$$

with the white noise amplitude, σ_F, corrected similarly to the dayside flux. The correction factor is computed using

$$C_\mathrm{corr}(\beta, \lambda) = 1 + g(\beta)\alpha_\mathrm{comp}(\lambda).$$

4.2. *Detector Models*

`SPCA` currently has four of the most common decorrelation models used on *Spitzer* IRAC 3.6 μm and 4.5 μm phase curves: 2D polynomials, BLISS mapping, a GP, and PLD. Each of these models and the decisions we made while implementing them are described in more detail below. While we have mostly followed the procedures laid out in the literature, we did make some judgement calls of our own where information was missing or unclear; as a result, the performance of our detector models may slightly differ from that of other pipelines.

System	β[a]	g[b]	$\alpha_{\rm comp}$[c]	$C_{\rm corr}$[d]
CoRoT-2	3.6	0.5921	0.3455	1.2046
WASP-12 (2010)	2.2	0.7827	0.1161	1.09085
WASP-12 (2013)	3.2	0.8593	0.1161	1.09976
WASP-103	2.6	0.8456	0.1460	1.1234

Table 1. Companion dilution correction parameters.

[a]Aperture radius.

[b]Fraction of companion's flux that falls within our aperture.

[c]The companion-to-host stellar flux ratio.

[d]The applied dilution correction factor.

It is possible to multiply our 2D polynomial, BLISS, and GP model with a simple linear model that depends on the PSF width. One can also add a linear slope in time to any detector model to capture long timescale stellar variability. There is also the possibility to add step functions at any of the Astronomical Observation Request (AOR) breaks where the telescope is re-pointed. Ultimately we decided not to consider the PSF width or any explicit function of time in this work to reduce the already very high computational cost of fitting all 17 phase curves with two different centroiding options each (FWM and PSF fitted), two different phase curve models, and 9–10 detector models, giving a total of 488 fits that take upwards of 20 wall-clock minutes each while using 12 parallel CPU threads. For a detailed look into the effects of PSF width and shape on *Spitzer*/IRAC photometry and potential methods to decorrelate them, see Challener et al. (2021) which was published after this work was submitted for review.

4.2.1. *2D Polynomials*

The 2D polynomials are parametric models which use the centroid positions as its covariates and was first used for *Spitzer*/IRAC data by Charbonneau et al. (2008). `SPCA` permits second- to fifth-order polynomial models, including all cross terms, and we try all four variants for all of our considered data sets. These models will be called "Poly#" in the mode string where # is the order of the polynomial model.

4.2.2. *Pixel Level Decorrelation*

PLD is a parametric model which uses normalized lightcurves for each individual pixel as its covariates and is described in detail by Deming et al. (2015). While `SPCA` can use the sum of the PLD stamps as the raw flux which is decorrelated, we found that the flux from aperture photometry was less noisy to begin with and produced cleaner phase curves after decorrelation. `SPCA` has two different option pairs that can be selected which gives a total of four variants. One can choose either first order PLD where the individual pixel light curves are the covariates, or one can use second order PLD (Zhang et al. 2018) which also includes the square of each pixel light curve. Following Zhang et al. (2018), we do not include any cross-terms in our second order PLD model. Deming et al. (2015) found that first order PLD performed best on eclipse observations when the centroid variation was less than 0.2 pixels. While second order PLD should help extend the applicability of PLD to larger centroid drifts, this has not been quantified. The other option is to use 3×3 or 5×5 pixel stamps to allow for a trade-off between capturing more stellar flux and capturing more background flux. For easier initialization of our detector models while fitting the data, we also put our pixel light curves (and their squared values where relevant) through a PCA algorithm and add a constant offset term. These models will be called "PLD#_NxN" in the mode string where # is the order of the PLD model, and NxN is the size of the pixel stamps.

4.2.3. *BLISS Mapping*

BLISS mapping is a non-parametric model that uses the centroid positions as its covariates and is described in detail by Stevenson et al. (2012). There is, however, a hyperparameter: the number of "knots" (x,y grid cells) used by the BLISS algorithm, which can be challenging to choose properly. With too few knots, the model becomes overly simple and results in discrepant retrieved astrophysical parameters, while too many knots can begin to over-fit the data, and in the limit you would have a knot for every single data point (Stevenson et al. 2012). We developed a routine similar to that described in Stevenson et al. (2012), where we compare the performance of a nearest-neighbour interpolation (NNI) algorithm against the BLISS algorithm. We first fix the number of knots to an

8×8 square grid and perform our ten `scipy.optimize.minimize` fits to optimize the astrophysical parameters. We then consider several different knot spacings in the range of 0.01–0.06 pixels per knot (with the same scale in x and y), based on the findings of Stevenson et al. (2012) for the secondary eclipse observations of HD 149026b. We run a single optimization routine with each of these knot spacings, and then pick the least dense spacing where the fitted σ_F with the BLISS algorithm is lower than that for NNI. However, for some data sets we find that BLISS outperforms NNI for all considered grid spacings, in which case we pick the most dense grid spacing that results in fewer than 50 utilized knots (limiting the model to be no more complex than our Poly5 models); in cases where there is a large spread in centroid position, the least dense BLISS model may still have more than 50 utilized knots, in which case we just select the least dense grid spacing. We then continue with the rest of our initial optimization routine (short MCMC runs and another round of MLE fits). These models will simply be called "BLISS" in the mode string.

4.2.4. *Gaussian Processes*

The GP model we use is a non-parametric model that uses the centroid positions as its covariates and is based on Gibson et al. (2012) and Evans et al. (2015). We used the python package `george` (Foreman-Mackey 2015) with the `BasicSolver` to implement the GP. We use a squared-exponential kernel with additive white noise in the form

$$\Sigma_{nm} = C^2 \exp\left(- \frac{(x_n - x_m)^2}{L_x^2} - \frac{(y_n - y_m)^2}{L_y^2} \right) + \delta_{nm}\sigma_F^2,$$

where (x_n,y_n) is the centroid position of the nth datum (and similarly for the mth datum), C is used to compute the covariance amplitude, L_x and L_y are the covariance lengthscales in the x and y directions, δ_{nm} is the Kronecker delta, and σ_F^2 is the aforementioned white noise amplitude normalized by the stellar flux. The choice of a squared-exponential kernel stems from the assumption that the detector sensitivity is a smooth function of the centroid position. This is similar in many ways to the Gaussian kernel regression methods used by Ballard et al. (2010), Knutson et al. (2012), and Lewis et al. (2013), but a GP is a more statistically robust, albeit computationally intensive, method. We chose not to include an additional Matérn $\nu = 3/2$ kernel as a function of time as was included by Evans et al. (2015).

We follow Evans et al. (2015) by placing a uniform prior on the natural logarithm of the GP lengthscales to ensure that the GP does not over-fit the data and is fitting for intra-pixel sensitivity variations rather than larger lengthscales; we chose limits of -3 and 0 as Evans et al. (2015) did not publish their limits. We also follow Evans et al. (2015) in placing a Gamma prior on C of the form $p(C) = \mathrm{Gam}(1, 100)$. During our initial 10 burn-ins, we randomly drew values of $\sqrt{C}$, $\ln L_x$, and $\ln L_y$ in the ranges (0.05,0.135), (-0.5,-1), and (-0.5,-1), respectively. As the GP model is exceptionally computationally expensive, we chose to reduce the number of burn-in steps in our MCMC runs to 1000; we confirmed that the MCMC had converged after this number of steps by visually examining the trace of the walkers afterwards. Even still, this required ∼100 CPU hours for each of the fits to MASCARA-1b's phase curve and ∼25 CPU hours for each the fits to KELT-16b's. As a result of this extremely high computational cost, we attempted to perform GP analyses on only HAT-P-7b from the previously published phase curves as our results for its phase curve appeared to be very strongly model dependent. These models will simply be called "GP" in the mode string.

5. VALIDATION AGAINST XO-3b ECLIPSES

To test our photometry and decorrelation techniques, we first considered the 10 secondary eclipses of the eccentric planet XO-3b collected using IRAC channel 2 (PID 90032) which were first published by Wong et al. (2014) and later extensively studied with many standard decorrelation techniques by Ingalls et al. (2016). We performed photometry on these data following the exact same methods as for the phase curve data, and treated each eclipse observation entirely independently. When fitting the data sets with our model suite, we chose to impose the following Gaussian priors in addition to all of the priors imposed on the phase curve data since these parameters were fairly poorly constrained by eclipse-only observations: $R_p = 0.08825 \pm 0.00037$, $e \cos \omega = 0.2700 \pm 0.0024$, and $e \sin \omega = -0.0613 \pm 0.0078$ (Wong et al. 2014). We still fit for the phase variations to ensure that our models remain unbiased due to the downward curvature of the phase curve near eclipse, but these parameters are primarily constrained by our physicality priors. We also only considered a first order sinusoidal phase curve model since the phase variations were poorly constrained by the out-of-eclipse baseline.

The retrieved eclipse depths for each of the 10 eclipses analyzed with all of our 16 detector models are plotted in Figure 2. While there is slight variance between models and between the median model for each eclipse, no clear or consistent bias is evident. This is summarized in Figure 3 which shows the mean and standard deviation of each models' fitted values for the 10 eclipses. Figure 3 also shows that, while there is a slight tendency to underestimate our uncertainty on the eclipse depth, the correction factor is close to unity which is consistent with the findings of Ingalls et al. (2016) and not 3 as had been suggested by Hansen et al. (2014) for early *Spitzer* eclipse observations. It is possible that this increased scatter between eclipse depths could be the result of astrophysical variations, but this would imply eclipse depth variability roughly twice as large as the maximum predicted level for hot Jupiters on circular orbits (53 ppm = 3.6% vs the $\leq$2% predicted by Komacek & Showman (2020); we note, however, that XO-3b is on a significantly eccentric orbit). Each of our models' average eclipse depth is consistent with the median eclipse depth from Ingalls et al. (2016), but our fitted uncertainties are all slightly larger than their median uncertainty. We also find no clear difference between decorrelating with PSF centroiding and FWM centroiding, but our aperture photometry was exclusively performed using FWM centroiding, so it is possible that aperture photometry performed using PSF centroiding would be better decorrelated with the PSF centroids.

We also computed the various statistics presented in Ingalls et al. (2016) to quantitatively assess the performance of each of our models (see Table 2). Specifically, we computed the error-weighted average eclipse depth, $\overline{D}$, the average eclipse depth uncertainty, $\overline{\sigma}$, the standard deviation in the eclipse depths from the 10 observations, SD, and the weighted uncertainty in the mean eclipse depth given the uncertainty from our MCMC, $\sigma_{\rm orig}$. The expected level of scatter between eclipse depths assuming only photon noise is $\sigma_{\rm phot} \approx 64$ ppm, so all decorrelation methods get within $\sim 3\times$ the photon limit (179 ppm). We then computed the "dispersion factor", $f_{\rm dis}$, that multiplies our uncertainties to account for the observed eclipse depth scatter between different eclipse observations, the total uncertainty in the average eclipse depth after inflating our error bars, $\sigma_{\rm TOT}$, the "repeatability" of

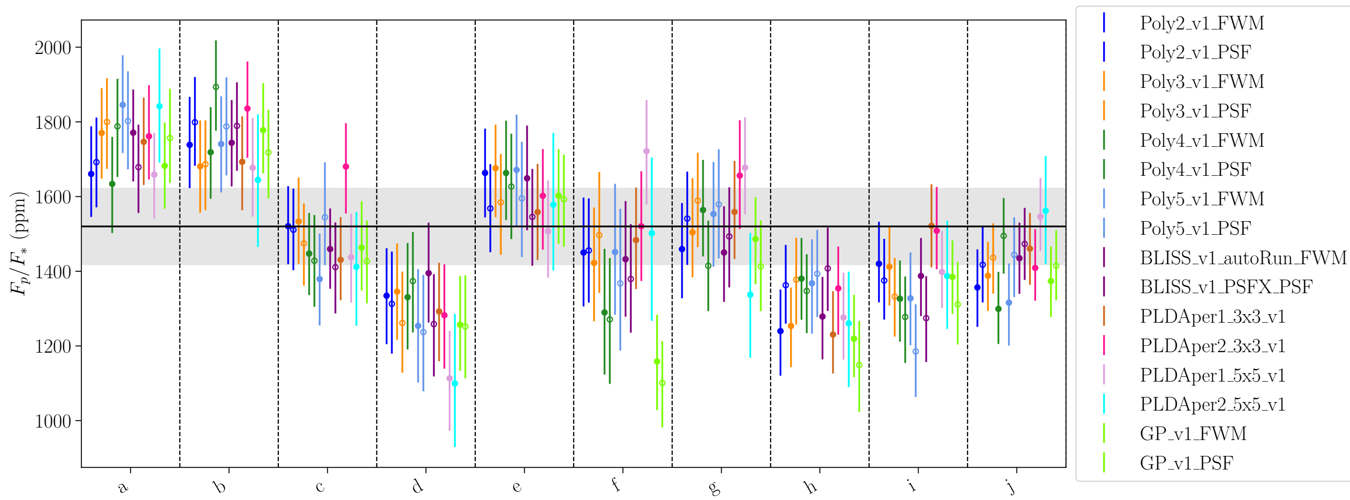

Figure 2. Eclipse depths for each of the 10 eclipse observations of XO-3b (named a–j), each independently analyzed with all of our detector models. The black line and shaded region show the median eclipse depth and median uncertainty on eclipse depth from Ingalls et al. (2016).

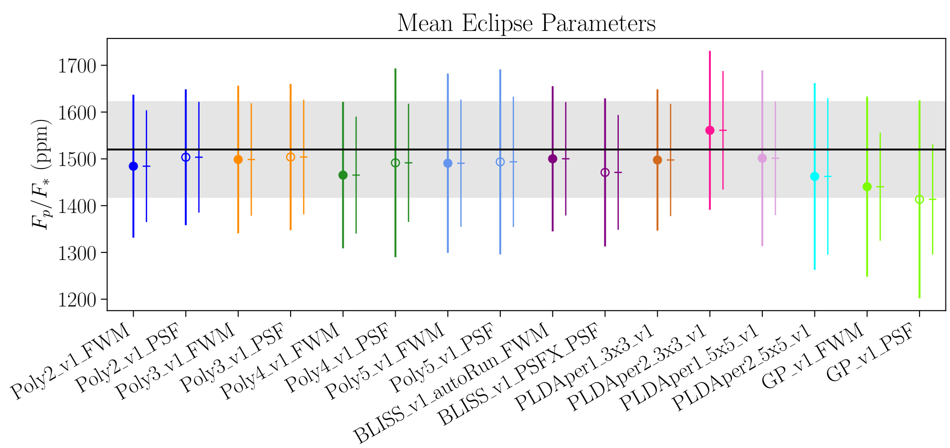

Figure 3. Mean and standard deviation of the 4.5 μm XO-3b eclipse depths fitted with each detector model are shown with solid points for FWM centroiding and hollow points for PSF centroiding. Meanwhile, there is another error bar with a horizontal line adjacent to each point which indicates the average uncertainty found from each independent eclipse fit. The black line and shaded region show the median eclipse depth and median uncertainty on eclipse depth from Ingalls et al. (2016). While there is a slight underestimation of the uncertainty on the eclipse depth with all models (the standard deviation in eclipse depths is larger that the reported uncertainty from individual eclipse observations), there is no clear bias in any of the models.

Mode	$\overline{D}$[a] (ppm)	$\overline{\sigma}$[b] (ppm)	SD[c] (ppm)	$\sigma_{\rm orig}$[d] (ppm)	$f_{\rm dis}$[e]	$\sigma_{\rm TOT}$[f] (ppm)	R[g] (ppm)	r[h]	a[i]
Poly2	1480	120	153	37	1.4	51	216	0.42	0.41
Poly2_PSFX	1500	118	145	37	1.3	48	205	0.44	0.44
Poly3	1485	120	158	37	1.4	53	223	0.41	0.40
Poly3_PSFX	1496	123	156	38	1.4	51	221	0.41	0.41
Poly4	1455	125	157	38	1.3	51	221	0.41	0.39
Poly4_PSFX	1490	126	202	39	1.7	65	285	0.32	0.31
Poly5	1483	136	192	42	1.5	65	271	0.33	0.33
Poly5_PSFX	1494	139	198	43	1.6	66	280	0.32	0.32
BLISS	1490	121	155	37	1.4	51	219	0.41	0.41
BLISS_PSFX	1476	123	158	38	1.4	52	224	0.40	0.39
PLDAper1_3x3	1492	120	151	37	1.3	50	213	0.42	0.42
PLDAper2_3x3	1549	127	170	39	1.4	56	240	0.38	0.37
PLDAper1_5x5	1496	122	188	38	1.5	58	266	0.34	0.34
PLDAper2_5x5	1465	168	200	52	1.3	67	282	0.32	0.31
GP	1435	116	193	36	1.7	61	272	0.33	0.31
GP_PSFX	1411	118	211	37	1.8	68	299	0.30	0.27
Average	1481	126	174	39	1.5	57	246	0.37	0.36

Table 2. XO-3b eclipse depth repeatability statistics following Ingalls et al. (2016). The expected level of scatter between eclipse depths assuming only photon noise is $\sigma_{\rm phot} \approx 64$ ppm.

[a]The error-weighted average eclipse depth.

[b]The average eclipse depth uncertainty.

[c]The standard deviation in the eclipse depths.

[d]The weighted uncertainty in the mean eclipse depth given the uncertainty from our MCMC.

[e]The "dispersion factor" that multiplies our uncertainties to account for the observed eclipse depth scatter between different eclipse observations.

[f]The total uncertainty in the average eclipse depth after inflating our error bars by $f_{\rm dis}$.

[g]The "repeatability" of our fits.

[h]The "reliability" of our fits.

[i]The "accuracy" of our fits with respect to the average eclipse depth from Ingalls et al. (2016).

our fits, R, the "reliability" of our fits, r. Finally, we compute the "accuracy", a, of our fits with respect to the average eclipse depth from Ingalls et al. (2016) which we consider to be the true eclipse depth. For the definitions of "repeatability", "reliability", and "accuracy" in the context of these model fits and their correlations, see Section 3.4 of Ingalls et al. (2016). Intriguingly, our lowest order polynomial models and our simplest PLD model rank the best in terms of repeatability, reliability, and accuracy, although there isn't a large spread in the performances of each of the 18 different detector models. It is unclear whether the performance of each of these models would extend equally well to longer duration phase curve observations which can either more densely sample the detector sensitivity if the telescope drifts slowly or is repointed, or can substantially drift across the detector resulting in larger pointing variations and a poorly sampled sensitivity map. However, Ingalls et al. (2016) suggest that BLISS is likely to perform best under situations with larger pointing variations.

Our model fits indicate that no one model consistently produces lower scatter in the residuals for the 64× binned data that we fitted. We also compare our fitted models to the unbinned data, adjusting only σ_F to give a $\chi^2/N_{\rm data}$ of 1. These values suggest that the lower order polynomial models and BLISS models outperform the higher order polynomial models and PLD models. For the higher order polynomial models, this may be indicative of the impact of centroiding uncertainty. For the PLD models, this may be the result of noisy pixel lightcurves that are better behaved in binned data (e.g. Deming et al. 2015; Zhang et al. 2018). Overall though, `SPCA`'s photometry and decorrelation techniques perform well on this validation test, and no one model clearly outperformed any others on the binned data; this is consistent with the findings of Ingalls et al. (2016), where BLISS, GP, and PLD models performed quite similarly (they did not consider polynomial models).

6. RESULTS

For each data set, we start by selecting the model with the lowest Bayesian Information Criterion (BIC), which we defined as:

$$\mathrm{BIC} = -2\ln(L) + N_{\rm par}\ln(N_{\rm dat}),$$

where $\ln(L)$ is the model log-likelihood, $N_{\rm par}$ is the number of fitted parameters, and $N_{\rm dat}$ is the number of fitted data. For our BLISS models, we consider $N_{\rm par}$ to be the number of BLISS knots which had one or more data points since Schwartz & Cowan (2017) showed that you can achieve the same results as BLISS by treating each knot as a fittable parameter in your MCMC. As is shown in Figure 6, for each phase curve there is always one model which vastly out-performs all other models; this model is typically BLISS. For that reason, we do not use averages or weighted averages from our different model fits.

6.1. *KELT-16b and MASCARA-1b*

For both of our newly observed and analyzed phase curves of KELT-16b and MASCARA-1b, the BLISS model with a first order sinusoidal phase curve and using FWM centroiding was the preferred mode; these fitted models are plotted in Figure 4. The fitted parameters for all considered models are available as `numpy` zip files in the Supplementary Data, and parameters of interest for the preferred phase curves are presented in Table 4. We also find updated orbital parameters for KELT-16b and MASCARA-1b using the orbital parameters of Talens et al. (2017) and Oberst et al. (2017) as Gaussian priors, respectively; our updated parameters are summarized in Table 3.

MASCARA-1b has strong systematics shortly after the first eclipse at a phase of ∼0.65 (BMJD = 58546.5) which do not show any clear correlation with sudden or unusual changes in centroid position or PSF width. This systematic noise is poorly handled by many of the detector models which results in strongly correlated residuals and wildly discrepant astrophysical parameters. Our BLISS and GP models, however, perform far better for this data set and are consistent with each other, with the BLISS model giving lower scatter in the model residuals. We also find that the results from our preferred BLISS model are robust to removing the affected data points from our fit. Meanwhile, the

Planet	t_0 (BJD)	P (days)	$e\cos\omega$	$e\sin\omega$	a/R_*	i (degrees)
KELT-16b	$2457247.24795^{+0.00018}_{-0.00019}$	$0.96899225^{+0.00000047}_{-0.00000046}$	$0.0016^{+0.0016}_{-0.0015}$	$0.013^{+0.015}_{-0.016}$	$3.171^{+0.082}_{-0.093}$	$83.5^{+1.8}_{-1.6}$
MASCARA-1b	$2457097.2782^{+0.0018}_{-0.0020}$	$2.1487760^{+0.0000029}_{-0.0000027}$	$0.00041^{+0.00052}_{-0.00055}$	$-0.0070^{+0.0059}_{-0.0050}$	$4.08^{+0.12}_{-0.15}$	$85.7^{+1.9}_{-1.7}$

Table 3. Updated orbital parameters from the new phase curves of KELT-16b and MASCARA-1b.

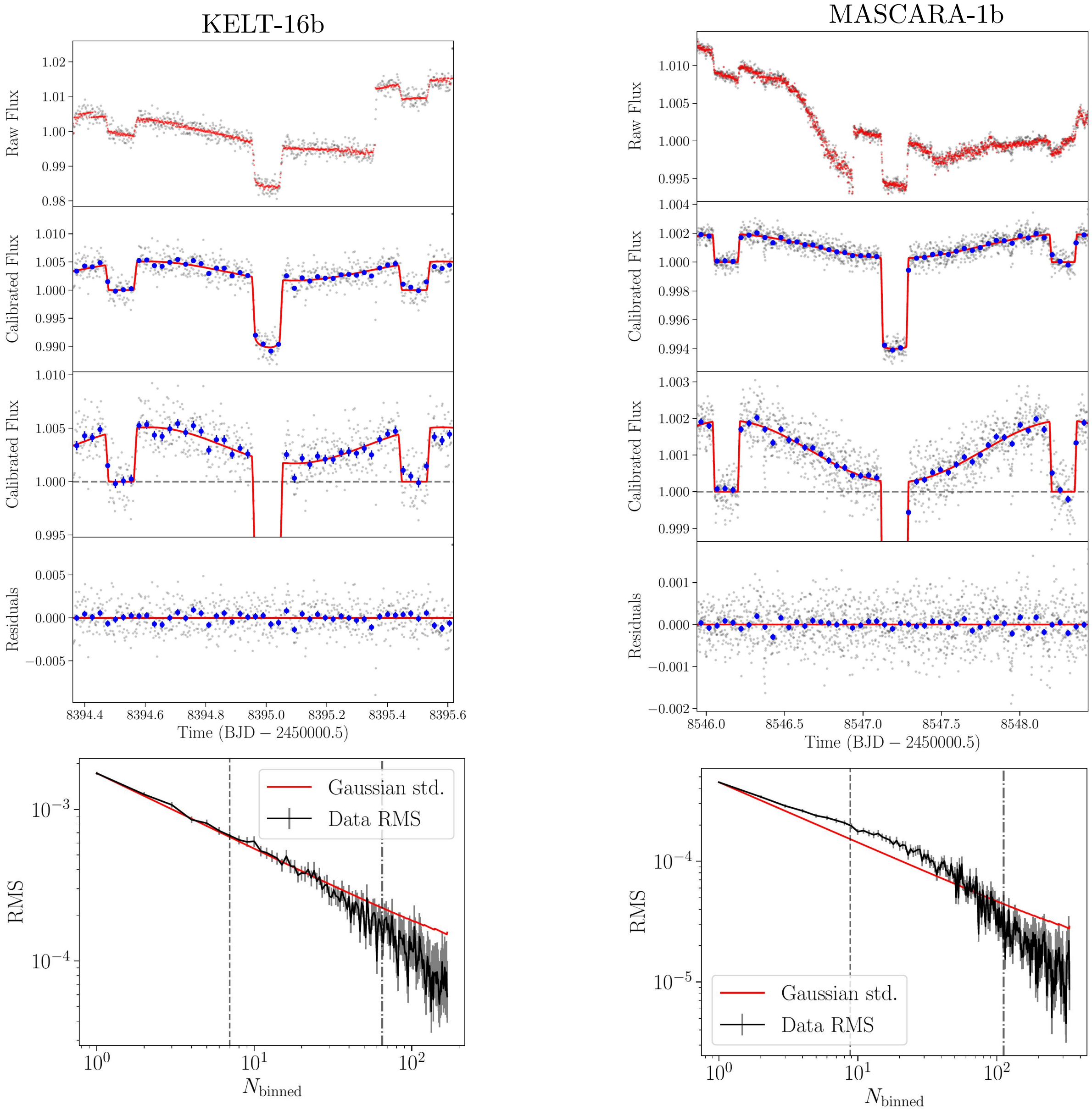

Figure 4. *Top:* Preferred model fits (BLISS_v1 using FWM centroiding) for KELT-16b and MASCARA-1b. The top four panels show raw photometry, photometry after correcting for detector systematics, a zoom-in on the calibrated data to show the phase variations, and the residuals from the fit. Vertical dashed lines indicate breaks between AORs, grey points are the 64× binned data which were fitted, blue points are further binned to 50 points per phase curve to show lower frequency noise levels, and the red lines indicate the best-fit model. *Bottom:* Red noise tests for the above fits, showing the decrease in the RMS of the residuals as the number of datapoints binned together (N_{binned}) increases, starting from our 64× binning. The red lines show the expected decrease in RMS assuming white noise. The timescale for transit/eclipse ingress and egress is indicated with a vertical, dashed line, while the full t_1–t_4 transit duration is shown with a vertical, dash-dotted line.

KELT-16b data are much simpler to fit and all models we consider are broadly consistent with each other, although the BLISS model gives a slightly more westward offset than the other models.

The pair of ultra-hot Jupiters MASCARA-1b and KELT-16b were chosen to allow for comparative studies since they share many physical characteristics in common. Both planets are highly irradiated (with irradiation temperatures of ∼3500 K), highly inflated ($R_\mathrm{p} \approx 1.4 R_\mathrm{jup}$), and have similar masses ($M_\mathrm{p} \approx 3 M_\mathrm{jup}$). The two main distinctions between the systems are the planets' orbital periods (∼1 day for KELT-16b, and ∼2 days for MASCARA-1b) and their host stars' effective temperatures (6200 K for KELT-16 and 7500 K for MASCARA-1b) which balance each other out to give roughly the same incident flux. As a result, any significant differences in the normalized phase curve amplitude or offset would potentially be due to differences in Coriolis forces or stellar spectra. Assuming a wind speed of 5 km/s for both planets and lengthscales equal to the planetary radii, we estimate mid-latitude Rossby numbers (Ro) of 0.91 and 0.47 for MASCARA-1b and KELT-16b, respectively. We also calculated the equatorial deformation radius (L_D) following Tan & Showman (2020) who showed that the equatorial jet width scales as roughly 1.8 times L_D; we find radii of 247 000 and 62 000 km (2.15 and 0.62 R_p) for MASCARA-1b and KELT-16b, respectively, assuming a Brunt–Väisälä frequency of $N \approx \sqrt{g/H}$. Both Ro and L_D suggest that MASCARA-1b would possess a significantly larger jet than KELT-16b which could result in an increased phase offset and a warmer nightside temperature for MASCARA-1b.

However, we find no significant differences between the dayside temperatures of the two planets and similarly no differences between the nightside temperatures. There is a preference for a westward offset in the phase curve of KELT-16b (38^{+16}_{-15} degrees W) which is also seen to a lesser extent for MASCARA-1b (6^{+11}_{-11} degrees W), but the two values differ by only 1.7σ. We therefore find no clear evidence for the impact of either different Coriolis forces or stellar spectra in the comparisons between the phase curve properties of these two particular planets. However, as we discuss below, there is evidence that stellar effective temperature plays a role in setting the phase amplitude of the broader hot Jupiter population, and it is possible that the opposing effects of changing Coriolis forces and stellar spectra may have nearly cancelled each other out. We also computed KELT-16b and MASCARA-1b's Bond albedos (-0.16 ± 0.38 and 0.26 ± 0.14, respectively) and recirculation efficiencies (0.309 ± 0.074 and 0.118 ± 0.038, respectively) after increasing our uncertainty on the effective temperatures following Pass et al. (2019) and then inverting equations 4 and 5 from Cowan & Agol (2011). Ultimately, we find that both planets have poor heat recirculation and, while the Bond albedos of these planets are poorly constrained with these single wavelength observations, they are consistent with zero reflected light as would be expected for ultra-hot Jupiters.

6.2. *Uniform Reanalyses and Model Comparisons*

For each phase curve, we start by choosing the best phase curve model (first or second order sinusoid) for each of our 9–10 different detector models using the BIC; this reduces the number of models we are comparing by a factor of 2. We also found no clear differences between the results using PSF centroiding and FWM centroiding, so we decided to focus solely on our FWM results to reduce the number of models we are comparing by another factor of 2.

In Figure 5 we highlight the different models' phase curve offsets for each planet compared to the literature values, while similar plots for phase curve semi-amplitude, eclipse depth, planet–star radius ratio, and nightside temperature are shown in Figures A1–A4 in the Appendix. Reassuringly, in most cases the retrieved parameters and uncertainties for each phase curve do not strongly depend on the detector model used, with most of the differences between model parameters being consistent at a $\sim 1\sigma$ level.

Comparing individual model performances for different planets, we can see that HD 189733b, HD 209458b, HAT-P-7b, and MASCARA-1b show especially large dispersion between different models' phase offsets. In the case of HAT-P-7b, this is driven by our models preferring an unusually flat phase curve compared to the literature; as the phase curve amplitude approaches zero, the phase offset becomes undefined in a manner similar to the argument of periapse becoming undefined for a circular orbit. It is unclear why our HAT-P-7b models differ so greatly from the published fit (Wong et al. 2016) as the raw photometry appears fairly clean and there do not appear to be unusual correlations with PSF width or other covariates. For MASCARA-1b, the large scatter in retrieved phase offset is a result of the previously mentioned strong detector systematics at a phase of ~ 0.65

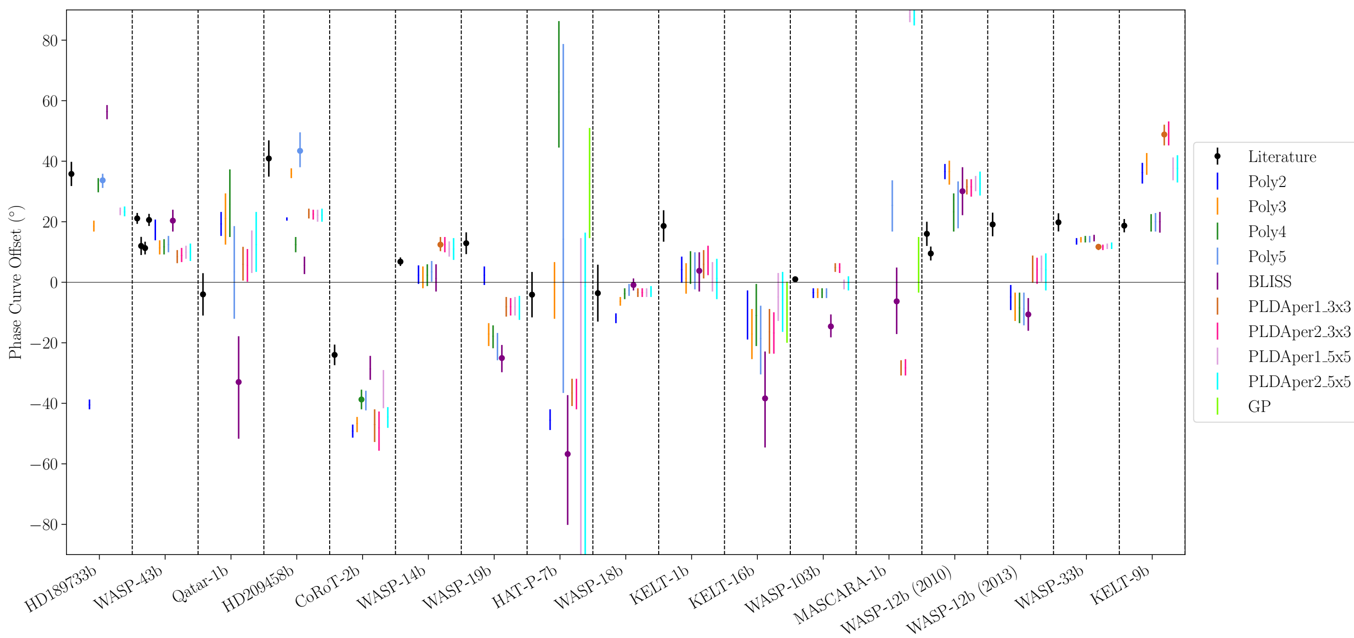

Figure 5. Phase curve offsets for all detector models using FWM centroiding and showing only the preferred astrophysical model. These offsets are compared to the previously published offsets for each phase curve indicated with black points. The first literature value for WASP-12b (2010) is from Cowan et al. (2012), and the second is from Bell et al. (2019). The literature values for WASP-43b are from Stevenson et al. (2017), Mendonça et al. (2018), Morello et al. (2019), and May & Stevenson (2020) from left to right. Similar figures for other astrophysical parameters can be found in the Appendix.

which is only well fit by the BLISS and GP models. Finally, for HD 189733b and HD 209458b, the large scatter is the result of the other detector models poorly fitting the strong "saw-tooth"-like systematic noise in these data sets. These "saw-tooth" systematics are sharply peaked, high frequency systematics present only in earlier *Spitzer* observations before changes were made to the cycling of the spacecraft battery's heater to mitigate this effect[5].

While our BLISS model is typically preferred, for HD 189733b, HD 209458b, CoRoT-2b, WASP-14b, WASP-33b, and KELT-9b it is strongly disfavoured compared to the preferred models (Poly5, Poly5, Poly4, PLDAper1_3x3, PLDAper1_3x3, and PLDAper1_3x3 respectively). While a better fit to these data sets with a BLISS model could likely be made using a more tailored approach—indeed,

[5] http://ssc.spitzer.caltech.edu/warmmission/news/21oct2010memo.pdf

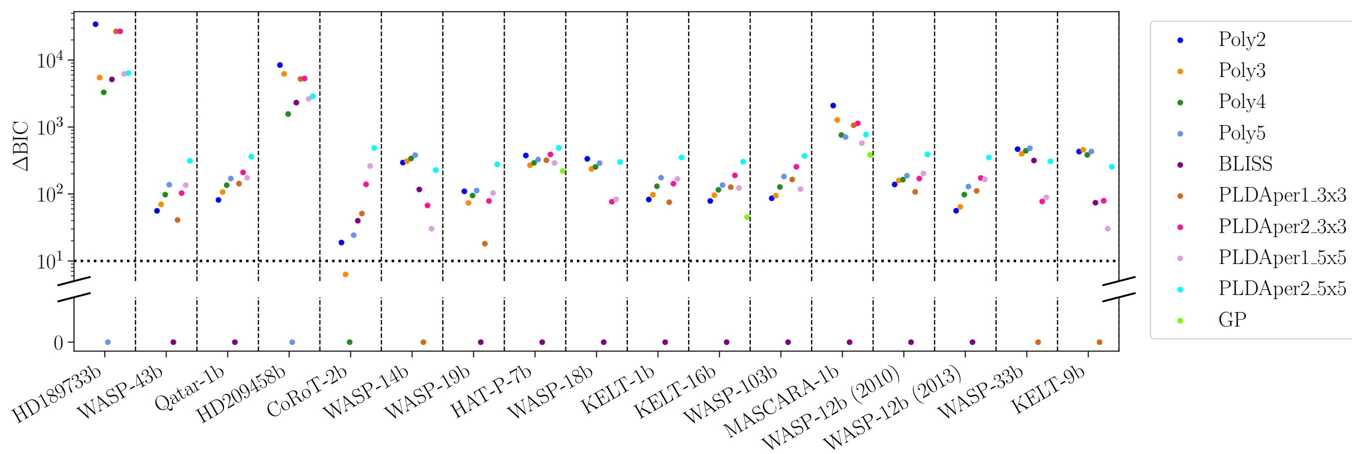

Figure 6. A comparison of the performance of each detector model for the full suite of models using the ΔBIC with respect to the preferred model. A dotted horizontal line indicates the minimum ΔBIC where there is no strong preference between models.

the phase curves of HD 189733b and HD 209458b were originally published using the Gaussian Kernel Regression technique which is similar in many respects to BLISS mapping—this lies beyond the scope of our current uniform reanalysis where we haven't tailored our algorithms to any data set in particular. The model fits to WASP-14b show an interesting feature where the Poly models and BLISS models all agree with each other, but all of the PLD models (where PLDAper1_3x3 is the preferred model) prefer larger phase curve semi-amplitudes, larger phase offsets, smaller eclipse depths, larger radii, and colder nightside temperatures. A similar effect is seen for some phase curves, but typically only for a single parameter (e.g. the phase offset for the 2013 observations of WASP-12b). Finally, while the BLISS models for WASP-33b are disfavoured, the retrieved phase curve parameters are consistent between the preferred PLDAper1_3x3 models and the BLISS models.

To further simplify comparisons between models, we decide to compare the fitted parameters from each model to the preferred model for that data set. In Figure 7, we plot histograms of these differences to search for model biases and compare model performances; we look in particular at phase curve semi-amplitude, phase offset, eclipse depth, radius, and nightside temperature. We also make population plots using our preferred models, showing the dependencies of the dayside temperature, nightside temperature, and phase offset on the irradiation temperature of the systems (Figure 9 and 10).

Compared to the preferred model, our Poly2 model's offsets, phase curve semi-amplitudes, and eclipse depths are frequently discrepant, and our Poly2 model often leaves noisy residuals compared to the preferred model. Meanwhile, our Poly3–Poly5 models typically perform quite well compared to the preferred model. Our BLISS algorithm also performs very well and is the preferred model for most phase curves, although there are cases where BLISS significantly differs from the preferred model. Our PLD models have larger than typical scatter about the preferred model's phase curve semi-amplitude, phase offset, and eclipse depth, and they also result in noisier residuals than the preferred model. For the three phase curves that we fitted with the GP models (HAT-P-7b, MASCARA-1b, and KELT-16b), the GP model was largely consistent with the preferred BLISS model, although the GP model prefers a positive phase offset for HAT-P-7b.

Aside from HD 189733b, HD 209458b, HAT-P-7b, and MASCARA-1b's phase curves, we find that the scatter between different models' phase offsets is on average only 1.17 ± 0.75 times (or 0.9 ± 3.8 degrees) larger than the fitted uncertainty from the bestfit model for each lightcurve. For HD 189733b, HD 209458b, HAT-P-7b, and MASCARA-1b we find that our fitted uncertainty underpredicts the scatter between models by 21, 2.0, 1.5, and 5.9 times, respectively (or 51, 5.2, 12, and 53 degrees, respectively). Taking all phase curves into consideration, we find that the scatter is 1.5 ± 4.8 times larger or 2 ± 17 degrees larger than the fitted uncertainties. In summary, for the majority of phase curve observations there is no evidence for a need to inflate phase offset uncertainties, but in rare cases the scatter between different models' offsets suggests that uncertainties computed using only a single detector model could be underestimated by a factor of 3 or more. These comparisons are complicated, however, by the fact that in almost every case there is a single model which drastically outperforms all others (see Figure 6). For this reason, we recommend that all future phase curve analyses explore a large range of detector models to simultaneously ensure that an optimal fit is found and to assess the dependence of phase offset on the decorrelation method used.

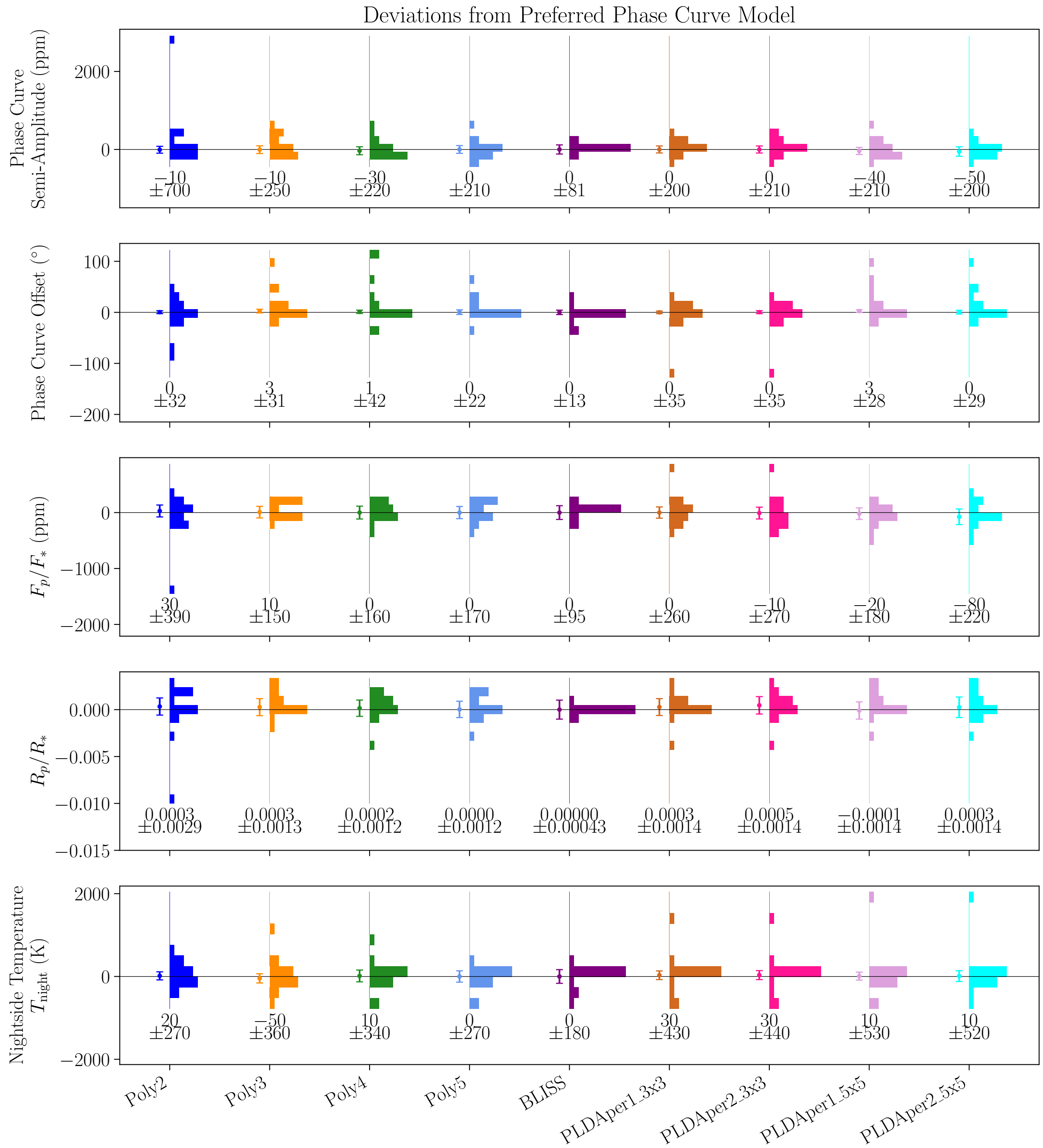

Figure 7. Histograms showing the bias and scatter of each model compared to the preferred model of each phase curve. Each histogram contains 17 values: one for each of the 17 phase curves. Beside each histogram is an error bar showing the average uncertainty for all fits with that model, and underneath each histogram is the observed median bias and scatter with respect to the preferred model. As can clearly be seen, some models occasionally produce wildly discrepant results. It is important to note, however, that this plot gives no indication as to how well each model fits the data sets. The strong performance by BLISS in these plots is mostly driven by the fact that the vast majority of data sets have BLISS as their preferred model.

6.3. *Comparisons with Literature Values*

Our preferred phase curve parameters from our two new and 15 reanalysed phase curves are presented in Table 4, while we have compiled the literature values from the 15 previously published phase curves that we have reanalyzed in Table 5. Since there is no consistent parameterization for phase curves and different works define the terms "dayside" and "nightside" differently, we needed to convert or compute some values from most papers. We define dayside as the observer facing hemisphere at mid-eclipse, and nightside as the observer facing hemisphere during mid-transit. We chose to compute our tabulated values using the published values and to use a Monte-Carlo simulation to propagate uncertainties. As a result, we chose to only tabulate/compute symmetric uncertainties for the literature values. Overall, we do not find significant evidence for biases or severe underestimation of uncertainties for all phase curve parameters, with phase offsets on average reproduced to within -8 ± 21 degrees (-1.6 ± 3.2 sigma) and normalized phase curve amplitudes (peak-to-trough divided by eclipse depth) on average reproduced to within -0.01 ± 0.24 (-0.1 ± 1.6 sigma). We also compare each model's performance against the literature values in a manner similar to Figure 7 in Figure 8.

WASP-43b is the most heavily scrutinized phase curve, with four analyses of this data set already published (Stevenson et al. 2017; Mendonça et al. 2018; Morello et al. 2019; May & Stevenson 2020). Our phase curve semi-amplitude, eclipse depth, and radius are consistent with all of these works. The more contentious issue is that of the phase curve's phase offset and nightside temperature. Stevenson et al. (2017) initially reported only a 2σ upper limit on the nightside temperature of 650 K, while all subsequent reanalyses (including ours) favour a significantly detectable nightside temperature of $\sim$800 K. As for the planet's phase offset, Stevenson et al. (2017) and May & Stevenson (2020) favour a larger phase offset (21 ± 2 °E) than Mendonça et al. (2018) and Morello et al. (2019) (12 ± 3 °E and 11 ± 2 °E). May & Stevenson (2020) claimed that the differences between the retrieved phase offsets is the result of temporal binning which was not used by Stevenson et al. (2017) and May & Stevenson (2020) but was used by Mendonça et al. (2018), Morello et al. (2019), and this work. Fitting the temporally binned photometry for all 17 phase curves with each of our detector models already required more than 2 000 CPU hours, and expanding this to unbinned photometry for all phase

Planet	Detector Model	R_p/R_*	F_p/F_* (ppm)	Semi-Amplitude (ppm)	Max Flux Offset (°E)	T_0 (K)	T_{day} (K)	T_{night} (K)
HD189733b	Poly5	$0.15639^{+0.00021}_{-0.00021}$	1797^{+24}_{-26}	654^{+36}_{-32}	$33.7^{+2.5}_{-2.2}$	1699^{+27}_{-27}	$1216.9^{+6.1}_{-6.4}$	929^{+26}_{-26}
WASP-43b	BLISS	$0.15935^{+0.00095}_{-0.0011}$	3650^{+140}_{-140}	1822^{+97}_{-110}	$20.4^{+3.6}_{-3.6}$	1994^{+90}_{-90}	1476^{+47}_{-46}	640^{+100}_{-110}
Qatar-1b	BLISS	$0.1464^{+0.0020}_{-0.0019}$	3090^{+270}_{-260}	1570^{+310}_{-250}	-33^{+19}_{-15}	2005^{+38}_{-38}	1535^{+61}_{-61}	900^{+180}_{-180}
HD209458b	Poly5	$0.12047^{+0.00039}_{-0.00042}$	1376^{+46}_{-40}	489^{+72}_{-68}	$43.4^{+5.4}_{-6.1}$	2052^{+23}_{-23}	1418^{+23}_{-19}	1009^{+71}_{-81}
CoRoT-2b	Poly4	$0.1704^{+0.0014}_{-0.0017}$	4880^{+200}_{-190}	2680^{+160}_{-130}	$-38.7^{+3.2}_{-3.2}$	2175^{+82}_{-82}	1756^{+44}_{-43}	873^{+51}_{-41}
WASP-14b	PLDAper1_3x3	$0.09561^{+0.00049}_{-0.00052}$	2327^{+69}_{-69}	843^{+39}_{-41}	$12.4^{+2.2}_{-2.5}$	2631^{+86}_{-86}	2401^{+50}_{-49}	1391^{+56}_{-61}
WASP-19b	BLISS	$0.1384^{+0.0019}_{-0.0019}$	5400^{+240}_{-250}	2170^{+220}_{-200}	$-25.0^{+4.7}_{-4.3}$	2993^{+52}_{-52}	2291^{+67}_{-66}	1380^{+120}_{-140}
HAT-P-7b	BLISS	$0.0774^{+0.0011}_{-0.0011}$	2220^{+110}_{-110}	480^{+160}_{-170}	-57^{+23}_{-19}	3145^{+57}_{-57}	2930^{+100}_{-100}	2520^{+240}_{-290}
WASP-18b	BLISS	$0.09831^{+0.00051}_{-0.00054}$	3935^{+100}_{-97}	1831^{+75}_{-89}	$-0.9^{+1.8}_{-2.2}$	3388^{+53}_{-53}	3151^{+59}_{-58}	960^{+140}_{-170}
KELT-1b	BLISS	$0.0742^{+0.0014}_{-0.0014}$	2400^{+120}_{-120}	1020^{+110}_{-110}	$3.8^{+6.8}_{-6.1}$	3435^{+77}_{-77}	3240^{+140}_{-140}	1350^{+230}_{-260}
KELT-16b	BLISS	$0.1074^{+0.0019}_{-0.0022}$	4810^{+330}_{-310}	1740^{+480}_{-460}	-38^{+16}_{-15}	3469^{+74}_{-74}	3070^{+160}_{-150}	1900^{+430}_{-440}
WASP-103b	BLISS	$0.11551^{+0.00093}_{-0.00095}$	5240^{+150}_{-150}	2500^{+120}_{-110}	$-14.6^{+3.6}_{-4.0}$	3540^{+100}_{-100}	2971^{+88}_{-87}	920^{+140}_{-160}
MASCARA-1b	BLISS	$0.07881^{+0.00084}_{-0.00087}$	1947^{+82}_{-85}	850^{+140}_{-130}	-6^{+11}_{-11}	3600^{+300}_{-300}	2952^{+100}_{-97}	1300^{+340}_{-340}
WASP-12b (2010)	BLISS	$0.1047^{+0.0015}_{-0.0014}$	4230^{+230}_{-230}	1790^{+270}_{-250} †	$30.1^{+7.9}_{-7.9}$ †	3673^{+81}_{-81}	2950^{+120}_{-120}	1550^{+250}_{-270}
WASP-12b (2013)	BLISS	$0.1047^{+0.0016}_{-0.0017}$	3940^{+210}_{-210}	1920^{+190}_{-180} †	$-10.6^{+5.4}_{-5.4}$ †	3674^{+82}_{-82}	2920^{+120}_{-120}	1110^{+250}_{-260}
WASP-33b	PLDAper1_3x3	$0.11009^{+0.00045}_{-0.00046}$	4431^{+56}_{-57}	1884^{+37}_{-39}	$11.71^{+1.1}_{-0.72}$	3932^{+53}_{-53}	3232^{+49}_{-49}	1559^{+39}_{-39}
KELT-9b	PLDAper1_3x3	$0.08044^{+0.00057}_{-0.00056}$	2889^{+46}_{-43}	703^{+48}_{-45}	$48.8^{+3.6}_{-3.2}$	5720^{+250}_{-250}	4450^{+220}_{-210}	3290^{+170}_{-170}

Table 4. Preferred SPCA model parameters for each of our fitted phase curves. The planet names for our two new phase curves are bolded. Note that no fits were made the the δ Scuti pulsations of WASP-33.

† WASP-12b's offsets and semi-amplitude are only from the first order sinusoid as there is a strong second order term which causes two peaks near quadrature.

Planet	Reference	R_p/R_*	F_p/F_* (ppm)	Semi-Amplitude (ppm)	Max Flux Offset (°E)	T_{day} (K)	T_{night} (K)
HD189733b	Knutson et al. (2012)	0.15580 ± 0.00019	$[1793 \pm 55]$	491 ± 45	$[35.8 \pm 4.0]$	1192.0 ± 9.0	928 ± 26
WASP-43b	Stevenson et al. (2017)	0.15890 ± 0.00050	3830 ± 80	$[1999 \pm 62]$	21.1 ± 1.8	1512 ± 25	< 650 @ 2σ
WASP-43b	Mendonça et al. (2018)	–	$[4060 \pm 100]$	$[1630 \pm 120]$	$[12.0 \pm 3.0]$	$[1545 \pm 47]$	$[914 \pm 75]$
WASP-43b	Morello et al. (2019)	$[0.1572 \pm 0.0010]$	$[3870 \pm 120]$	$[1800 \pm 96]$	11.3 ± 2.1	$[1522 \pm +47]$	$[730 \pm 97]$
WASP-43b	May & Stevenson (2020)	–	$[3660 \pm 120]$	1613 ± 83	20.6 ± 2.0	$[1478 \pm 45]$	$[838 \pm 65]$
Qatar-1b	Keating et al. (2020)	0.1450 ± 0.0010	3000 ± 200	920 ± 110	-4.0 ± 7.0	1557 ± 35	1167 ± 71
HD209458b	Zellem et al. (2014)	0.12130 ± 0.00030	1317 ± 50	$[545 \pm 58]$	40.9 ± 6.0	1499 ± 15	972 ± 44
CoRoT-2b	Dang et al. (2018)	0.16970 ± 0.00090	4400 ± 200	$[1700 \pm 200]$	-24.0 ± 3.4	1693 ± 17	$[730 \pm 140]$
WASP-14b	Wong et al. (2015)	0.09421 ± 0.00059	2247 ± 86	786 ± 23	$[6.8 \pm 1.4]$	2402 ± 35	1380 ± 65
WASP-19b	Wong et al. (2016)	0.1427 ± 0.0021	$[5840 \pm 290]$	2370 ± 220	$[12.9 \pm 3.6]$	2357 ± 64	$[1180 \pm 160]$
HAT-P-7b	Wong et al. (2016)	0.07769 ± 0.00078	$[1900 \pm 60]$	1040 ± 175	$[-4.1 \pm 7.5]$	2682 ± 49	$[1010 \pm 290]$
WASP-18b	Maxted et al. (2013)	0.09870 ± 0.00072	3790 ± 210	$[1830 \pm 110]$	$[-3.6 \pm 9.4]$	$[3050 \pm 110]$	$[980 \pm 230]$
KELT-1b	Beatty et al. (2019)	0.07710 ± 0.00030	2083 ± 70	979 ± 54	18.6 ± 5.2	2902 ± 74	1050 ± 200
WASP-103b	Kreidberg et al. (2018)	0.1164 ± 0.0011	5690 ± 140	$[2360 \pm 150]$	1.00 ± 0.40	3154 ± 99	1440 ± 110
WASP-12b (2010)	Cowan et al. (2012)	0.1054 ± 0.0014	3900 ± 300	$[2000 \pm 150]$ †	16.0 ± 4.0 †	$[2840 \pm 150]$	$[960 \pm 250]$
WASP-12b (2010)	Bell et al. (2019)	0.10656 ± 0.00085	4360 ± 140	$[2163 \pm 98]$ †	9.5 ± 2.3 †	2989 ± 66	790 ± 150
WASP-12b (2013)	Bell et al. (2019)	0.1049 ± 0.0010	3920 ± 150	$[1640 \pm 150]$ †	19.1 ± 3.9 †	2854 ± 74	1340 ± 180
WASP-33b	Zhang et al. (2018)	0.1030 ± 0.0011	4250 ± 160	1792 ± 94	19.8 ± 3.0	3209 ± 88	1500 ± 120
KELT-9b	Mansfield et al. (2020)	0.08004 ± 0.00041	3131 ± 62	$[953 \pm 37]$	18.7 ± 2.2	4566 ± 138	2556 ± 99

Table 5. Previously published model parameters for each of the phase curves we consider. Parameters reported using a different phase curve parameterization are converted and indicated with brackets. A dash indicates where the values cannot be computed from the published values. The offset and eclipse depth from Mendonça et al. (2018) were not originally published and come from May & Stevenson (2020). The day and nightside temperatures for Mendonça et al. (2018) and May & Stevenson (2020) were calculated using the radius from Stevenson et al. (2017) since they did not publish their radius.

† WASP-12b's offsets and semi-amplitude are only from the first order sinusoid as there is a strong second order term which causes two peaks near quadrature.

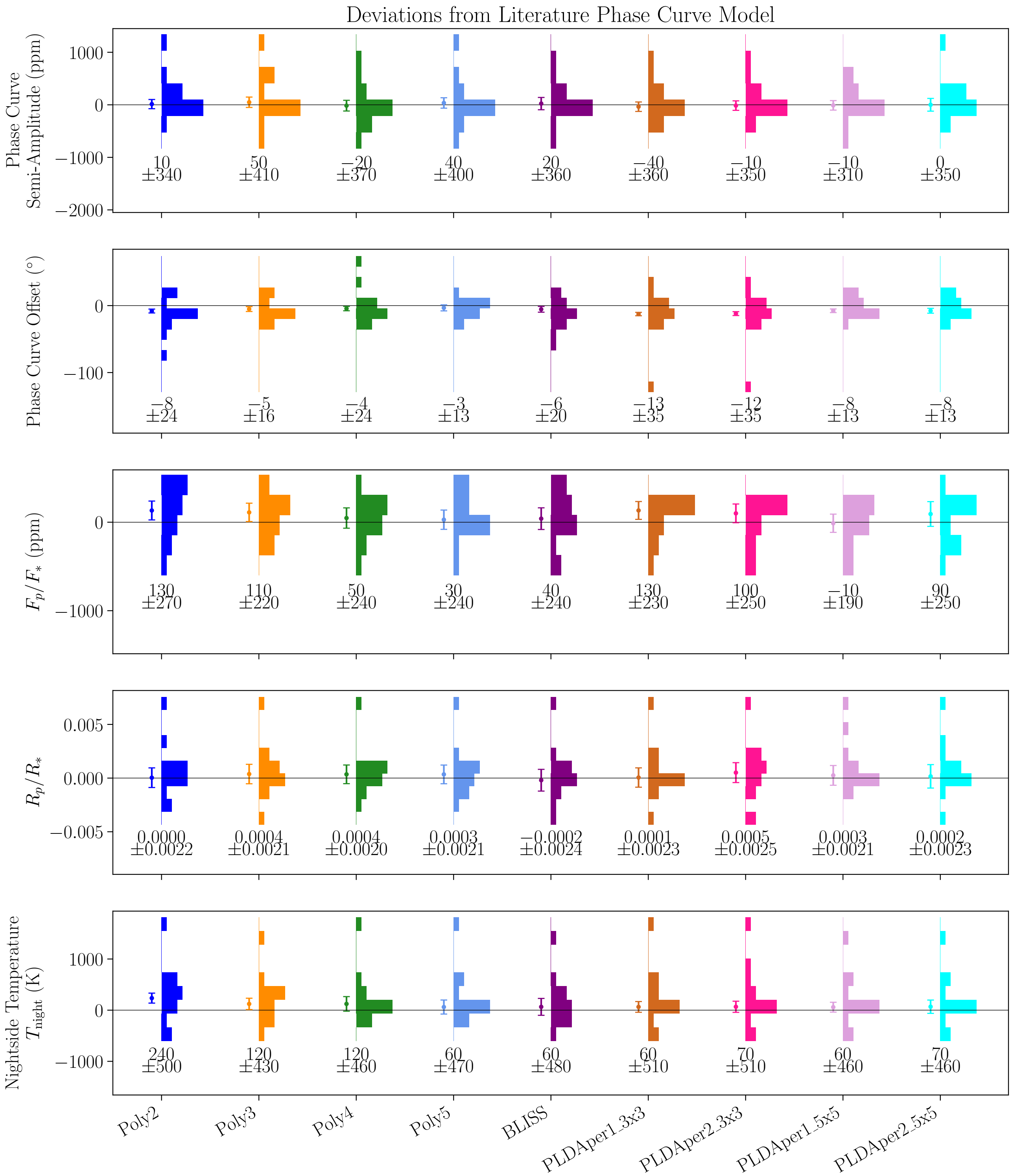

Figure 8. Histograms showing the bias and scatter of each model compared to the first published literature value for each phase curve. Each histogram contains 15 values: one for each of the 15 previously published phase curves.

curve fits would require more than 125 000 CPU hours (or 434 days using our 12× multi-threading computer) optimistically assuming all of detector models scaled linearly with the number of input data. However, we did try fitting just the WASP-43b unbinned phase curve with our preferred detector model (BLISS) and found that our phase offset and nightside temperature was unchanged. Including a linear slope in time also did not affect our phase offset or nightside temperature. Instead, we find that the phase offset inferred by our models depends on the choice of phase curve model, as our 4-parameter (v2) phase curve models are consistent with those of Stevenson et al. (2017) and May & Stevenson (2020), while our 2-parameter phase curve models (v1) are consistent with Mendonça et al. (2018) and Morello et al. (2019). Ultimately, we cannot decide between these two discrepant offsets as the ΔBIC between the two phase curve models for our preferred BLISS detector model is only 3.7 (insignificantly favouring the 20.4 ± 3.6 offset from the v2 model). For reference, Stevenson et al. (2014b) found phase offsets ranging from roughly -6 to 17 degrees east in the *Hubble*/WFC3 bandpass.

For HD 189733b, we retrieve a slightly larger phase curve semi-amplitude (2.9σ) than that reported by Knutson et al. (2012). For Qatar-1b, our models prefer a larger phase curve semi-amplitude (2.2σ) and larger uncertainty on the phase offset ($\pm17°$ vs $\pm7°$) than published by Keating et al. (2020), making it appear more consistent with WASP-43b. For HD 209458b, we find a significantly colder dayside temperature (3.2σ) than that published by (Zellem et al. 2014). We retrieve a significantly westward phase offset for CoRoT-2b, consistent with the findings of Dang et al. (2018), but with a larger phase offset (3.1σ) than their reported value. We also find a significantly larger phase curve semi-amplitude (4.0σ) for CoRoT-2b than was reported by Dang et al. (2018). Our preferred model's values for WASP-14b were all consistent with their previously published values to within 2σ (Wong et al. 2015). For WASP-19b, we find the phase offset changes direction with respect to that published by Wong et al. (2016) ($25.0^{+4.7}_{-4.3}$ degrees *west* rather than 12.9 ± 3.6 degrees *east*; 6.6σ). It is unclear why the phase offset is so different for this dataset as there were not particularly strong detector systematics or unusual variations in centroid position or PSF width. For HAT-P-7b, our models suggest a much shallower phase curve (1.9σ) than that reported by Wong et al. (2016).

As a result of the smaller phase curve semi-amplitude, we also find a far larger uncertainty on the phase offset and larger scatter between our detector models. For WASP-18b, our preferred model's values are consistent with the literature values (Maxted et al. 2013) to within 1σ. For reference, the *Hubble*/WFC3 phase offset reported by (Arcangeli et al. 2019) for WASP-18b was 4.5 ± 0.5 east, while we find an offset of -0.9 ± 2.2 degrees east at 4.5 μm.

For KELT-1b, we find a hotter dayside temperature (2.2σ) than that reported by Beatty et al. (2019). Our models for the WASP-103b data suggest a marginally westward offset ($-14.6^{+3.6}_{-4.0}$ degrees) compared to the previously published eastward offset at 4.5 μm (1.00 ± 0.40 degrees; differing by 2.2σ) and a colder nightside (2.2σ) than that reported by Kreidberg et al. (2018). For reference, Kreidberg et al. (2018) found phase offsets of -0.3 ± 0.1 degrees east in the *Hubble*/WFC3 bandpass and 2.0 ± 0.7 degrees east in the 3.6 μm bandpass. For WASP-12b, we retrieve a moderately westward first order sinusoidal phase offset for the 2013 observations which is discrepant at 4.3σ compared to the moderately eastward offset from Bell et al. (2019). Interestingly, this would be consistent with the observed change from an eastward phase offset in 2010 to westward phase offset in 2013 seen for the channel 1 observations of WASP-12b (Bell et al. 2019). We also still find evidence for very strong second order phase variations in both 4.5 μm phase curves of WASP-12b, consistent with the findings of Cowan et al. (2012) and Bell et al. (2019).

For WASP-33b, only our retrieved radius varied significantly (6.0σ) from the published value from Zhang et al. (2018). Leaving unmodelled the strong variability of the host star WASP-33A (seen clearly in our residuals in the Supplementary Information) could potentially have led to this difference. It is notable, however, that no other phase curve parameters were strongly affected. Finally, our models for KELT-9b prefer a lower semi-amplitude (4.2σ) and a larger phase offset (7.4σ) with a smaller eclipse depth (3.2σ) and hotter nightside temperature (3.7σ) than that reported by Mansfield et al. (2020). Given that modelling the stellar pulsations reported by Wong et al. (2020) had only a negligible effect on the retrieved phase curve parameters for Mansfield et al. (2020), the differences for KELT-9b are unlikely to be the result of our choice to neglect them. An increased nightside temperature for KELT-9b would only further increase the evidence that the latent heat-like effects of H_2 dissociation/recombination operate in ultra-hot Jupiter atmospheres as was predicted by Bell & Cowan (2018).

6.4. *Population Level Trends*

We also used the Pearson's correlation coefficient (r) to re-evaluate population level trends in phase curve parameters using our reanalyses. We summarize here the most relevant pairs for which there is a p-value below 0.05. To fit trends, we use an orthogonal distance regression routine (`scipy.odr`) to find the best-fit linear trend given the uncertainties in both x and y directions while performing a Monte Carlo over the x and y values to determine the uncertainty in the fitted parameters.

First, we confirm a positive correlation between irradiation temperature and radius ($r = 0.69$; $p = 0.0020$) which is consistent with the well known phenomenon of hot Jupiter radius inflation (e.g., Guillot & Showman 2002; Laughlin et al. 2011). We also find tentative evidence for a negative correlation between normalized phase curve amplitude (peak-to-trough divided by eclipse depth) and stellar effective temperature ($r = -0.51$; $p = 0.034$), while the normalized phase curve amplitude does not appear to be correlated with irradiation temperature or dayside temperature. This could potentially be explained through the lower energy photons preferentially emitted by cooler stars being absorbed higher in the planetary atmosphere where radiative timescales are much more rapid.

We confirm that 4.5 μm dayside brightness temperature is strongly correlated with irradiation temperature ($r = 0.96$; $p < 10^{-9}$), and we find that the best-fit slope of $T_{\rm day,bright}$ vs T_0 is 0.818 ± 0.011 when neglecting the extreme outlier KELT-9b. Meanwhile, the equilibrium temperature (assuming zero albedo and uniform recirculation) follows $T_{\rm eq} \equiv 0.71\,T_0$. Previously, Beatty et al. (2019) found a slope of 0.94 ± 0.08 for the 4.5 μm dayside brightness temperatures from 11 hot Jupiter phase curves, Garhart et al. (2020) found a median slope of 0.79 for 36 hot Jupiters using the error-weighted average of the 3.6 and 4.5 μm brightness temperatures from eclipse observations, and Baxter et al. (2020) found a slope of 0.84 ± 0.04 using 4.5 μm eclipse observations of 78 hot Jupiters. The steep slope at 4.5 μm dayside brightness temperature, combined with a shallower slope at 3.6 μm, is believed to be caused by changing temperature–pressure profiles (Garhart et al. 2020) resulting in a transition

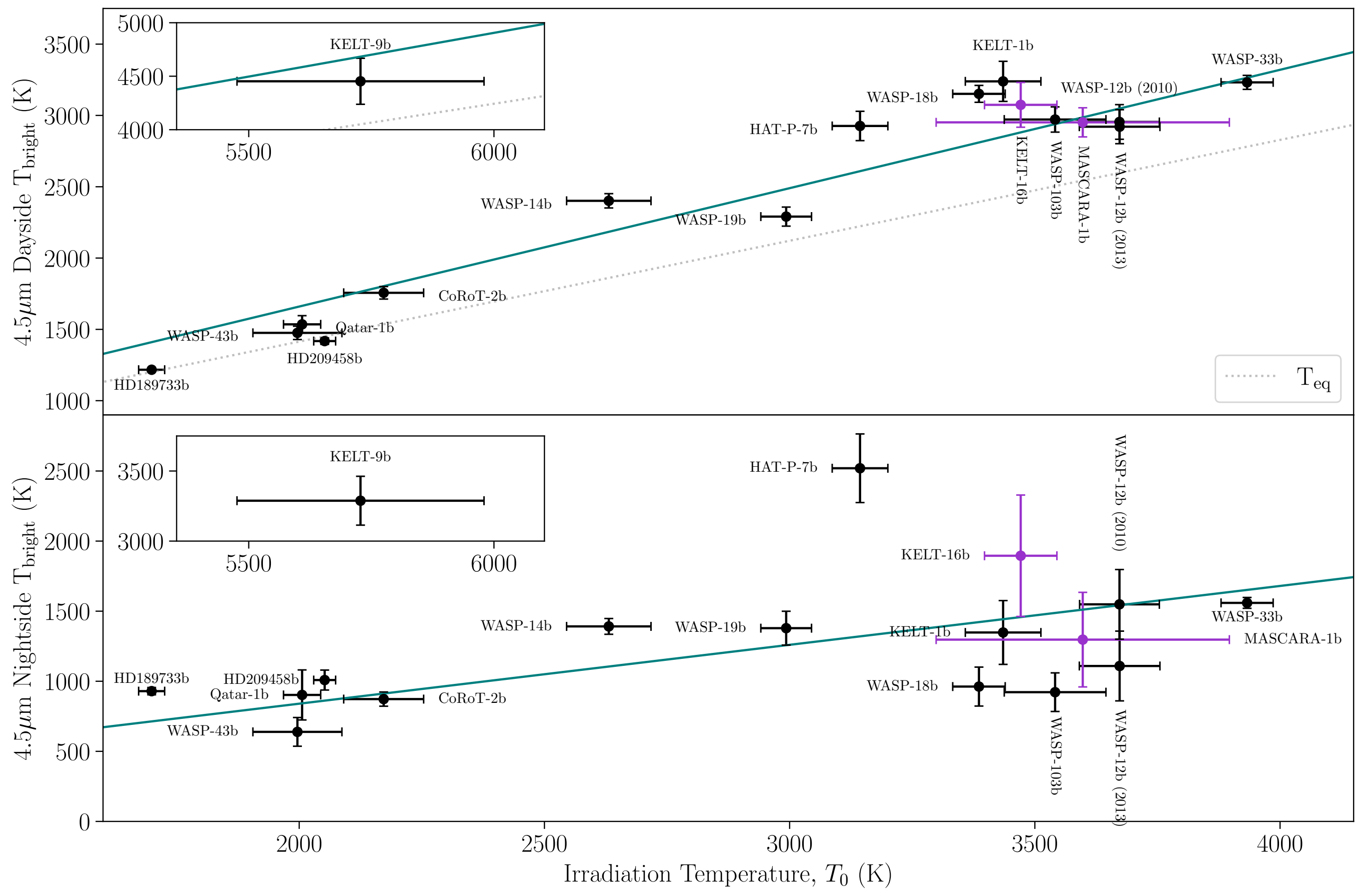

Figure 9. Day and nightside brightness temperatures as a function of irradiation temperature for all considered planets, using the preferred model selected by `SPCA`. Our new planets KELT-16b and MASCARA-1b are highlighted in purple. KELT-9b has been place in an inset with the same scale size as it lies far beyond the bounds of the plot. A dotted line in the top panel shows the relationship between irradiation temperature and equilibrium temperature (assuming zero Bond albedo and uniform recirculation) and is present in the KELT-9b inset figure as well. A teal line indicates the fitted slopes of 0.818 ± 0.011 for $T_{\rm day,bright}$ vs T_0 and 0.421 ± 0.011 for $T_{\rm night,bright}$ vs T_0.

between seeing CO in absorption for colder planets and emission for hotter planets (Baxter et al. 2020).

We also confirm a significant, fairly shallow dependence of nightside brightness temperature on irradiation temperature ($r = 0.73$; $p = 0.00089$) which has a slope of 0.421 ± 0.011 when neglecting the extreme outlier KELT-9b; a nearly flat trend was previously reported by Keating et al. (2019) and Beatty et al. (2019). Keating et al. (2019) didn't compute a slope, but using the effective nightside temperatures published in their Table 1 we compute a slope of 0.44 ± 0.01. Meanwhile, Beatty et al. (2019) applied different phase curve inversion methods and found a much shallower slope of 0.08 ± 0.11 for the 4.5 μm brightness temperatures. The interpretation from these two works was that this weak dependence of nightside temperatures on irradiation temperature is driven by a cloud layer that ubiquitously covers hot Jupiter nightsides; silicate clouds were a preferred species as they condense at the $\sim$1000 K temperatures observed on the nightsides of these planets. The extremely hot nightside temperature of KELT-9b has been attributed to the latent heat-like effects of H_2 dissociation/recombination Mansfield et al. (2020) as was predicted by Bell & Cowan (2018).

Unlike Zhang et al. (2018), we find no correlation between phase offset and irradiation temperature, nor is any obvious trend visible by eye (Figure 10). We do, however, find that the orbital period is correlated with the heat recirculation efficiency ($r = 0.61$, $p = 0.0087$). This positive correlation between heat recirculation efficiency and orbital period is consistent with that predicted by Komacek et al. (2017), although they also predicted a strong dependence on irradiation temperature for which we do not find evidence. We find no significant correlation between phase offset and normalized phase curve amplitude ($r = -0.20$; $p = 0.45$), but we do find evidence for a correlation between the more physically meaningful absolute magnitude of the phase offset and normalized phase curve amplitude relationship ($r = -0.55$; $p = 0.021$; Figure 11). When we fit for a trend between the normalized phase curve amplitude and the absolute magnitude of the phase offset, we find a slope of -0.0082 ± 0.0015 and a y-intercept of 0.976 ± 0.027.

We find that the Bond Albedo is not strongly correlated with the planetary mass, the logarithm of the planetary mass, or the logarithm of the surface gravity ($r = -0.39, -0.44, -0.38$; $p = 0.12, 0.08, 0.13$, respectively). Zhang et al. (2018) previously reported a negative correlation between Bond Albedo and planetary mass, and they suggested this could be the result of decreased lofting of cloud particles with increased surface gravity (although they also found no significant correlation with surface gravity). The dependence of cloud particle lofting on surface gravity has been predicted (e.g., Marley et al. 1999; Heng & Demory 2013) and has been observed for brown dwarfs where lower surface gravity objects exhibit increased cloudiness (Faherty et al. 2016).

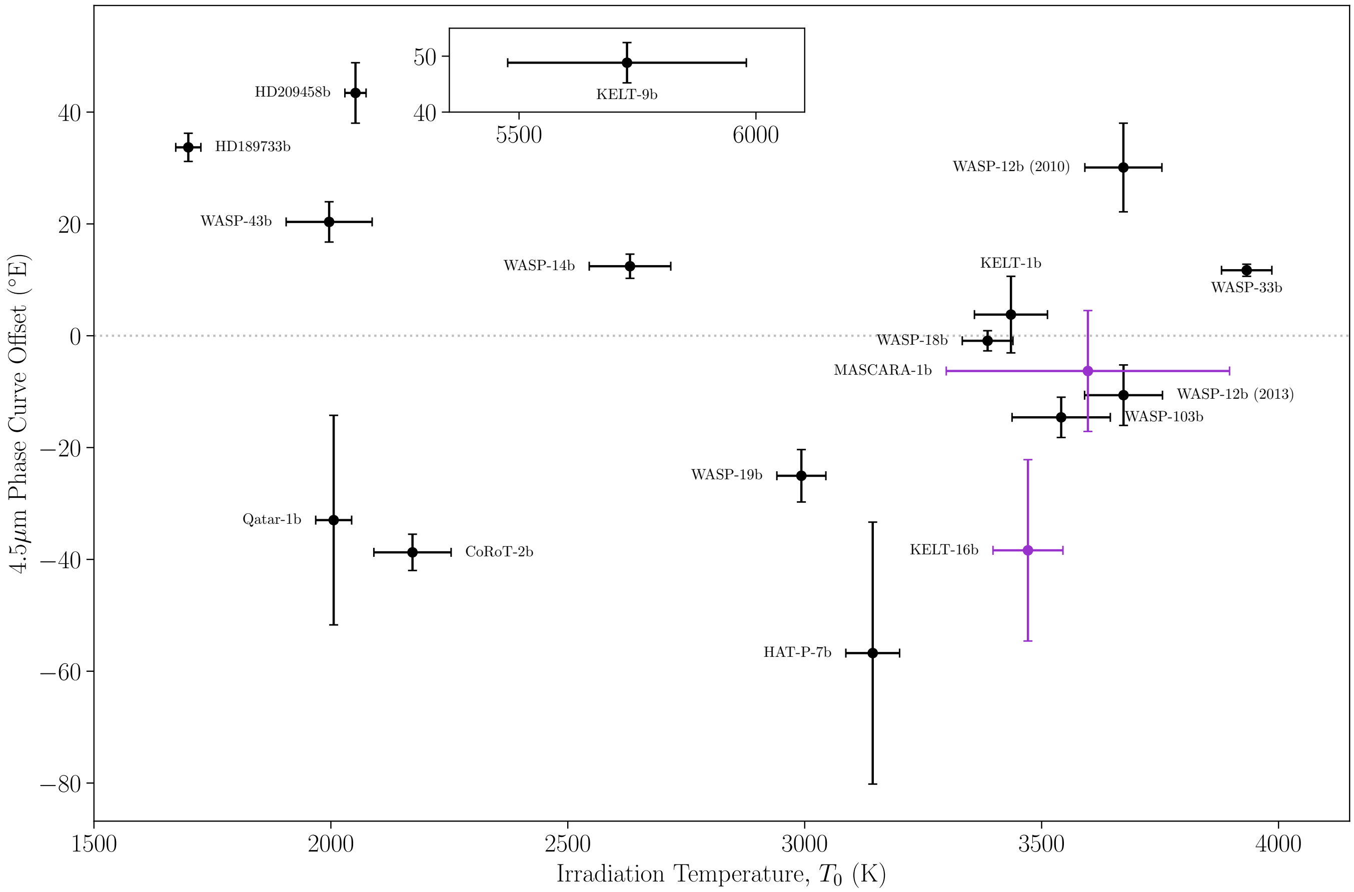

Figure 10. Phase curve offsets as a function of irradiation temperature for all considered planets, using the preferred model selected by `SPCA`. Our new planets KELT-16b and MASCARA-1b are highlighted in purple. KELT-9b has been place in an inset with the same scale size and vertical position as it lies far beyond the bounds of the plot.

7. DISCUSSION AND CONCLUSIONS

We have developed an open-source, modular pipeline for the reduction and decorrelation of *Spitzer*/IRAC channel 1 and 2 photometry, incorporating versions of some of the most popular decorrelation methods in the literature. We invite anyone interested in contributing their decorrelation method to visit our GitHub (`https://github.com/lisadang27/SPCA`). We first validated the implementation of our pipeline on the ten repeated eclipse observations of XO-3b, finding all our models perform equally well on these data with our fitted uncertainty on each eclipse depth only slightly underestimating the scatter between the ten eclipse observations. We then used this pipeline

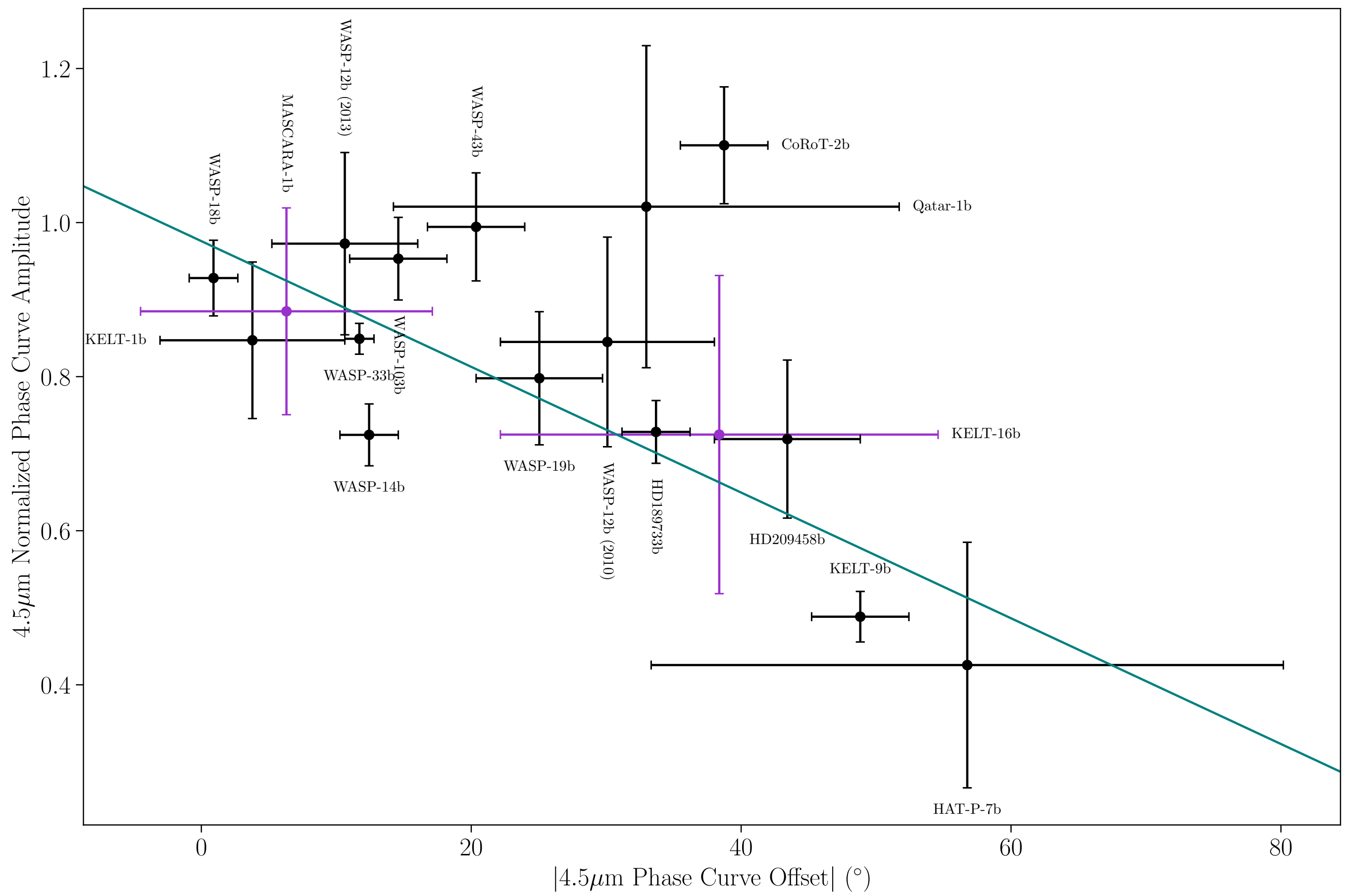

Figure 11. Normalized phase curve amplitudes (peak-to-trough divided by eclipse depth) as a function of the absolute value of phase curve offset for all considered planets, using the preferred model selected by `SPCA`. Our new planets KELT-16b and MASCARA-1b are highlighted in purple. A teal line indicates the fitted relationship with a slope of -0.0082 ± 0.0015 and a y-intercept of 0.976 ± 0.027. While WASP-43b and CoRoT-2b have normalized phase curve amplitudes greater than unity, this is caused by the significant phase offset of the systems which cause the eclipse depth to be significantly lower than the phase curve maximum.

to perform the uniform reanalysis of 15 *Spitzer* phase curve observations and analyse the new phase curves of ultra-hot Jupiters MASCARA-1b and KELT-16b. We use these analyses to test for the reproducibility of the literature values and perform a comparison of decorrelation models across 17 different phase curves; something previously only done for individual phase curves (e.g. Wong et al. 2015; Dang et al. 2018; Bell et al. 2019; Keating et al. 2020) or the 10 repeated eclipse observations of XO-3b (Ingalls et al. 2016).

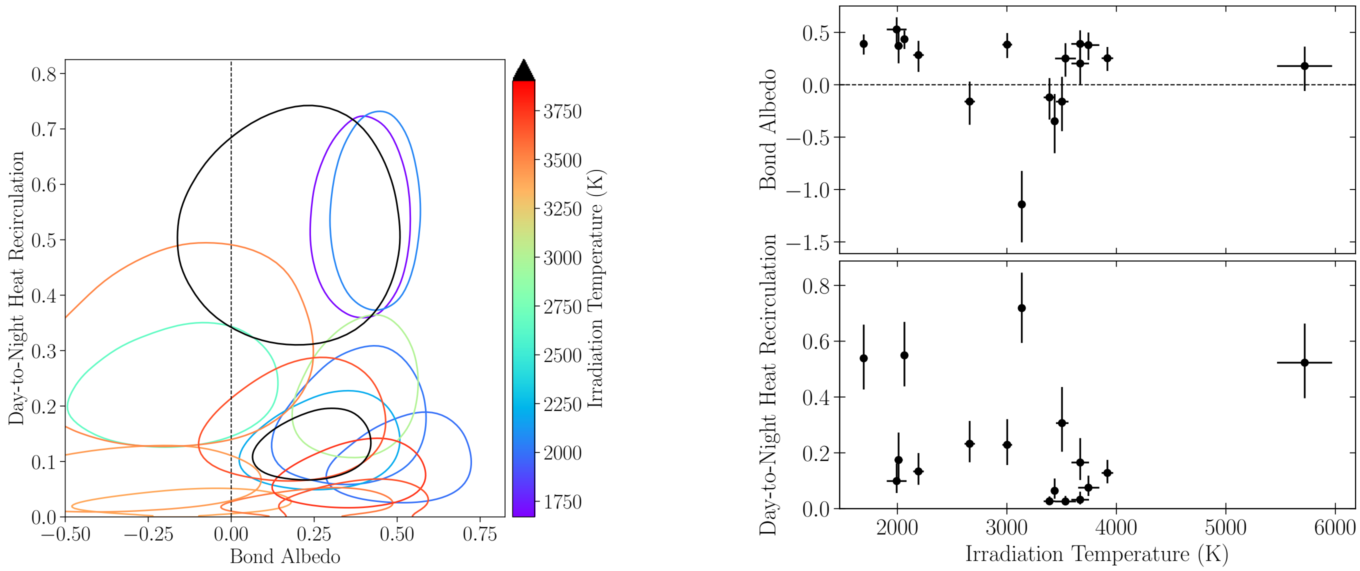

Figure 12. Left: An updated version of Figure 3 from Schwartz et al. (2017) showing the relationships between Bond albedo and day–night heat recirculation. Significant differences exist between this figure and that of Schwartz et al. (2017) as we consider only the 4.5 μm phase curves and have followed the procedure of Pass et al. (2019) to account for underestimated uncertainties in inferring effective temperatures using only one or a few photometric bands. Right: the same parameters shown as 1D trends with irradiation temperature.

For our decorrelation model comparisons, we find that our BLISS model tends to perform the best as evaluated by the BIC, where we consider each of the occupied BLISS knots a fitted parameter. For most phase curves, our higher complexity 2D Polynomial models (Poly3–5), our PLD models, and our BLISS model all give consistent results. However, there are cases like HD 189733b, HD 209458b, HAT-P-7b, and MASCARA-1b where the retrieved results do strongly depend on the model used.

We find that our reanalysis of WASP-43b's channel 2 phase curve is consistent to within $\sim 2\sigma$ of all of the values published by Mendonça et al. (2018), Morello et al. (2019), and May & Stevenson (2020), but we do find a significantly hotter nightside than was published by Stevenson et al. (2017). Using WASP-43b as a test case, we found that our BLISS results were not affected by temporal binning; this is consistent with the findings of May & Stevenson (2020) which showed that phase curve offsets and nightside temperatures are not affected by temporal binning when using their BLISS algorithm without an additional PSF-width model. We instead find that the retrieved offset for the WASP-43b phase curve changes significantly depending on the phase curve model used, with first order models reproducing the phase offsets of Mendonça et al. (2018) and Morello et al. (2019) and second order models reproducing the phase offsets of Stevenson et al. (2017) and May & Stevenson (2020); there is inadequate statistical evidence to differentiate these two models, but the second order model's offset of 20.4 ± 3.6 °E is marginally preferred (ΔBIC ~ 3.7). We find that Qatar-1b, WASP-14b, WASP-18b, WASP-103b, and the 2010 observations of WASP-12b the only other phase curves for which we reproduce all literature values within $\sim 2\sigma$, and we find that our retrieved phase offsets and nightside temperatures often differ from their published values, while eclipse depths and radii are typically consistent with the literature.

Our novel observations of MASCARA-1b and KELT-16b suggest these two ultra-hot Jupiters have quite similar phase curves, despite their orbital period, and thus likely their rotational periods, differing by a factor of two. KELT-16b's and MASCARA-1b's energy budgets are poorly constrained but consistent with zero Bond albedo and fairly inefficient recirculation. We also find that there is minimal diversity in the phase curves of similarly irradiated ultra-hot Jupiters WASP-18b, KELT-1b, KELT-16b, WASP-103b, and MASCARA-1b, with all planets having similar dayside temperatures, nightside temperatures, and phase offsets (Figures 9 and 10) despite masses ranging from to 1.5 to 27 $M_{\rm Jup}$ and periods ranging from 1 to 2 days. While these cooler ultra-hot Jupiters don't show strong evidence for the effects of H_2 dissociation/recombination, the hot nightsides and large phase offsets of WASP-33b and KELT-9b do imply heat transport far greater than would be predicted in the absence of H_2 dissociation/recombination.

Using our reanalyzed and new phase curve observations, we confirm significant trends in the 4.5 μm brightness temperatures of the dayside and nightside hemispheres as a function of irradiation temperature. However, we do not find clear evidence for previously reported trends in phase offset with irradiation temperature. We also find evidence that normalized phase curve amplitude is correlated with stellar effective temperature and that day–night heat recirculation is correlated with orbital period. Finally, we find that normalized phase curve amplitude does not appear to be correlated with phase offset but does appear to be correlated with the absolute value of phase offset

Overall, while our different decorrelation models often retrieve similar phase curve parameters, significant differences can arise between different models as well as between our preferred model and the literature values. We find differences of up to $\sim 30°$ in the phase offset between our preferred model and the literature value, but ultimately, our preferred models are consistent with published phase offsets to within -8 ± 21 degrees (-1.6 ± 3.2 sigma) and normalized phase curve amplitudes are on average reproduced to within -0.01 ± 0.24 (-0.1 ± 1.6 sigma). Additional studies on the reproducibility of phase curve parameters (and especially offsets) with and without temporal binning need to be performed on a large number of phase curves to ensure that any conclusions hold for the entire collection of 4.5 μm and 3.6 μm *Spitzer* phase curves. Finally, we recommend that the principles of open-source and modular code be applied in the coming era of *JWST*, reducing redundant labour and increasing reproducibility and uniformity.

ACKNOWLEDGEMENTS

This work is based on observations made with the *Spitzer* Space Telescope, which was operated by the Jet Propulsion Laboratory, California Institute of Technology under a contract with NASA. T.J.B. acknowledges support from the McGill Space Institute Graduate Fellowship, the Natural Sciences and Engineering Research Council of Canada's Postgraduate Scholarships-Doctoral Fellowship, and from the Fonds de recherche du Québec – Nature et technologies through the Centre de recherche en astrophysique du Québec. Support for this work was also provided to US-based investigators by NASA through an award issued by JPL/Caltech. J.M.D acknowledges support from the Amsterdam Academic Alliance (AAA) Program, and the European Research Council (ERC) European Union's Horizon 2020 research and innovation program (grant agreement no. 679633; Exo-Atmos). This work is part of the research programme VIDI with project number 016.Vidi.189.174, which is (partly) financed by the Dutch Research Council (NWO). Finally, we have also made use of open-source software provided by the Python, Astropy, SciPy, and Matplotlib communities.

DATA AVAILABILITY

The raw observations used in this work are freely accessible on the *Spitzer* Heritage Archive. The fitted parameters for each considered model are available as numpy zip files in the Supplementary Data. The data presented in each figure will be shared on reasonable request to the corresponding author.

REFERENCES

Arcangeli J., et al., 2019, A&A, 625, A136

Ballard S., et al., 2010, PASP, 122, 1341

Baxter C., et al., 2020, A&A, 639, A36

Beatty T. G., Marley M. S., Gaudi B. S., Colón K. D., Fortney J. J., Showman A. P., 2019, AJ, 158, 166

Bechter E. B., et al., 2014, ApJ, 788, 2

Bell T. J., Cowan N. B., 2018, ApJL, 857, L20

Bell T. J., et al., 2019, MNRAS, 489, 1995

Bergfors C., Brandner W., Henning T., Daemgen S., 2011, in Sozzetti A., Lattanzi M. G., Boss A. P., eds, IAU Symposium Vol. 276, The Astrophysics of Planetary Systems: Formation, Structure, and Dynamical Evolution. pp 397–398, doi:10.1017/S1743921311020503

Butler R. P., et al., 2006, ApJ, 646, 505

Cartier K. M. S., et al., 2017, AJ, 153, 34

Challener R. C., et al., 2021, The Planetary Science Journal, 2, 9

Charbonneau D., et al., 2005, ApJ, 626, 523

Charbonneau D., Knutson H. A., Barman T., Allen L. E., Mayor M., Megeath S. T., Queloz D., Udry S., 2008, ApJ, 686, 1341

Cowan N. B., Agol E., 2011, ApJ, 729, 54

Cowan N. B., Machalek P., Croll B., Shekhtman L. M., Burrows A., Deming D., Greene T., Hora J. L., 2012, ApJ, 747, 82

Crossfield I. J. M., Barman T., Hansen B. M. S., Tanaka I., Kodama T., 2012, ApJ, 760, 140

Cubillos P., et al., 2013, ApJ, 768, 42

Dang L., et al., 2018, Nature Astronomy, 2, 220

Deming D., Knutson H. A., 2020, Nature Astronomy, 4, 453

Deming D., et al., 2015, ApJ, 805, 132

Demory B.-O., et al., 2016, Nature, 532, 207

Evans T. M., Aigrain S., Gibson N., Barstow J. K., Amundsen D. S., Tremblin P., Mourier P., 2015, MNRAS, 451, 680

Faherty J. K., et al., 2016, ApJS, 225, 10

Foreman-Mackey D., 2015, George: Gaussian Process regression, Astrophysics Source Code Library (ascl:1511.015)

Foreman-Mackey D., Hogg D. W., Lang D., Goodman J., 2013, PASP, 125, 306

Gaia Collaboration 2018, VizieR Online Data Catalog, p. I/345

Garhart E., et al., 2020, AJ, 159, 137

Gibson N. P., Aigrain S., Roberts S., Evans T. M., Osborne M., Pont F., 2012, MNRAS, 419, 2683

Guillot T., Showman A. P., 2002, A&A, 385, 156

Hansen C. J., Schwartz J. C., Cowan N. B., 2014, MNRAS, 444, 3632

Harrington J., Hansen B. M., Luszcz S. H., Seager S., Deming D., Menou K., Cho J. Y.-K., Richardson L. J., 2006, Science, 314, 623

Heng K., Demory B.-O., 2013, ApJ, 777, 100

Ingalls J. G., et al., 2016, AJ, 152, 44

Keating D., Cowan N. B., Dang L., 2019, Nature Astronomy, 3, 1092

Keating D., et al., 2020, AJ, 159, 225

Kervella P., et al., 2008, A&A, 488, 667

Kipping D. M., 2013, MNRAS, 435, 2152

Knutson H. A., et al., 2009, ApJ, 690, 822

Knutson H. A., et al., 2012, ApJ, 754, 22

Komacek T. D., Showman A. P., 2020, ApJ, 888, 2

Komacek T. D., Showman A. P., Tan X., 2017, ApJ, 835, 198

Kreidberg L., 2015, PASP, 127, 1161

Kreidberg L., et al., 2018, AJ, 156, 17

Laughlin G., Crismani M., Adams F. C., 2011, ApJL, 729, L7

Lewis N. K., et al., 2013, ApJ, 766, 95

Mansfield M., et al., 2020, ApJL, 888, L15

Marley M. S., Gelino C., Stephens D., Lunine J. I., Freedman R., 1999, ApJ, 513, 879

Maxted P. F. L., et al., 2013, MNRAS, 428, 2645

May E. M., Stevenson K. B., 2020, AJ, 160, 140

Mendonça J. M., Malik M., Demory B.-O., Heng K., 2018, AJ, 155, 150

Morello G., Danielski C., Dickens D., Tremblin P., Lagage P. O., 2019, AJ, 157, 205

Moutou C., et al., 2011, A&A, 527, A63

Nelder J. A., Mead R., 1965, The computer journal, 7, 308

Oberst T. E., et al., 2017, AJ, 153, 97

Parmentier V., Crossfield I. J. M., 2018, Exoplanet Phase Curves: Observations and Theory. Springer International Publishing, p. 116, doi:10.1007/978-3-319-55333-7˙116

Pass E. K., Cowan N. B., Cubillos P. E., Sklar J. G., 2019, MNRAS, 489, 941

Rajpurohit A. S., Allard F., Rajpurohit S., Sharma R., Teixeira G. D. C., Mousis O., Rajpurohit K., 2018, A&A, 620, A180

Schröter S., Czesla S., Wolter U., Müller H. M., Huber K. F., Schmitt J. H. M. M., 2011, A&A, 532, A3

Schwartz J. C., Cowan N. B., 2017, PASP, 129, 014001

Schwartz J. C., Kashner Z., Jovmir D., Cowan N. B., 2017, ApJ, 850, 154

Stevenson K. B., et al., 2012, ApJ, 754, 136

Stevenson K. B., Bean J. L., Seifahrt A., Désert J.-M., Madhusudhan N., Bergmann M., Kreidberg L., Homeier D., 2014a, AJ, 147, 161

Stevenson K. B., et al., 2014b, Science, 346, 838

Stevenson K. B., Bean J. L., Madhusudhan N., Harrington J., 2014c, ApJ, 791, 36

Stevenson K. B., et al., 2017, AJ, 153, 68

Talens G. J. J., et al., 2017, A&A, 606, A73

Tan X., Showman A. P., 2020, ApJ, 902, 27

Wong I., et al., 2014, ApJ, 794, 134

Wong I., et al., 2015, ApJ, 811, 122

Wong I., et al., 2016, ApJ, 823, 122

Wong I., et al., 2020, AJ, 160, 88

Zellem R. T., et al., 2014, ApJ, 790, 53

Zhang M., et al., 2018, AJ, 155, 83

APPENDIX

A. PRIORS

The priors used throughout our fitting are described in Table A1.

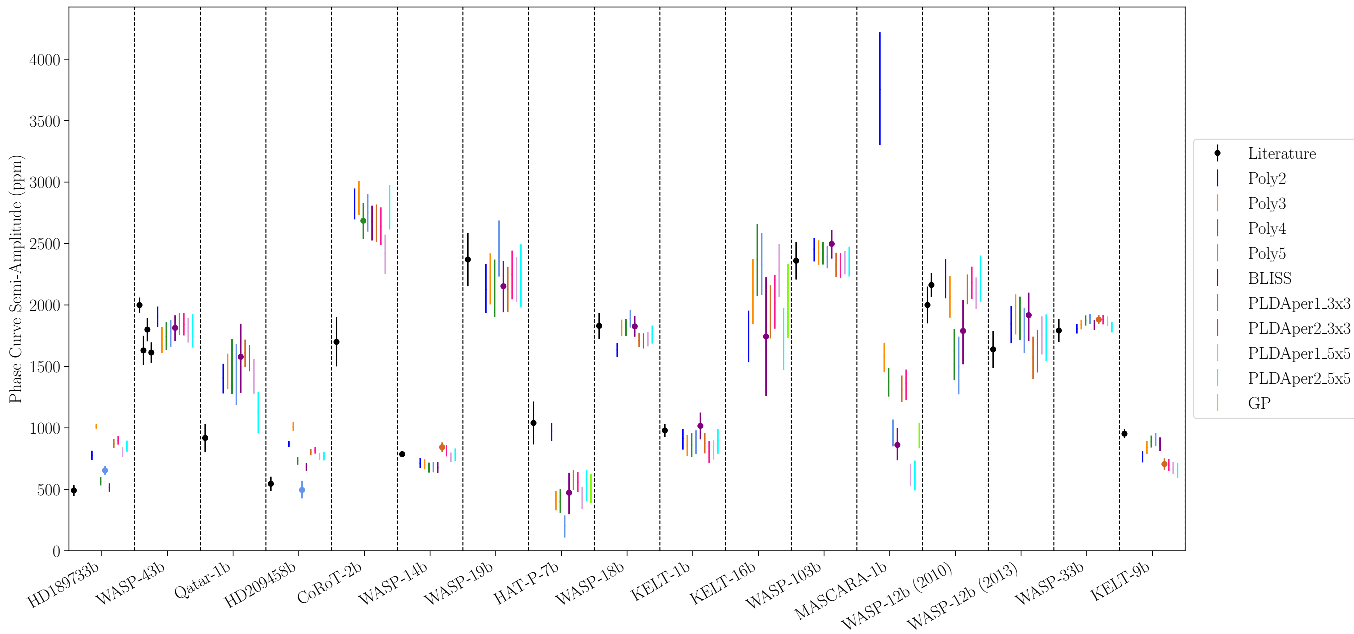

Figure A1. Phase curve semi-amplitudes for all detector models using FWM centroiding, and the previously published semi-amplitude for each phase curve. The first literature value for WASP-12b (2010) is from Cowan et al. (2012), and the second is from Bell et al. (2019). The literature values for WASP-43b are from Stevenson et al. (2017), Mendonça et al. (2018), Morello et al. (2019), and May & Stevenson (2020) from left to right.

Table A1. A summary of all the priors used in the model fitting. Uniform priors were used where there are inequalities below, Gaussian priors were used to constrain astrophysical parameters to the most precise published values from the NASA Exoplanet Archive (`https://exoplanetarchive.ipac.caltech.edu/`), and parameters were unconstrained where Free is written. The $p_{i,1}$ parameters are the first order PLD terms, and $p_{i,2}$ are the second order PLD terms

Parameter	Prior
t_0 (BMJD)	Gaussian
R_p/R_*	$0 < R_p/R_* < 1$
a/R_*	Gaussian
i (degrees)	Gaussian
P (days)	Gaussian
F_p/F_*	$0 < F_p/F_* < 1$
C_1	Positive Phase Curve
D_1	Positive Phase Curve; $\lvert \mathrm{arctan2}(D_1, C_1) \rvert < 90°$
C_2	Positive Phase Curve (if present)
D_2	Positive Phase Curve (if present)
σ_F (white noise)	$0 < \sigma_F < 1$
Limb Darkening	$0 < q_1 < 1$; $0 < q_2 < 1$
$e\cos(\omega)$	$-1 < e\cos(\omega) < 1$
$e\sin(\omega)$	$-1 < e\sin(\omega) < 1$
Poly Instrumental Variables	Free (if present)
GP Instrumental Variables	$-3 < \ln(L_x) < 0$ (if present); $-3 < \ln(L_y) < 0$ (if present); $p(C) = \mathrm{Gam}(1, 100)$ (if present)
PLD Instrumental Variables	$-3 < p_{i,1} < 3$ (if present); $-500 < p_{i,2} < 500$ (if present)
BLISS Instrumental Variables	None

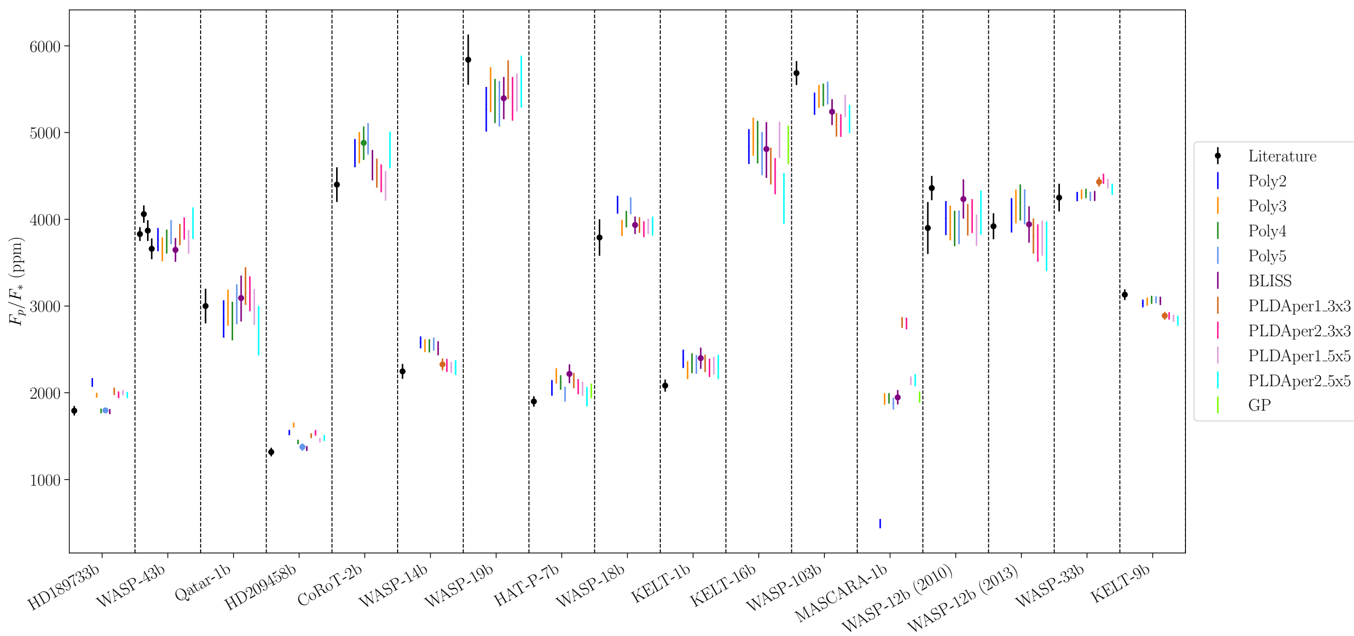

Figure A2. Dayside fluxes for all detector models using FWM centroiding, and the previously published dayside fluxes for each phase curve. The first literature value for WASP-12b (2010) is from Cowan et al. (2012), and the second is from Bell et al. (2019). The literature values for WASP-43b are from Stevenson et al. (2017), Mendonça et al. (2018), Morello et al. (2019), and May & Stevenson (2020) from left to right.

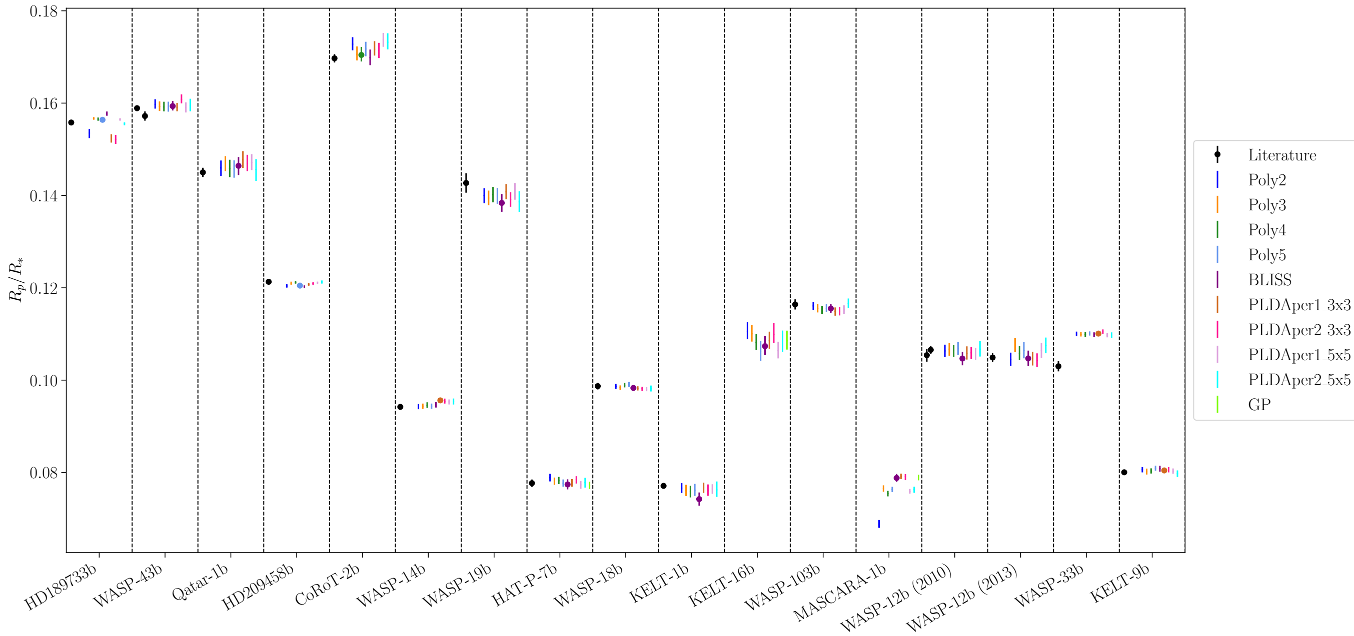

Figure A3. Radii for all detector models using FWM centroiding, and the previously published radii for each phase curve. The first literature value for WASP-12b (2010) is from Cowan et al. (2012), and the second is from Bell et al. (2019). The literature values for WASP-43b are from Stevenson et al. (2017) and Morello et al. (2019) from left to right.

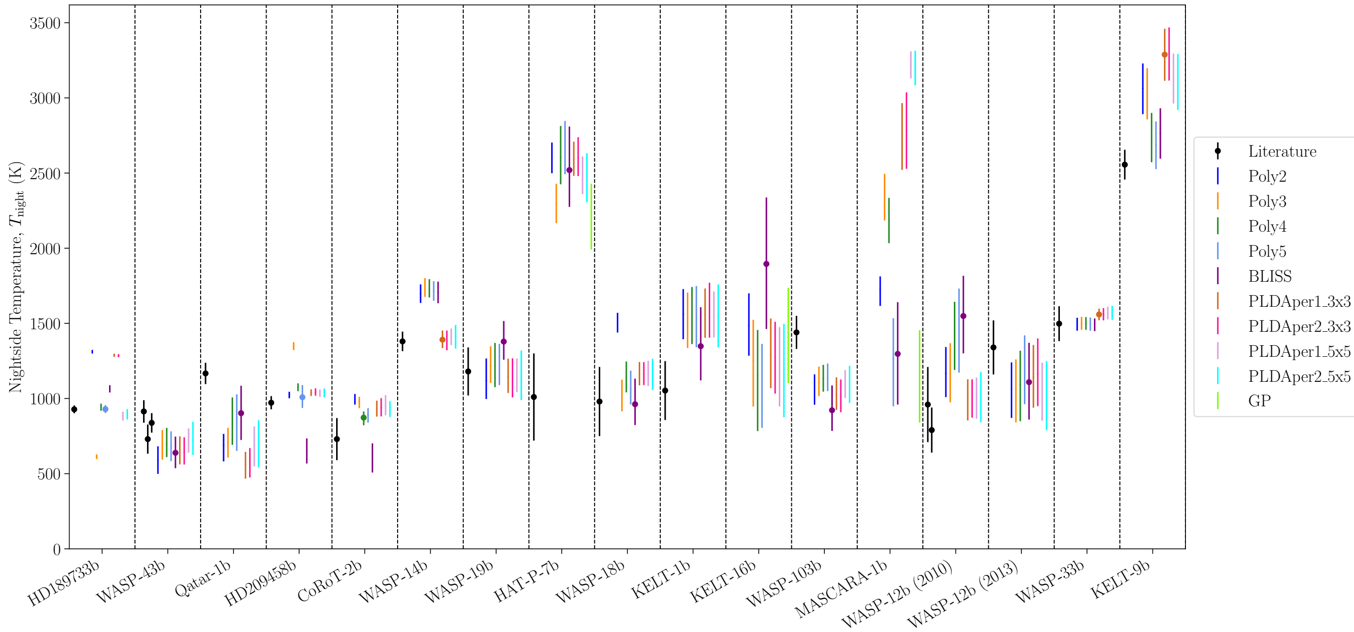

Figure A4. Nightside temperatures for all detector models using FWM centroiding, and the previously published nightside temperatures for each phase curve. The first literature value for WASP-12b (2010) is from Cowan et al. (2012), and the second is from Bell et al. (2019). The literature values for WASP-43b are from Mendonça et al. (2018), Morello et al. (2019), and May & Stevenson (2020) from left to right, while Stevenson et al. (2017) found a 2σ upper limit of 650 K.

SUPPLEMENTARY INFORMATION

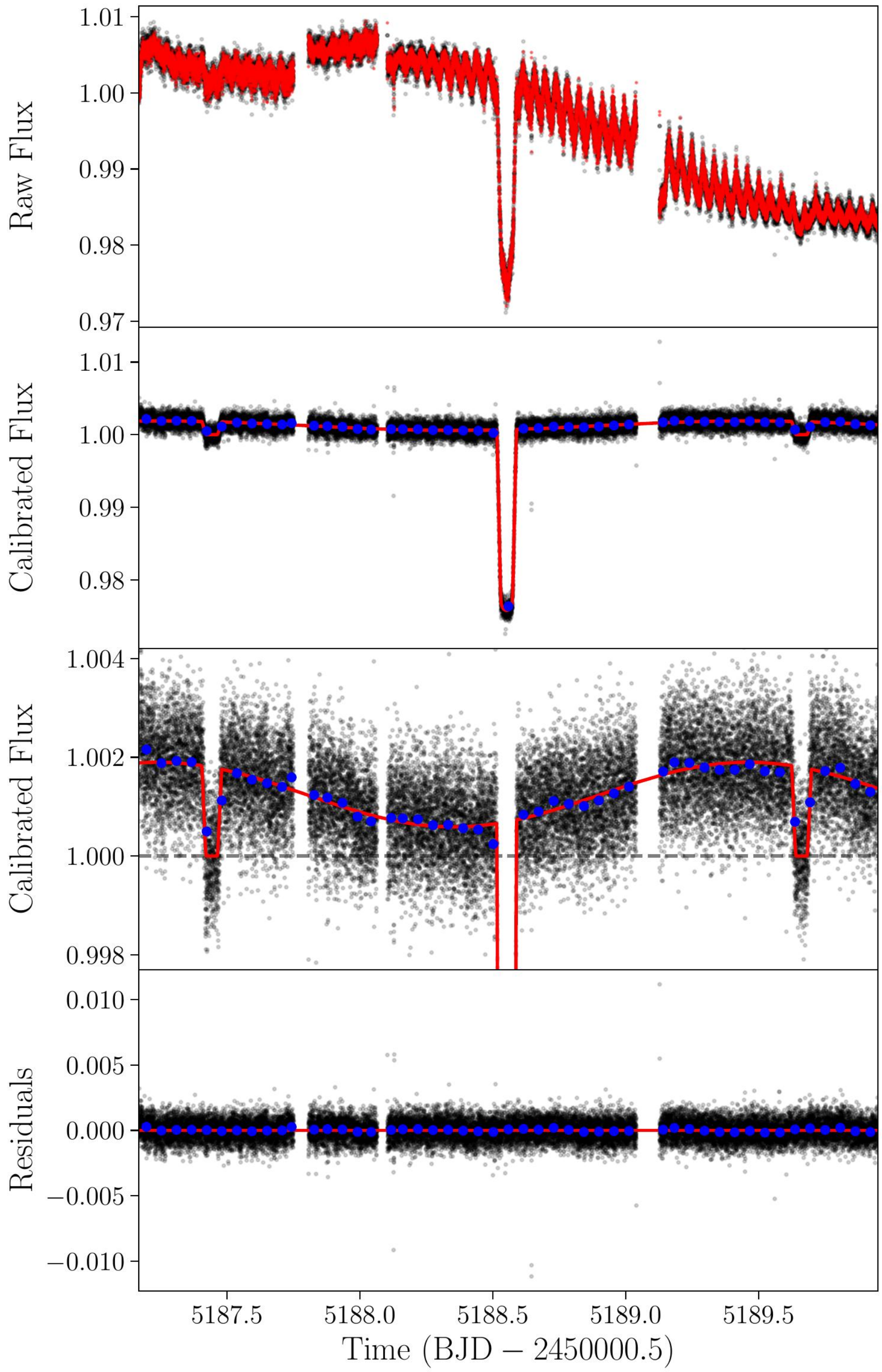

Figure A5. Preferred model fit (Poly5_v1) for HD 189733b.

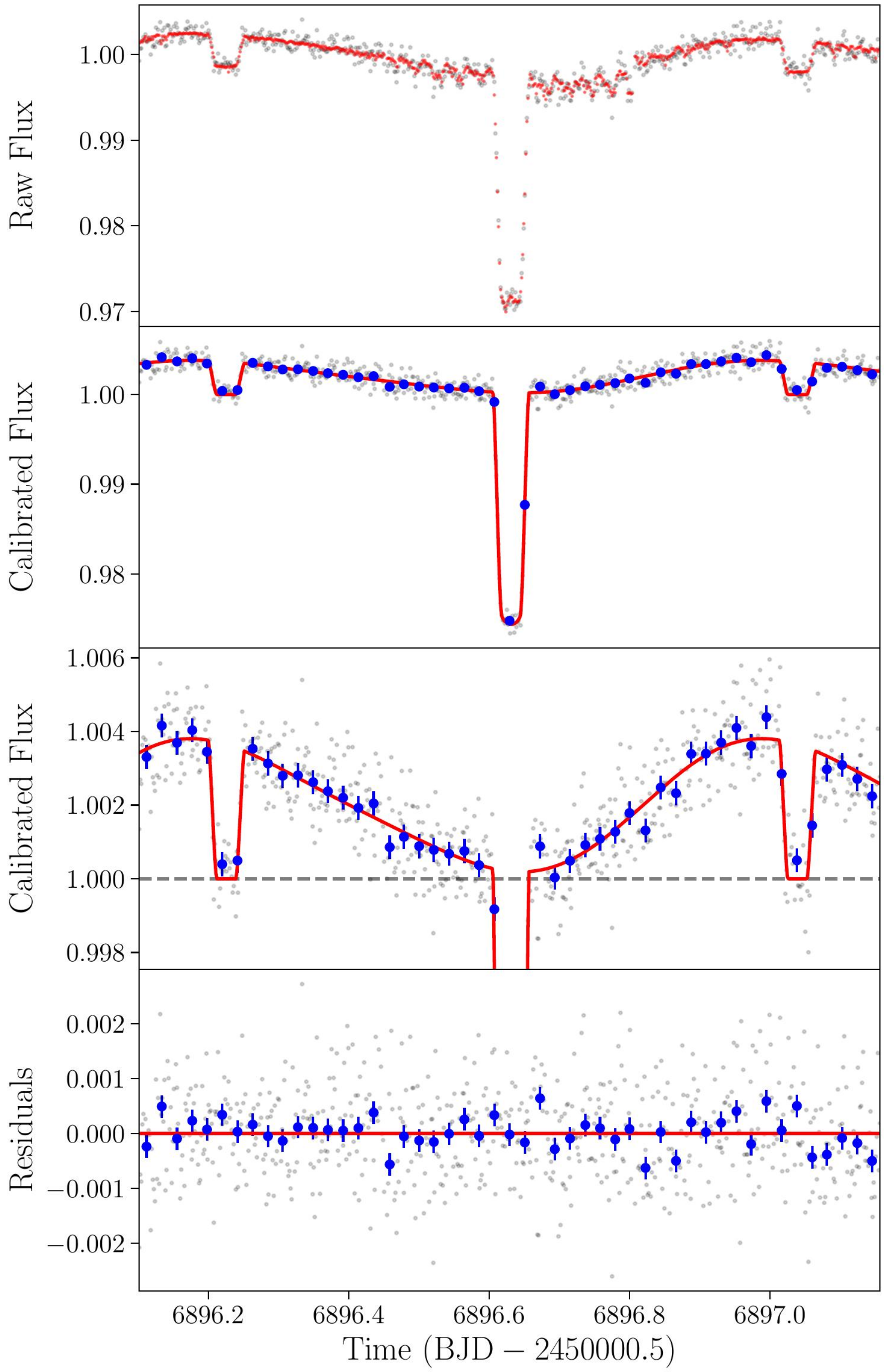

Figure A6. Preferred model fit (BLISS_v2) for WASP-43b.

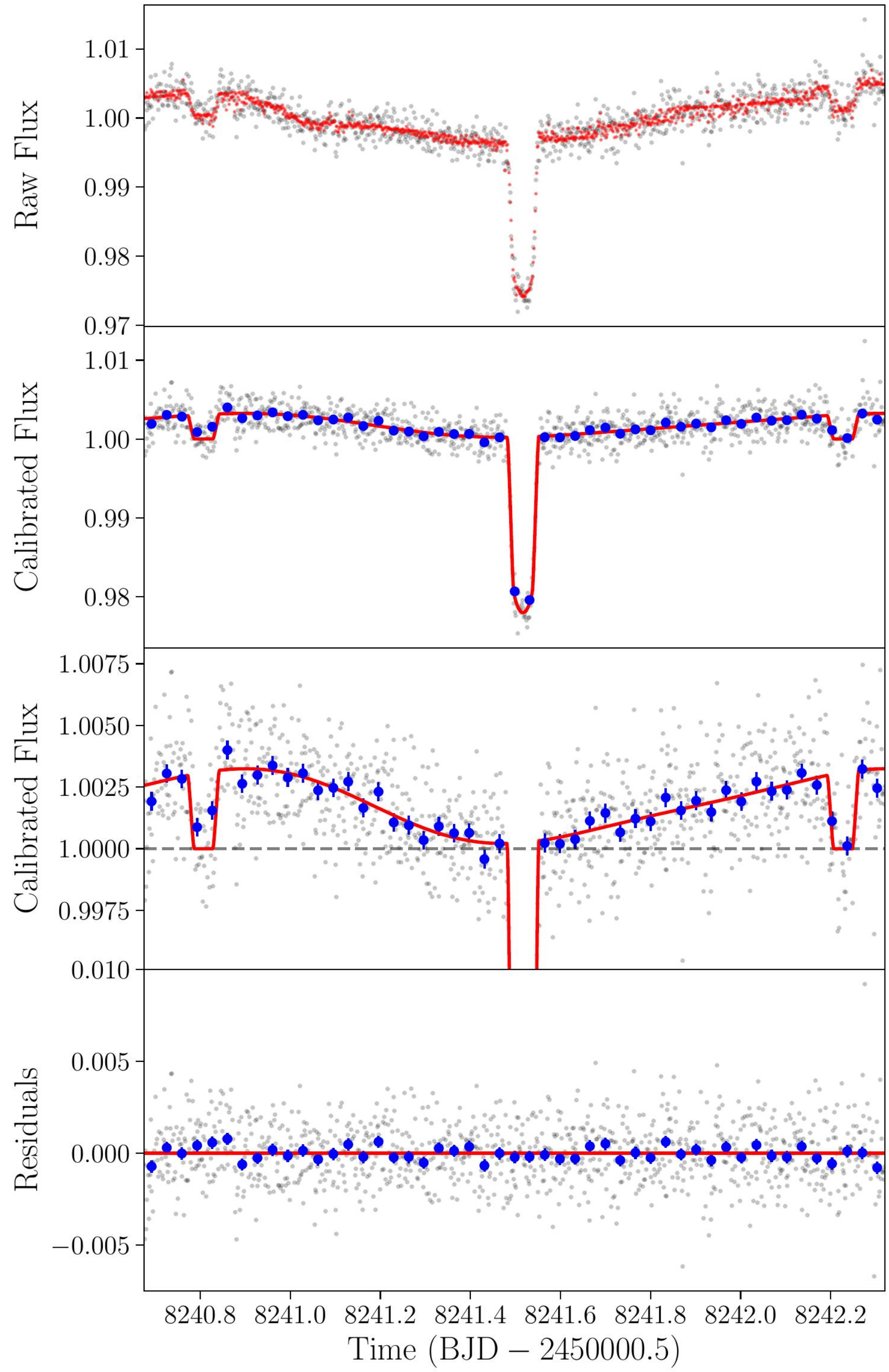

Figure A7. Preferred model fit (BLISS_v2) for Qatar-1b.

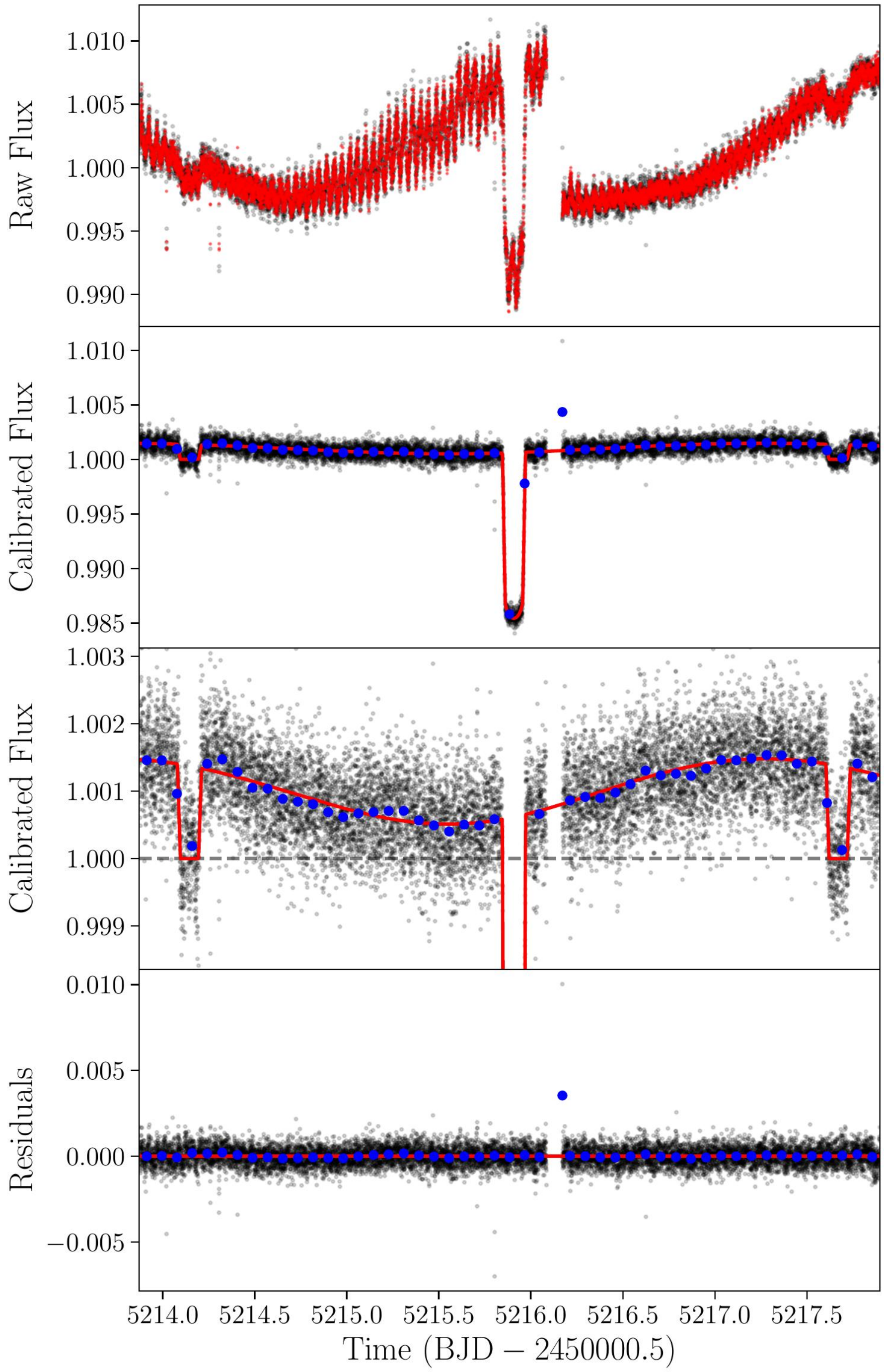

Figure A8. Preferred model fit (Poly5_v1) for HD 209458b.

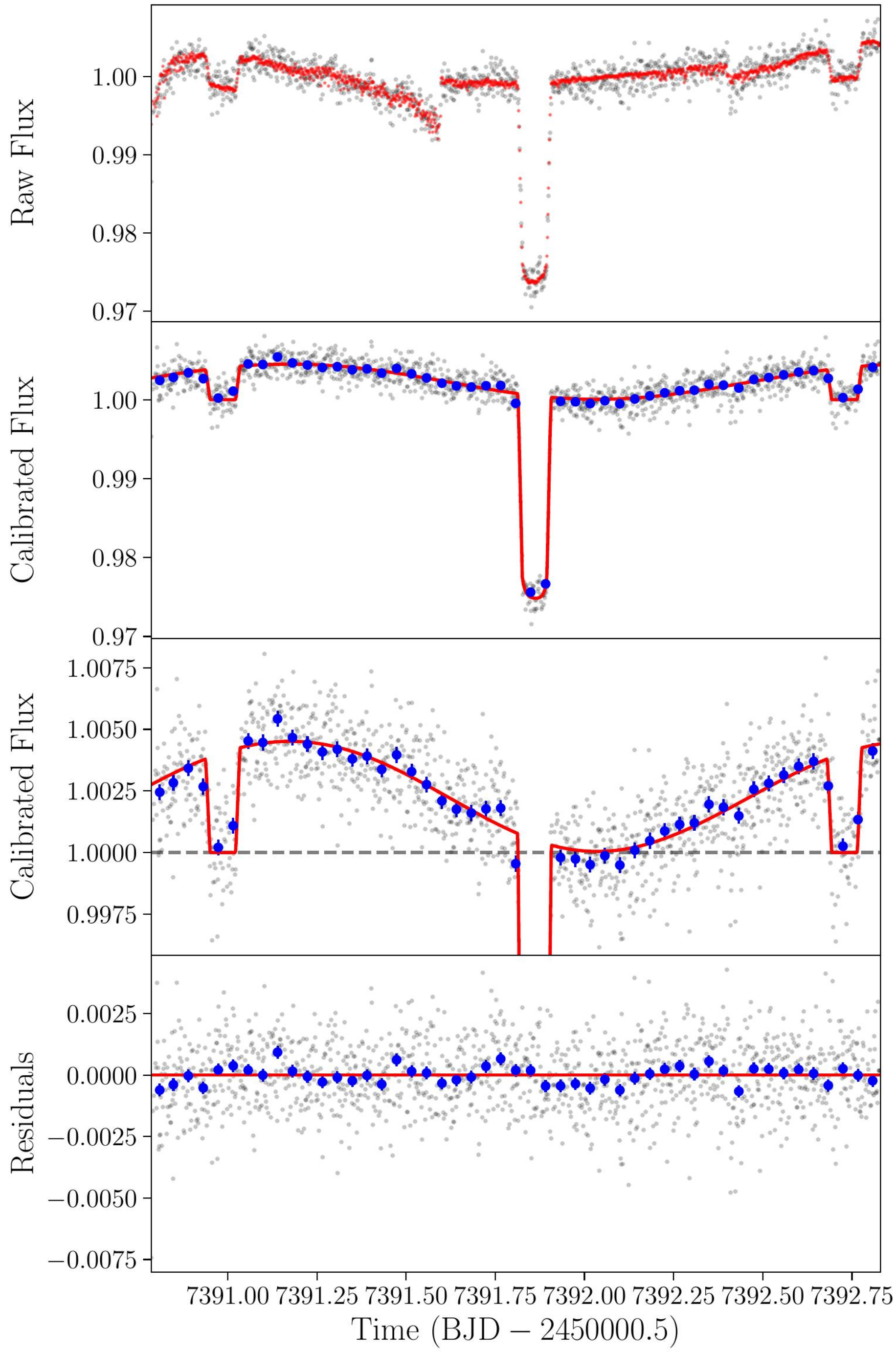

Figure A9. Preferred model fit (Poly4_v1) for CoRoT-2b.

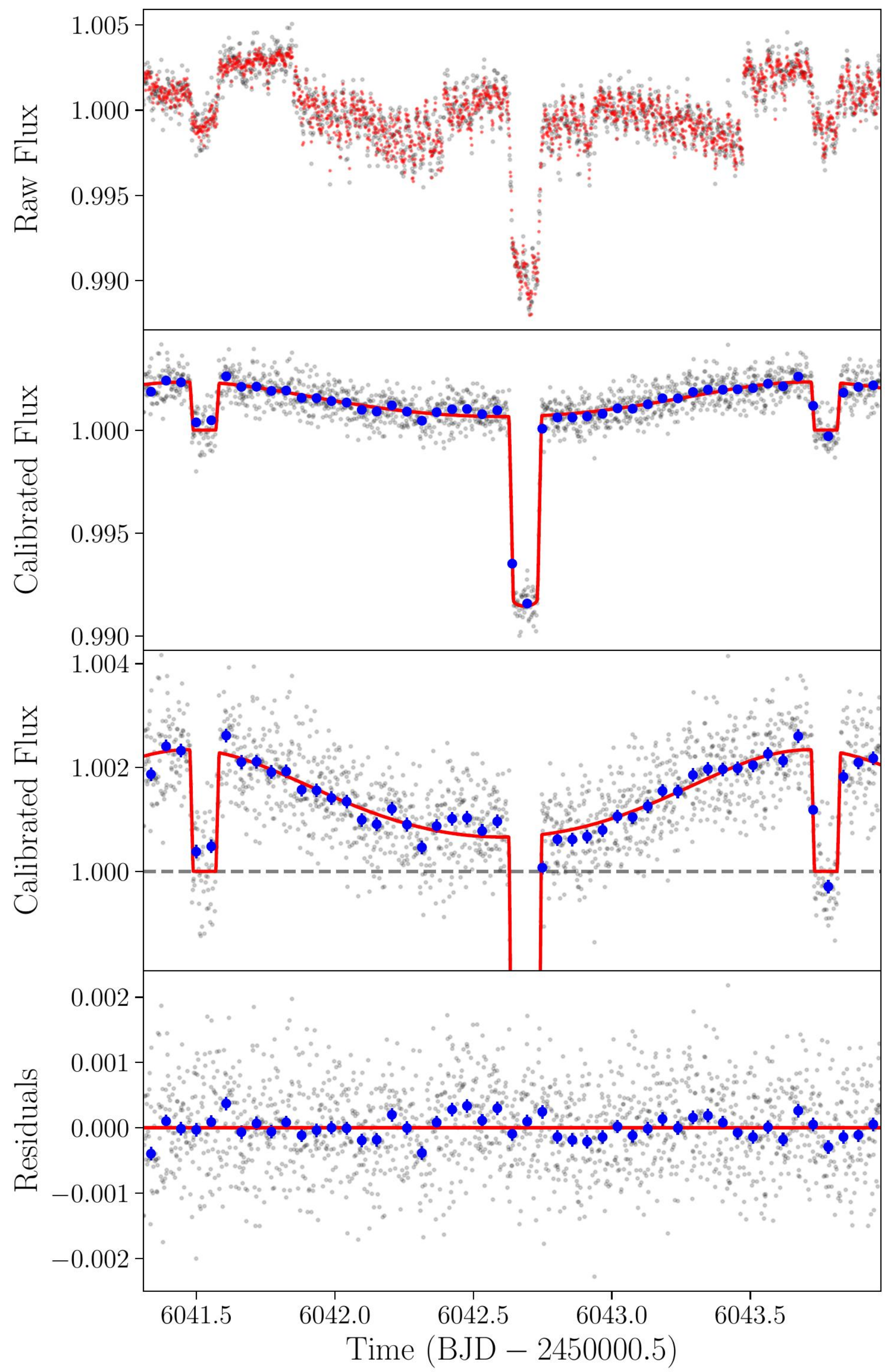

Figure A10. Preferred model fit (PLDAper1_3x3_v1) for WASP-14b.

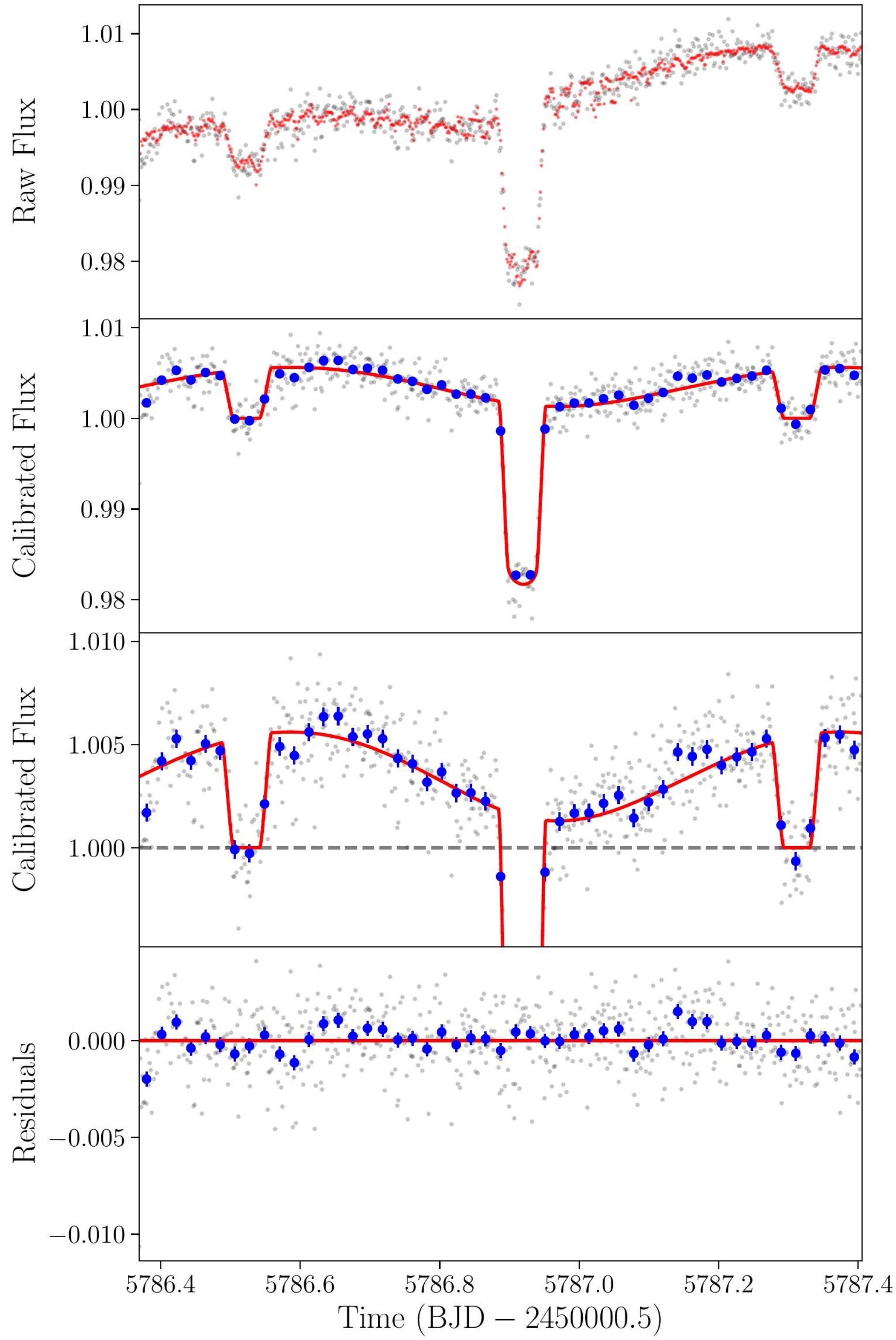

Figure A11. Preferred model fit (BLISS_v1) for WASP-19b.

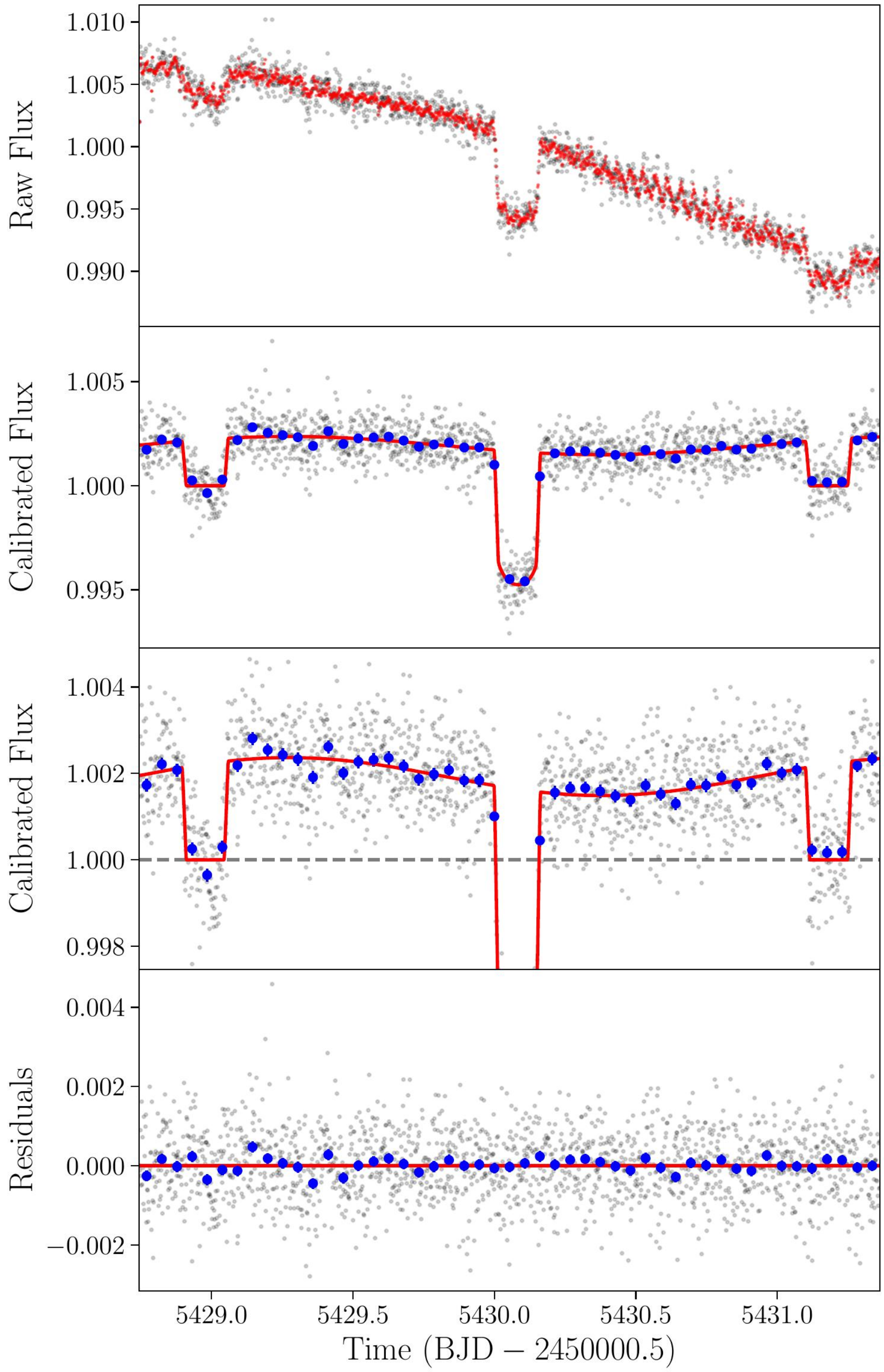

Figure A12. Preferred model fit (BLISS_v1) for HAT-P-7b.

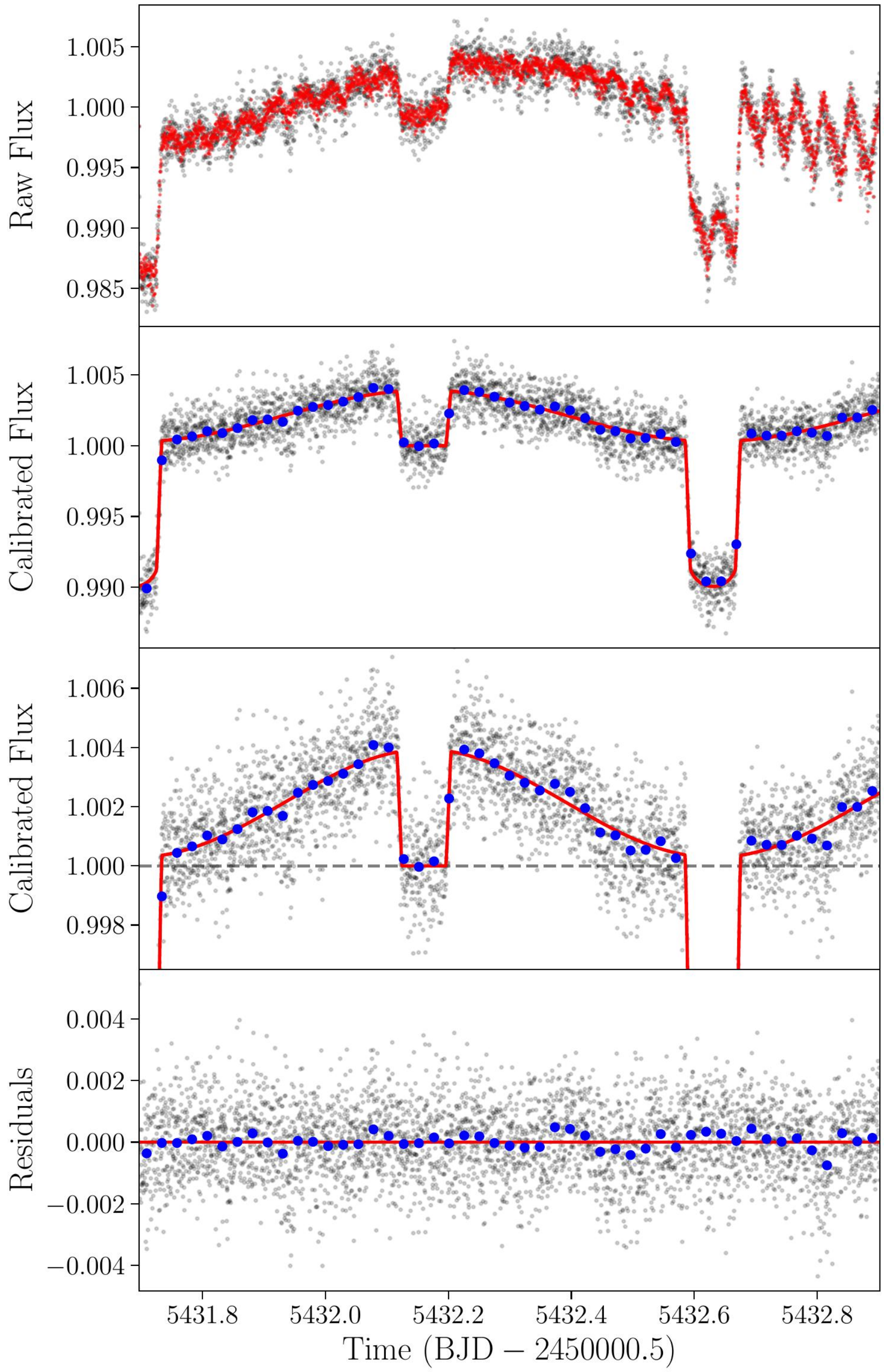

Figure A13. Preferred model fit (BLISS_v1) for WASP-18b.

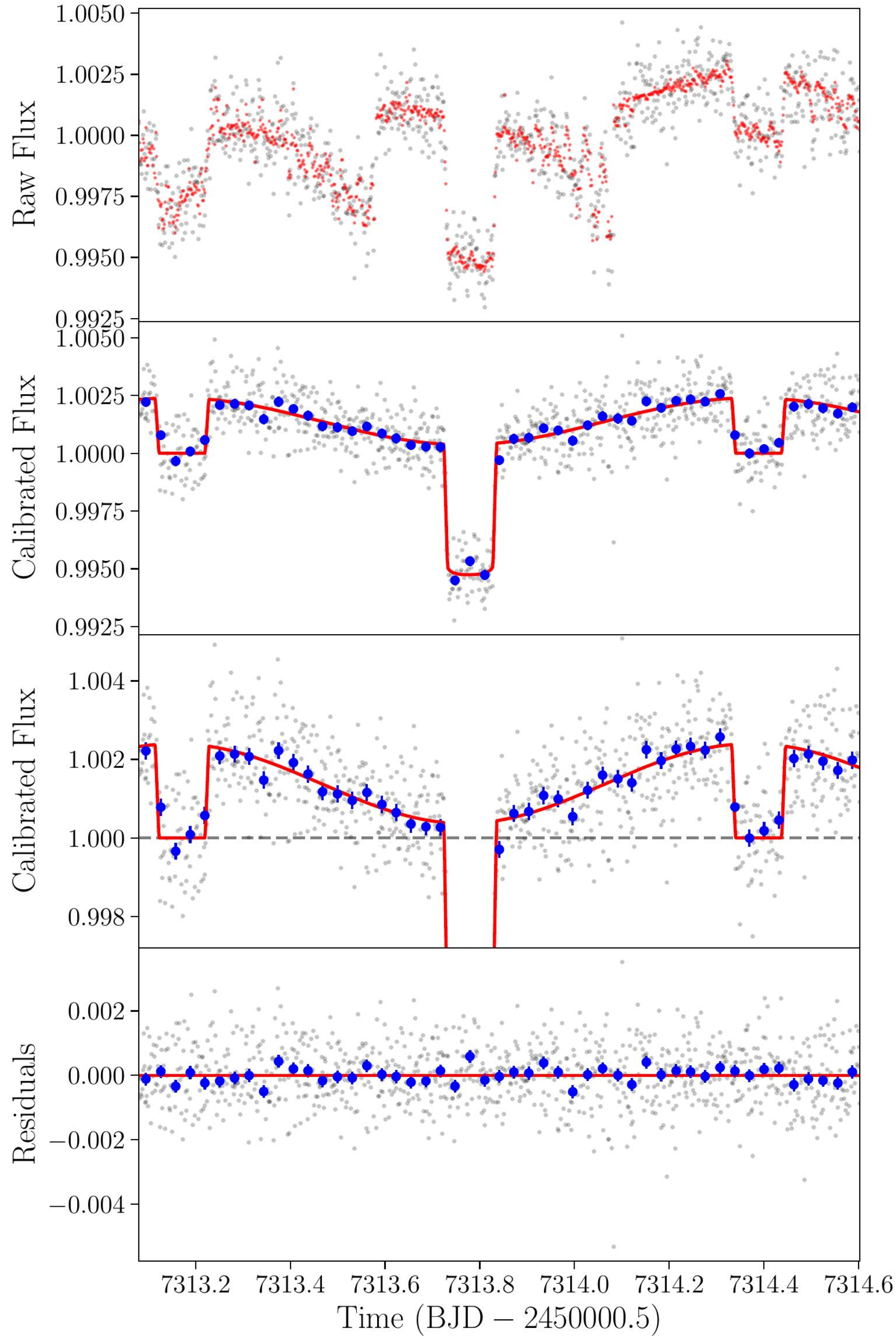

Figure A14. Preferred model fit (BLISS_v1 with PSF centroiding) for KELT-1b.

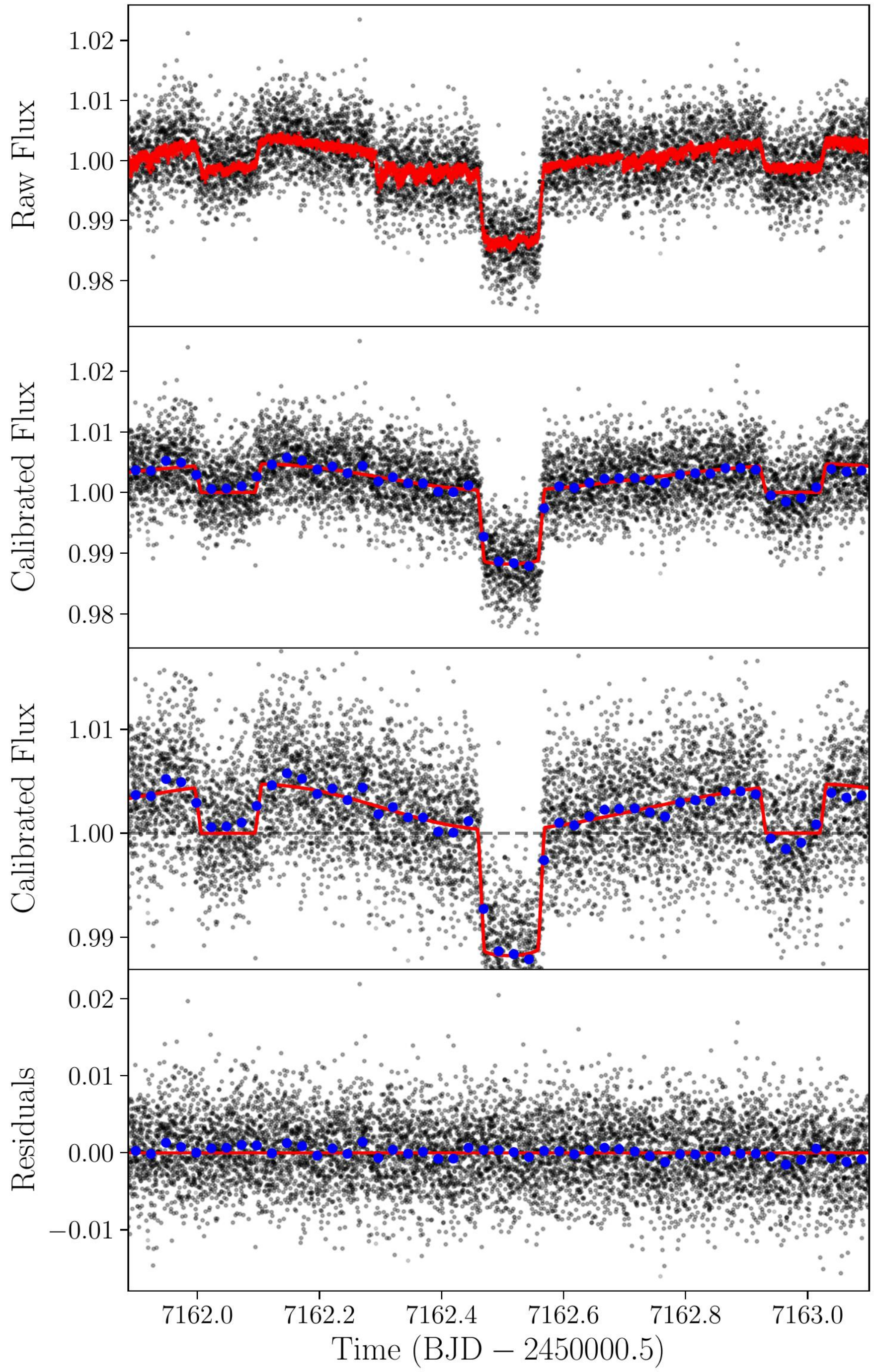

Figure A15. Preferred model fit (BLISS_v2) for the unbinned WASP-103b photometry.

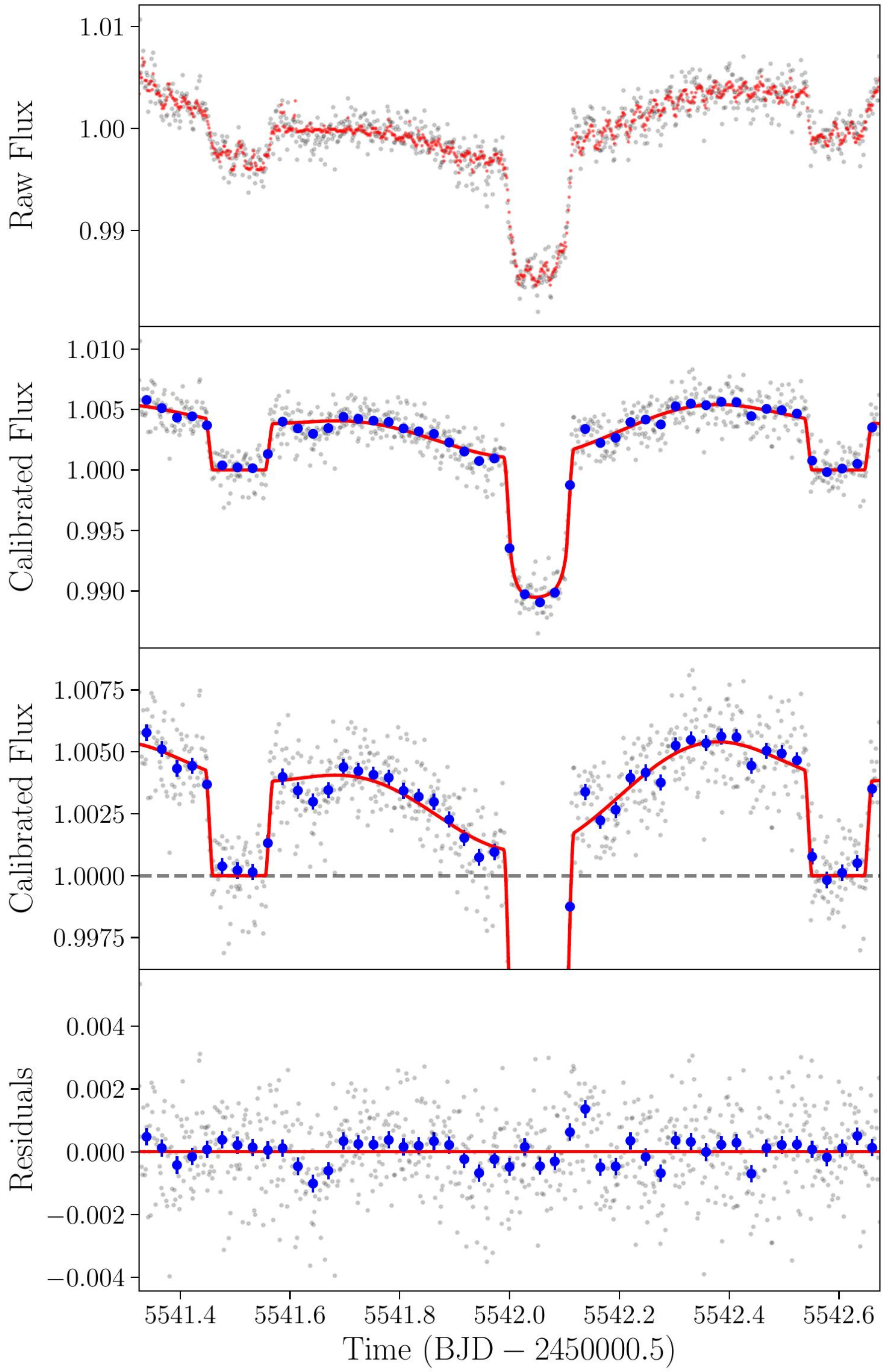

Figure A16. Preferred model fit (BLISS_v2) for WASP-12b (2010).

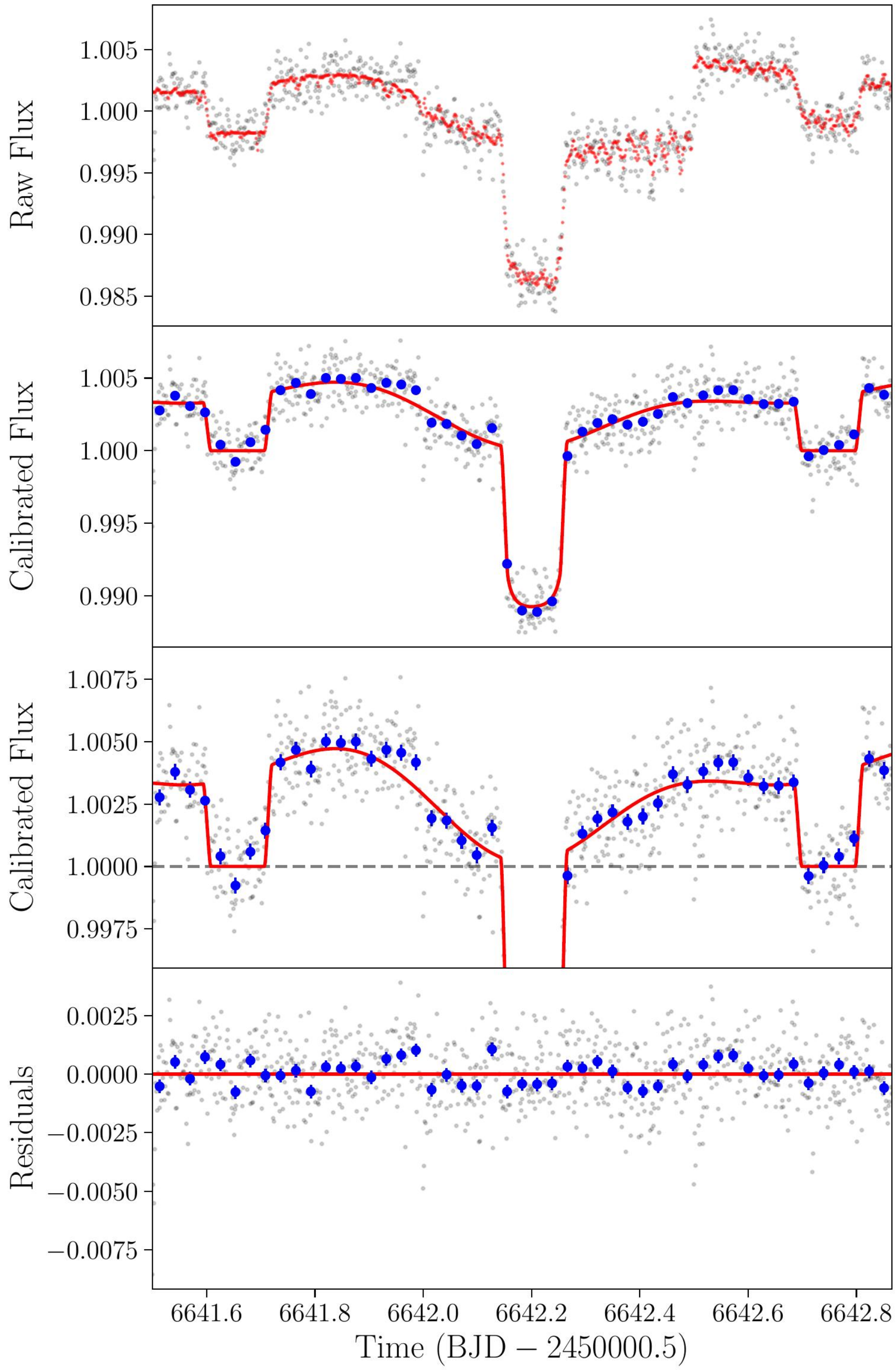

Figure A17. Preferred model fit (BLISS_v2) for WASP-12b (2013).

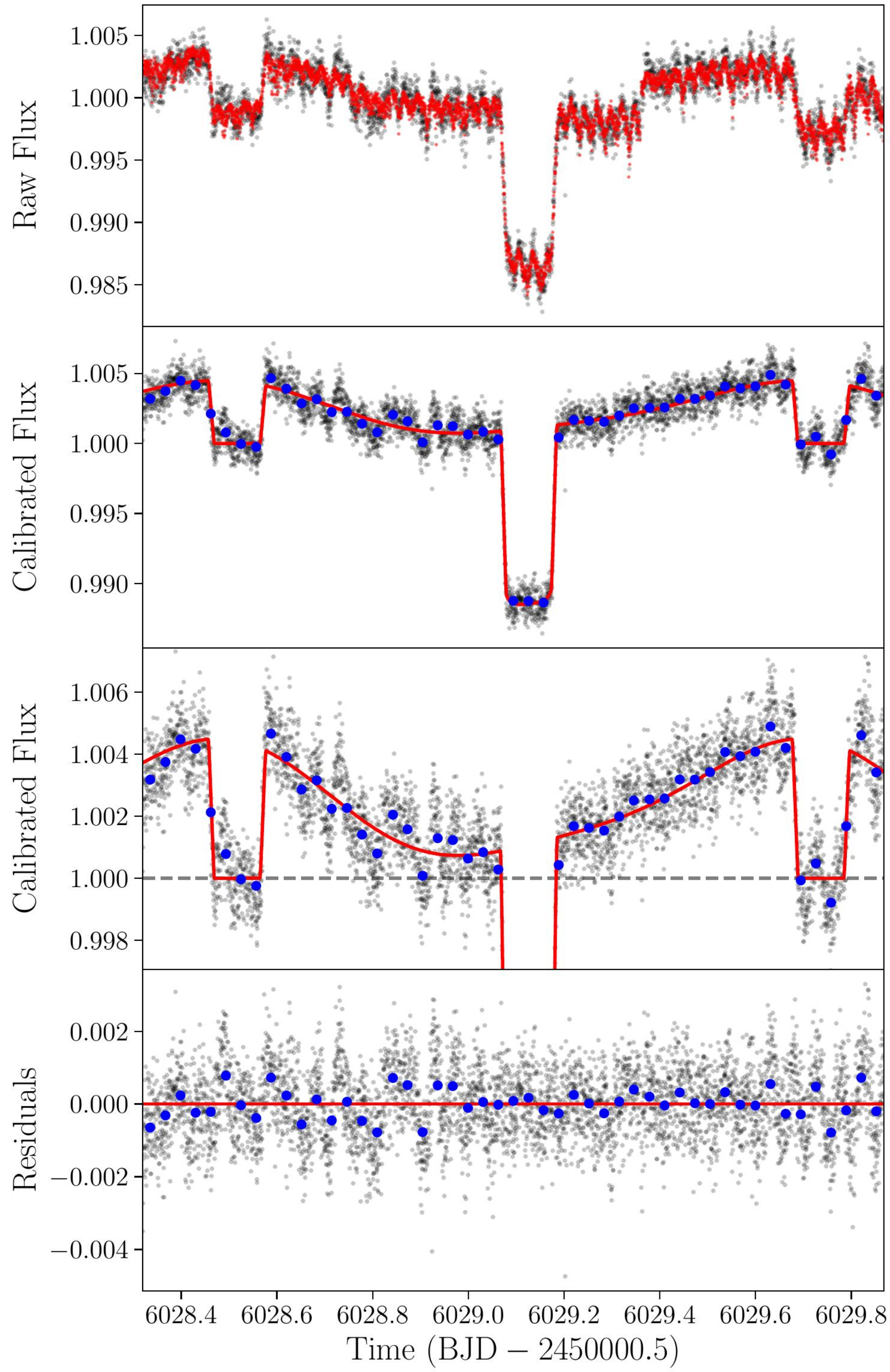

Figure A18. Preferred model fit (PLDAper1_3x3_v2) for WASP-33b. The high frequency residual noise is caused by the unmodelled variability of the host star.

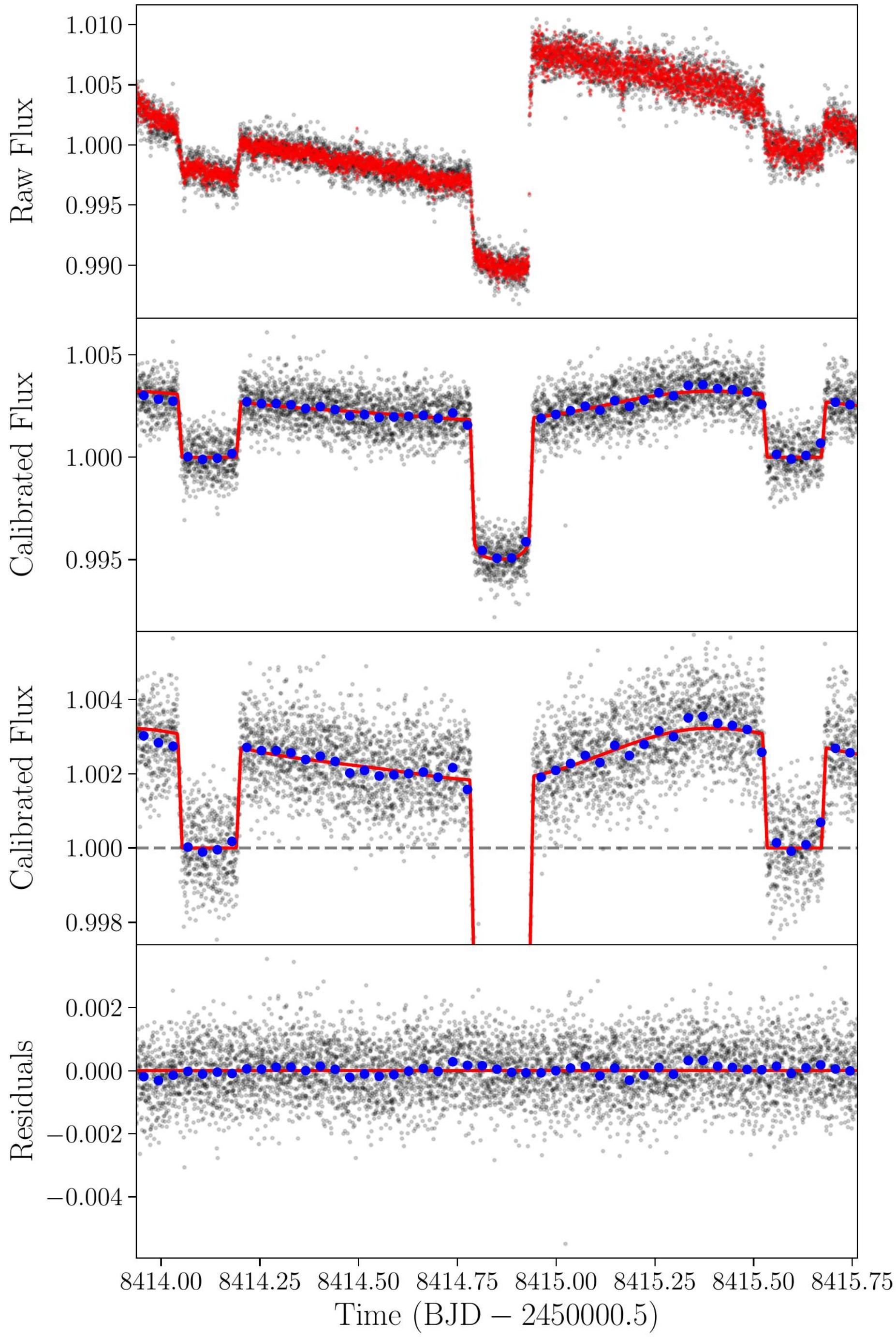

Figure A19. Preferred model fit (PLDAper1_3x3_v2) for KELT-9b.

Epilogue

The `SPCA` pipeline co-developed by Lisa Dang and myself was also used by Keating et al. (2020, for which Lisa and I were both co-authors) to analyze the 3.6 and 4.5 μm phase curves of Qatar-1b. Dylan Keating also used an earlier version of our `SPCA` pipeline to test the reproducibility of the KELT-9b phase curve as was discussed by Mansfield et al. (2020). Lisa Dang is also using the `SPCA` pipeline to analyze the *Spitzer*/IRAC phase curve observations of the eccentric orbit hot Jupiter XO-3b; this work is currently in prep. with myself as a co-author. I also used the same code used to generate Figure 12 of Bell et al. (2021) to provide Figure 7 from (Fortney et al., 2021), using instead the literature values for each phase curve. Additionally, I have reanalyzed all of the previously published 3.6 μm phase curve observations with an older version of the `SPCA` pipeline, but I decided to leave the reanalysis of those (much noisier and harder to decorrelate) observations for a future publication. Looking forward, I have talked with Giuseppe Morello about incorporating his pixel-ICA decorrelation technique (Morello et al., 2019) for *Spitzer*/IRAC observations into our `SPCA` pipeline. Further, two McGill undergraduate students (Samson Mercier and Alex Gass) under the supervision of Lisa Dang and Nicolas Cowan are currently using our `SPCA` pipeline to test the reproducibility of the 55 Cancri e phase curve observations which were omitted from Bell et al. (2021) due to the enormity of that data set and the significant differences between that data set and the phase curve observations of other hot Jupiters. Finally, I was a co-author on the paper which presented the current observing strategy for *ARIEL*'s exoplanet phase curve program which will uniformly measure the phase curves of $\sim$35 exoplanets (Charnay et al., 2021).

Discussion and Conclusion

Comprehensive Discussion

In this thesis, I have gathered together four published works presenting theoretical, optical, and infrared characterization of ultra-hot Jupiter atmospheres. Together, these papers formulate and test a new theory for ultra-hot Jupiter atmospheric composition and heat transport. I summarize the main results from these works below and provide updates from the literature since the publication of these papers.

In Bell et al. (2017), I presented the optical eclipse spectrum of WASP-12b as observed by *Hubble*/STIS which showed that the ultra-hot Jupiter reflects $< 6\%$ of its incident starlight across the instrument's 290–570 nm bandpass. This was in stark contrast to the detection of reflected light at blue wavelengths from the much cooler HD 189733b which is the only other hot Jupiter with spectrally resolved reflected light observations (Evans et al., 2013). Combined with previous eclipse observations of WASP-12b spanning 1–8 μm, our optical eclipse observations suggested that the $\sim$3000 K dayside of WASP-12b was devoid of clouds and consisted primarily of atomic hydrogen and helium. This showed that the dayside atmospheres of ultra-hot Jupiters are similar to those of stars, with most molecules—including the dominant constituent H_2—becoming thermally dissociated. Since the publication of Bell et al. (2017), Hooton et al. (2019) published ground-based photometric optical eclipse depths in the near-infrared i′-band which suggest eclipse depth variability which was also previously seen in the z′-band (López-Morales et al., 2010; Föhring et al., 2013). von Essen et al. (2019) also published ground-based eclipse depths of WASP-12b in the V-band which probes the same wavelengths as the two longest wavelength bins in Bell et al. (2017). While the second eclipse measured by von Essen et al. (2019) was consistent with Bell et al. (2017), the first and third eclipses measured by von Essen et al. (2019) differed significantly from Bell et al. (2017), lending further evidence for optical eclipse depth variability on WASP-12b. However, no eclipse depth variability was seen in the TESS-band over the ∼27 days that the system was observed by TESS (Owens et al., 2021).

Meanwhile, hot Jupiters are far cooler on their nightsides because they rotate synchronously with their orbital period (giving one permanently illuminated hemisphere; e.g., Guillot et al. 1996), and the radiative timescale of their atmosphere scales as T^{-3} which renders heat transport through advection minimally effective, especially for ultra-hot Jupiters. Realizing that this enormous day–night temperature contrast would result in atomic hydrogen from the daysides of ultra-hot Jupiters recombining into molecules on their nightsides, I sought to model the potential thermodynamic impacts of the $H_2 \leftrightarrow 2H$ process on the atmospheres of these planets; the formation of H_2 is an extremely exothermic process used on Earth for high-temperature welding. Building on a previously published semi-analytical energy balance model for hot Jupiters (Cowan & Agol, 2011a), I developed a theory that accounts for the heating and cooling effects of H_2 recombination and dissociation in ultra-hot Jupiter atmospheres (Bell & Cowan, 2018). Numerically solving these equations across the planet's atmosphere, I found that this $H_2 \leftrightarrow 2H$ cycle acts in a manner similar to latent heat and significantly increases the efficiency of day–night heat transport. This model qualitatively explained the unusually large phase offsets of WASP-12b and WASP-33b known at the time (Cowan et al., 2012; Zhang et al., 2018) and successfully predicted the large phase offset and extremely hot nightside temperature of KELT-9b (Mansfield et al., 2020, for which I was a co-author). The TESS phase curve of KELT-9b may even suggest that the nightside of the planet is so hot that it remains significantly atomic (Wong et al., 2020b). The TESS phase curve of WASP-33b suggests that the planet also shows far greater day–night heat recirculation than would be predicted in the absence of H_2 dissociation (von Essen et al., 2020). The `Bell_EBM` code was also independently used by Daylan et al. (2019) and Keating et al. (2019), and Keating et al. (2019) found that the H_2 dissociation model was best able to fit the collection of previously published nightside temperatures. A subsequent analytical model developed by Komacek & Tan (2018) and a full general circulation model developed by Tan & Komacek (2019) later confirmed the importance of this $H_2 \leftrightarrow 2H$ cycle. Other works also studied the effects of H_2 dissociation and molecular dissociation in general on the thermal structure of ultra-hot Jupiters (e.g., Parmentier et al., 2018; Lothringer et al., 2018).

Building on the expertise I developed with precise reduction and analysis of space-based observations from my *Hubble*/STIS observations (Bell et al., 2017), I co-wrote `SPCA` which is an open-source reduction and analysis pipeline for *Spitzer*/IRAC channel 1 and 2 phase curve observations. In Bell et al. (2019), I used an early form of the `SPCA` pipeline to test the reproducibility of Cowan et al.'s (2012) finding that the WASP-12 system showed enormous ellipsoidal variations at 4.5 μm (implying the planet's radius from the sub-solar point to anti-solar point was nearly twice as large as the radius from the morning terminator to the evening terminator) while no such signal was seen at 3.6 μm. In this work, I refitted Cowan et al.'s (2012) original phase curves and analysed a new set of phase curve observations of WASP-12b which confirmed the astrophysical nature of the signal reported by Cowan et al. (2012). I also showed that the observations could not be explained by tidal distortion or star spots and were instead best explained by CO emission from a stream of gas being stripped from the planet which is consistent with earlier near-UV transit observations which showed that the planet was rapidly losing mass (e.g., Fossati et al., 2010). I have led a successful 2021A proposal to observe the WASP-12 system with CFHT/SPIRou to test my hypothesis by observing the 2.4 μm emission feature of CO and to test a new hypothesis for the observed orbital decay of the planet: rapid mass loss through the planet's L2 Lagrange point. I have also led a successful Cycle 28 proposal to observe the phase curve of WASP-12b with *Hubble*/WFC3 which will provide further insight into the thermal structure of the planet and will measure longitudinal variations in the relative abundances of H_2O and H^-.

A partial *Hubble*/WFC3 phase curve of WASP-12b was previously collected in 2012 (Program 12230, PI: M. R. Swain) but was only recently published by Arcangeli et al. (2021); these observations consist of three visits over a span of five days which collected five *Hubble* orbits around eclipse, five *Hubble* orbits around transit, and two *Hubble* orbits after transit near the time when the planet was near quadrature. Arcangeli et al. (2021) find no evidence for an increase in flux near quadrature which is consistent with the hypothesis of CO emission from Bell et al. (2019), but the multi-epoch nature of these observations leads to increased uncertainties and stronger systematic effects (e.g., for a similar multi-epoch phase curve study with *Spitzer* Krick et al., 2016). Comparing these multi-epoch phase curve observations with my team's full-orbit phase curve observations will provide an interesting test of the reproducibility of the multi-epoch phase curve technique for *Hubble*/WFC3 observations. Using TESS observations, Owens et al. (2021) also do not see an increase in flux near quadrature. Owens et al. (2021) also find an eastward phase offset in the TESS phase curve that was consistent with the phase offset at 3.6 μm in the 2010 observations but 3.8σ discrepant with the westward phase offset seen in the 2013 3.6 μm phase curve (Bell et al., 2019). While Arcangeli et al. (2021) do not report a phase offset from their multi-epoch phase curve observations, their observations appear to prefer a marginally westward phase offset.

Our `SPCA` pipeline was also used to analyse the new phase curves of the hot Jupiter Qatar-1b (Keating et al., 2020, for which I was a co-author) and the ultra-hot Jupiters KELT-16b and MASCARA-1b (Bell et al., 2021). This most recent work of mine (Bell et al., 2021) also performs the first comprehensive reanalysis of 4.5 μm *Spitzer* phase curves while using a wide range of detector models to test the reproducibility of 15 previously published phase curve analyses and to test for dependencies on the decorrelation model used. This enormous undertaking, requiring the manipulation of $\sim$300 GB of observations and the fitting of 488 models requiring in excess of 2 000 CPU hours total, was only possible due to the highly automated and optimized nature of our `SPCA` pipeline. These numerous reanalyses show that the retrieval of phase curve parameters is usually independent of the detector model used, but there are rare cases when the detector systematics are far worse than typical where strong model dependencies arise. My reanalyses are also typically consistent with the literature, although we identify several cases where one or more of our fitted parameters are inconsistent with those in the literature. Using our uniform reanalyses, we also measure numerous population-level trends such as that of dayside and nightside temperatures with irradiation temperature or normalized phase curve amplitude with stellar effective temperature. Through this uniform reanalysis, we can also confirm the strong deviation in the nightside temperatures of ultra-hot Jupiters (and especially KELT-9b) compared to their cooler cousins which is indicative of the increased heat-transport provided by H_2 dissociation/recombination (Bell & Cowan, 2018; Komacek & Tan, 2018; Tan & Komacek, 2019). A similar reproducibility study for Spitzer's previously published 3.6 μm phase curves (as well as a uniform analysis of all *Spitzer* phase curves ever collected) is left for future work as phase curves taken with channel 1 tend to be far noisier and harder to decorrelate due to the worse undersampling of the star's point-spread function.

Moving forwards, it is critical that the field of exoplanetary atmospheric characterization moves towards increased reproducibility through open-source code. In the era of *Spitzer* and *Hubble*, nearly all research teams chose to write their own proprietary reduction and decorrelation pipelines which resulted in a great deal of redundant labour and potentially unreproducible (or at least non-uniform) conclusions. Also, while some open-source pipelines do exist, they are not always easily usable which significantly reduces the likelihood that an independent team will use the pipeline, making it essentially proprietary. Consistent, transparent pipelines will also be especially critical for future survey missions like *ARIEL* which will characterize $\sim$1000 exoplanets.

In my near future, I will work to develop an `SPCA`-like pipeline for *Hubble*/WFC3 observations (in preparation for my WASP-12b phase curve). *Hubble*/WFC3 shows systematics similar to those of the *Hubble*/STIS instrument, although with its own unique challenges. To date, only one open-source pipeline exists for *Hubble*/WFC3 observations[1], and it does not support phase curve observations; an additional, independent, and easily usable open-source pipeline will allow for greater tests of reproducibility and a reduction in redundant labour from each research team needing to develop their own pipeline. In addition, I will also make an open-source reduction and decorrelation pipeline for *JWST*/MIRI LRS observations in my role as a postdoctoral researcher under the supervision of Thomas Greene at NASA Ames. While this pipeline will first be used to analyze guaranteed time observations led by Thomas Greene, the idea is to make the pipeline open-source and easily usable from the start to avoid repeating the same mistake of having many proprietary pipelines as was previously done for *Spitzer*/IRAC and *Hubble*/WFC3 observations.

Conclusion

Over the past 33 years, there has been an explosion in the number of confirmed planets thanks to survey missions like *Kepler*, which discovered a third of all confirmed exoplanets[2]. Meanwhile, much of exoplanet atmospheric characterization has been performed through individual studies with major observatories like *Hubble* and *Spitzer*. *JWST* will continue this legacy in the coming years while providing a far larger spectral range and a significantly reduced photon noise limit. Meanwhile, the *ARIEL* mission will finally bring exoplanetary atmospheric characterization into an era of survey studies with the detailed characterization of ∼1000 exoplanets.

Among the thousands of confirmed exoplanets, a new class called "ultra-hot Jupiters" has recently been identified. These planets have daysides as hot as some stars and nightsides as hot as the daysides of the more typical hot Jupiters. In my thesis, I showed that the

[1] Iraclis: `https://github.com/ucl-exoplanets/Iraclis`

molecular hydrogen gas that comprises the atmospheres of these planets becomes thermally dissociated on their hot daysides which absorbs some of the incident stellar energy, and when that gas is carried toward the cooler nightside, the atomic hydrogen recombines into molecular hydrogen and releases the heat absorbed from the dayside. Thermal dissociation and photodissociation will also play an important role in the vertical temperature profiles of ultra-hot Jupiters as the dominant opacity sources change between different atomic, ionic, and molecular sources. Given the extremely hot nature of these planets, their atmospheres are also expected to be mostly devoid of clouds and highly coupled to the planetary magnetic fields. As such, these planets may offer the clearest path forwards to constraining future development of non-ideal, magnetohydrodynamic models which will have far-reaching impacts as the still poorly understood effects of magnetic fields are expected to play an important role in the atmospheres of all hot planets. Ultra-hot Jupiters are also among the most easily characterizable planets, and studying these planets' atmospheres also allows us to test and develop new technology and observing methods with the eventual goal of characterizing smaller, more temperate worlds.

References

Agúndez M., Parmentier V., Venot O., Hersant F., Selsis F., 2014, A&A, 564, A73
Arcangeli J., et al., 2018, ApJL, 855, L30
Arcangeli J., et al., 2019, A&A, 625, A136
Arcangeli J., Désert J. M., Parmentier V., Tsai S. M., Stevenson K. B., 2021, A&A, 646, A94
Armstrong D. J., de Mooij E., Barstow J., Osborn H. P., Blake J., Saniee N. F., 2016, Nature Astronomy, 1, 0004
Assmann R., 1902, Über die Existenz eines wärmeren Luftstromes in der Höhe von 10 bis 15km
Bastien P., et al., 2014, in Ramsay S. K., McLean I. S., Takami H., eds, SPIE Conference Series Vol. 9147, Ground-based and Airborne Instrumentation for Astronomy V. p. 91471S, doi:10.1117/12.2056789
Batygin K., Stanley S., 2014, ApJ, 794, 10
Batygin K., Stevenson D. J., 2010, ApJL, 714, L238
Baxter C., et al., 2020, A&A, 639, A36
Baxter C., et al., 2021, A&A, 648, A127
Beatty T. G., Marley M. S., Gaudi B. S., Colón K. D., Fortney J. J., Showman A. P., 2019, AJ, 158, 166
Beatty T. G., et al., 2020, AJ, 160, 211
Bell T. J., Cowan N. B., 2018, ApJL, 857, L20
Bell T. J., et al., 2017, ApJL, 847, L2
Bell T. J., et al., 2019, MNRAS, 489, 1995
Bell T. J., et al., 2021, MNRAS, 504, 3316
Beltz H., Rauscher E., Brogi M., Kempton E. M. R., 2021, AJ, 161, 1
Berdyugina S. V., Berdyugin A. V., Fluri D. M., Piirola V., 2008, ApJL, 673, L83
Birkby J. L., 2018, Spectroscopic Direct Detection of Exoplanets. p. 16, doi:10.1007/978-3-319-55333-7˙16
Birkby J. L., de Kok R. J., Brogi M., de Mooij E. J. W., Schwarz H., Albrecht S., Snellen I. A. G., 2013, MNRAS, 436, L35
Bond I. A., et al., 2017, MNRAS, 469, 2434
Bott K., Bailey J., Kedziora-Chudczer L., Cotton D. V., Lucas P. W., Marshall J. P., Hough J. H., 2016, MNRAS, 459, L109
Bott K., Bailey J., Cotton D. V., Kedziora-Chudczer L., Marshall J. P., Meadows V. S., 2018, AJ, 156, 293
Bourrier V., et al., 2020, A&A, 637, A36

Campbell B., Walker G. A. H., Yang S., 1988, ApJ, 331, 902
Carroll B. W., Ostlie D. A., 2006, An introduction to modern astrophysics and cosmology. Pearson Addison-Wesley
Cauley P. W., Shkolnik E. L., Llama J., Lanza A. F., 2019, Nature Astronomy, 3, 1128
Charbonneau D., Brown T. M., Latham D. W., Mayor M., 2000, ApJL, 529, L45
Charbonneau D., Brown T. M., Noyes R. W., Gilliland R. L., 2002, ApJ, 568, 377
Charbonneau D., et al., 2005, ApJ, 626, 523
Charbonneau D., Knutson H. A., Barman T., Allen L. E., Mayor M., Megeath S. T., Queloz D., Udry S., 2008, ApJ, 686, 1341
Charnay B., et al., 2021, Experimental Astronomy,
Chauvin G., Lagrange A. M., Dumas C., Zuckerman B., Mouillet D., Song I., Beuzit J. L., Lowrance P., 2005, A&A, 438, L25
Christensen P. R., Pearl J. C., 1997, J.~Geophys.~Res., 102, 10875
Cooper C. S., Showman A. P., 2006, ApJ, 649, 1048
Cowan N. B., Agol E., 2011a, ApJ, 726, 82
Cowan N. B., Agol E., 2011b, ApJ, 729, 54
Cowan N. B., Agol E., Charbonneau D., 2007, MNRAS, 379, 641
Cowan N. B., Machalek P., Croll B., Shekhtman L. M., Burrows A., Deming D., Greene T., Hora J. L., 2012, ApJ, 747, 82
Crossfield I. J. M., Hansen B. M. S., Harrington J., Cho J. Y.-K., Deming D., Menou K., Seager S., 2010, ApJ, 723, 1436
Crossfield I. J. M., Knutson H., Fortney J., Showman A. P., Cowan N. B., Deming D., 2012, ApJ, 752, 81
Crossfield I. J. M., et al., 2020, ApJL, 903, L7
Dang L., et al., 2018, Nature Astronomy, 2, 220
Daylan T., et al., 2019, arXiv e-prints, p. arXiv:1909.03000
Daylan T., et al., 2021, AJ, 161, 131
Deming D., Seager S., Richardson L. J., Harrington J., 2005, Nature, 434, 740
Deming D., et al., 2015, ApJ, 805, 132
Demory B.-O., et al., 2013, ApJL, 776, L25
Demory B.-O., et al., 2015, MNRAS, 450, 2043
Demory B.-O., et al., 2016, Nature, 532, 207
Désert J.-M., et al., 2011, ApJL, 731, L40
Dobbs-Dixon I., Cumming A., Lin D. N. C., 2010, ApJ, 710, 1395
Drummond B., et al., 2018a, ApJL, 855, L31
Drummond B., Mayne N. J., Manners J., Baraffe I., Goyal J., Tremblin P., Sing D. K., Kohary K., 2018b, ApJ, 869, 28
Drummond B., et al., 2020, A&A, 636, A68
Esteves L. J., De Mooij E. J. W., Jayawardhana R., 2015, ApJ, 804, 150
Evans T. M., et al., 2013, ApJL, 772, L16
Evans T. M., Aigrain S., Gibson N., Barstow J. K., Amundsen D. S., Tremblin P., Mourier P., 2015, MNRAS, 451, 680
Fazio G. G., et al., 2004, ApJs, 154, 10
Föhring D., Dhillon V. S., Madhusudhan N., Marsh T. R., Copperwheat C. M., Littlefair S. P., Wilson R. W., 2013, MNRAS, 435, 2268

Foreman-Mackey D., Hogg D. W., Lang D., Goodman J., 2013, PASP, 125, 306
Fortney J. J., Lodders K., Marley M. S., Freedman R. S., 2008, ApJ, 678, 1419
Fortney J. J., Dawson R. I., Komacek T. D., 2021, Journal of Geophysical Research (Planets), 126, e06629
Fossati L., et al., 2010, ApJL, 714, L222
Fressin F., et al., 2013, ApJ, 766, 81
Fulton B. J., et al., 2017, AJ, 154, 109
Garhart E., et al., 2020, AJ, 159, 137
Gaudi B. S., et al., 2017, Nature, 546, 514
Gaudi B. S., Seager S., Mennesson B., Kiessling A., Warfield K. R., Habitable Exoplanet Observatory Science Technology Definition Team 2018, Nature Astronomy, 2, 600
Gibson N. P., Aigrain S., Roberts S., Evans T. M., Osborne M., Pont F., 2012, MNRAS, 419, 2683
Goodman J., Weare J., 2010, Communications in Applied Mathematics and Computational Science, 5, 65
Guillot T., Burrows A., Hubbard W. B., Lunine J. I., Saumon D., 1996, ApJL, 459, L35
Hammond M., Pierrehumbert R. T., 2018, ApJ, 869, 65
Hansen J. E., Hovenier J. W., 1974, Journal of Atmospheric Sciences, 31, 1137
Harrington J., Hansen B. M., Luszcz S. H., Seager S., Deming D., Menou K., Cho J. Y.-K., Richardson L. J., 2006, Science, 314, 623
Hastings W. K., 1970, Biometrika, 57, 97
Hatzes A. P., Cochran W. D., Endl M., McArthur B., Paulson D. B., Walker G. A. H., Campbell B., Yang S., 2003, ApJ, 599, 1383
Heng K., 2017, Exoplanetary Atmospheres: Theoretical Concepts and Foundations
Heng K., Frierson D. M. W., Phillipps P. J., 2011, MNRAS, 418, 2669
Henry G. W., Marcy G. W., Butler R. P., Vogt S. S., 2000, ApJL, 529, L41
Hoeijmakers H. J., et al., 2018, Nature, 560, 453
Hooton M. J., de Mooij E. J. W., Watson C. A., Gibson N. P., Galindo-Guil F. J., Clavero R., Merritt S. R., 2019, MNRAS, 486, 2397
Howard A. W., et al., 2012, ApJS, 201, 15
Hu R., Demory B.-O., Seager S., Lewis N., Showman A. P., 2015, ApJ, 802, 51
Hubeny I., Burrows A., Sudarsky D., 2003, ApJ, 594, 1011
Jansen T., Kipping D., 2020, MNRAS, 494, 4077
Keating D., Cowan N. B., Dang L., 2019, Nature Astronomy, 3, 1092
Keating D., et al., 2020, AJ, 159, 225
Kimble R. A., et al., 1998, ApJL, 492, L83
King M. D., Platnick S., Menzel W. P., Ackerman S. A., Hubanks P. A., 2013, IEEE Transactions on Geoscience and Remote Sensing, 51, 3826
Knollenberg R. G., Hunten D. M., 1980, J.~Geophys.~Res., 85, 8039
Knutson H. A., et al., 2007, Nature, 447, 183
Knutson H. A., et al., 2009a, ApJ, 690, 822
Knutson H. A., Charbonneau D., Cowan N. B., Fortney J. J., Showman A. P., Agol E., Henry G. W., 2009b, ApJ, 703, 769
Knutson H. A., et al., 2012, ApJ, 754, 22
Komacek T. D., Tan X., 2018, Research Notes of the American Astronomical Society, 2, 36

Komacek T. D., Showman A. P., Tan X., 2017, ApJ, 835, 198
Kreidberg L., et al., 2014, Nature, 505, 69
Kreidberg L., et al., 2018, AJ, 156, 17
Kreidberg L., et al., 2019, Nature, 573, 87
Krick J. E., et al., 2016, ApJ, 824, 27
Langton J., Laughlin G., 2008, ApJ, 674, 1106
Lanotte A. A., et al., 2014, A&A, 572, A73
Laughlin G., Deming D., Langton J., Kasen D., Vogt S., Butler P., Rivera E., Meschiari S., 2009, Nature, 457, 562
Lee E. J., Chiang E., 2016, ApJ, 817, 90
Lewis N. K., et al., 2013, ApJ, 766, 95
Liang M.-C., Seager S., Parkinson C. D., Lee A. Y. T., Yung Y. L., 2004, ApJL, 605, L61
Lines S., et al., 2018, A&A, 615, A97
Lines S., Mayne N. J., Manners J., Boutle I. A., Drummond B., Mikal-Evans T., Kohary K., Sing D. K., 2019, MNRAS, 488, 1332
Liou K.-N., 2002, An introduction to atmospheric radiation. Elsevier
López-Morales M., Coughlin J. L., Sing D. K., Burrows A., Apai D., Rogers J. C., Spiegel D. S., Adams E. R., 2010, ApJL, 716, L36
Lothringer J. D., Barman T., Koskinen T., 2018, ApJ, 866, 27
Louden T., Wheatley P. J., 2015, ApJL, 814, L24
Lyot B., 1929, Ann. Observ. Paris (Meudon), 8, 1
Maciejewski G., et al., 2016, A&A, 588, L6
Madhusudhan N., 2012, ApJ, 758, 36
Madhusudhan N., Amin M. A., Kennedy G. M., 2014, ApJL, 794, L12
Madhusudhan N., Agúndez M., Moses J. I., Hu Y., 2016, Space Sci. Rev., 205, 285
Majeau C., Agol E., Cowan N. B., 2012, ApJL, 747, L20
Mansfield M., et al., 2020, ApJL, 888, L15
Marley M. S., Ackerman A. S., Cuzzi J. N., Kitzmann D., 2013, Clouds and Hazes in Exoplanet Atmospheres. p. 367, doi:10.2458/azu_uapress_9780816530595-ch15
Marois C., Macintosh B., Barman T., Zuckerman B., Song I., Patience J., Lafrenière D., Doyon R., 2008, Science, 322, 1348
Marois C., Zuckerman B., Konopacky Q. M., Macintosh B., Barman T., 2010, Nature, 468, 1080
Masuda K., 2014, ApJ, 783, 53
Maxted P. F. L., et al., 2013, MNRAS, 428, 2645
May E. M., et al., 2021, arXiv e-prints, p. arXiv:2107.03349
Mayor M., Queloz D., 1995, Nature, 378, 355
Mendonça J. M., Tsai S.-m., Malik M., Grimm S. L., Heng K., 2018, ApJ, 869, 107
Mennesson B., et al., 2016, in MacEwen H. A., Fazio G. G., Lystrup M., Batalha N., Siegler N., Tong E. C., eds, Society of Photo-Optical Instrumentation Engineers (SPIE) Conference Series Vol. 9904, Space Telescopes and Instrumentation 2016: Optical, Infrared, and Millimeter Wave. p. 99040L, doi:10.1117/12.2240457
Menou K., 2012a, ApJ, 745, 138
Menou K., 2012b, ApJL, 754, L9

Metropolis N., Rosenbluth A. W., Rosenbluth M. N., Teller A. H., Teller E., 1953, J.~Chem.~Phys., 21, 1087
Miller-Ricci Kempton E., Rauscher E., 2012, ApJ, 751, 117
Morello G., Danielski C., Dickens D., Tremblin P., Lagage P. O., 2019, AJ, 157, 205
Morley C. V., Fortney J. J., Marley M. S., Zahnle K., Line M., Kempton E., Lewis N., Cahoy K., 2015, ApJ, 815, 110
Morley C. V., Knutson H., Line M., Fortney J. J., Thorngren D., Marley M. S., Teal D., Lupu R., 2017, AJ, 153, 86
Moses J. I., et al., 2013, ApJ, 777, 34
Niemann H. B., et al., 1996, Science, 272, 846
Nugroho S. K., Kawahara H., Masuda K., Hirano T., Kotani T., Tajitsu A., 2017, AJ, 154, 221
Öberg K. I., Murray-Clay R., Bergin E. A., 2011, ApJL, 743, L16
Owens N., de Mooij E. J. W., Watson C. A., Hooton M. J., 2021, MNRAS,
Parmentier V., Crossfield I. J. M., 2018, Exoplanet Phase Curves: Observations and Theory. Springer International Publishing, p. 116, doi:10.1007/978-3-319-55333-7˙116
Parmentier V., Fortney J. J., Showman A. P., Morley C., Marley M. S., 2016, ApJ, 828, 22
Parmentier V., et al., 2018, A&A, 617, A110
Parmentier V., Showman A. P., Fortney J. J., 2020, MNRAS,
Parviainen H., et al., 2021, A&A, 645, A16
Patra K. C., Winn J. N., Holman M. J., Yu L., Deming D., Dai F., 2017, AJ, 154, 4
Perez-Becker D., Showman A. P., 2013, ApJ, 776, 134
Perna R., Menou K., Rauscher E., 2010a, ApJ, 719, 1421
Perna R., Menou K., Rauscher E., 2010b, ApJ, 724, 313
Pierrehumbert R. T., 2010, Principles of Planetary Climate. Cambridge University Press
Rackham B. V., Apai D., Giampapa M. S., 2018, ApJ, 853, 122
Rackham B. V., Apai D., Giampapa M. S., 2019, AJ, 157, 96
Rasio F. A., Tout C. A., Lubow S. H., Livio M., 1996, ApJ, 470, 1187
Rauscher E., Kempton E. M. R., 2014, ApJ, 790, 79
Rauscher E., Menou K., 2012, ApJ, 750, 96
Rauscher E., Menou K., 2013, ApJ, 764, 103
Rauscher E., Menou K., Seager S., Deming D., Cho J. Y. K., Hansen B. M. S., 2007, ApJ, 664, 1199
Roberge A., Moustakas L. A., 2018, Nature Astronomy, 2, 605
Roberge A., Seager S., 2018, The "Spectral Zoo" of Exoplanet Atmospheres. Springer International Publishing, p. 98, doi:10.1007/978-3-319-55333-7˙98
Rodler F., Kürster M., Henning T., 2010, A&A, 514, A23
Rogers T. M., 2017, Nature Astronomy, 1, 0131
Rogers T. M., Komacek T. D., 2014, ApJ, 794, 132
Rogers T. M., Showman A. P., 2014, ApJL, 782, L4
Roman M. T., Kempton E. M. R., Rauscher E., Harada C. K., Bean J. L., Stevenson K. B., 2021, ApJ, 908, 101
Sagan C., Chyba C., 1997, Science, 276, 1217
Schwartz J. C., Kashner Z., Jovmir D., Cowan N. B., 2017, ApJ, 850, 154

Shapiro A. I., Solanki S. K., Krivova N. A., Schmutz W. K., Ball W. T., Knaack R., Rozanov E. V., Unruh Y. C., 2014, A&A, 569, A38
Showman A. P., Guillot T., 2002, A&A, 385, 166
Showman A. P., Polvani L. M., 2011, ApJ, 738, 71
Showman A. P., Fortney J. J., Lian Y., Marley M. S., Freedman R. S., Knutson H. A., Charbonneau D., 2009, ApJ, 699, 564
Shporer A., et al., 2019, AJ, 157, 178
Shvartzvald Y., et al., 2017, ApJL, 840, L3
Sing D. K., et al., 2011, MNRAS, 416, 1443
Sing D. K., et al., 2016, Nature, 529, 59
Smith B. A., et al., 1982, Science, 215, 504
Snellen I. A. G., de Kok R. J., de Mooij E. J. W., Albrecht S., 2010, Nature, 465, 1049
Spake J. J., et al., 2018, Nature, 557, 68
Stevenson K. B., et al., 2010, Nature, 464, 1161
Stevenson K. B., et al., 2012a, ApJ, 754, 136
Stevenson K. B., et al., 2012b, ApJ, 755, 9
Stevenson K. B., Bean J. L., Madhusudhan N., Harrington J., 2014, ApJ, 791, 36
Stevenson K. B., et al., 2017, AJ, 153, 68
Swain M. R., Vasisht G., Tinetti G., 2008, Nature, 452, 329
Swain M. R., Vasisht G., Tinetti G., Bouwman J., Chen P., Yung Y., Deming D., Deroo P., 2009, ApJL, 690, L114
Tan X., Komacek T. D., 2019, ApJ, 886, 26
Taylor J., Parmentier V., Line M. R., Lee E. K. H., Irwin P. G. J., Aigrain S., 2021, MNRAS, 506, 1309
Teisserenc de Bort L., 1902, Account. Makes. Acad Sessions. Sci. Paris, 134, 987
The LUVOIR Team 2019, arXiv e-prints, p. arXiv:1912.06219
Tinetti G., et al., 2007, Nature, 448, 169
Trainer M. G., et al., 2004, Astrobiology, 4, 409
Venot O., Hébrard E., Agúndez M., Dobrijevic M., Selsis F., Hersant F., Iro N., Bounaceur R., 2012, A&A, 546, A43
Werner M. W., et al., 2004, ApJs, 154, 1
Wiktorowicz S. J., 2009, ApJ, 696, 1116
Wiktorowicz S. J., Nofi L. A., Jontof-Hutter D., Kopparla P., Laughlin G. P., Hermis N., Yung Y. L., Swain M. R., 2015, ApJ, 813, 48
Wolszczan A., Frail D. A., 1992, Nature, 355, 145
Wong I., et al., 2015, ApJ, 811, 122
Wong I., et al., 2016, ApJ, 823, 122
Wong I., et al., 2020a, AJ, 159, 104
Wong I., et al., 2020b, AJ, 160, 88
Wong I., et al., 2020c, AJ, 160, 155
Yee S. W., et al., 2020, ApJL, 888, L5
Youdin A. N., 2011, ApJ, 742, 38
Zellem R. T., et al., 2014, ApJ, 790, 53
Zhang J., Kempton E. M. R., Rauscher E., 2017, ApJ, 851, 84
Zhang M., et al., 2018, AJ, 155, 83

de Wit J., Gillon M., Demory B. O., Seager S., 2012, A&A, 548, A128
de Wit J., Lewis N. K., Langton J., Laughlin G., Deming D., Batygin K., Fortney J. J., 2016, ApJL, 820, L33
de Wit J., et al., 2017, ApJL, 836, L17
von Essen C., et al., 2019, A&A, 628, A115
von Essen C., Mallonn M., Borre C. C., Antoci V., Stassun K. G., Khalafinejad S., Tautvaišienė G., 2020, A&A, 639, A34
von Essen C., et al., 2021, A&A, 648, A71

List of Abbreviations

AOR Astronomical Observation Request
ARIEL Atmospheric Remote-sensing Infrared Exoplanet Large-survey
BCD Basic Calibrated Data (File)
BIC Bayesian Information Criterion
BLISS BiLinearly-Interpolated Subpixel Sensitivity (Mapping)
BMJD Barycentric Modified Julian Date
CoRoT COnvection, internal ROtation and Transiting planets (Telescope)
CPU Central Processing Unit
CV Cataclysmic Variable (Star)
EBM Energy Balance Model
ESA European Space Agency
FITS Flexible Image Transport System (File)
FWM Flux-Weighted Mean
GCM General Circulation Model
GO General Observer (Proposal)
GP Gaussian Process
HAT Hungarian-made Automated Telescope
HD Henry Draper (Catalogue)
HST Hubble Space Telescope
ICA Independent Component Analysis
IRAC Infrared Array Camera (*Spitzer* Instrument)
IRAF Image Reduction and Analysis Facility (Software)
JWST James Webb Space Telescope
KELT Kilodegree Extremely Little Telescope
LTE Local Thermal Equilibrium
MAP Maximum A Posteriori (Estimate)
MASCARA Multi-site All-Sky CAmeRA (Telescopes)
MC Monte-Carlo
MCMC Markov Chain Monte-Carlo
MHD Magnetohydrodynamics
MLE Maximum Likelihood Estimation
NASA National Aeronautics and Space Administration
NaN Not a Number
NNI Nearest-Neighbour Interpolation
NUV Near Ultra-Violet

OLR Outgoing Longwave Radiation
PCRS Pointing Calibration and Reference Sensor (*Spitzer* Instrument)
PDF Probability Density Function
PI Principal Investigator (Proposal)
PID Program Identifier Number
PLD Pixel Level Decorrelation
POET Photometry for Orbits, Eclipses, and Transits (*Spitzer* Data Pipeline)
ppm Parts Per Million
PSF Point-Spread Function
Qatar Qatar Exoplanet Survey
RAM Random Access Memory
RMS Root Mean Square
SPCA Spitzer Phase Curve Analysis (*Spitzer* Data Pipeline)
STIS Space Telescope Imaging Spectrograph (*Hubble* Instrument)
SW Shortwave (Radiation)
TESS Transiting Exoplanet Survey Satellite
T-P Temperature-Pressure (Profile)
UHJ Ultra-hot Jupiter
UV Ultra-Violet
WASP Wide Angle Search for Planets
WFC3 Wide Field Camera 3 (*Hubble* Instrument)
XO XO Project (Telescope)